ABSTRACT

Title of Document: FATIGUE PROPERTIES OF GRAPHENE INTERCONNECTS ON FLEXIBLE SUBSTRATES

Gary Paradee, Doctor of Philosophy, 2014

Directed By: Dr. Aris Christou, Materials Science and Engineering, University of Maryland

This thesis represents the first determination of the fatigue behavior of Graphene as interconnect material electronic components on flexible substrates. The potential application of this interconnect material is for displays on flexible substrates where fatigue resistance is required due to the stress placed on the interconnect during mechanical bending.

As the display is cyclically deformed (fatigued) during normal operation, cracks in the interconnect layer initiate and propagate leading to the lineout failure condition. The major contribution of this work is to show that Graphene is a superior interconnect material to the present state of the art Indium Tin Oxide (ITO) due to its electrical, optical and mechanical properties.

The experimental approach in this thesis is based on Graphene samples which were fabricated on Silicon Nitrite (Si_3N_4)/Polyethylene Naphthalate (PEN) substrates. For comparison, both patterned and uniform ITO films ITO films on Si_3N_4/PEN were fabricated. The results of the in-depth characterization of Graphene are reported and based on Atomic Force Microscopy (AFM), Raman Spectroscopy and Scanning Electron Microscopy (SEM) are reported.

The fatigue characteristics of ITO were determined at stress amplitudes ranging from 2000 MPa to 400 MPa up to 5000 cycles. The fatigue characteristics of Graphene were determined at stress amplitudes ranging from 80 GPa to 40 GPa up to 5000 cycles. The fatigue S-N curves were determined and showed that Graphene's endurance limit is 40 GPa. Beyond the endurance limit, there is no observable high cycle or low cycle fatigue indication for Graphene on a flexible substrate such as PEN. The microstructural analysis by SEM and AFM did not reveal normal fatigue crack growth and propagation.

This thesis presents the first comprehensive behavior of Graphene in a bending fatigue stress environment present in numerous flexible electronic applications. The design and stress environments for safe operation has been defined.

FATIGUE PROPERTIES OF GRAPHENE INTERCONNECTS ON FLEXIBLE SUBSTRATES

By

Gary Paradee

Dissertation submitted to the Faculty of the Graduate School of the

University of Maryland, College Park, in partial fulfillment

of the requirements for the degree of

Doctor of Philosophy

2014

Advisory Committee:
Professor Aris Christou, Chair
Professor Tom Martin
Professor Patrick McCluskey
Professor Isabel Lloyd
Professor Sreeramamurthy Ankem

© Copyright by

Gary Paradee

2014

Acknowledgements

I must thank everyone who contributed to the completion of this work, there are truly too many single everyone out.

I would like to thank my advisor, Dr. Aris Christou, for his guidance, patience and support throughout my graduate studies at Maryland. I would also like to thank the members of my dissertation committee for their support during my research. I also want to thank Dr. Tom Martin and Mr. Jim McIntyre from L-3 Communications for constant support with the experimental and modeling aspect of my work.

I want to thank Mr. Wonseok Hwang for his immense help with all of the AFM characterization we did, those long hours in the AFM dungeon and your help with Photoshop. I also want to thank Dr. Victor Ontiveros, Mr. Reuel Smith and Mr. Mohammed Fardini Nuhi for their help with reviewing concepts of reliability engineering with me, even if it did take me multiple tries to fully understand it. I want to thank Mr. Hannes Greve and Giovanni Flores and other members of CALCE who have helped with experimental design, sample preparation and SEM work, without them my research would not have gone so smoothly.

I must thank my colleagues in the Materials Science for their constant support and the countless hours of help discussing the challenges of research. Specifically, my thanks to Dave, Paris, Josh, Amy, Keith, Sean and Will.

Thanks, to all my running club friends for providing me a great stress outline. For moments of peace each week during our runs and food adventures afterwards.

Table of Contents

Acknowledgements ii
Table of Contents iii
List of Tables v
List of Figures vii
Chapter 1 : Introduction/Problem Statement 1
1.1. Problem Statement 1
1.2. Introduction to Displays 3
1.3. Failure Modes in Flexible Displays 4
1.3.1. Channeling Cracking/Delamination 4
1.3.2. The Role of Moisture 7
1.3.3. Fatigue 9
1.3.4. Lineouts: A Critical Reliability Concern 11
1.3.5. Failure mode, effects, and criticality analysis (FMECA) of Line Outs . 13
Chapter 2 : Interconnect Materials for Flexible Displays 18
2.1. Indium Tin Oxide (ITO) 19
2.1.1. Optical and Electrical Properties of ITO 21
2.1.2. Mechanical Properties of ITO 24
2.2. Graphene 34
2.2.1. Crystal Structure 34
2.2.2. Fabrication Techniques 36
2.2.3. Electrical Properties of Graphene 44
2.2.4. Optical Properties of Graphene 56
2.2.5. Mechanical Properties of Graphene 57
2.3. ITO vs. Graphene 63
Chapter 3 : Experimental Setup 65
3.1. Test Setup for Patterned ITO Devices 65
3.2. Test Setup for uniform films of ITO and Graphene 67
3.3. Sample Design/Fabrication 70
3.3.1. Patterned ITO Samples 70
3.3.2. Uniform ITO Samples 75
3.3.3. Uniform Graphene Samples 77
Chapter 4 : Mechanical Stresses in Thin Films 81
4.1. Internal Stresses 81
4.2. External Stresses 83
4.3. Mechanical test methods for Flexible Displays 85
4.4. Modeling of Bending Stresses in ITO and Graphene 88
4.4.1. Stoney's Equation 88
4.4.2. Finite Element Analysis using ANSYS 92
4.4.3. Determination of Mandrel Sizes for Fatigue Experiments 101
Chapter 5 : Results 103
5.1. Graphene Fabrication Vendor Selection 103
5.1.1. Raman Spectroscopy 103
5.1.2. Atomic Force Microscopy 108
5.2. Characterization of Graphene before testing 111

5.3. Fatigue testing 123
5.3.1. Patterned ITO Samples 123
5.3.2. Uniform ITO Samples 134
5.3.3. Uniform Graphene Samples 143
5.4. Summary 154
Chapter 6 : Conclusions and Future Work 156
6.1. Summary 156
6.2. Thesis Contributions 159
6.3. Future Work 159
Appendix A: Raman Spectroscopy 162
Appendix B: Atomic Force Microscopy Images 163
Appendix C: Stoney's Equation and ANSYS 173
Appendix D: Fatigue Simulations and Results 179
Appendix E: Scanning Electron Microscopy Images 197
References 200

List of Tables

Table 1.1: Comparison of ORT and WVTR values of PET and nylon substrates containing thin film coatings 8
Table 1.2: FMEC Analysis showing causes of horizontal Line Outs 15
Table 1.3: FMECA analysis of Line Outs in flexible displays 16
Table 2.1: Summary of Figure of Merits for Ag and ITO 19
Table 2.2: Electrical Properties of 100 nm thick films of amorphous and crystalline ITO 23
Table 2.3: Comparison of COS in ITO layers under Tension or Compression 27
Table 2.4: Weibull values for different COS values for ITO lines of varying widths 30
Table 2.5: Summary of Growth Conditions for CVD of Graphene on Cu from literature 39
Table 2.6: Summary of the various properties of ITO of Graphene 63
Table 3.1: Summary of Processing Conditions and Material Properties for Multilayer ITO Samples 72
Table 4.1: Summary of elastic properties of PEN, ITO and Graphene used in Stoney's equation calculations for bending stresses in ITO/PEN and Graphene/PEN samples 89
Table 4.2: Summary of Mechanical Properties used for ANSYS Analysis 93
Table 4.3: Effect of mandrel size on the bending stress in each of the layers of Figure 4.12a for mandrel diameters ranging from 1.79 mm to 7.94 mm for 0.05 µm thick ITO traces 96
Table 4.4: Effect of ITO trace thickness on the bending stress in each of the layers of Figure 4.12a for mandrel diameters ranging from 1.79 mm to 7.94 mm 97
Table 4.5: Effect of Mandrel diameter on Bending Stress in ITO or Graphene layers for mandrel diameters ranging from 1-4 mm 99
Table 4.6: Summary of FEA work to determine the mandrel diameters for experimental work 101
Table 5.1: Summary of Graphene Coverage Analysis for 12 Different Samples 114
Table 5.2: Summary of Average RMS Roughness Measurements for Bare PEN, Si_3N_4/PEN, ITO on Si_3N_4/PEN and Graphene on Si_3N_4/PEN 116
Table 5.3: Summary of Total Change in RMS Roughness for the various fabrication steps used to create the final samples of uniform ITO and Graphene samples 116
Table 5.4: Profile of Life Tests performed on Patterned ITO Samples 123
Table 5.5: Effect of Trace width on C and m parameters of Power-Law model used to fit the patterned ITO data 127
Table 5.6: Summary of Weibull and Lognormal goodness of fit for Patterned ITO Samples 130

Table 5.7: Mean cycles to Failure for Patterned ITO samples tested at stress amplitudes of 500, 1000 and 2000 MPa respectively for trace widths of 0.5 μm, 0.75 μm and 1.5 μm respectively. 132
Table 5.8: IPL-Weibull parameter estimation for 0.5, 0.75 and 1.5 um trace data .. 133
Table 5.9: Summary of Stress-Life Data for bending fatigue studies for uniform ITO on Si_3N_4/PEN samples tested at 600, 500 and 400 MPa respectively........ 140
Table 5.10: Summary of Weibull and Lognormal goodness of fit for Uniform ITO Samples 141
Table 5.11: Mean cycles to Failure for uniform ITO samples tested at stress amplitudes of 600, 500, 450 and 400 MPa respectively 142
Table 5.12: IPL-Weibull parameter estimation for Uniform ITO on Si_3N_4/PEN Samples tested at 600, 500 and 400 MPa respectively 143
Table 5.13: Summary of Stress-Life Data for bending fatigue studies uniform Graphene on Si_3N_4/PEN samples tested at 80, 60, 50 and 40 GPa respectively 148
Table 5.14: Summary of Weibull and Lognormal goodness of fit for Uniform Graphene Samples 149
Table 5.15: Mean cycles to Failure for uniform Graphene samples tested at stress amplitudes of 80, 60, 50 and 40 GPa respectively 150
Table 5.16: IPL-Weibull parameter estimation for Uniform Graphene on Si_3N_4/PEN Samples tested at 600, 500 and 400 MPa respectively 151
Table 5.17: IPL-Weibull parameter estimation for patterned ITO, uniform ITO on Si_3N_4/PEN and uniform Graphene on Si_3N_4/PEN samples 152
Table 6.1: Summary of IPL-Weibull Parameter estimation for patterned ITO, Uniform ITO and Uniform Graphene Samples 158

List of Figures

Figure 1.1: Illustration of Layer Stack Structure in Flexible Displays 3
Figure 1.2: Common Failure Modes in Layered Film Devices 4
Figure 1.3: After initial de-bonding, film buckling occurs creating additional film stresses 5
Figure 1.4: Illustration of 2 Cases leading to Channel Cracking 6
Figure 1.5: Illustration of typical SN Curve 10
Figure 1.6: Illustration of Vertical/Horizontal Line-Outs on a Display...................... 12
Figure 1.7: Schematic of Interconnects in displays 12
Figure 1.8: Schematic of display components used in the FMEA Analysis............... 14
Figure 2.1: Bixbyite Crystal Structure of ITO 20
Figure 2.2: SEM Image depicting "Rice Field" microstructure of ITO 20
Figure 2.3: Effect of Film Thickness on Surface Morphology of ITO Films on glass with film thicknesses of a) 162 nm b) 270 nm c) 540 nm and d) 840 nm 21
Figure 2.4: Effect of ITO Film thickness on Sheet Resistance and Resistivity 22
Figure 2.5: Effect of O_2 Concentration on resistivity of ITO Films 22
Figure 2.6: Optical transmittance vs. wavelength for ITO films on PET with thicknesses of 114.5, 87.2 and 25 nm respectively... 24
Figure 2.7: Change in Resistance of ITO coated PET as a function of strain for three different thicknesses (• - 105 nm, □ – 42 nm and ○ – 16.8 nm) respectively. The dotted line represents the stress-strain curve for ITO coated PET............................. 25
Figure 2.8: Biaxial Tensile failure of a 200 nm thick ITO on HC polymer 26
Figure 2.9: Crack Progression of 100 nm ITO on HC polymer during tensile loading (along the horizontal direction) with a) Unstrained ITO b) at 1.28 % strain with the arrow indicating a coating defect leading to failure initiation c) at 1.42% strain and d) at 3.42% strain... 26
Figure 2.10: Optical microscopy images showing the evolution of cracking of ITO layer in tension where strain increases from 2% to 3.3% from left to right 27
Figure 2.11: Schematic Illustration of Series Crack Resistance Model in ITO 28
Figure 2.12: Weibull plot showing effect ITO line width on COS............................. 30
Figure 2.13: a) Change in resistance vs. number of cycles for three different radii of curvature.. 31
Figure 2.14: Change in resistance vs. number of cycles showing crack growth rate . 32
Figure 2.15: 3D Surface showing the interaction between (a) bending diameter and number of cycles; (b) bending diameter and sample width; and (c) sample width and bending frequency for fatigued ITO on PET samples 33
Figure 2.16: 2D hexagonal lattice of Graphene highlighting the unit cell (gray) and the zigzag and armchair edges 35
Figure 2.17: Bernal and Rhombohedral stacking of Graphene................................... 35

Figure 2.18: SEM Images illustrating effect of various growth conditions (Temperature, Pressure and Methane Flow Rate) on resulting microstructure where the scale bar is 10 µm...... 39
Figure 2.19: Effect of H_2 Partial Pressure on Graphene grain shape. Scales bars are 10 µm (top two images) and 3 µm (bottom two images)...... 40
Figure 2.20: Schematic Illustrating Fabrication of Graphene on PET...... 42
Figure 2.21: Schematic illustrating transfer process of Graphene on Cu foil to PET 43
Figure 2.22: Schematic Illustration of Roll to Roll Fabrication Process for Graphene 43
Figure 2.23: Graphene sub-lattice where each lattice A atom is surrounded by 3 atoms on the B lattice...... 44
Figure 2.24: Band structure of Graphene showing the conduction and valence bands meeting at the Dirac points (blue dots)...... 45
Figure 2.25: Modulation of resistivity in Graphene using gate voltage...... 45
Figure 2.26: Measured conductivity of Graphene as a function of gate voltage or carrier density...... 46
Figure 2.27: Conductivity vs. Gate voltage for 5 different Graphite on SiO_2 samples showing effect of sample quality. Insert shows a detailed view of the density-dependent conductivity near the Dirac point....... 48
Figure 2.28: Effect of 2D Graphene and Impurity layer distance on conductivity...... 49
Figure 2.29: Comparison of Hwang et al. developed theory with experimental data 50
Figure 2.30: Graphene conductivity calculated using a combination of short and long range scatterers...... 50
Figure 2.31: Effect of Current Annealing technique on suspended Graphene on SiO_2 51
Figure 2.32: Calculated resistivity vs. scaled temperature, T/T_F for different $r_s = 0.88$, 2.2, 0.1, and 0.01 (from top to bottom). Insert shows a magnifed view of the low temperature limit ($T < 0.5T_F$)...... 54
Figure 2.33: Hall mobility of holes as function of temperature for monolayer Graphene with varying carrier densities...... 54
Figure 2.34: Optical transmittance of n-layer Graphene films at 550 nm as a function of the number of Graphene layers...... 57
Figure 2.35: Illustration of AFM nano-indentation setup to determine mechanical properties of Graphene...... 58
Figure 2.36: Load vs. Deflection curves obtained using nano-indentation AFM of Graphite flakes on SiO_2...... 59
Figure 2.37: Stress-Strain Curve for Graphene as measured using nano-indentation AFM...... 59
Figure 2.38: Stress-Strain Curves for both the Zigzag and armchair directions via MD Simulations...... 60

Figure 2.39: a) Schematic of Single Axis Linear miniature motorized stage used for test b) % Change in Resistance as a function of strain for Graphene 61
Figure 2.40: Schematic of SEM + nano-indentor Setup b-h) Illustration of Indentation Process to test Graphene samples 62
Figure 2.41: % Change in Resistance as a function of Strain for Graphene samples tested using SEM + nano-indentation setup... 62
Figure 3.1: Block diagram of fatigue test setup for patterned ITO samples 65
Figure 3.2: Bending fatigue setup used for patterned ITO samples 66
Figure 3.3: Block diagram of fatigue test setup for uniform ITO or Graphene samples 68
Figure 3.4: Bending fatigue setup used for uniform ITO or Graphene samples......... 68
Figure 3.5: Updated sample mounting system used for uniform ITO or Graphene samples.. 69
Figure 3.6: Mandrels (13, 8, 6, 5 and 1.62 mm) used to perform fatigue studies on uniform ITO or Graphene samples 70
Figure 3.7: Cross Section View of Multilayer ITO Samples for Bending Fatigue Tests 71
Figure 3.8: SEM image showing the effect of PTS-9 deposition on the surfaces of planarized and uncoated PEN 72
Figure 3.9: Photolithography masked used to fabricate samples with patterned ITO traces with widths of 1.5, 0.7 and 0.3 μm respectively.. 73
Figure 3.10: a) Schematic of TAB Bonding Card b) Illustration showing the connection the TAB card makes 74
Figure 3.11: Image of ITO Samples TAB Bonded with Silver Epoxy Attached a) Back View b) Front View 75
Figure 3.12: Cross Section View of Uniform ITO Samples for Bending Fatigue Tests 76
Figure 3.13: Drawing of Uniform ITO film.. 76
Figure 3.14: Uniform ITO on Si_3N_4/PEN sample with silver-epoxy leads 77
Figure 3.15: Cross Section view of Graphene samples used for Bending Fatigue Tests 78
Figure 3.16: Drawing of Graphene test sample 78
Figure 3.17: Illustration of "Floating Graphene" transfer technique 79
Figure 3.18: Image of Uniform Graphene on Si_3N_4/PEN sample with silver-epoxy leads 80
Figure 4.1: Bilayer structure bent to a specific radius of curvature using a cylinder . 84
Figure 4.2: Schematic Representation of Uniaxial Test Method 85
Figure 4.3: Detailed schematic of Uniaxial Testing Method 86
Figure 4.4: Schematic of Two Point Bending Method 86
Figure 4.5: Schematic of Biaxial Test Method 87

Figure 4.6: Polyimide foil with a-Si/SiN islands after deformation under the biaxial test method 87
Figure 4.7: Schematic Illustration of Cyclic Mandrel Test Method 88
Figure 4.8: Effect of Graphene layer thickness on bending stress in Graphene layer using Stoney's Equation 90
Figure 4.9: Effect of PET layer thickness on bending stress in Graphene layer using Stoney's Equation 90
Figure 4.10: Effect of ITO layer thickness on bending stress in ITO layer using Stoney's Equation 91
Figure 4.11: Effect of PET layer thickness on bending stress in ITO layer using Stoney's Equation 91
Figure 4.12: Cross section view of a) patterned ITO b) uniform ITO and c) uniform Graphene on Si_3N_4/PEN substrates. 93
Figure 4.13: a) ANSYS Model used for modeling patterned ITO on Si_3N_4/PEN b) ANSYS Model used for modeling uniform ITO or Graphene on Si_3N_4/PEN 94
Figure 4.14: Stress distribution in the bending direction (x-direction) for a patterned ITO Sample bent to a radius of curvature of 2 mm for a) ITO layer b) Si_3N_4 layer c) PTS-R9 layer and d) PEN layer 95
Figure 4.15: Effect of mandrel size on the bending stress in each of the layers a) ITO b) Si_3N_4 c) PTS-R9 and d) PEN of Figure 4.12a for mandrel diameters ranging from 1.79 mm to 7.94 mm for 0.05 μm thick ITO traces 96
Figure 4.16: Effect of ITO trace thickness on the bending stress in each of the layers of Figure 4.12a for mandrel diameters ranging from 1.79 mm to 7.94 mm 97
Figure 4.17: Stress distribution in the bending direction (x-direction) for a uniform ITO/PEN and uniform Graphene/PEN sample bent to a radius of curvature of 2 mm for a) ITO layer b) Graphene layer c)) PEN layer 98
Figure 4.18: Effect of Mandrel diameter on Bending Stress in ITO or Graphene layers for mandrel diameters ranging from 1-4 mm 100
Figure 5.1: a) Raman Spectra of Graphene b) Effect of Number of Layers on 2D Peak 104
Figure 5.2: Raman spectra of a monolayer of Graphene on SiO_2 (Graphenesquare) 105
Figure 5.3: Raman spectra of a bare PET 106
Figure 5.4: Raman spectra of a monolayer of Graphene on PET (ACS Materials) .. 106
Figure 5.5: Raman spectra of monolayer of Graphene on PET (Graphene Square) . 107
Figure 5.6: Raman spectra of monolayer of Graphene on PET (Graphene Supermarket) 107
Figure 5.7: Raman spectra of monolayer of Graphene on SiO_2 and bare PET showing bare PET's overlapping peaks 108
Figure 5.8: 10x10 um AFM (Tapping Mode) Image of ACS Material sample 109
Figure 5.9: 5x5 um AFM (Tapping Mode) Image of Graphene Platform sample 109

Figure 5.10: 1x1 um AFM (Tapping Mode) Image of Graphene Supermarket Sample 110
Figure 5.11: Raman Spectra of Graphene Samples for Initial Characterization....... 111
Figure 5.12: 20x20 μm grid used for Graphene coverage analysis using Raman spectroscopy 112
Figure 5.13a-l: 20x20 μm grids showing results Graphene coverage (red regions) analysis using Raman spectroscopy for 12 different samples 113
Figure 5.14: 20x20 μm Tapping mode AFM images of a) Bare PEN b) Si_3N_4/PEN c) ITO/Si_3N_4/PEN and d) Graphene/Si_3N_4/PEN used for the surface roughness analysis 115
Figure 5.15: a) 10x10 um AFM (Tapping Mode) phase images of a) Si_3N_4/PEN and b) Graphene surface 117
Figure 5.16: 10x10 um AFM (Tapping Mode) phase image of Graphene-Planarized PEN Interface 118
Figure 5.17: SE-SEM image of Graphene on Si_3N_4/PEN at the interface between the Graphene and Si_3N_4/PEN 119
Figure 5.18: 10x10 um AFM (Tapping Mode) phase image of Graphene- Si_3N_4/PEN Interface 120
Figure 5.19: Height profile between the 2 green circles in Figure 5.18 showing surface roughness of Graphene on Si_3N_4/PEN 121
Figure 5.20: 10x10 um AFM (Tapping Mode) height image of Si_3N_4/PEN with green line denoting line across which height profile measurements were made 122
Figure 5.21: Height profile of green line shown in Figure 5.20 122
Figure 5.22: Resistance vs. Number of Cycles for a patterned ITO Sample 124
Figure 5.23: Effect of a) Radius of Curvature b) Trace Width on change in resistance in ITO Samples 125
Figure 5.24: Stress vs. Number of Cylces for patterned ITO samples on Si_3N_4/PEN with trace widths of 0.5, 0.75 and 1.5 μm respectively under stress amplitudes of 500, 100 and 2000 MPa respectively 126
Figure 5.25: Life vs. Stress Curves for Fatigue Tests done at 3 Different Stress Levels (500, 1000 and 2000 MPa) for a 0.5 um wide ITO trace with 95% confidence bounds and the red line denoting the mean life 131
Figure 5.26: Life vs. Stress Curves for Fatigue Tests done at 3 Different Stress Levels (500, 1000 and 2000 MPa) for a 0.75 um wide ITO trace with 95% confidence bounds and the line denoting red the mean life 131
Figure 5.27: Life vs. Stress Curves for Fatigue Tests done at 3 Different Stress Levels (500, 1000 and 2000 MPa) for a 1.5 um wide ITO trace with 95% confidence bounds and the red line denoting the mean life 132
Figure 5.28: 30x30 um AFM (Tapping Mode) a) height image b) phase image of uniform untested uniform ITO on Si_3N_4/PEN substrate 134

Figure 5.29: SE-SEM image of untested uniform ITO on Si_3N_4/PEN substrate 135
Figure 5.30: Change in Normalized Resistance ($\Delta R/R_o$) vs. Number of Cycles for an ITO on Si_3N_4/PEN tested at 600 MPa 136
Figure 5.31: Change in Normalized Resistance ($\Delta R/R_o$) vs. Number of Cycles for ITO on Si_3N_4/PEN tested at 600, 500 and 400 MPa 137
Figure 5.32: Change in Strain vs. Number of Cycles for ITO on Si_3N_4/PEN samples tested at 600, 500 and 400 MPa for the first 50 cycles 139
Figure 5.33: Stress vs. Number of Cycles for Uniform ITO Samples on Si_3N_4/PEN 140
Figure 5.34: Life vs. Stress Curves for Fatigue Tests done at 4 Different Stress Levels (600, 500, 450 and 400 MPa) for Uniform ITO Samples on Si_3N_4/PEN with 95% confidence bounds and red line denoting mean life 142
Figure 5.35: Stress-Strain Curve for Graphene as measured using nano-indentation AFM 144
Figure 5.36: Change in Normalized Resistance ($\Delta R/R_o$) vs. Number of Cycles for a uniform Graphene on Si_3N_4/PEN sample tested at 80 GPa 145
Figure 5.37: Change in Normalized Resistance ($\Delta R/R_o$) vs. Number of Cycles for uniform Graphene on Si_3N_4/PEN samples tested at 80, 60, 50 and 40 GPa 146
Figure 5.38: Change in Strain vs. Number of Cycles for uniform Graphene on Si_3N_4/PEN samples tested at 80, 60, 50 and 40 GPa for the first 50 cycles 147
Figure 5.39: Stress vs. Number of Cycles for Uniform Graphene Samples on Si_3N_4/PEN 148
Figure 5.40: Life vs. Stress Curves for Fatigue Tests done at 4 Different Stress Levels (80, 60, 50, and 40 MPa) for uniform Graphene samples on Si_3N_4/PEN with 95% confidence bounds and red line denoting mean life 150
Figure 5.41: SE-SEM images of the Graphene-Si_3N_4/PEN interface illustrating crack formation/propagation (white lines) for samples tested at applied bending stress amplitudes of a) 80 GPa and b) 60 GPa 153

Chapter 1 : Introduction/Problem Statement

1.1. Problem Statement

The present thesis presents the first determination of the fatigue properties and response of Graphene as an interconnect material for flexible displays. Flexible electronics are defined as electronic components fabricated on flexible plastic substrates. There are many potential applications of flexible electronics including flexible displays, sensors for aircraft and cars, solar cells and biomedical sensors. The major reliability problems that plague flexible displays include moisture permeation, the complex interactions at the interfaces of the layer stack structure of flexible display devices and the mechanical stresses induced during normal use of a flexible display.

The technical contribution this thesis makes is the resolution of the flexible display condition known as lineouts. The lineout condition is caused by the brittle nature of the present, state of practice, interconnect material Indium Tin Oxide (ITO). As the display is bent (fatigued) during normal operation, cracks in the interconnect layer initiate and propagate leading to the lineout condition. One of the major contributions of this work is the introduction of Graphene as the preferred interconnect material in comparison to ITO due to its combination of electrical, optical and mechanical properties.

The experimental approach consists of the fabrication of the designed test samples, the development of test procedures for the fatigue phenomena, the construction of the necessary apparatus and finally, the validation of the experimental

results through material characterization techniques. In this work, Graphene samples were fabricated on Silicon Nitrite (Si_3N_4)/Polyethylene Naphthalate (PEN) substrate. Additionally, both patterned and uniform ITO films on Si_3N_4/PEN were fabricated. In order to evaluate the quality of the fabricated samples, a non-destructive methodology was developed using a combination of Atomic Force Microscopy (AFM), Raman Spectroscopy and Scanning Electron Microscopy (SEM) in order to analyze the surface coverage/uniformity and identify number of layers for the Graphene samples.

In order to investigate the fatigue properties of Graphene, a custom experimental setup was developed which allows for real-time monitoring of Graphene property changes. During the development of this custom experimental setup, analytical expressions for bending stresses and finite element modeling were used to optimize the design of the samples and the experimental setup. Finite element models were developed for both ITO and Graphene and were used to simulate the effect of various mandrel sizes and the corresponding bending stresses generated in the samples. These calculations coupled with the stress-strain curves for both ITO and Graphene were used to determine the appropriate mandrel sizes for the fatigue experiments.

Both Graphene and ITO samples were tested under a variety of stress ampltidues using the developed fatigue apparatus. The results of the fatigue experiments were then applied to develop a probabilistic fatigue life model for Graphene and ITO. Additionally, the microstructural evolution of Graphene and ITO during fatigue and changes in physical properties of Graphene and ITO on flexible substrates was investigated. The results show that Graphene does not have the

expected classical fatigue behavior, but has no observable fatigue deformation up to the limits of the present experimental work.

1.2. Introduction to Displays

Flexible displays consist of a layer stack structure consisting of a plastic substrate, active matrix array, display material, a common electrode and an encapsulation layer as pictured in Figure 1.1 below:

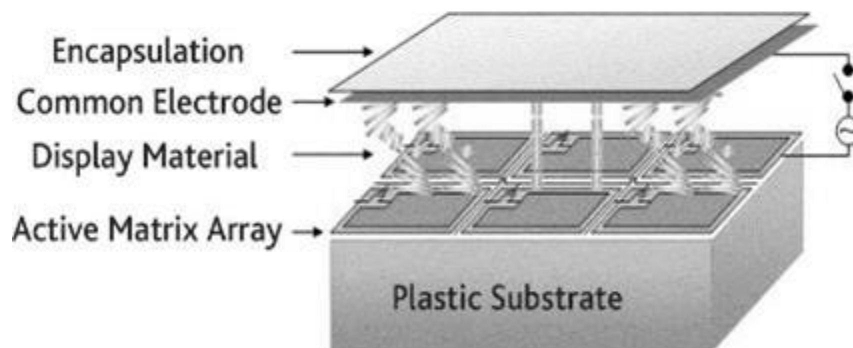

Figure 1.1: Illustration of Layer Stack Structure in Flexible Displays [1]

The active matrix layer shown above in Figure 1.1 consists of a grid of thin film transistors (TFTs) that individually control pixels on the display. Each pixel is addressed in the matrix by row and column signals that represent gate source and source connects in the TFT backplane. In order to display an image, a voltage is applied to the gate of the TFT which acts as a switch to transfer the image data (voltage) from the source line to the bottom electrode. This in turn illuminates each pixel to an appropriate intensity in order to display the appropriate image.

1.3. Failure Modes in Flexible Displays

1.3.1. Channeling Cracking/Delamination

The dominant failure mechanism for thin film layered devices under stress involves the growth and propagation of micro-cracks [2]. This failure mechanism depends on the substrate's elastic modulus, film adhesion and film cohesion. The two most common types of failures for brittle films on flexible substrates are film cracking/channeling and delamination. An illustration of the two types of failure modes is shown below in Figure 1.2:

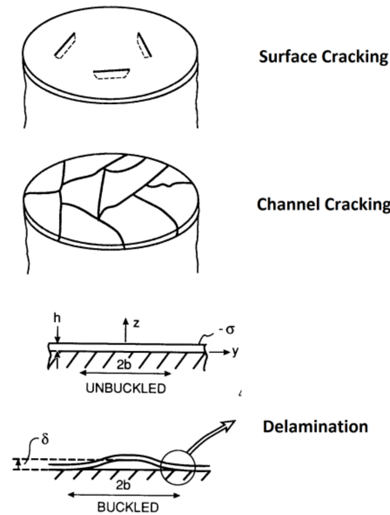

Figure 1.2: Common Failure Modes in Layered Film Devices [2]

Thin films in compression undergo 3 stages until failure: delamination from the substrate, buckling of the film and finally cracking of the film. Delamination of the film is related to adhesion issues leading to sliding induced delamination. Once a film has started to de-bond from the substrate (as shown below in Figure 1.3), the length of the deboned film will keep increasing until a critical length is reached and the film will start

buckling. The expression for the critical length was derived by Suo et al. [3] and is shown below:

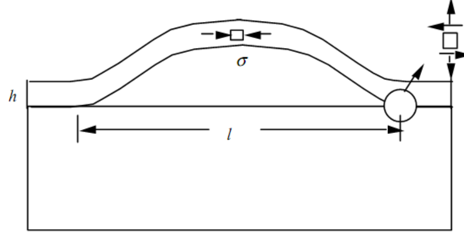

Figure 1.3: After initial de-bonding, film buckling occurs creating additional film stresses [3]

$$l_c = \frac{\pi h_{film}}{\sqrt{3\left(1-v_{film}^2\right)}}\sqrt{\frac{E_{film}}{\sigma_{film}}} \qquad (1.1)$$

where h_{film} is the film thickness, v_{film} is the Poisson's ratio of the film, E_{film} is the elastic modulus of the film and σ_{film} is the stress in the film.

The mechanics of single angle and multilayered films on flexible substrates has been studied extensively [2]–[4]. The main assumption is that the film initially has a defect as a result of the fabrication process that will propagate with a depth equal to the film thickness. The crack will propagate until it is arrested at the interface and then it will propagate laterally in the film, uninhibited until it meets another crack or the edge of the film. When a crack propagates through a material, there is an associated elastic energy reduction with the creation of new crack surfaces. Therefore it is very important to determine the critical stress needed for crack initiation. Here, two cases need to be considered: Case A when the pre-existing crack size is much smaller than the film thickness and Case B when the pre-existing crack size is comparable to the

film thickness. In case A, the crack will propagate both towards the interface and laterally in the film while in Case B the crack will only propagate laterally in the film. An illustration of Case A and B is shown below in Figure 1.4:

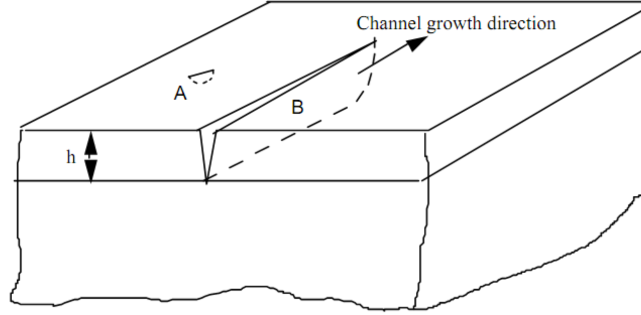

Figure 1.4: Illustration of 2 Cases leading to Channel Cracking[3]

In Case A, for an infinite homogenous material, a pre-existing crack will propagate when the crack driving force equals or exceeds the material's crack resistance (Γ_f):

$$\Gamma_f = \frac{Y\sigma^2 a}{E_f} \tag{1.2}$$

where Y is a dimensionless parameter depending on the geometry [5], σ is the intrinsic stress, a is the crack size and E_f is the elastic modulus of the film. Here the critical stress for crack initiation depends on the size of the pre-existing defect which can be difficult to be measure. For case B, when the lateral crack length exceeds several times the film thickness, the driving force reaches a steady state value given by [2]:

$$G = Z(\alpha, \beta)\frac{(1 - \upsilon_f^2)\sigma^2 h}{E_f} \tag{1.3}$$

where h is the film thickness, σ is the intrinsic stress, E_f and E_s are the elastic moduli of the film and substrate, ν_f and ν_s are the Poisson's ratio of the film and substrate

respectively. The Z term is a constant that depends on the crack type and the elastic mismatch between the film and the substrate where α and β are the Dundurs' parameters given by [2]:

$$\alpha = \frac{\overline{E_f} - \overline{E_s}}{\overline{E_f} + \overline{E_s}} \tag{1.4}$$

$$\beta = \frac{\overline{E_f}(1 - v_f)(1 - 2v_s) - \overline{E_s}(1 - v_s)(1 - 2v_f)}{2(1 - v_f)(1 - v_s)(\overline{E_f} + \overline{E_s})} \tag{1.5}$$

where:

$$\overline{E_f} = \frac{E_f}{(1 - v_f^2)} \tag{1.6}$$

$$\overline{E_s} = \frac{E_s}{(1 - v_s^2)} \tag{1.7}$$

One can calculate the critical stress required to propagate a channel crack given the elastic properties of the film and the substrate, the film thickness and the film crack resistance.

1.3.2. The Role of Moisture

The third failure mechanism of flexible displays that will be reviewed is moisture permeation. With the development of thin film organic electronics, the sensitivity of these organic layers to water vapor is a reliability concern. In Organic Light Emitting Diodes (OLED) devices, Ca and Li (low work function metals) are used to inject electrons from the cathode to the organic luminescent layers. Hydrolysis of the cathode metals creates nonconductive regions in the electrode which results in non-emissive "black spots" and pixel shrinkage [6], [7] . An OLED device on

Polyethylene terephthalate (PET) can only survive for a few hours in atmospheric conditions if a barrier layer isn't used. Display manufactures require devices that have water vapor permeation rates (WVTW) of < 10^{-5} g/m^2 per day at 25°C and 40% relative humidity [8]. An inorganic layer deposited using Physical Vapor Deposition (PVD) or Chemical Vapor Deposition (CVD) is used to inhibit water and oxygen diffusion through the organic layers. By depositing this organic layer, the respective WVTW and Oxygen permeation rates (OTR) can be reduced leading to longer device lifetimes as shown below:

Table 1.1: Comparison of ORT and WVTR values of PET and nylon substrates containing thin film coatings [9]

Normalized to 1 mil thickness	OTR (cm^3 (STP)/m^2 per day per atm)	WVTR (g/m^2 per day) at 90-100% RH
PET/SiOx	2	1.1
PET/AlOx	1.5	5
PET/ITO	1.56	0.2
PET/Al	0.31-1.55	0.31-1.55
PET	79	10.7

For many of the inorganic layers seen in Table 1.1, the presence of defects in the deposited films causes the WVTR values to be higher than their bulk film counterparts because these defects act as fast vapor permeation pathways [10]–[18]. Due to the presence of defects, a multilayer barrier layer structure is utilized because the increased layers act as additional barriers to oxygen and water vapor diffusion through the layer stack structure. The permeation through a multilayer structure can be described using a 1-D series resistance model known as the ideal laminate theory [18], [19]. The permeability of each layer, P, is given by:

$$P = DS \tag{1.8}$$

and the permeability of the entire multilayer structure is:

$$\frac{1}{P_t} = \frac{1}{P_1} + \frac{1}{P_2} + \cdots + \frac{1}{P_n} \tag{1.9}$$

where D and S are the diffusivity and solubility of the respective bulk materials, P_t is the total permeability through the multilayer structure and P_1, P_2 and P_n are the permeability rates through the respective layers.

The permeation rates obtained from the ideal laminate theory were found to be several orders of magnitude lower than observed values due to the discrepancy between permeation of bulk and thin film organic materials. The surface coverage and pinhole/defect models [11]–[13], [19] were developed to more accurately describe permeation in single layer systems. In both of these models, diffusion through defects in the organic thin films is assumed to dominate the steady-state permeability. For multilayer structures, the polymer interlayer theory proposes that the vapor diffusion is dominated by in-plane diffusion through the polymer layers between widely spaced defects in the oxide layers [15], [20], [21].

1.3.3. Fatigue

Fatigue is a critical failure mechanism during the normal operation of a flexible display. Fatigue is defined as failure due to cyclic deformation and there are two main types of characterization methodologies associated with fatigue. The first method is the Stress-Life method which is traditionally known as the SN method. The S-N method is still used in situations where the applied stress remains predominately in

the elastic range of the material which results in materials having longer lifetimes. For materials/applications that exist in the low cycle regime, the stress-life method is not the best method to describe fatigue behavior. Instead the Strain-Life approach is more suitable because the low cycle regime corresponds to applied strains that contain a significant plastic component. The division between low cycle and the high cycle regime is generally considered to be 10^5 cycles.

The main component of the Stress-Life Method is the S-N diagram. The SN Curve is a plot of stress vs. the number of cycles to failure. The SN curve is usually plotted on a log-log scale and an example SN Curve is shown below in Figure 1.5:

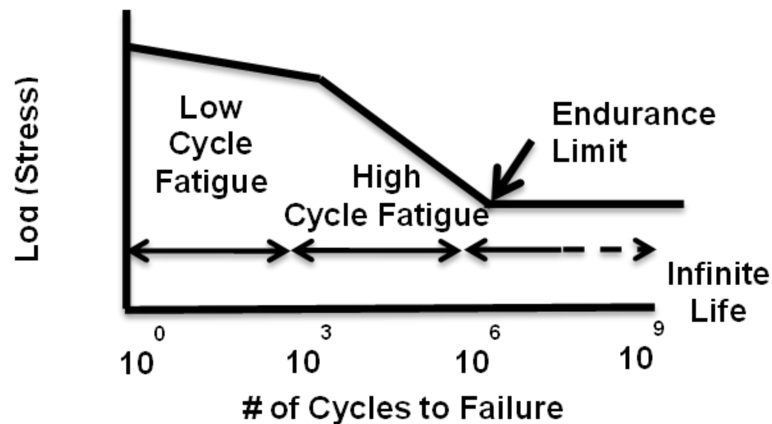

Figure 1.5: Illustration of typical SN Curve

In the present experiments, low cycle fatigue experiments have been carried out in order to reduce costs and the time required to complete all testing. Several models have been used to describe low cycle fatigue behavior which are classified by the driving force parameter used to characterize the fatigue damage process. The two fatigue driving force parameters used are the plastic strain range and the inelastic strain energy density. The two main models include the Plastic Strain Range Model

developed by Coffin-Mason and the energy based fatigue model developed by Morrow. The Coffin-Manson fatigue model (Equation 1.9) [22]–[24] which is often used for low cycle fatigue analysis assumes that fatigue failure is strictly due to plastic deformation and the elastic strain range has a negligible effect on the low cycle fatigue life.

$$N_f^m \Delta\varepsilon_p = C \tag{1.9}$$

where N_f = Number of Cycles to Failure, $\Delta\varepsilon_p$ is the plastic strain range, C is the fatigue ductility coefficient and m is the fatigue exponent. These constants are determined empirically.

The Morrow Model [25] is used to predict the low cycle fatigue life in terms of the strain energy density and it can be expressed by the following expression:

$$N_f^n W_p = K \tag{1.10}$$

where N_f = Number of Cycles to Failure, W_p is the strain energy density, A is a material constant and n is the fatigue exponent. These constants are determined empirically.

1.3.4. Lineouts: A Critical Reliability Concern

The forth failure mechanism that will be reviewed is a condition known as Lineouts. Lineouts are undesired vertical/horizontal lines of red, green, blue, black or white observed by the end-user as seen in Figure 1.6 below:

Figure 1.6: Illustration of Vertical/Horizontal Line-Outs on a Display [1]

This condition is caused by variety of different modes, but the main mechanism that will be focused on in this study is gate line impedance buildup. Recall that displays are made up of an array of pixels that are each individually controlled by a corresponding TFT. These transistors are connected to one another via gate line interconnects. A schematic of this is shown below in Figure 1.7:

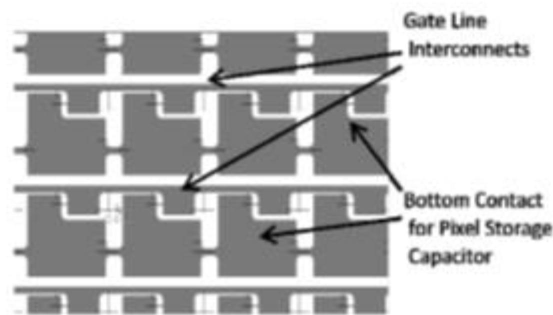

Figure 1.7: Schematic of Interconnects in displays [1]

During normal display operation, for an image to be displayed, first a voltage is sent to each individual TFT in the display array. This voltage biases the TFT causing the corresponding pixel to be illuminated, where the voltage determines the intensity of the light. Now consider, when impedance is built up at the gate, this causes the applied voltage to be insufficient to bias the transistor and the drive voltage is not

transferred from the source to the drain of the TFT. This result in the display image data initiating from the column TAB drivers does not bias the individual pixels in a particular row of the display. The end visual result as observed by the user is a "line out".

1.3.5. Failure mode, effects, and criticality analysis (FMECA) of Line Outs

Failure Modes and Effects Analysis (FMEA) is a design assurance technique used to identify and minimize the effects of potential problems in a product or process design [26]–[28]. As discussed in the previous section, there are 4 different types of failure mechanisms for flexible displays and FMEA was used to determine which one is the most critical. There are two types of FMEA Analysis: Top Down and Bottom Up approaches. In the top down approach, the analyst begins with a block diagram of the system and correlates failures observed at the system level with failure modes in the system black diagram. This process is repeated until the analyst reaches the required level of identification of failure modes in the system. In the bottom up approach, the analyst identifies all of the components of the system. Next the analyst identifies the failure modes of each of these components and how component failure affects the system. This process is repeated until a low level failure mode is found at the highest level of the system and is observed by the end user.

In general, a complete FMEA for an entire display is a lengthy and involved task. Since the scope of this investigation revolves around line outs as observed by the end

user, only those failure modes that propagate and manifest themselves as such shall be considered in this analysis.

FMEA analysis on the factors leading to end user observation of horizontal line outs in the display was conducted by Martin et al [1]. In this FMEA analysis, both a top down and bottom up approach were utilized. A schematic diagram of the components involved in the display system that contribute to horizontal lines outs is shown below in Figure 1.8:

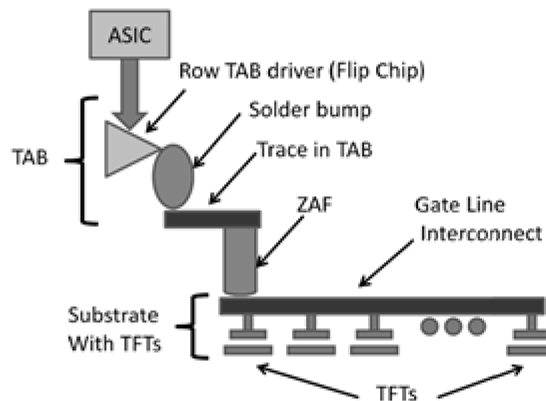

Figure 1.8: Schematic of display components used in the FMEA Analysis [1]

The results of both the top down and bottom up approaches were compared and the resulting abridged version of the FMEA identifying failure modes contributing to horizontal lines outs is shown below in Table 1.2. As seen in Table 1.2 below, 10 unique failure modes leading to horizontal lineouts were identified. The failure modes specific to thin film transistors (TFT) were not included in this list of 10 because the FMEA analysis didn't yield any TFT failure modes that lead to line outs.

Table 1.2: FMEA Analysis showing causes of horizontal Line Outs [1]

	Failure Mode	Local Effect	System Effect	Severity Class
1	Internal failure leading to timing errors	Incorrect signals to shift registers for both Row/Column synchronizing	Intermittent Line Outs or Entire Picture Unreadable	II
2	Internal failure leading to commands not being fed into row shift register driver circuit	No Voltage applied to an entire row	Horizontal Line Out	II
3	Internal failure leading to commands not being fed into column shift register driver circuit	No Voltage applied to an entire column	Vertical Line Out	II
4	Open Circuit on output of flip chip driver	No Voltage applied to row	Horizontal Line Out	II
5	Degraded voltage on output of flip chip driver	Low Voltage applied to a row	Horizontal Line Out	II
6	Cracked Solder bump leading to open circuit	No Voltage applied to row	Horizontal Line Out	II
7	Open condition in Flex Traces	No Voltage applied to row	Horizontal Line Out	II
8	Open condition between TAB and substrate	No Voltage applied to row	Horizontal Line Out	II
9	High Impedance of Gate Line Interconnect	Not enough voltage to bias TFT	Horizontal Line Out	II
10	Open Gate Condition	Drive voltage to display image not transferred to drain of TFT	Individual Pixel Outage	II

Using the FMEA results shown above, a criticality analysis was performed. The criticality analysis is a combination of the probability that a failure mode will occur with the impact that failure mode has on the system. The failure mode criticality number, C_m, is used to rank each of the potential failure modes based on the mode's occurrence and impact. The equation for the criticality analysis is given below:

$$C_m = \beta\alpha\lambda T \quad (1.11)$$

where β is the failure effect probability, α is the failure mode ratio, λ is the failure rate and T is the operating time. The β value is the conditional probability that the failure effect with its respective criticality classification will occur when a failure mode occurs. β values range from 0 (no effect) to 1 (actual loss). The α value is the probability that will fail in the identified mode of failure [26], [27]. The criticality analysis was performed on the identified failure modes for line-outs shown in Table 1.2 and the results are shown below in Table 1.3. The failure rate was assumed to be 0.001 and the operating time was assumed to be 8766 hours or 1 year of operation.

Table 1.3: FMECA analysis of Line Outs in flexible displays

Component	Failure Mode	Local Effect	System Effect	Severity Class	Failure Effect Probability, β	Failure Mode Ratio, α	Failure Rate, λ	Operating Time, T (hours)	Criticality Number, C_m
Display Driver ASIC	Internal failure leading to timing errors	Incorrect signals to shift registers for both Row/Column synchronizing	Intermittent Line Outs or Entire Picture Unreadable	II	0.33	0.33	0.001	8766	0.9546174
Display Driver ASIC	Internal failure leading to commands not being fed into row shift register driver circuit	No Voltage applied to an entire row	Horizontal Line Out	II	0.33	0.33	0.001	8766	0.9546174
Display Driver ASIC	Internal failure leading to commands not being fed into column shift register driver circuit	No Voltage applied to an entire column	Veritical Line Out	II	0.33	0.33	0.001	8766	0.9546174
Row TAB Driver Circuit	Open Circuit on output of flip chip driver	No Voltage applied to row	Horizontal Line Out	II	0.25	0.5	0.001	8766	1.09575
Row TAB Driver Circuit	Degraded voltage on output of flip chip driver	Low Voltage applied to a row	Horizontal Line Out	II	0.25	0.5	0.001	8766	1.09575
Row TAB Driver Solder Joint to Flip Chip	Cracked Solder bump leading to open circuit	No Voltage applied to row	Horizontal Line Out	II	0.75	1	0.001	8766	6.5745
Row Tab Flex Traces	Open condition in Flex Traces	No Voltage applied to row	Horizontal Line Out	II	0.5	1	0.001	8766	4.383
Row TAB ZAF Connect	Open condition between TAB and substrate	No Voltage applied to row	Horizontal Line Out	II	0.5	1	0.001	8766	4.383
Substrate Row Line Interconnects	High Impedance of Gate Line Interconnect	Not enough voltage to bias TFT	Horizontal Line Out	II	1	1	0.001	8766	8.766
Internal TFT Failure	Open Gate Condition	Drive voltage to display image not transferred to drain of TFT	Individual Pixel Outage	II	0.5	1	0.001	8766	4.383

As shown in Table 1.3, the failure mode with the highest criticality number was high impedance of the gate line interconnect. The remainder of this dissertation is organized into four chapters. Chapter 2 is a literature review of the properties and fabrication techniques for both ITO and Graphene. Chapter 3 will discuss the experimental approach for determining the fatigue properties of ITO and Graphene. In Chapter 4, the bending stress in the ITO and Graphene films using analytical expressions and finite element analysis (FEA) will be discussed. Chapter 5 will review the development of the probabilistic fatigue life model development for both Graphene and ITO and the results of any structure property relations for Graphene and ITO. Finally, the conclusions of this dissertation as well as its contributions and any suggestions for future research are provided in Chapter 6.

Chapter 2 : Interconnect Materials for Flexible Displays

Interconnects electrically connect various components to one another on an integrated circuit (IC) board. On chip interconnects such as Al, Cu and Au have been used previously due to their excellent conductivity properties. As device structures have gotten smaller and smaller due to Moore's law, issues with timing delays, stress migration and Electromigration have become more impactful to device reliability [29], [30].

Materials used for flexible display interconnects need to be conductive and transparent. Materials that are both transparent and conductive can be broken into 3 classes: very thin pure metals, highly doped organic polymers and doped wide band gap oxide or nitride semiconductors.

A figure of merit, ϕ, can be defined in order to help with material selection that considers the ratio of the optical transmittance of a material (at 550 nm) to its sheet resistance [31]:

$$\phi = (x/\rho)\exp(-10\alpha x) \tag{2.1}$$

where α is the visible absorption coefficient, x is the film thickness and ρ is the resistivity of the material. Organic polymers can be eliminated as a candidate because they have low mobilities (< 1 $cm^2/V \cdot s$), low carrier density, poor transparency and they are very sensitive to oxygen and water vapor [9]. Metals are also not ideal candidates because of Electromigration, timing issues and most metals are not

transparent. Now, ϕ was calculated for a metal such as Silver and an oxide such as Indium Tin Oxide (ITO) for comparison purposes as summarized in Table 2.1:

Table 2.1: Summary of Figure of Merits for Ag and ITO [9]

Ag	ITO
$\alpha = 10^8 cm^{-1}\ at\ 550\ nm$	$\alpha = 10^3 cm^{-1}\ at\ 550\ nm$
$\rho = 1.6x10^{-6}\ \Omega \cdot \text{cm}$	$\rho = 1.6x10^{-4}\ \Omega \cdot \text{cm}$
t = 1 nm	t = 1000 nm
$\phi = 0.023\ \Omega^{-1}$	$\phi = 0.22\ \Omega^{-1}$
Both have an optical transmittance of 90%	

From Table 2.1, ITO demonstrates an order of magnitude higher figure of merit when compared to Ag with a thickness 1000x higher. This increased thickness is also beneficial because there are some difficulties with growth of uniform, contiguous films at the 1 nm scale. Finally, despite both Ag and ITO having a 90% optical transmittance value, ITO has a 2 orders of magnitude higher sheet resistance which is more desirable. For these reasons, thermally conductive oxides (TCO's) such as ITO are the preferred material for interconnects.

2.1. Indium Tin Oxide (ITO)

The most widely used TCO material used in active matrix display device applications is Indium Tin Oxide, In_2O_3 (ITO). Crystalline ITO has the bixbyite crystal structure consisting of an 80 atom unit cell with Ia3 space group and a lattice parameter of 1 nm with an arrangement based on stacking of InO_6 coordination groups. The structure is a face centered cubic array of cations where the tetrahedral interstitial positions are occupied by anions. The bixbyite crystal structure may be visualized

with respect to a simpler face-centered cubic fluorite (CaF_2) 2 x 2 x 2 supercell with just one quarter of the anion sites vacant [9], [32], [33]. An illustration of the bixbyite crystal structure and Scanning Electron Microscope (SEM) images of the microstructure of ITO are shown below in Figures 2.1 and 2.2 respectively:

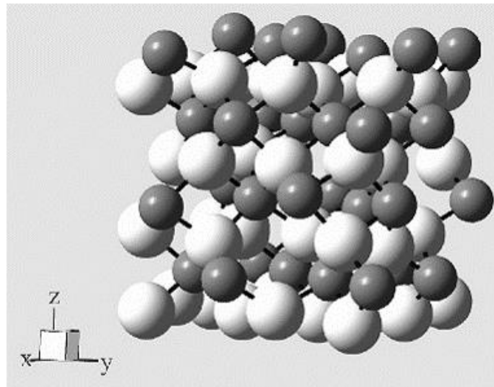

Figure 2.1: Bixbyite Crystal Structure of ITO[9]

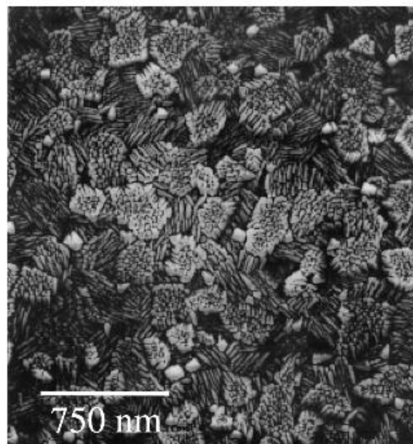

Figure 2.2: SEM Image depicting "Rice Field" microstructure of ITO [9]

2.1.1. Optical and Electrical Properties of ITO

ITO films are typically grown using DC magnetron sputtering using a ceramic sintered In_2O_3 target containing 3-10% SnO_2 at temperatures between 250 °C and 350 °C. The effect of various sputtering deposition conditions has been extensively studied and will be covered in the next section.

ITO film growth can be categorized into three stages. The first stage occurs when small islands of isolated ITO islands form on the surface of the substrate. In the 2nd stage, the ITO islands grow and coalesce partially with one another. In the final stage, a continuous layer is formed after the islands have fully coalesced with one another [34]–[37]. Liang et al. [38] studied the effect of film thickness on surface morphology using SEM as shown in Figure 2.3a – 2.3d where the film surface roughness increased with increasing film thickness due to the (100) preferred texture evolution for ITO.

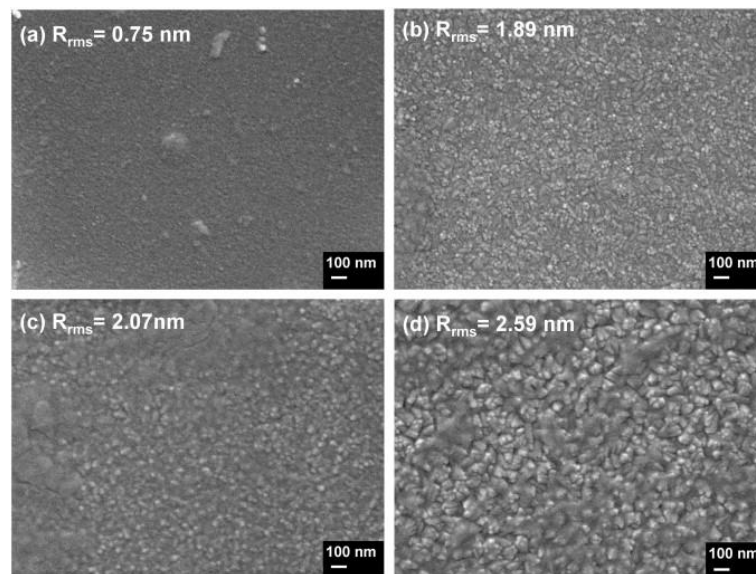

Figure 2.3: Effect of Film Thickness on Surface Morphology of ITO Films on glass with film thicknesses of a) 162 nm b) 270 nm c) 540 nm and d) 840 nm [38]

The effect of film thickness on electrical properties of ITO films has been well investigated [37], [39]. As shown in Figure 2.4, sheet resistance decreases with film thickness for films < 350 nm thick. Grain boundaries limit carrier transport by acting as traps. As films get thicker, the grains within the material get bigger reducing the grain boundary density. This leads to a decrease in grain boundary scattering and an increase in carrier density/mobility which leads to decrease in sheet resistance.

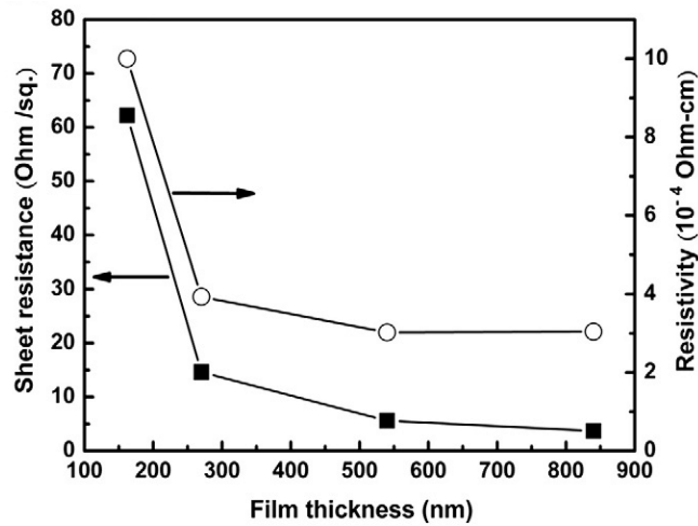

Figure 2.4: Effect of ITO Film thickness on Sheet Resistance and Resistivity [40]

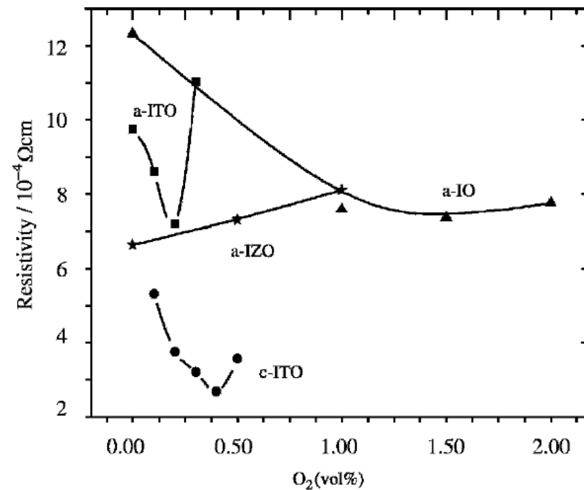

Figure 2.5: Effect of O_2 Concentration on resistivity of ITO Films [9]

The effect of Oxygen partial pressure during the sputtering deposition is shown above in Figure 2.5. In Figure 2.5, both amorphous and crystalline ITO films were grown to a thickness of 100 nm using identical power (0.25 W/cm^2) and total Ar pressure using varying ratios of O_2/Ar. Doping in crystalline ITO comes from two sources: tetravalent Sn substituting in for In in the bixbyite structure and the creation of doubly charged oxygen vacancies [41] . As seen in Figure 2.5 and Table 2.2 below, crystalline ITO has a higher carrier density and corresponding lower resistivity than its amorphous counterpart. This can be attributed to the additional carriers being supplied by the substitutional Sn present in the crystalline form of ITO that are not present in the amorphous phase of ITO.

Table 2.2: Electrical Properties of 100 nm thick films of amorphous and crystalline ITO [9]

	Resistivity (Ω·cm)	Carrier Density (cm^{-3})	Mobility (cm^2/V·s)
Crystalline ITO	2.23×10^{-4}	6.03×10^{20}	46.4
Amorphous ITO	7.18×10^{-4}	2.18×10^{20}	41.4

Additionally, the role of the sputtering power during deposition is important to consider. Higher sputtering power leads to increased film resistivity which is a result of the plasma induced ion damage on the surface of the sample. For this reason, process variables such as sputter gas pressure and target-to-substrate distance are important and are adjusted to reduce the energy of ions incident on the growth surface during deposition[9], [42][43], [44].

The effect of film thickness on the optical transmittance of ITO films on PET was studied by Ali et al. [45]. In visible region of the spectra (400-700 nm), the optical transmittance is approximately 85%. The concentration of oxygen vacancies strongly affects the transmittance because free electrons act as scattering sights reducing the transparency. Based on the results seen in this section, ITO has the appropriate optical and electrical properties to be an interconnect for flexible displays.

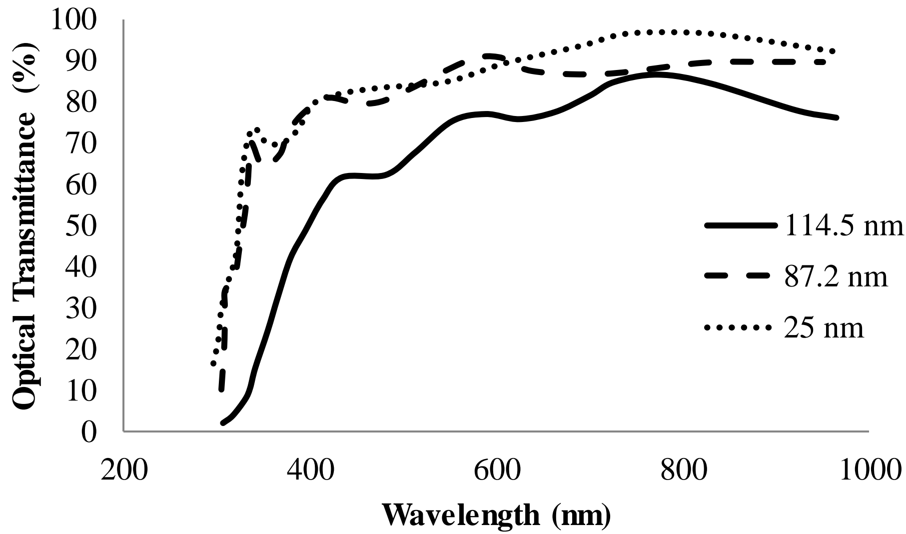

Figure 2.6: Optical transmittance vs. wavelength for ITO films on PET with thicknesses of 114.5, 87.2 and 25 nm respectively [45]

2.1.2. Mechanical Properties of ITO

The elastic modulus and Poisson's ratio of ITO were found to be 116 GPa and 0.35 respectively [46], [47] . The mechanical properties of ITO films in published literature have been tested using the uniaxial test method, two point bend test and the cyclic mandrel method. The following section will discuss the results of that work.

In general, when an ITO film is mechanically deformed, localized stress concentrations form around defect sites acting as crack initiation sites. As the strain in the film increases, the crack density and crack propagation both increase. Cairns et al [48] studied the effect of ITO film thickness on electrical measurements under tensile loads using film thicknesses of 105, 42 and 16.8 nm respectively. The change in normalized resistance as a function of strain is shown in Figure 2.7 below:

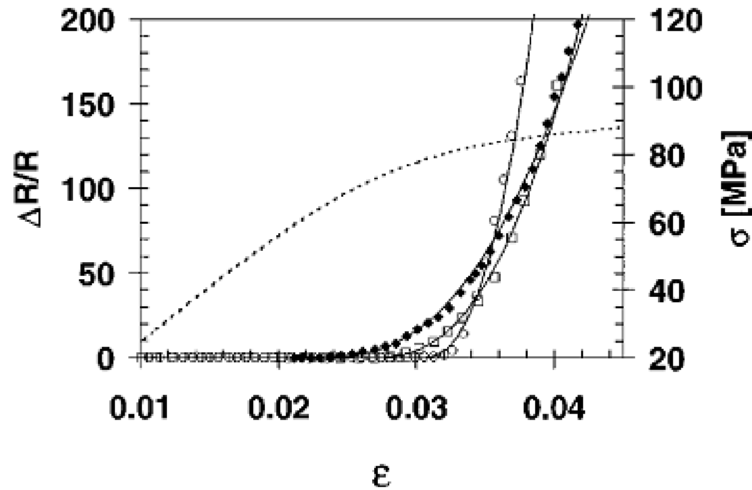

Figure 2.7: Change in Resistance of ITO coated PET as a function of strain for three different thicknesses (• - 105 nm, □ – 42 nm and ○ – 16.8 nm) respectively. The dotted line represents the stress-strain curve for ITO coated PET. [48]

As seen in Figure 2.7, the resistance increases sharply after a critical strain value is achieved. This is consistent with behavior of thin ceramic films on ductile substrates. The critical strain, ε_c, for cracking is inversely proportional to the film thickness, d, : $\varepsilon_c \approx d^{-\frac{1}{2}}$. The effect of test method (uniaxial vs. biaxial) for 100 nm ITO films on hard coated (HC) polymer substrates is shown in Figures 2.8 and 2.9.

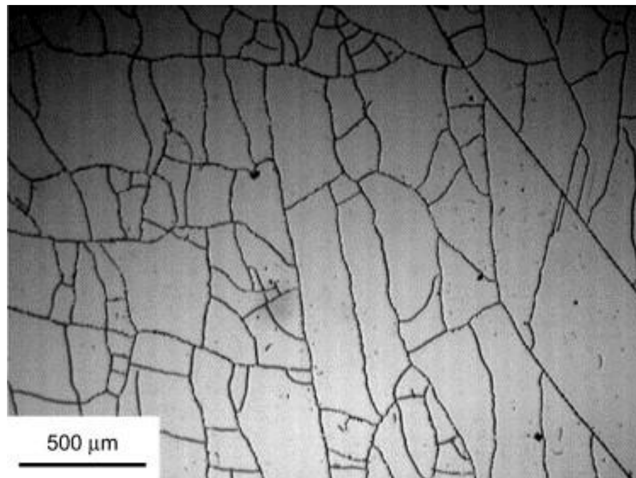

Figure 2.8: Biaxial Tensile failure of a 200 nm thick ITO on HC polymer [49]

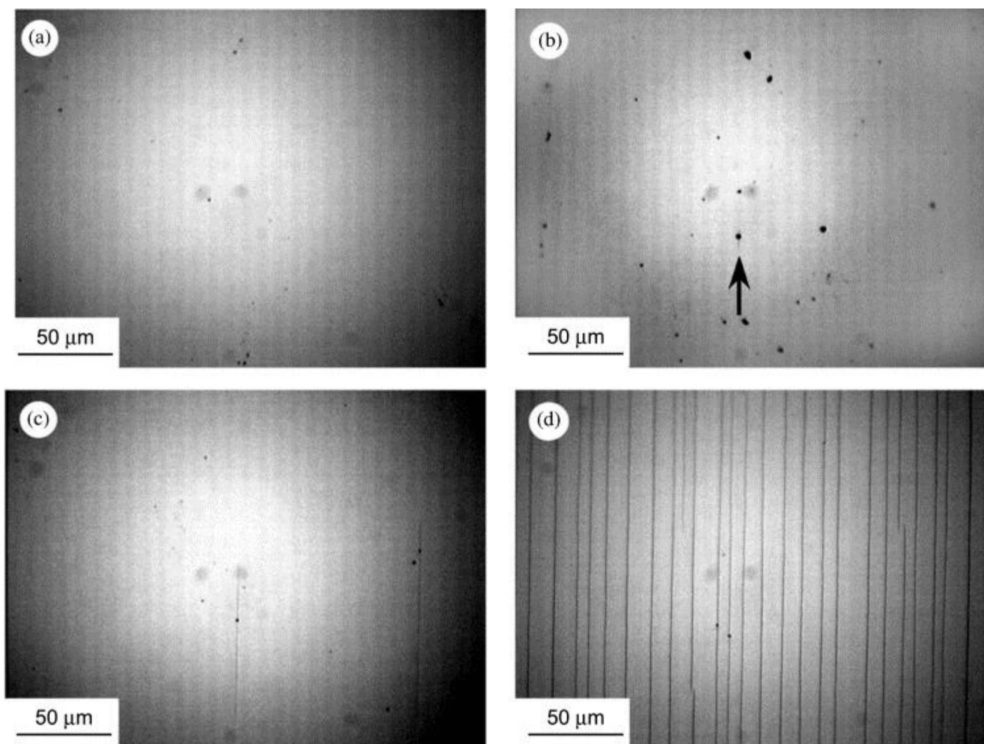

Figure 2.9: Crack Progression of 100 nm ITO on HC polymer during tensile loading (along the horizontal direction) with a) Unstrained ITO b) at 1.28 % strain with the arrow indicating a coating defect leading to failure initiation c) at 1.42% strain and d) at 3.42% strain [49]

As seen in Figures 2.8, for uni-axial loading, cracks initiate at defect sites and propagate at higher strain values until failure. Cracks propagate perpendicular to the

direction of the applied tensile stress. In contrast, cracks formed under the biaxial test method also initiate at defect sites but have more curved crack propagation paths. The two test methods can also be compared in terms of the crack onset strain (strain required to cause 10% resistance change in ITO Films) as shown in Table 2.3, the COS in tension and compression is comparable.

Table 2.3: Comparison of COS in ITO layers under Tension or Compression [9]

ITO Thickness (nm)	Bending COS	Tensile COS
50	1.77	1.835
100	1.45	1.42
200	1.56	1.45

Cairns et al. [50] studied the effect of strain on the crack density in ITO films. The optical microscopy images shown in Figure 2.10, illustrate the increased crack density with increasing strain. This increase in crack density corresponds to a more pronounced change in resistance of the system.

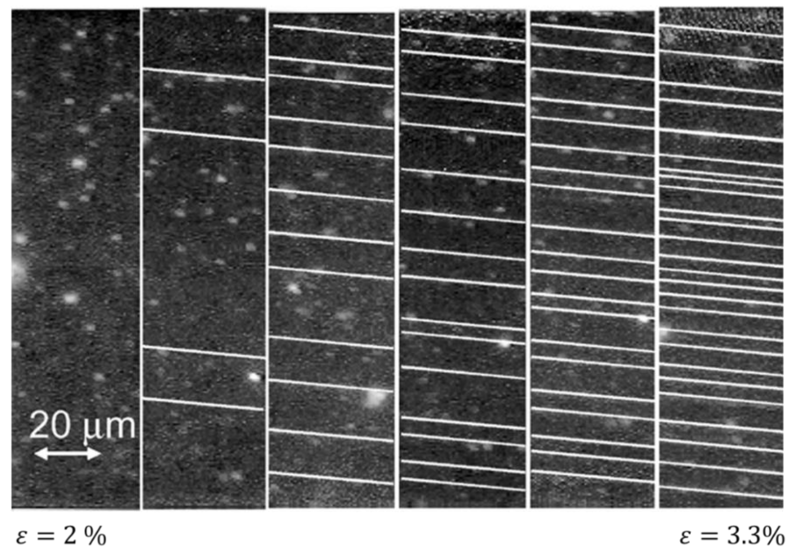

Figure 2.10: Optical microscopy images showing the evolution of cracking of ITO layer in tension where strain increases from 2% to 3.3% from left to right [48]

Cairns et al. [50] proposed a simple physical model, analogous to a series resistance model, that describes the change in resistance as a function of strain as well as the effect of cracks. At some critical strain, an initial crack is formed in the ITO layer. As the strain is increased, additional cracks form as shown in Figure 2.10. These cracks are separated by a small amount of ITO and its volume is assumed to be constant. The constant volume allows for a non-linear increase in resistance of a crack as the width increases as seen in Figure 2.11 below.

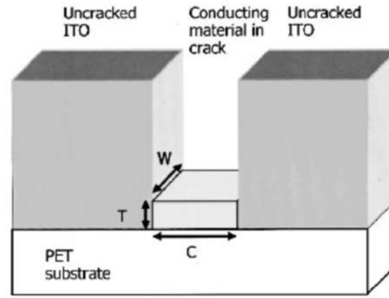

Figure 2.11: Schematic Illustration of Series Crack Resistance Model in ITO [50]

The resistance associated with the ith crack is given by:

$$R_i = \frac{\rho C_i}{A} = \frac{\rho C_i^2}{V} \tag{2.2}$$

where ρ is the resistivity of the ITO, C_i is extent of crack opening of the ith crack, A is the cross-sectional area of the material in the crack and V is the fixed volume. C_i is assumed to be zero at the point of crack initiation and increases with increasing strain. The width of the ith crack formed at a strain of ε_{ci} is:

$$C_i = D(\varepsilon - \varepsilon_{ci}) \tag{2.3}$$

where ε is the instantaneous strain, ε_{ci} is the strain at which the crack forms and D is the length scale. Assuming the volume of ITO in this separation zone is constant, the resistance is defined as:

$$R_i = \frac{\rho D^2(\varepsilon - \varepsilon_{CI})^2}{V} \tag{2.4}$$

Therefore, the total resistance of all of the cracks in an ITO layer assuming n is the number of cracks at strain ε is:

$$R_{total} = \sum_{i=1}^{n} \frac{\rho D^2(\varepsilon - \varepsilon_{CI})^2}{V} \tag{2.5}$$

The number of cracks per unit length is:

$$n_d = \frac{1}{\langle S \rangle} \tag{2.6}$$

where S is the average distance between cracks.

ITO is commonly used as a transparent anode layer as a uniform film, so the focus of the first portion of this section is discussion of the mechanical deformation of uniform ITO films. The remainder of this section will focus on the mechanical properties of patterned ITO structures. Bouten et al. [51] found that wide etched lines (0.3-10 mm) with good edge quality had failure distributions that were similar to those of uniform layers cut from coated foils characterized by poor quality. Crawford et al. [9] studied various ITO interconnect traces varying from 10-300 μm wide using the 2 point bend method in order to obtain COS values . The results of this study are shown below in Figure 2.12 and Table 2.4:

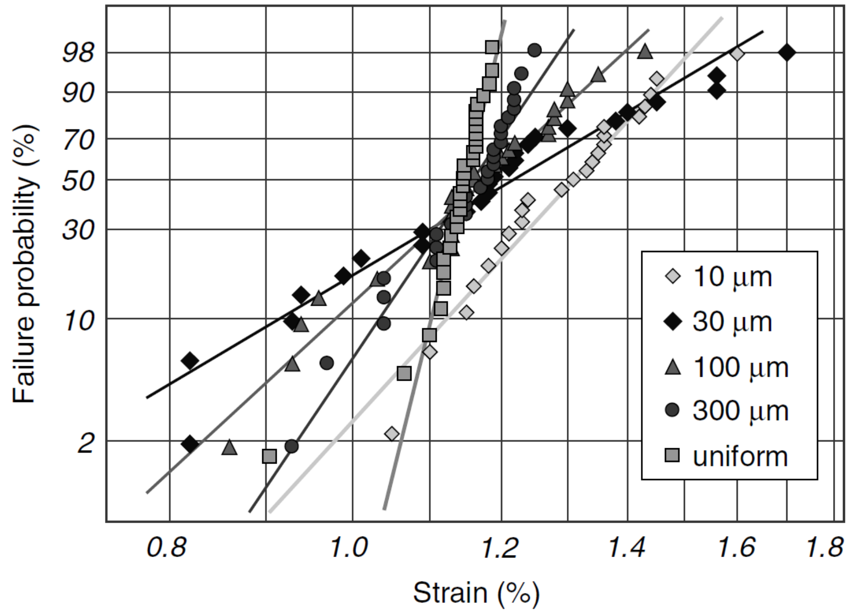

Figure 2.12: Weibull plot showing effect ITO line width on COS [9]

Table 2.4: Weibull values for different COS values for ITO lines of varying widths [9]

Width (μm)	Weibull Modulus (m)	COS
10	12.1	1.35
30	6.6	1.29
100	10.3	1.22
300	16.5	1.19
15,000	45.6	1.16

As shown in Table 2.4, COS increases slightly with decreasing line width. A large amount of scatter is observed in the measured strain for narrower ITO lines which is reflected by the lower weibull moduli. The weibull moduli shown in Table 2.4 are comparble to those of bulk ceramic materials $(5 \leq m \leq 12)$ where the defect size distribution controls the failure strain.

This section has presented published work on the mechanical properties of uniform and patterned ITO films. However, these methods all lack the ability to determine the number of cycles to failure ITO can sustain under bending conditions.

Therefore, published work on ITO using the cyclic mandrel test method and similar setups will now be discussed. In 2005, Cairns et al. [50] studied the fatigue behavior of ITO using the cyclic mandrel test method. The change in resistance as a function of number of cycles for three different radii of curvature is shown below in Figure 2.13 and 2.14

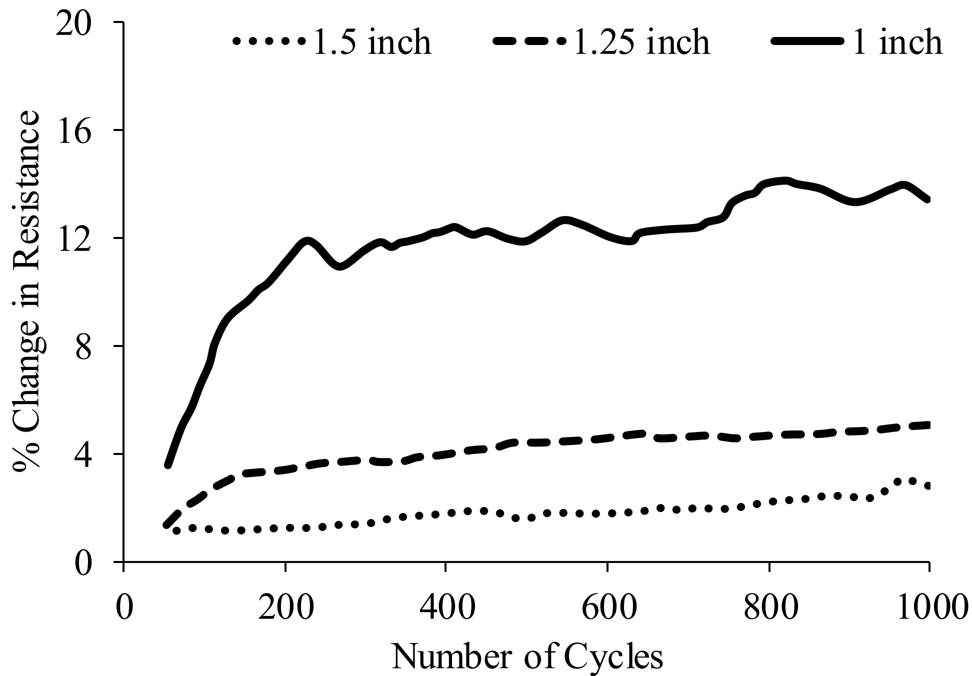

Figure 2.13: a) Change in resistance vs. number of cycles for three different radii of curvature [52]

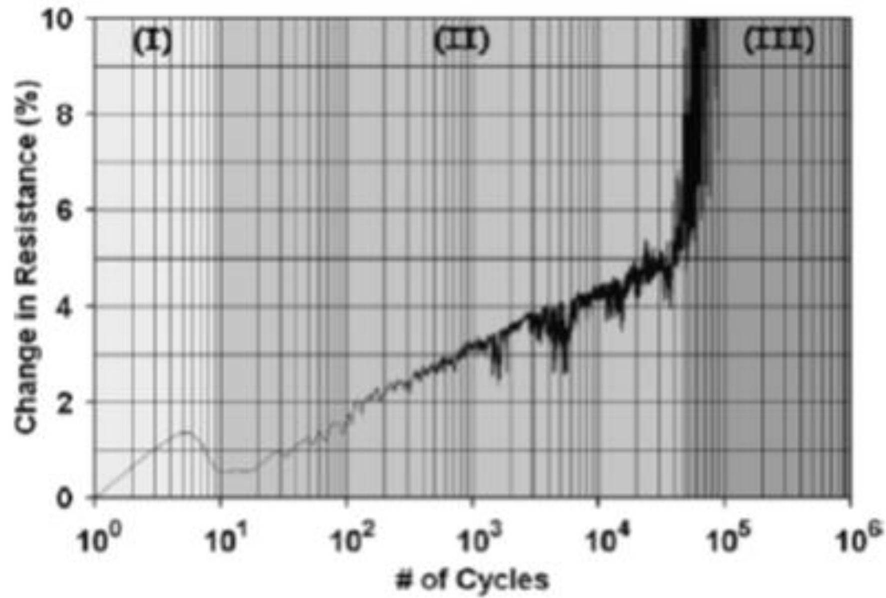

Figure 2.14: Change in resistance vs. number of cycles showing crack growth rate [52]

As seen in Figure 2.13, smaller radii of curvature lead to more pronounced changes in the percent change electrical resistance (PCER) due to increased strain values. The initial jump in the PCER values is due to deformation of the polymer substrate. The changes in PCER after this initial spike are associated with the deformation of the conducting layer as cracks initiate and propagate through the layer. Crack growth in ITO/PET samples (shown in Figure 2.14) is similar to the crack growth observed in most metals. As seen in Figure 2.14, the PCER can be broken into 3 different regions. In the first region, PCER increases due to changes in the sample's dimension until an equilibrium width is obtained (50-100 cycles). The second region features a gradual linear increase in resistance which is due to crack initiation and propagation. The third and final region is due to severe cracking leading to sample failure.

In 2011, Alzoubi et al.[53] studied the behavior of ITO films on PET under high cycle bending fatigue to see the effect of radius of curvature, sample width and test frequency on fatigue life. The results of this study are shown below in Figure 2.15a-c:

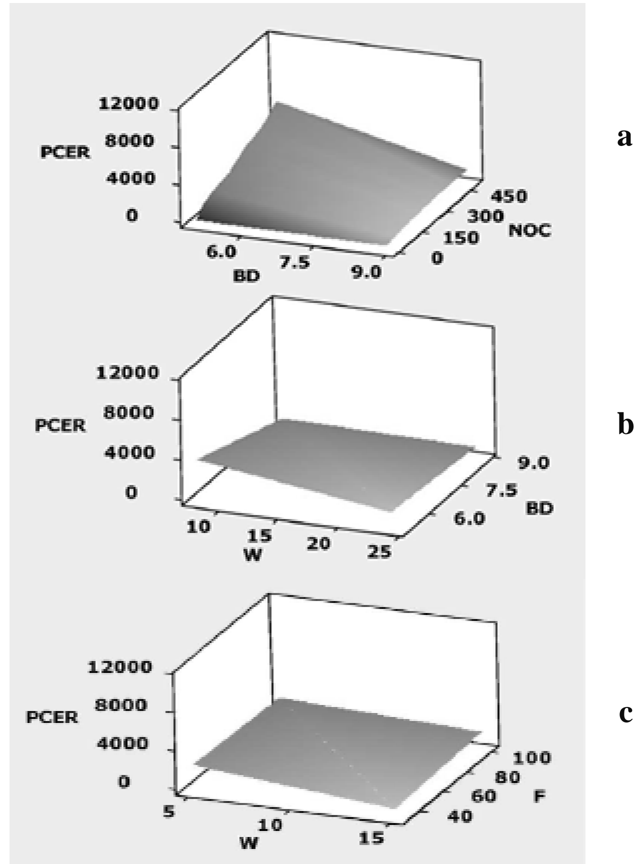

Figure 2.15: 3D Surface showing the interaction between (a) bending diameter and number of cycles; (b) bending diameter and sample width; and (c) sample width and bending frequency for fatigued ITO on PET samples [54]

In Figure 2.15a, the effect of bending diameter doesn't come into play until higher number of cycles. In Figure 2.15b, there is an observable effect of sample width on fatigue behavior. Wider samples take longer for cracks to propagate and therefore take longer to see a comparable PCER when compared to narrow width samples. In Figure 2.15c, there isn't a noticeable change in the PCER as a function of frequency, despite in most cases where frequency is a prime factor in fatigue behavior.

As seen in this section, fatigue experiments have been conducted on uniform ITO films, however fatigue experiments on patterned ITO structures have not been performed.

2.2. *Graphene*

As seen in the previous section, ITO meets the appropriate electrical and optical transparency requirements to be a interconnect material for flexible displays. However, it is plagued by reliability issues related to film cracking due to internal and external stresses. In the next section, Graphene a promising alternative will be discussed including a discussion of the structure of Graphene, fabrication methods and properties of Graphene films.

2.2.1. Crystal Structure

Graphene has an atomic number of 6 so electrons occupy the $1s^2, 2s^2, 2p_x^1$ and $2p_y^1$ and it is a tetravalent element. Only 2/3 of the 2p orbitals participate in the hybridization forming three sp2 orbitals. These sp2 orbitals are bonded together at an angle of 120° forming the planar hexagonal, "honeycomb" lattice structure of Graphene. The interatomic lattice parameter of Graphene is 1.42 Å, while the inter-plane distance is 3.35 Å [55]. The crystal structure of Graphene is shown in Figure 2.16 where the unit cell is highlighted in gray and the armchair and zigzag directions are also highlighted.

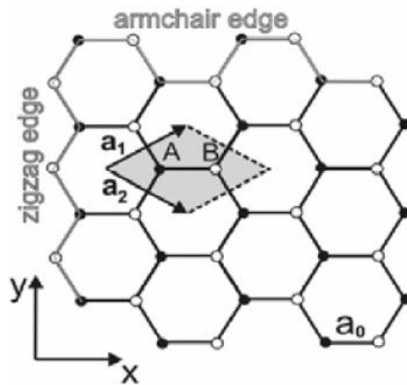

Figure 2.16: 2D hexagonal lattice of Graphene highlighting the unit cell (gray) and the zigzag and armchair edges [56]

Three different stacking structures exist for Graphene layers: simple hexagonal, Bernal stacking (ABAB) and Rhombohedral (ABC). In simple hexagonal, the second layer of carbon atoms sits directly on top of the first layer. An illustration of Bernal and Rhombohedral stacking is shown below in Figure 2.17 where in ABA and ABC, the 2nd layer of carbon atoms is offset from the first layer:

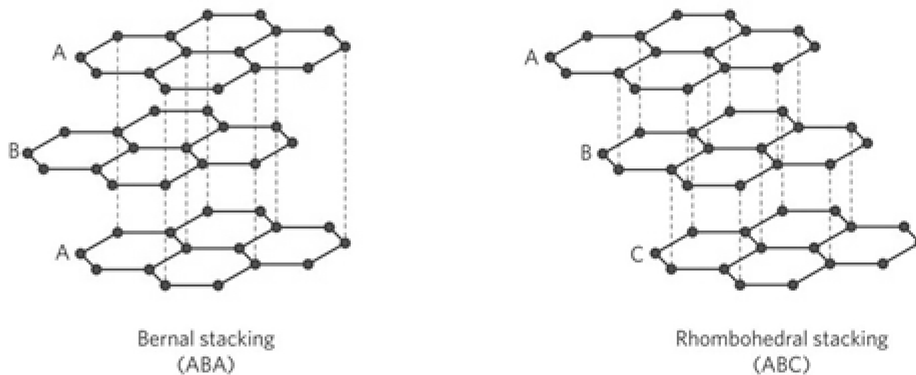

Figure 2.17: Bernal and Rhombohedral stacking of Graphene [57]

2.2.2. Fabrication Techniques

Graphene has been fabricated using a variety of techniques including mechanical exfoliation, chemical exfoliation, reduced Graphene oxide, synthesis using molecular precursors and chemical vapor deposition. This section will discuss in more detail mechanical exfoliation, chemical vapor deposition and finally transferring Graphene to an arbitrary substrate.

Mechanical exfoliation is a process where a mechanical force is used to extract Graphene layers from bulk graphite. The main methods to do this include using an adhesive tape to transfer Graphene from one layer to another or by using another material to cleave off sheets of Graphene from the bulk (micromechanical exfoliation, ultrasonic treatment and milling).

The adhesive transfer method is a quick, easy process that can produce high quality large area Graphene sheets. The drawbacks of this method include that it does not produce a high enough yield for many applications and some residuals are left on the Graphene surface after transfer. Micromechanical exfoliation is typically done using an AFM tip which has several drawbacks including: complexity, low output yield and it can induce strain and defects on the surface of the samples. Ultrasonic treatment and milling are both promising routes for producing high output yields but they still have their limitations [56], [58]–[62].

Chemical vapor deposition (CVD) is one of the most popular fabrication techniques for Graphene because of its ability to deposit uniform large area films and it's well established in industry. In CVD, a precursor gas such as methane (CH_4) is flowed into a vacuum chamber at elevated temperature. The precursor decomposes followed by Carbon atoms depositing on the desired substrate. The two most commonly used substrates for Graphene CVD growth are Ni and Cu.

High quality graphite has been grown on Ni because the lattice mismatch between (111) Nickel and Graphene is less than 1% [63]. After continued study, it was found that control over the number of Graphene layers when using Ni can be limited. This can be attributed to the fact that Ni has a large carbon solubility (0.6 wt% at 1326 °C) [64]. Above 800 °C, carbon and nickel form a solid solution. Below 800 °C, the solubility of carbon decreases so that during cooling, carbon segregation is rapid within Ni grains and heterogeneous at grain boundaries which results in non-uniform Graphene growth [56].

Continuous thin Graphene films with Graphene layer numbers ranging from 1 to 10 layers can be grown on polycrystalline Ni films at temperatures between 900 °C and 1000 °C by using several techniques to combat carbon's high solubility in Ni. Reina et al.[65] fabricated polycrystalline Graphene films using a low concentration carbon precursor source at ambient pressure at temperatures between 900 °C and 1000 °C. CVD growth of Graphene on Ni can be assisted using three separate techniques including the use of a diluted precursor gas aids in limiting the carbon supply,

lowering deposition pressures and using quick cooling times to prevent segregation of carbon. Wrinkles are typically observed on single or few layer Graphene (FLG) samples on Ni caused by either defects or differences in CTE values between Graphene and Ni [66]. In 2010, Zhang et al. [67] studied the effect of using single crystal vs. polycrystalline Ni substrates at ambient pressures and found that the single crystal Ni substrates yielded better Graphene coverage (90% vs. 72%). Zhang et al. stated the reason for this improved Graphene coverage was the elimination of grain boundaries and the smoother surface of single crystal Ni.

Copper is the other most commonly metal substrate used for Graphene growth. Copper has a low carbon solubility at high temperature (0.008 wt% at 1084 °C [68]) which results in high uniformity single layer Graphene films which has been demonstrated by several researchers using various carbon allotropes [69]–[71] when compared to Ni. Graphene can be grown on Cu because of its low reactivity with carbon which is due to its very stable electron configuration. Generally, 1-3 layers of Graphene have been grown on Cu foils by CVD using a variety of conditions shown in Table 2.5:

Table 2.5: Summary of Growth Conditions for CVD of Graphene on Cu from literature [64]

Growth Pressure (Torr)	Temperature (°C)	# Graphene Layers	Reference
0.5	1000	1 (95 %)	[72]
11	1000	1 (93%)	[73]
50	850-900	Few Layers	[74]
760	1000	1,2	[75]
0.39	800	1,2,3	[76]
0.1-0.5	1000	1,	[77]
0.5	950	1,2	[78]
1.6	1000	1	[79]

Depending on the growth conditions, the respective microstructure of the Graphene film can be very different as shown in Figures 2.18 and 2.19 in work done by Li et al. [80], Vlassiouk et al. [81] and Wu et al. [82]:

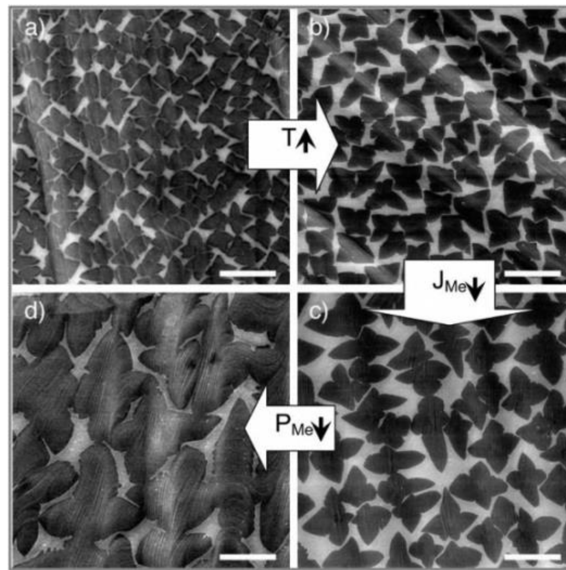

Figure 2.18: SEM Images illustrating effect of various growth conditions (Temperature, Pressure and Methane Flow Rate) on resulting microstructure where the scale bar is 10 µm [81]

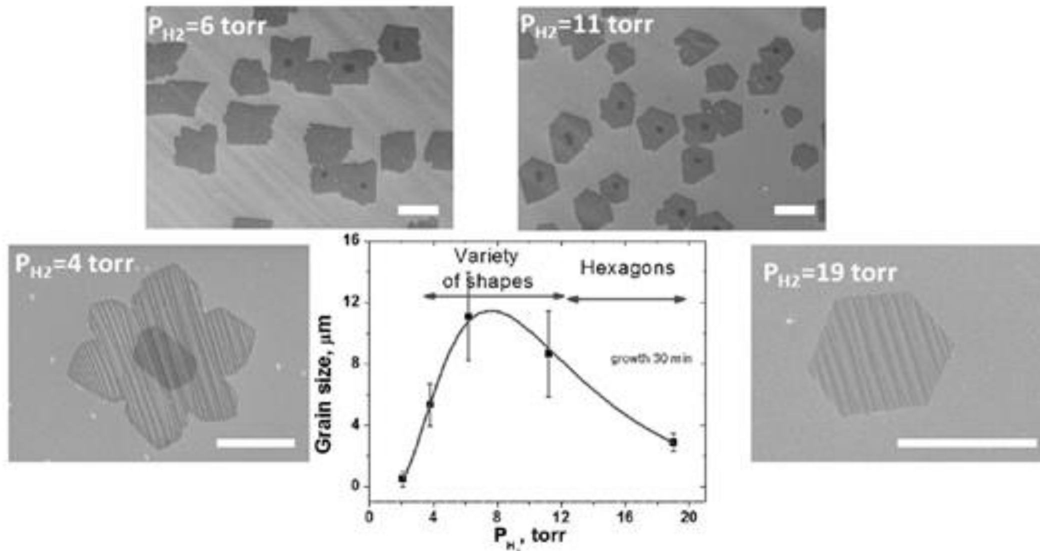

Figure 2.19: Effect of H_2 Partial Pressure on Graphene grain shape. Scales bars are 10 µm (top two images) and 3 µm (bottom two images)

As shown in Figure 2.18, the nucleation density decreases with: increasing temperature, decreasing Methane flow rate and partial pressure. In addition, at atmospheric conditions, the shape of the Graphene grains depends greatly on the partial pressure of the Methane precursor. The solubility of Carbon in Copper is very low, so the Hydrogen in the Methane precursor is used as a co-catalyst promoting Graphene growth. As shown in Figure 2.19, at low H_2 partial pressures, irregular/rectangular grains form while at high H_2 partial pressures, hexagonal grains form. These shapes both have to do to with the Cu lattice that Graphene is being deposited on, rectangular grains are associated with the (111) in Cu foil, while the hexagonal grains are associated with the Graphene layer, where at low H_2 partial pressures, the (111) Cu lattice dominates growth.

The growth conditions also play an important role in the effect of defect formation in the Graphene films which has a detrimental effect on the mechanical properties. Through MD simulations several researchers Hao et al. [83] and Ansari et. [84] have shown a reduction in strength through the introduction of defects.

With CVD's ability to produce uniform large area Graphene films, a major research push is in techniques to transfer Graphene from a metal foil (Ni or Cu) to another substrate including Si/SiO_2, Sapphire (Al_2O_3) and polymer substrates. Several of these techniques will be discussed in the next section

One of the methods used to transfer Graphene to another substrate is through the use of Graphene carrier, Polydimethylsiloxane (PDMS) or Poly(methyl methacrylate) (PMMA), has been performed by several researchers [72], [85]–[87]. In this process, first a layer of PDMS or PMMA is spin-coated on the surface of the Graphene/metal foil. Next the polymer/Graphene/metal stack is suspended on the surface of an etching solution,$FeCl_3$ or $Fe(NO_3)_3$ for Cu and NaOH for Ni, to remove the respective metal foil. Once the metal foil is removed, the polymer/Graphene stack is rinsed in de-ionized water to remove any remaining containments from the etching solution. Next the polymer/Graphene stack is transferred to the surface of the desired substrate. Finally acetone is used to remove the PMMA or PDMS yielding Graphene on the substrate of choice. A schematic of this process is shown below in Figure 2.20:

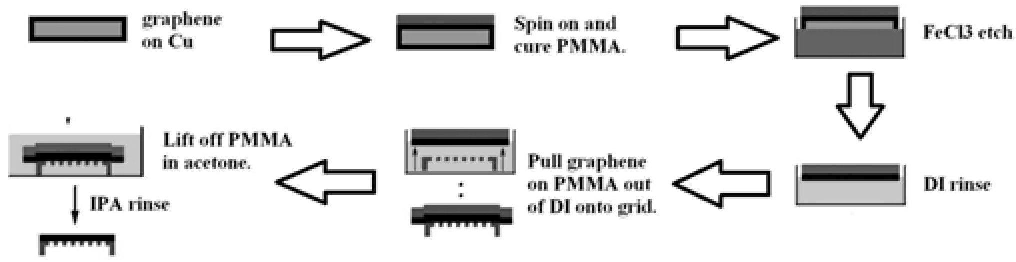

Figure 2.20: Schematic Illustrating Fabrication of Graphene on PET [88]

Despite the simplicity of this method, there are still some drawbacks to this technique including cracking in the Graphene film after removal of the polymer carrier caused by surface roughness differences between the Graphene and new substrate as well as the fact PMMA cures into a hard coating. Additionally residual acetone contamination is present on the Graphene surface as a result of the PMMA etch process.

An alternative to the polymer carrier method is the hot rolling/hot pressing method, where the metal foil/Graphene stack is hot pressed onto the desired substrate. Next the whole structure is dipped in an etching solution to remove the metal foil yielding Graphene on the desired substrate. A schematic of this is shown below in Figure 2.21 for a Graphene on Cu foil transferred to PET.

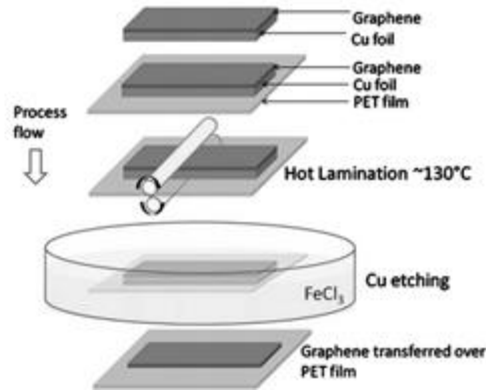

Figure 2.21: Schematic illustrating transfer process of Graphene on Cu foil to PET [89]

Another alternative transfer method is the roll to roll transfer method as seen in Figure 2.22 below. In the roll to roll setup, a CVD grown Graphene film on a Cu foil is attached to a thermal release tape by application of a soft pressure between two rollers. Next, the layer stack structure is fed through an etchant bath to remove the Cu foil yielding Graphene on adhesive tape. The Graphene on adhesive tape is then reinserted into the rollers with the desired target substrate and rolled at an elevated temperature (90-120 °C) which transfers the Graphene to the target substrate.

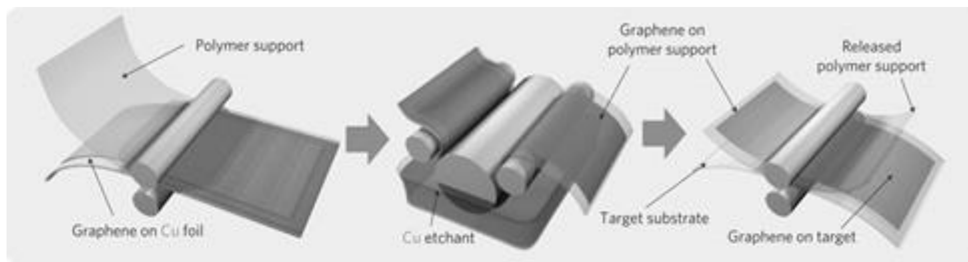

Figure 2.22: Schematic Illustration of Roll to Roll Fabrication Process for Graphene [79]

The electrical, optical and mechanical properties of Graphene will be highlighted in the next sections

2.2.3. Electrical Properties of Graphene

Graphene has three unique electrical characteristics that make it of interest including a vanishing carrier density at Dirac points, existence of pseudo-spin and the relativistic nature of carriers due to its lattice structure as shown below in Figure 2.23.

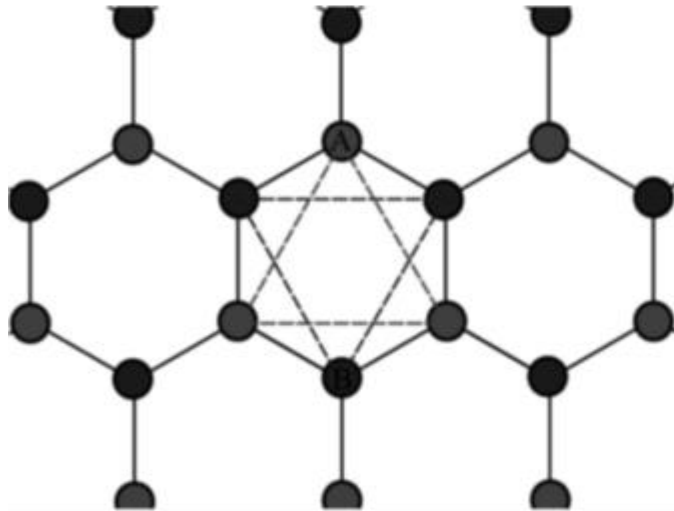

Figure 2.23: Graphene sub-lattice where each lattice A atom is surrounded by 3 atoms on the B lattice [90]

The band structure of Graphene can be described using a simple nearest neighbor tight bonding approaching considering a single Π electron per atom [91]–[94]:.

$$E^{\pm}\left(k_x, k_y\right) = \pm\gamma_o \sqrt{1 + 4\cos\frac{\sqrt{3k_x a}}{2}\cos\frac{k_y a}{2} + 4\cos^2\frac{k_y a}{2}} \qquad (2.7)$$

Graphene is a zero gap semiconductor with a vanishing density of states at the Dirac point with no energy gap between the valence and conduction bands as shown below in Figure 2.24.

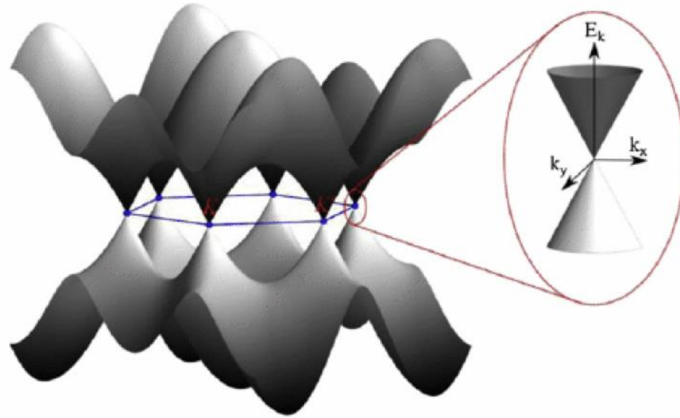

Figure 2.24: Band structure of Graphene showing the conduction and valence bands meeting at the Dirac points (blue dots) [56]

In 2007, Geim et al. [95] showed that Graphene demonstrates a ambi-polar electric field effect (as shown in Figure 2.25 below) where charge carriers can be tuned continuously between electrons and holes in concentrations as high as 10^{13} cm^{-2} and their mobilities can exceed 15,000 $cm^2/V{\cdot}s$ under ambient conditions [61], [96]–[98].

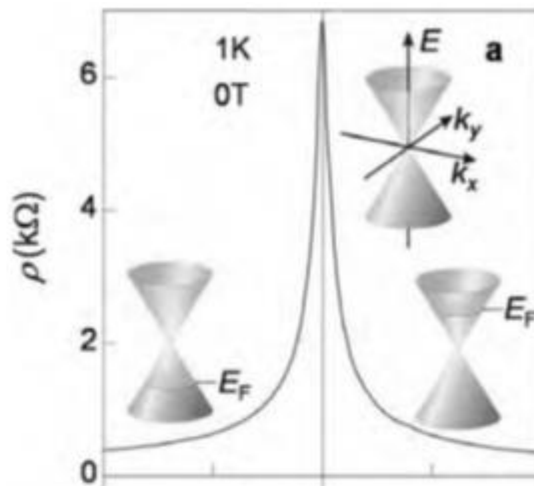

Figure 2.25: Modulation of resistivity in Graphene using gate voltage [95]

The Dirac point can be moved closer back to 0 V by reducing the number of surface contaminants in the Graphene film using annealing in ultrahigh vacuum or an H_2/Ar atmosphere [99] or through the application of a higher current density into the sample

[100]. The theoretical charge carrier density at the Dirac point should go to zero, however several researchers ([96], [98]) have shown a finite conductivity remains caused by the presence of charged impurities, thermal excitation and ripples in the Graphene layer [96], [101], [102]. The mobility of Graphene films on various substrates can range from 15,000 to 200,000 $cm^2/V \cdot s$ [61], [96]–[98], [103], [104].

Boltzmann transport theory is used to describe Graphene transport for carrier densities, n, ($n >> n_i$), where n_i is the impurity density for a homogenous system. The conductivity was found to increase linearly with the carrier density concentration as shown below in Figure 2.26

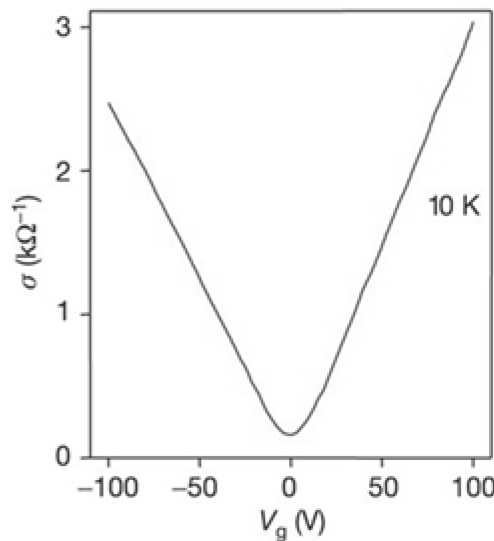

Figure 2.26: Measured conductivity of Graphene as a function of gate voltage or carrier density [98]

This behavior was explained using the long range Coulomb disorder model by several researchers [105]–[112]. In 2006, Hwang et al. [107] developed a carrier transport model for 2D Graphene accounting for scattering by random charged impurities which are assumed to be the dominant scattering mechanism. Intrinsic Graphene as is

a zero-gap semiconductor where at T = 0 and no applied gate voltage, no free carriers exist. All experimental Graphene samples are extrinsic, because there are invariably some free carriers present in the system. Transport close to the Dirac point is dominated by two effects of the charged impurities in the system: the carrier density is determined by the screened, charged impurity potential and the conductivity is dominated by the charged impurity scattering. However, the system breaks up into spatially inhomogeneous conduction puddles of 2D electron and hole droplets due to extrinsic randomly charged impurity centers. When a gate voltage is applied, free carriers (electrons or holes) are introduced into the system. First, it is assumed that the system is a homogenous 2D carrier system of electrons or holes with a carrier density, n, induced by a gate voltage, V_g. The conductivity can be found assuming Boltzmann transport theory by the following expression:

$$\sigma = \frac{e^2 v_f^2}{2} D(E_F)\tau(\epsilon E_F) \tag{2.8}$$

where σ is the conductivity, e is the charge of an electron, v_f is the carrier velocity at the Fermi Energy, E_F is the Fermi energy and τ is the transport scattering time. Assuming a random distribution of charged centers with density n_i, the scattering time τ at T = 0 is given by [113], [114]:

$$\frac{1}{\tau} = \frac{r_s^2}{\tau_o}\left\{\frac{\pi}{2} - \frac{4d}{dr_s}\left[r_s^2(2r_s)\right]\right\} \tag{2.9}$$

where $\tau_o^{-1} = 2\sqrt{\pi} n_i v_F / \sqrt{n}$ and $-1 + \frac{\pi}{2}x + (1 - x^2)f(x)$ with

$$f(x) = \begin{Bmatrix} \frac{1}{\sqrt{1-x^2}}\cosh^{-1}\frac{1}{x} & for\ x < 1 \\ \frac{1}{\sqrt{x^2-1}}\cosh^{-1}\frac{1}{x} & for\ x > 1 \end{Bmatrix} \quad (2.10)$$

Since the interaction parameter, r_s, is independent of the carrier density, the scattering time can be simply $\tau \approx \sqrt{n}$. This is further supported by the fact that conductivity is a function of the density of states which in turn is also a function of the carrier density. The effect of carrier density (gate voltage) on conductivity is shown below in Figure 2.27:

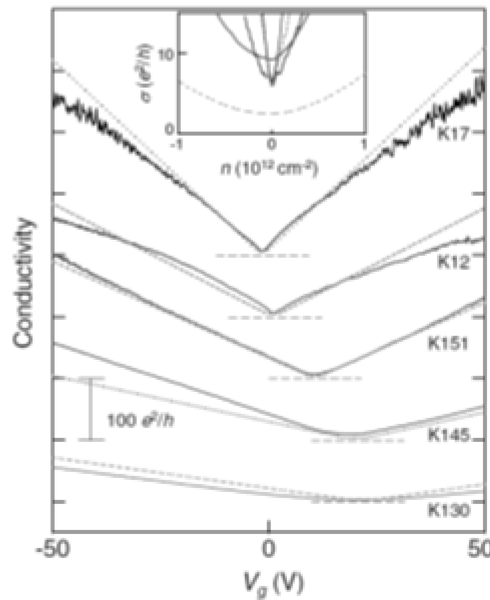

Figure 2.27: Conductivity vs. Gate voltage for 5 different Graphite on SiO_2 samples showing effect of sample quality. Insert shows a detailed view of the density-dependent conductivity near the Dirac point. [115]

In Figure 2.27, the samples that were termed of poorer quality ($\mu_L < 5000$ cm^{2}V^{-1}s^{-1}) exhibit a very board and smooth maximum near the Dirac point followed by a linear relationship of σ with respect to V_g. For samples with better quality ($\mu_L > 10000$

$cm^2V^{-1}s^{-1}$), the conductivity curves form a cusp around the Dirac point followed by a sub-linear increase in the electron and hole regimes. This difference suggests different scattering mechanisms may dominate these regions where the mechanism changes from long range scattering (ionized impurity scattering) to short range scattering such as atomic defects in the lattice [107], [110].

In 2007, Hwang et al [107] studied 2D carrier transport in gated Graphene monolayers where scattering occurred by random charged impurity centers with a density, n_i. In this work, Hwang developed a theory for high current density samples ($n > 10^{12}$ cm^{-2}) that was validated using experimental data [61], [96], [98]. Hwang et al. found that the calculated Graphene conductivity is limited by screened charged impurities and increases with n/n_i and the distance between the 2D Graphene and 2D impurity layer, d, as shown in Figures 2.28 and 2.29 below:

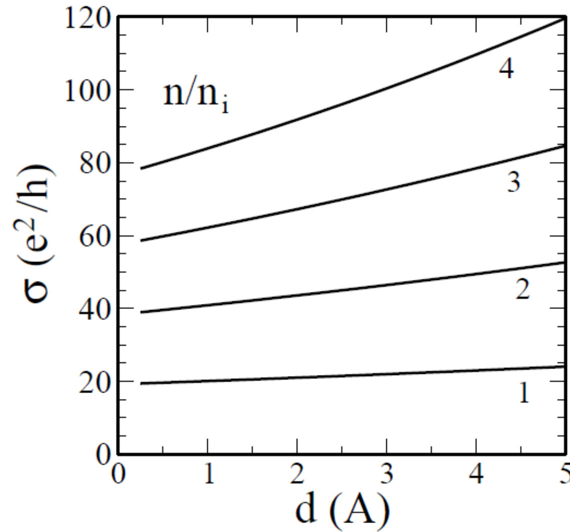

Figure 2.28: Effect of 2D Graphene and Impurity layer distance on conductivity [107]

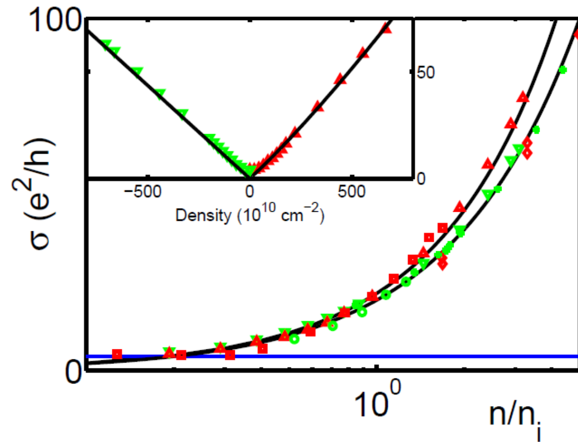

Figure 2.29: Comparison of Hwang et al. developed theory with experimental data [107]

In Figure 2.29, the black lines are the predicted theoretical values, the triangles correspond to $n_i = 2.3 \times 10^{12}$ cm^{-2}, the circles and squares correspond to $n_i = 3.4 \times 10^{12} cm^{-2}$ and the diamonds correspond to $n_i = 0.43 \times 10^{12}$ cm^{-2}. The solid blue line shows the minimum conductivity value of $4e^2/h$. Hwang et al. also found that conductivity can be dominated by both long range and short range disorder as shown in Figure 2.30 below:

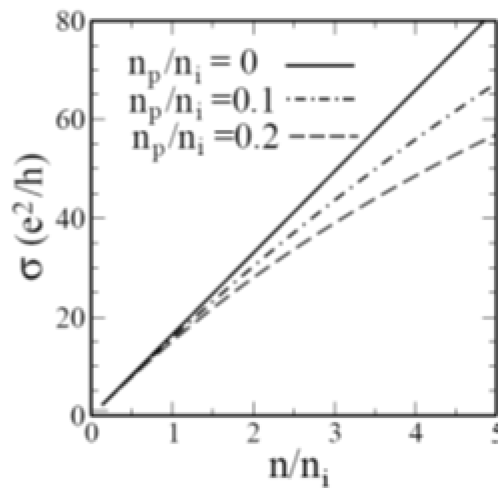

Figure 2.30: Graphene conductivity calculated using a combination of short and long range scatterers [107]

In Figure 2.30, for small n_d/n_i, the conductivity is linear while for large n_d/n_i, the conductivity is sub-linear. The flattening in the high density region is believed to be attributed to the crossover behavior caused by the competition between short and long range scatterers.

In 2008, Bolotin et al. [103] studied the electron mobility of monolayer suspended Graphene on SiO_2. Bolotin et al found the mobility of the suspended Graphene samples to be ~ 28,000 $cm^2V^{-1}s^{-1}$ at $n = 2x10^{11}$ cm^{-2}. This value leads to the conclusion that the scattering is caused by residual impurities absorbed on the Graphene surface. These containments were removed by sending a large current through the sample which heats up the sample allowing most of residuals from the fabrication process to desorb. This process was found to improve only suspended Graphene samples, while unsuspended samples did not show a large improvement in properties which is a result of impurities trapped at the interface between Graphene and the substrate.

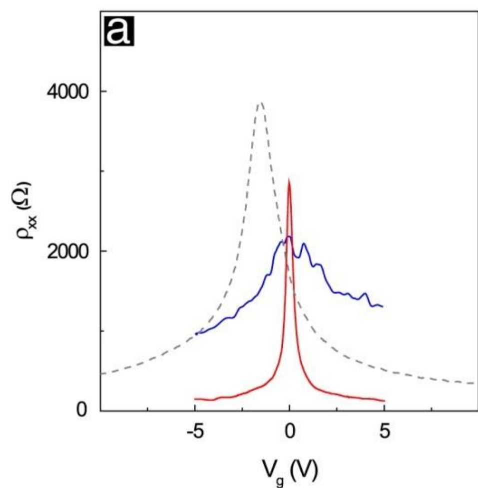

Figure 2.31: Effect of Current Annealing technique on suspended Graphene on SiO_2 [103]

As shown in Figure 2.30, the resistivity of the sample decreases substantially by approximately a factor of 8 (blue curve vs. red curve) far away from the Dirac point. The width of the Dirac peak decreases by about a factor of 20, while the maximum resistivity of the device doesn't change. In terms of mobility, at n = $2x10^{11}$ cm^{-2} the mobility increased by approximately a factor of 10 from 28,000 $cm^2V^{-1}s^{-1}$ to 230,000 $cm^2V^{-1}s^{-1}$.

The temperature dependent Graphene transport properties can be divided into two groups: phonon scattering based mechanisms or electronic mechanism without any phonon effects. In 2009, Hwang et al. [116] developed a model describing the temperature dependent conductivity due to screening and energy averaging from Boltzmann's transport theory. Hwang et al. developed temperature dependent conductivity equations for both low temperatures ($T << T_F$) and high temperatures ($T/T_F >> 1$) as shown below where T_F is the Fermi Temperature:

For Low Temperature ($T \ll T_F$):

$$\frac{\sigma(T)}{\sigma_o} \approx 1 - C_1\left(\frac{T}{T_F}\right)^2 \tag{2.11}$$

where C_1 is a positive constant depending on the interaction parameter, r_s, and σ_o is given by:

$$\sigma_o = \frac{e^2 v_F^2 D(E_F)\tau_o}{2} \tag{2.12}$$

where e is the charge of an electron, v_f is the carrier velocity at the Fermi Energy, E_F is the Fermi energy and τ is the transport scattering time.

For High Temperature ($T/T_F >> 1$):

$$\frac{\sigma(T)}{\sigma_o} \approx C_2 \left(\frac{T}{T_F}\right)^2 \tag{2.13}$$

where C_2 is a positive constant depending on the interaction parameter

Hwang et al. [116] numerically simulated the effect of temperature on resistivity for Graphene on SiO_2 samples using r_s values ranging from 0.88 to 0.01. As shown in Figure 2.32, in the high temperature regime ($T/T_F >> 1$), the resistivity decreases quadratically while in the low temperature regime ($T << T_F$), the resistivity increases slightly quadratically. Similar to other 2D parabolic systems, at high temperatures, Graphene exhibits insulating behavior while at low temperatures Graphene exhibits metallic behavior.

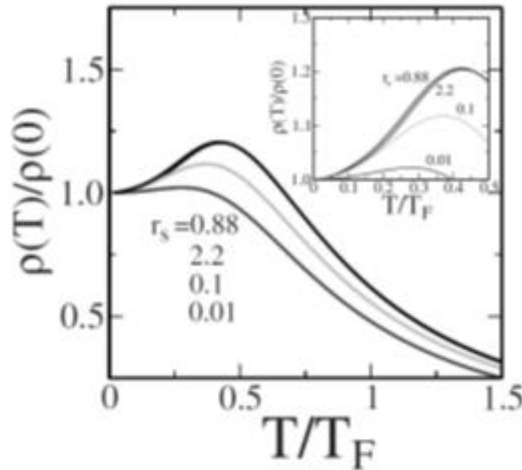

Figure 2.32: Calculated resistivity vs. scaled temperature, T/T_F for different r_s = 0.88, 2.2, 0.1, and 0.01 (from top to bottom). Insert shows a magnifed view of the low temperature limit ($T < 0.5T_F$) [116]

The temperature dependent resistivity of Graphene has been investigated experimentally by numerous researchers [117]–[120]. In each of these works, the mobility of Graphene samples was found to decrease with increasing temperature as shown below in Figure 2.33.

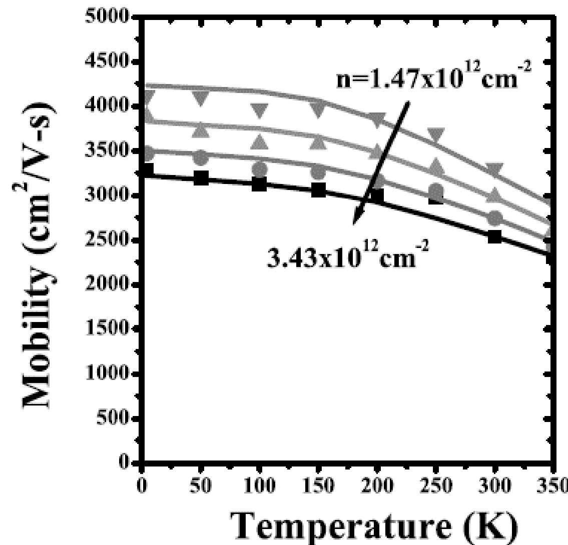

Figure 2.33: Hall mobility of holes as function of temperature for monolayer Graphene with varying carrier densities [119]

As shown in Figure 2.33, after 200K, the mobility of Graphene decreases significantly caused by scattering of thermally excited surface polar phonons from the SiO_2 substrate [106], [120], [121]. The SiO_2 phonons at the substrate/Graphene interface modulate the polarizability, which produces an electric field that couples to the Graphene carriers limiting their mobility.

Lattice vibrations are inevitable sources of scattering and can dominate transport near room temperature. Phonons are an intrinsic scattering source that reduces mobility. There are three main types of phonon scattering that need to be considered: intravalley acoustic phonon, intravalley optical phonon and intervalley phonon scattering. Intravalley acoustic phonon scattering is caused by low energy phonons and is considered to be an elastic process. The temperature-dependent phonon limited resistivity, ρ_{ph}, was determined for two regimes: for when the temperature was larger or smaller than the Block-Grüneisen temperature, T_{BG}. T_{BG} is used for low-density electron systems where only a small fraction of acoustic phonons can scatter off electrons because the Fermi surface can be a lot smaller than the size of the Brillion zone [122]. For temperatures below TBG, $\rho_{ph} \propto T$ while for temperatures above T_{BG}, $\rho_{ph} \sim T^4$ [123]–[125]. The effect of intravalley optical phonon scattering caused by low momentum ($q \approx 0$), high energy (200 meV) optical phonons is generally negligible. Intervalley scattering is normally caused by the emission and absorption of high momentum, high energy acoustic or optical phonons which can be important at high temperatures because of relatively low phonon energy [126].

Several researchers have studied the effect of phonon scattering on resistivity. In general, experimentally measured resistivity is dominated by extrinsic (impurity) scattering. The impurity contribution to resistivity also has a temperature dependence caused by Fermi statistics and screening. The experimentally determined phonon contribution can be determined using Matthiessen's rule shown below:

$$\rho_{tot} = \rho_{ph} + \rho_i \tag{2.14}$$

where ρ_{tot} is the total resistivity which is a sum of the phonon resistivity, ρ_{ph}, and the impurity and defect resistivity, ρ_i. Two different research groups have shown differing behavior with regards to phonon contribution to resistivity. Chen et al. [120] found that the extracted phonon contribution is strongly density dependent while Morozov et al. [127] found that resistivity has a power law (T^5) temperature dependence and the phonon contribution is independent of carrier density.

2.2.4. Optical Properties of Graphene

Numerous researchers have determined the optical transmittance of monolayer Graphene to be 97.6% as shown in Figure 2.34 [79], [128]:

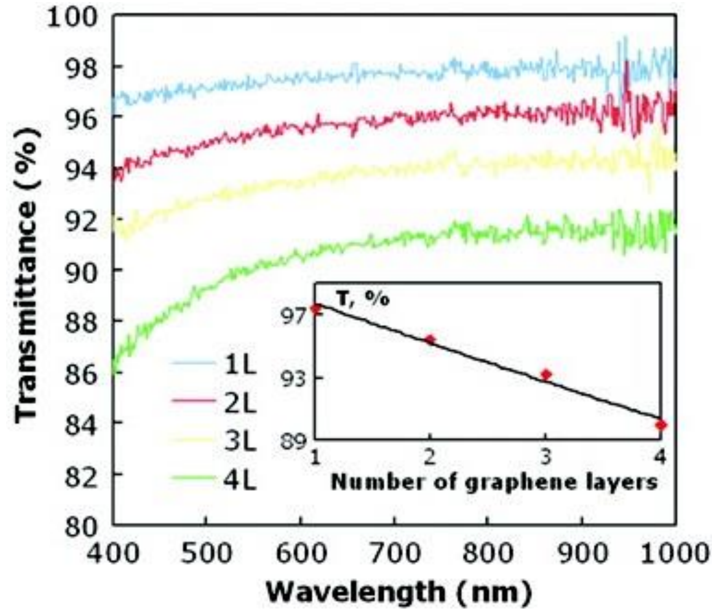

Figure 2.34: Optical transmittance of n-layer Graphene films at 550 nm as a function of the number of Graphene layers [128]

As shown in Figure 2.34, the optical transmittance of Graphene is very high with a monolayer Graphene having an optical transparency of 97.6%. As the number of layers is increased, there is decrease in the transparency of the Graphene films. Nair et al. [129] found that the transparency of Graphene decreases as a function of the number of layers described by the following expression due to increased scattering effects:

$$T = 100 - 2.3N \qquad (2.15)$$

where T is the optical transmittance in % and N is the number of Graphene layers.

2.2.5. Mechanical Properties of Graphene

In previous sections, the electrical and optical properties of Graphene have been presented demonstrating that Graphene is superior material for interconnects when

compared to ITO. One of the key reliability issues with using ITO is its mechanical stability. The next section will discuss the mechanical properties of Graphene.

The mechanical properties of Graphene have mainly been characterized using nano-indentation Atomic Force Microscopy (AFM) and through Molecular Dynamics (MD) Simulations.

In 2008, Lee et al in 2008 [130] used AFM nano-indentation to determine the mechanical properties of 5x5 mm array of circular wells (1.5 µm or 1 µm diameter with a 500 nm depth) on 300 nm SiO_2 layer. The Graphite flakes were mechanically deposited onto the substrate. During the test, the AFM tip is used to puncture the Graphene layer and the corresponding load and deflection curves were measured. A schematic of this is shown in Figure 2.35 [130]:

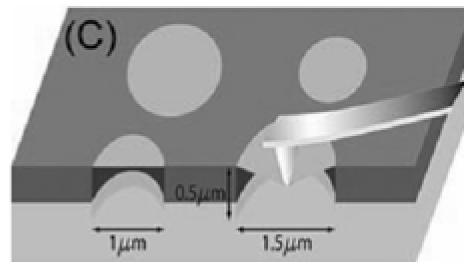

Figure 2.35: Illustration of AFM nano-indentation setup to determine mechanical properties of Graphene [130]

Using the load vs. deflection curves shown below in Figure 2.36 and modeling the test configuration as a thin clamped, linear elastic circular membrane under a spherical indenter as a function of the applied load, a stress-strain curve was produced as shown in Figure 2.37 [130]:

$$\sigma_m^{2D} = \left(\frac{F E^{2D}}{4\pi R}\right)^{\frac{1}{2}} \qquad (2.16)$$

where σ_m^{2D} is the max stress, R is the Indenter tip, E^{2D} is the 2-D Elastic Modulus and F is the applied load.

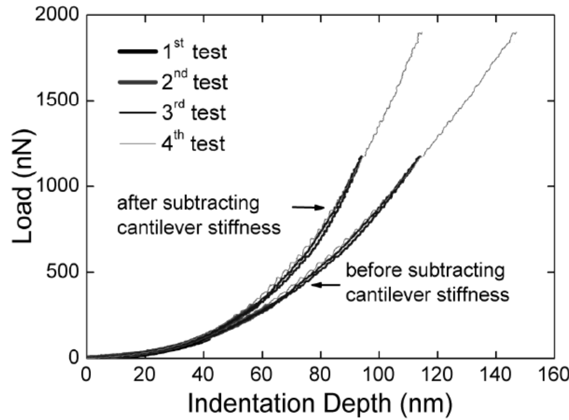

Figure 2.36: Load vs. Deflection curves obtained using nano-indentation AFM of Graphite flakes on SiO_2 [130]

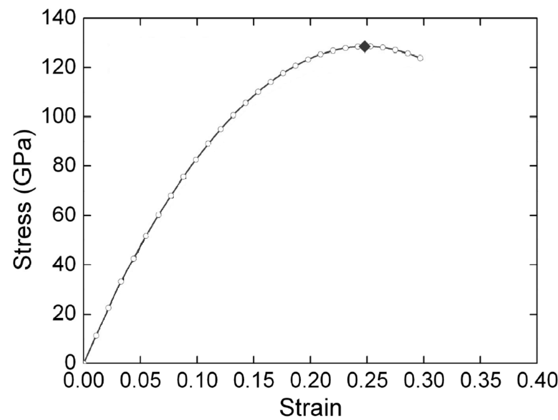

Figure 2.37: Stress-Strain Curve for Graphene as measured using nano-indentation AFM [130]

From Figure 2.37, Graphene has an elastic modulus of 1 TPa and a ultimate strength of 120 GPa, making it one of the strongest known materials. Additional MD simulations of the mechanical properties of Graphene done by Zhao et al. [131]

confirm these values. In addition, Zhao et al, studied the effect of armchair vs. zigzag directions on the mechanical properties and found that the zigzag direction was slightly stronger than the armchair direction. The stress-strain curves created as a result of the MD simulations performed by Zhao et al. are shown in Figure 2.38.

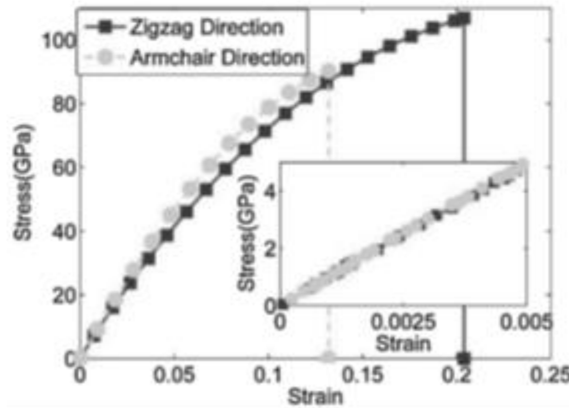

Figure 2.38: Stress-Strain Curves for both the Zigzag and armchair directions via MD Simulations [131]

Similar to the work done on ITO, several researchers have looked at mechanical deformation (uniaxial tensile or bending) of Graphene and the effect it has on the electrical properties of Graphene films. In 2011, Fu et al.[132] fabricated Graphene layers on Cu foils using CVD and then transferred the Graphene to a PDMS substrate. The samples were 40 µm x 20µm in size and tested using a single axis linear miniature motorized stage. An illustration of the test setup and the change in resistance as a function of strain is shown below in Figure 2.39a and 2.39b:

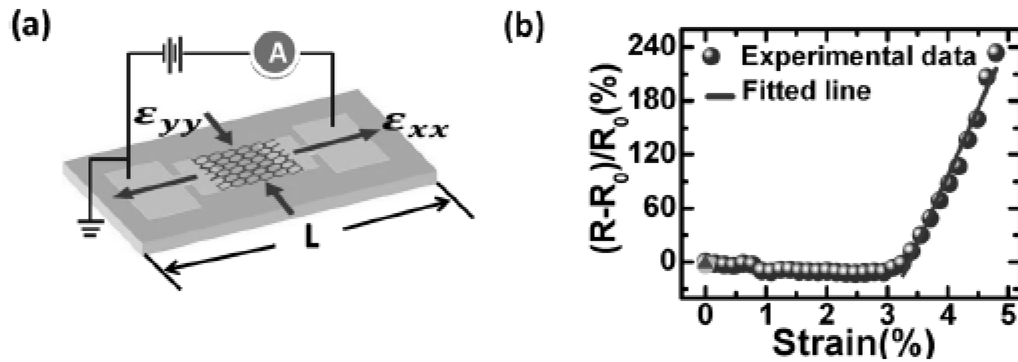

Figure 2.39: a) Schematic of Single Axis Linear miniature motorized stage used for test b) % Change in Resistance as a function of strain for Graphene [132]

In 2011, Huang et al. [133] studied the electrical properties of Graphene films deformed using a nano-indentation method. Samples were fabricated first by mechanically exfoliating Graphite flakes onto a Si/SiO_2 substrate using the "Scotch Tape" method. Then Graphene ribbons with widths between 1.5 to 4 μm and lengths between 0.8 and 1.2 μm were fabricated using E-beam lithography and plasma etching. These samples were then tested using a custom nano-indentation setup that incorporates an SEM and a nano-indentation device. During testing, the wedge tip is pushed into the Graphene sample until the sample is deformed and then it is unloaded. A schematic of the test setup is shown below in Figures 2.40a and 2.40b. Figures 2.40 c-h illustrate the indentation process used to determine the mechanical properties of the Graphene samples. The % change in resistance as a function of strain is shown in Figure 2.41 respectively:

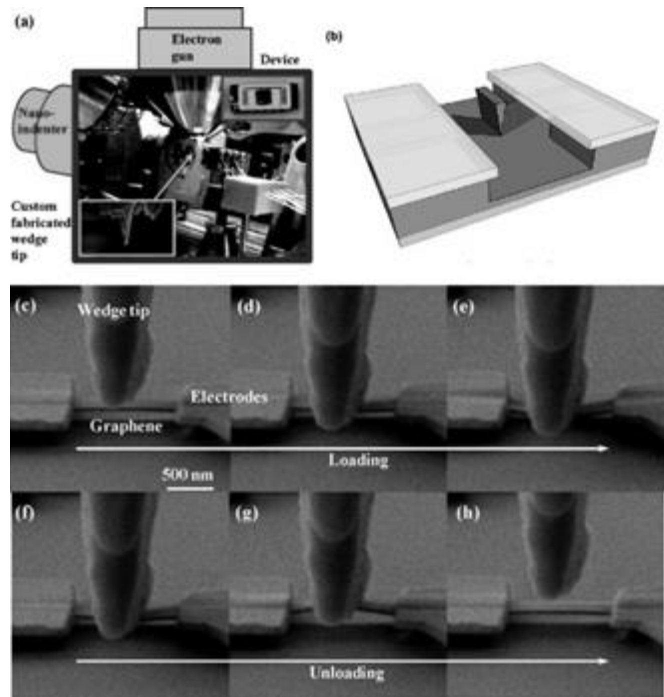

Figure 2.40: Schematic of SEM + nano-indentor Setup b-h) Illustration of Indentation Process to test Graphene samples [133]

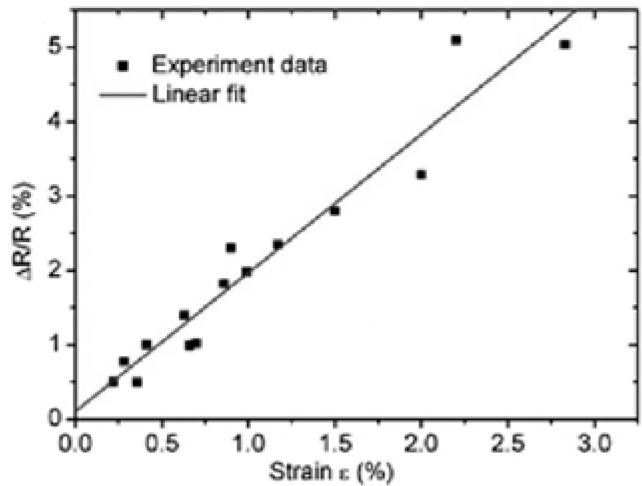

Figure 2.41: % Change in Resistance as a function of Strain for Graphene samples tested using SEM + nano-indentation setup [133]

As seen in Figure 2.41, similar to the ITO films, applying a strain to the Graphene films induces a change in electrical resistance where after some critical value, the

strain starts increasing. The initial work presented here has shown that a consistent range of values for COS to get a 10% change in electrical resistance for Graphene has yet to be established. If the work done by Huang et al is the standard for Graphene, then Graphene can withstand higher strain values before it reaches a 10% change in resistance than its ITO counterpart.

Additionally, unlike ITO where there have been some published fatigue studies, no published fatigue studies on Graphene films has been published.

2.3. *ITO vs. Graphene*

After reviewing the mechanical, electrical and optical properties of ITO and Graphene, a summary of the various properties of Graphene and ITO is given below in Table 2.6:

Table 2.6: Summary of the various properties of ITO of Graphene [128]

Property	Graphene	ITO
Sheet Resistance	100-300 Ω/□	30-80 Ω/□
Mobility	15,000-200,000 $cm^2/V\cdot s$	10-70 $cm^2/V\cdot s$
Optical Transparency	97.8% (Monolayer) 95% (Bi-Layer) 93% (Tri-Layer)	90%
Elastic Modulus	1 TPa	116 GPa
Critical Strain to achieve 10% change in Resistance	5-10%	1-2%

Based on the electrical, optical and mechanical properties, Graphene appears to be the superior interconnect material to ITO. Another disadvantage of ITO is its cost. The main reason, Graphene is being considered is because of its superior mechanical properties with the potential to eliminate line outs by reducing/eliminating

interconnect cracking during normal use of a flexible displays. The next chapter will discuss the dedicated test setup that was designed and developed in order to investigate the fatigue properties of Graphene and ITO.

Chapter 3 : Experimental Setup

In order to perform the necessary bending fatigue experiments, a dedicated test system was designed, fabricated and integrated for this research. In this work, two types of test systems were created: one for testing patterned ITO samples while the other type was used to test uniform film samples of ITO or Graphene. The following sections will discuss these two types of systems and the three types of test samples used in the present experimental work.

3.1. *Test Setup for Patterned ITO Devices*

A test setup based on the cyclic mandrel test method [52] was developed by Tom Martin in his PhD work [1]. This same setup was modified to allow for testing of both uniform ITO and Graphene samples. A flowchart illustrating how the setup operates is shown in Figure 3.1:

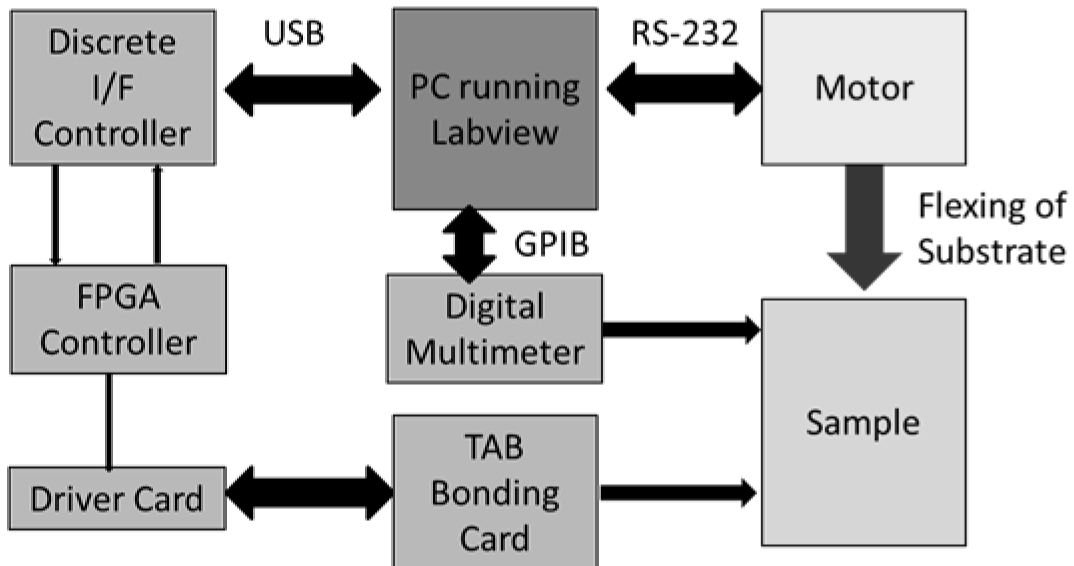

Figure 3.1: Block diagram of fatigue test setup for patterned ITO samples [1]

In the test setup, a stepper motor is controlled by a LabView program. When the test is started, this program instructs the motor to push an acrylic mandrel into the sample, bending the sample to a set radius of curvature. Once the sample has been bent, the program sends a command to obtain a resistance measurements from the sample in the bent condition. This setup can be used to measure resistance for individual traces (ITO samples) or the sheet resistance of uniform films of either Graphene or ITO using a digital multi-meter (DMM). Once the measurement is completed, the program sends a command to the motor to relax the sample. This process is repeated until the desired failure criterion is achieved. Next, a more detailed description of the individual components of the test setup will be discussed.

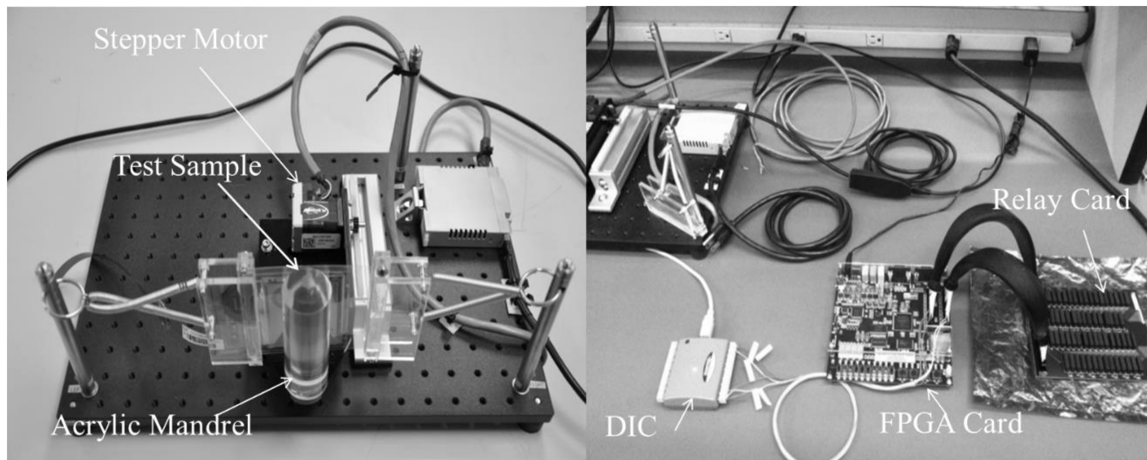

Figure 3.2: Bending fatigue setup used for patterned ITO samples

In the setup shown above in Figure 3.2, the stepper motor pushes the acrylic mandrel into the sample bending it to a set radius of curvature. The acrylic mandrel shown in Figure 3.2 has a diameter of 38.1 mm, but this mandrel can be swapped for any size depending on the desired testing conditions. After the sample is bent, the program needs to send a command to measure the resistance of the sample. This achieved by,

first the PC sends a signal to the discrete interface controller (DIC) which in turns sends a signal to the field programmable gate array (FPGA) circuit card connected to a relay card. The FPGA is designed to rapidly drive and take resistance measurements of each of the individual traces. Next the program, relaxes the substrate and repeats this process of bending/unbending until the desired failure criterion is met.

In order to prevent damage to exposed traces, it was decided to not completely wrap the substrate around the mandrel. Since, only a portion of the trace is being mechanically bent, the resistance of the bent portion is calculated using the following equation:

$$\Delta R_{inferred} = \Delta R_{measured} \left(\frac{TL}{AL}\right) \tag{3.1}$$

where TL is the entire trace length and AL is the length subjected to mechanical stress. The failure threshold was set to be a percentage of the inferred change in resistance to the initial resistance of the trace where:

$$\frac{\Delta R_{Inferred}}{R_{Initial}} x100\% \geq 110\% \tag{3.2}$$

The failure criterion of 10% was based on the SPICE circuit simulation results of a failure threshold defined to be when the gate line resistance exceeds 450 kΩ [1].

3.2. *Test Setup for uniform films of ITO and Graphene*

The setup used earlier for patterned ITO samples was modified in order to conduct measurements for uniform films. The simplified setup works exactly like the setup

discussed in Section 3.1. A simplified block diagram for this setup and illustration of the setup is shown below in Figures 3.3 – 3.5.

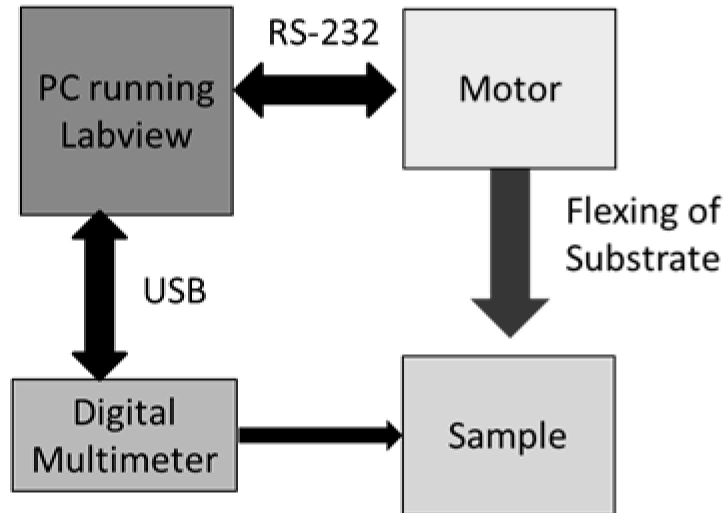

Figure 3.3: Block diagram of fatigue test setup for uniform ITO or Graphene samples

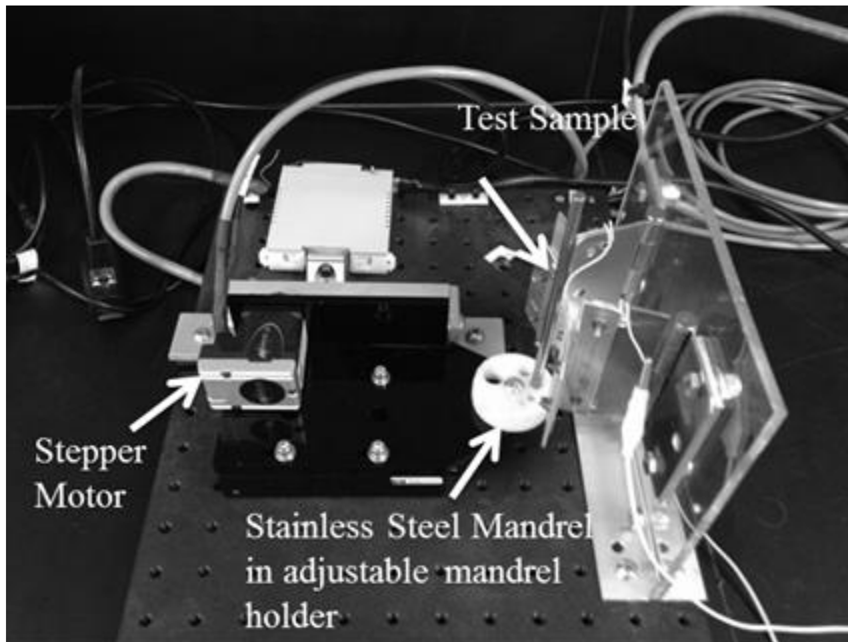

Figure 3.4: Bending fatigue setup used for uniform ITO or Graphene samples

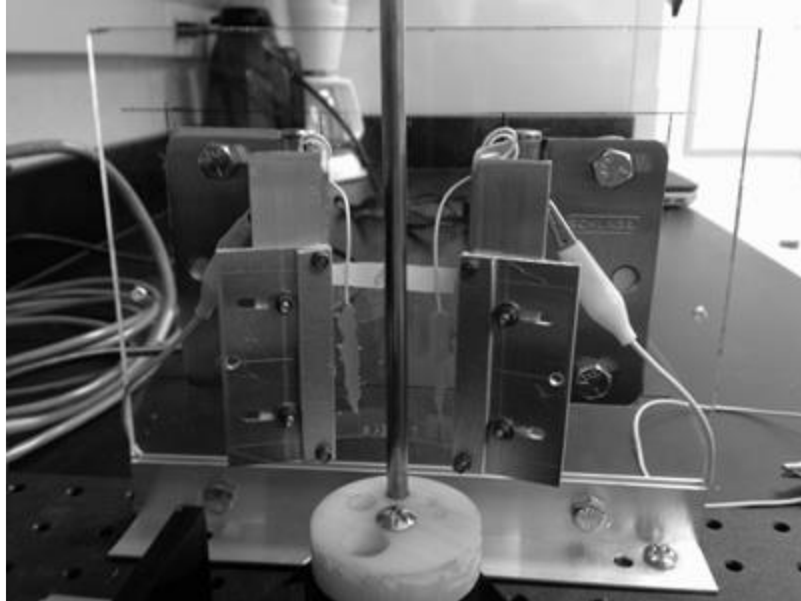

Figure 3.5: Updated sample mounting system used for uniform ITO or Graphene samples

In this updated test setup, the samples are again clamped down and held in position using a hinge system instead of a spring system in order to increase the robustness of the system. Additionally, as seen in Figure 3.4, a variety of different stainless steel mandrels with diameters including 5, 6, 8 and 13 mm respectively can be used (pictured in Figure 3.6). In this simplified setup, the DIC and FPGA cards are no longer needed due to the reduction in the number of resistance measurements required per cycle.

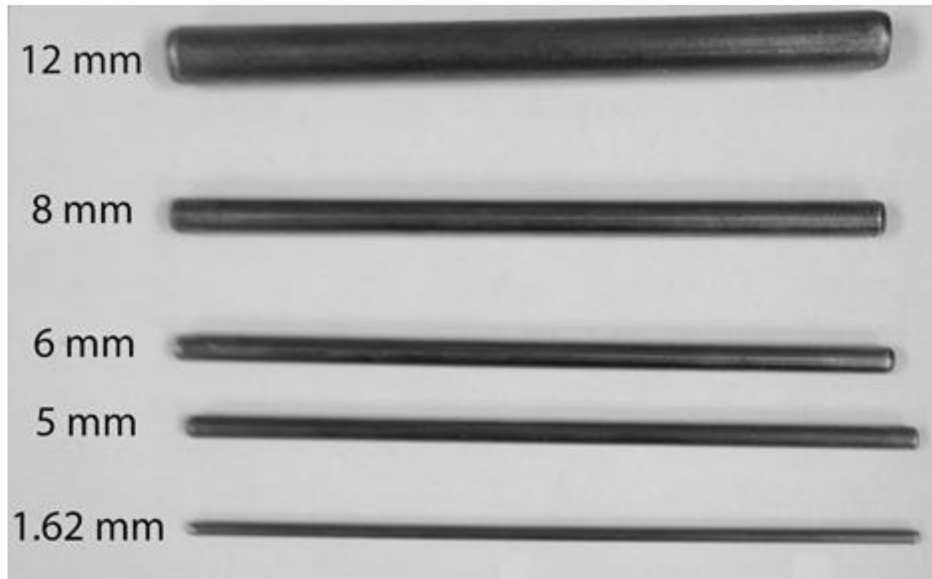

Figure 3.6: Mandrels (13, 8, 6, 5 and 1.62 mm) used to perform fatigue studies on uniform ITO or Graphene samples

The dedicated test systems for both patterned and uniform film samples of either ITO or Graphene has been discussed, the next few sections will discuss sample design and fabrication techniques to create all of the test structures.

3.3. *Sample Design/Fabrication*

3.3.1. Patterned ITO Samples

Patterned ITO samples fabricated by the Flexible Display Center (FDC) in AZ similar to the ones use in the work by Martin [1] were used for the experimental work. The fabricated samples will consist of a layer stack structure as shown below in Figure 3.7:

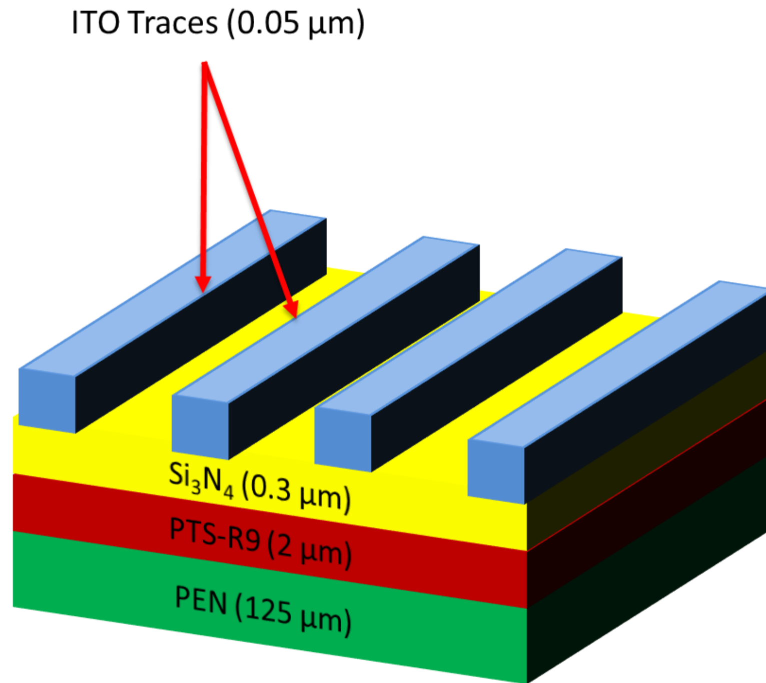

Figure 3.7: Cross Section View of Multilayer ITO Samples for Bending Fatigue Tests

The layer stack structure shown above in Figure 3.4 starts with a Polyethylene Naphthalate (PEN) substrate (DuPoint Teonix Q65FA) with a thickness of 125 µm. In literature, typically ITO is grown on PET substrates but PEN was selected due to it's superior thermal deformation (higher T_g) and improved electrically stability at elevated temperatures [134]. Next, a 2 µm planarization layer (PTS-R9) is deposited using a spin coating technique at 200 °C in order to improve the surface uniformity of the PEN substrate (as seen below in Figure 3.8).

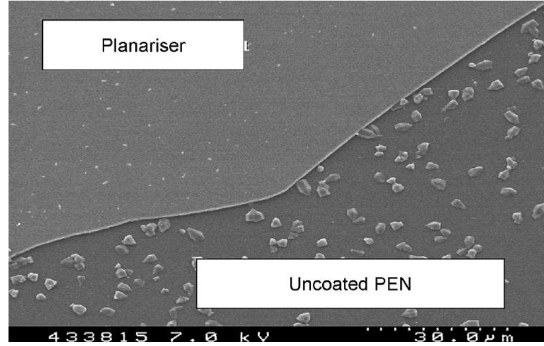

Figure 3.8: SEM image showing the effect of PTS-9 deposition on the surfaces of planarized and uncoated PEN [135]

Next, a 0.3 μm buffer layer is deposited on the PTS-R9/PEN stack using Plasma Enhanced Chemical Vapor Deposition (PECVD) at 180 °C. Finally the interconnect layer of ITO was deposited using direct current (DC) magnetron sputtering. A summary of the processing conditions and material properties of this layer stack structure are given in Table 3.1 below [1], [49], [104], [130], [136], [137]:

Table 3.1: Summary of Processing Conditions and Material Properties for Multilayer ITO Samples

Layer	Substrate	Planarization	Buffer	Trace
Material	PEN	PTS-R9	Si_3N_4	ITO
Thickness (μm)	125	2	0.3	0.05
Process	N/A	Spin Coat	PECVD	DC Magnetron Sputtering
Process Temp (°C)	N/A	200	180	98
Young's Modulus (GPa)	3.7	2.52	122.5	116
Poisson's Ratio	0.33	0.25	0.23	0.35
Density (g/cm^3)	1.36	0.959	2.5	6.8
CTE (ppm/°C)	21.5	17.5	2.2	9.25

In order to investigate the influence of trace width on the electrical response during bending, the interconnect layer for the ITO samples was patterned using

photolithography. There are a total of 60 traces in varying widths with 6 sets of 10 traces at the following widths: 1.5, 0.75 and 0.5 µm, all with a thickness of 0.05 µm. Figure 3.9 below shows the photolithography mask used to pattern the traces onto the samples:

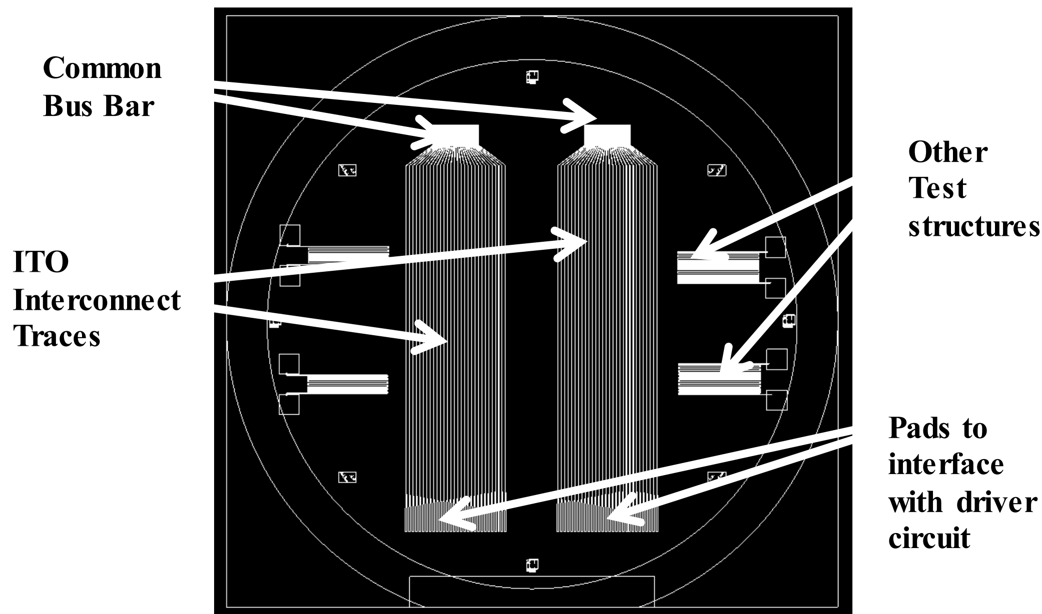

Figure 3.9: Photolithography masked used to fabricate samples with patterned ITO traces with widths of 1.5, 0.7 and 0.3 µm respectively [1]

As seen in Figure 3.8, pads are used to connect the individual traces to the driver circuit. The physical connection between the traces and the driver circuit is done using a tape automated bonding process (TAB) card. The TAB card consists of a polyamide film containing a flip chip that is programmed to take row/column signals and convert them to unique row/column line to address each pixel in the array. An anisotropic conductive film (ACF) is used as the conducting element between the TAB's on the driver circuit and PEN substrate respectively. A cross-section view of a TAB card and the connection it forms between the driver circuit and substrate is shown in Figures 3.10a and 3.10b

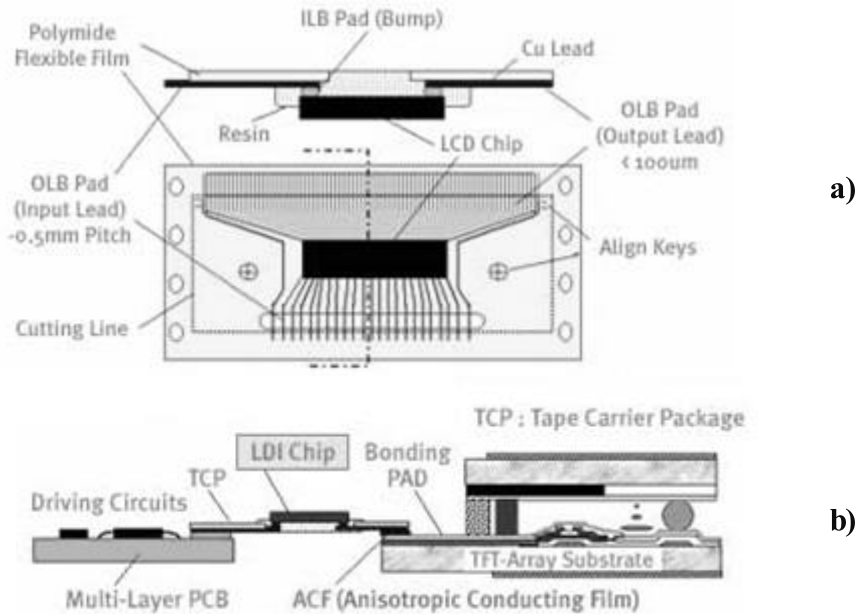

Figure 3.10: a) Schematic of TAB Bonding Card b) Illustration showing the connection the TAB card makes [138]

Once, the sample has been TAB bonded, silver conductive epoxy (Resinlab 1233) is used to attach leads for the DMM to take resistance measurements during bending. For the patterned ITO samples, the silver epoxy is applied as an entire strip, while for the uniform samples, the silver epoxy is applied as points. The silver epoxy was applied to each sample using a Fisnar JB1113N automatic liquid dispenser. An image of the sample with the TAB card and silver epoxy with leads attached is shown below in Figure 3.11. The sample is now ready to be mounted into the test setup discussed earlier and tested.

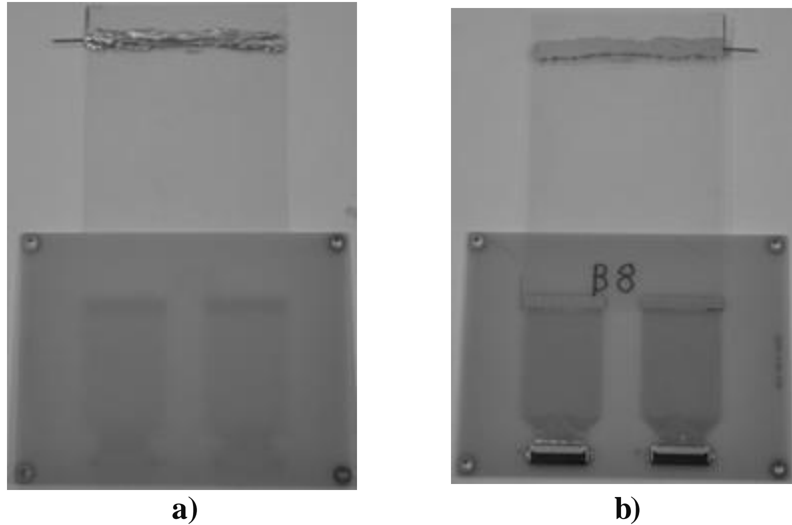

a) b)

Figure 3.11: Image of ITO Samples TAB Bonded with Silver Epoxy Attached a) Back View b) Front View

3.3.2. Uniform ITO Samples

Uniform ITO films were fabricated in order to compare the fatigue properties of ITO to Graphene. These uniform films were fabricated using similar conditions as the patterned ITO samples fabricated by the Flexible Display Center (FDC) in AZ minus the photolithography patterning step. The fabricated samples will consist of a layer stack structure as seen below in Figure 3.12. The dimensions of this layer stack structure are a 50 mm x 50 mm square of ITO on top of the a 50 mm x 50 mm square of Si_3N_4/PEN substrate as shown in Figure 3.13:

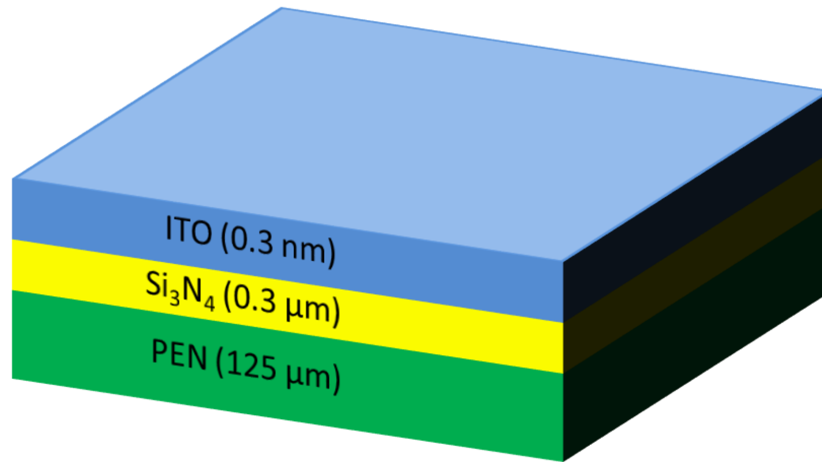

Figure 3.12: Cross Section View of Uniform ITO Samples for Bending Fatigue Tests

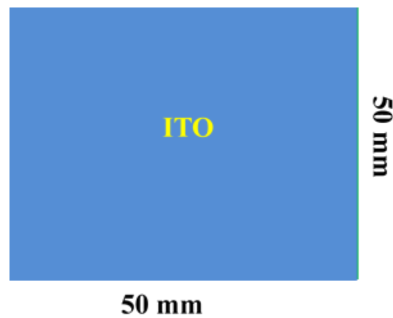

Figure 3.13: Drawing of Uniform ITO film

Silver epoxy is used to create four contacts on the surface of the ITO film sample for resistance measurements during bending fatigue. Adhesive tape is used to provide additional mechanical support to ensure sustained contact between the leads and the sample surface during fatigue experiments. An image of the uniform ITO sample prior to being mounted into the test setup discussed earlier in Section 3.2 is shown below in Figure 3.14.

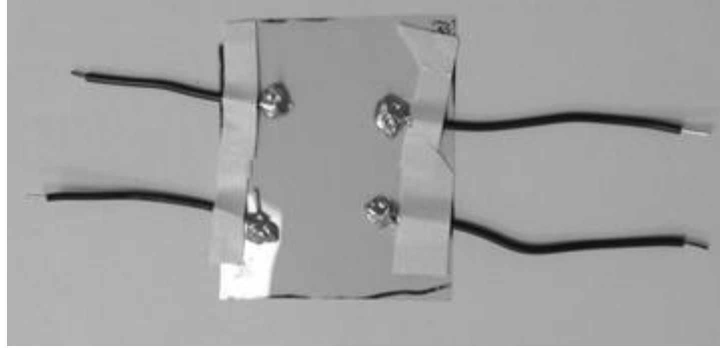

Figure 3.14: Uniform ITO on Si_3N_4/PEN sample with silver-epoxy leads

3.3.3. Uniform Graphene Samples

Monolayer Graphene samples used for the bending fatigue studies consist of a tri-layer structure starting with a 125 µm layer of PEN (DuPoint Teonix Q65FA) with a 0.3 µm Si_3N_4 grown using Plasma Enhanced Chemical Vapor Deposition (PECVD) at 180 °C and finally a monolayer (0.34 nm) of Graphene. The Si_3N_4/PEN bi-layer structure was fabricated at the FDC and then sent to a commercial vendor, for Graphene deposition/transfer due to lack of familiarity in Graphene fabrication and lack of equipment. A cross section view of the final sample to be used for testing is shown below in Figure 3.15:

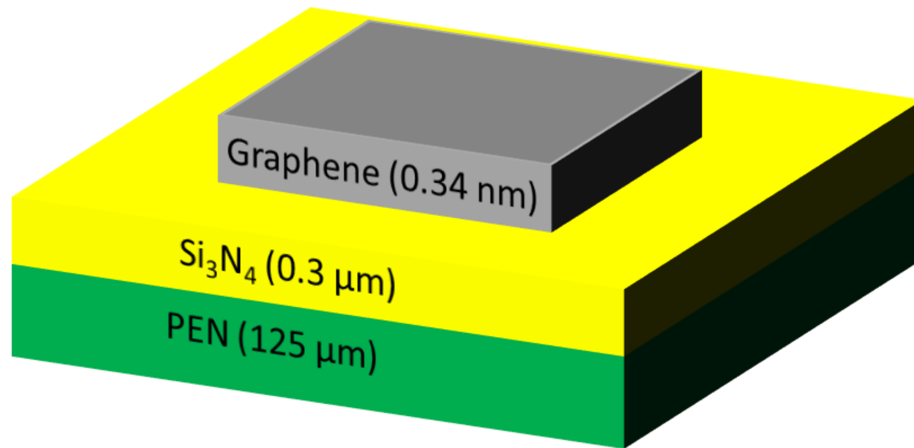

Figure 3.15: Cross Section view of Graphene samples used for Bending Fatigue Tests

Based on the experimental setup, the dimensions of the Graphene sample were determined to be a 25 mm x 25 mm square of Graphene at the center of a 50 mm x 50 mm piece of Si_3N_4/PEN. The size of the planarized PEN was chosen so that the sample could fit into the current experimental setup. The 25 mm x 25 mm monolayer Graphene square was placed at the center of the Si_3N_4/PEN substrate to ensure that it would be fully bent during testing. Additionally, a 25 mm x 25 mm square was chosen due to limitations in current fabrication processing conditions in producing uniform high quality Graphene films. A schematic of the Graphene test sample is shown below in Figure 3.16 where the green square is the Si_3N_4/PEN substrate and the black square is the Graphene layer:

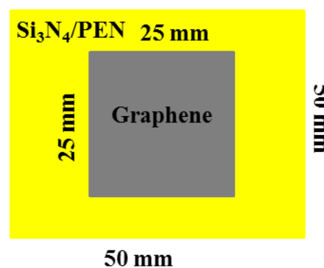

Figure 3.16: Drawing of Graphene test sample

Three Graphene film vendors were identified as potential candidates for sample fabrication to including ACS Materials, Graphene Supermarket and Graphene Platform. 25 mm x 25 mm samples of monolayer Graphene on PET were ordered from each of the companies in order to determine the respective film qualities from each of the vendors. Each of the vendors initially fabricated Graphene on Cu using CVD and next used the "Floating Graphene" transfer technique [128] to fabricate the Graphene/PET samples as shown below in Figure 3.17:

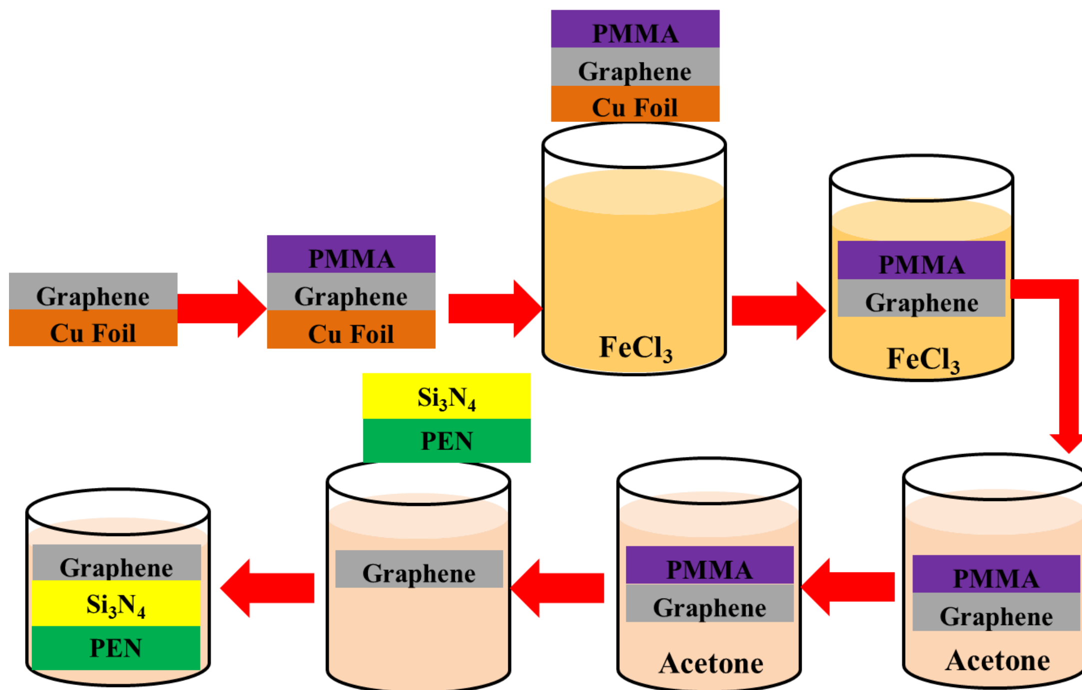

Figure 3.17: Illustration of "Floating Graphene" transfer technique [128]

In the floating Graphene technique, first Graphene is grown via chemical vapor deposition onto a copper foil. Next a thin layer of Poly(methyl methacrylate) (PMMA) is spin coated on top of the Graphene/Cu structure. Next this, tri-layer structure is dipped into a solution of $FeCl_3$ to etch away the Cu foil. The

Graphene/PMMA stack is then rinsed with DI water and placed into a solution of acetone. The Acetone then etches away the PMMA layer leaving a layer of floating Graphene in Acetone. Next the Graphene is removed from the Acetone solution and placed on top of the Si_3N_4/PEN substrate. Finally, the Graphene/Si_3N_4/PEN stack is rinsed with DI water and left to dry which yields in Graphene on Si_3N_4/PEN.

Silver epoxy is then used to attach four contacts on the surface of the Graphene sample for resistance measurements during bending fatigue. An image of the uniform Graphene sample prior to being mounted into the test setup discussed earlier in Section 3.2 is shown below in Figure 3.18.

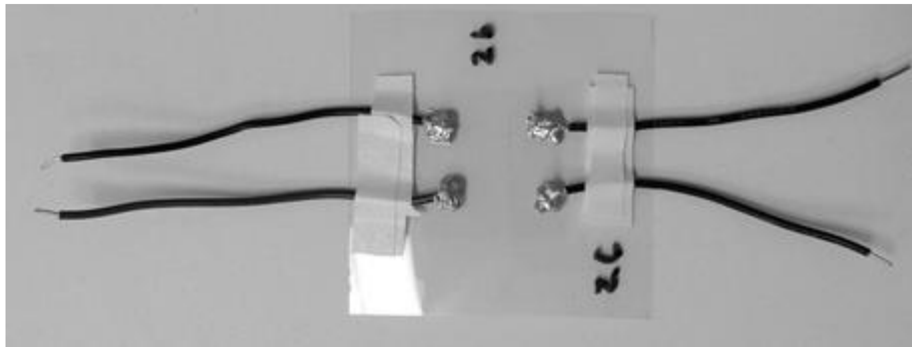

Figure 3.18: Image of Uniform Graphene on Si_3N_4/PEN sample with silver-epoxy leads

This chapter has discussed the dedicated test system that was designed in order to perform fatigue bending studies of patterned ITO, uniform and uniform Graphene films on top of Si_3N_4/PEN substrates. Additionally, the fabrication and design of the three test samples has also been discussed. The next chapter will focus on the mechanical stress in the films caused by bending.

Chapter 4 : Mechanical Stresses in Thin Films

Based on the Failure Modes and Effects Criticality Analysis (FMECA) analysis, line outs were determined to be the most critical failure mechanism for flexible displays [26]–[28]. In order to understand and investigate this failure mechanism, first stresses in multilayer films is reviewed. The stresses present in thin film devices can be broken down into two categories, internal forces caused during fabrication and external forces. This section will discuss the two categories in greater detail and then the results of finite element analysis using ANSYS [139] will be presented for patterned ITO, uniform ITO and uniform Graphene samples on Si_3N_4/PEN.

4.1. *Internal Stresses*

Stresses can be created due to incompatibilities between the film and substrate in terms of differences in thermal expansion coefficients, phase transformations with volume changes, film densification and epitaxial defects. Typically, thin films are grown under vacuum conditions at elevated temperatures. The first type of strain produced during fabrication is due to the lattice mismatch between the substrate and the film. As the film is being deposited onto the substrate, it must either be stretched or compressed to fit into the lattice sites of the substrate. The corresponding misfit strain created because of this lattice mismatch is:

$$\varepsilon_{lattice\,misfit} = \frac{a_{film} - a_{substrate}}{a_{substrate}} \tag{4.1}$$

where a_{film} and $a_{substrate}$ are the lattice constants of the film and substrate respectively. The amount of misfit strain due to the thermal property differences is given by:

$$\varepsilon_{CTE\ misfit} = (\alpha_{film} - \alpha_{subsrate})(T - T_o) \tag{4.2}$$

where ε_{misfit} is the misfit strain, α_{film} and $\alpha_{substrate}$ are the film and substrate coefficients of thermal expansion respectively, T is the deposition temperature and T_o is room temperature . Once deposition is completed, the sample cools back down to room temperature. Since both the film and substrate have different coefficients of thermal expansion values, they will want to contract at different rates leading to additional strain in the system.

Internal stresses are largely due to material property differences between the film and the substrate. Therefore it is important to understand internal stresses for films on stiff or compliant substrates. When a film is grown on a stiff substrate, the substrate has a higher elastic modulus than the film. This results in the film being stretched and the creation of a biaxial stress in the plane of the film. The film stress, σ_f, can be found using the misfit strain, ε_m, by:

$$\sigma_{film} = \varepsilon_m E_F^* \tag{4.3}$$

where E_F^* is the biaxial elastic modulus of the film. The stress in the substrate is much smaller than the film resulting in the substrate being bent with a radius of curvature defined by Stoney's Equation [140]:

$$R = \frac{\overline{E_s} t_s^2}{6 t_f R} \tag{4.4}$$

where σ_f is the bending stress in the film, E_s is the elastic modulus of the substrate, ν_s is the Poisson's ratio of the substrate, t_s and t_f are the substrate and film thicknesses respectively and R is the radius of curvature. In contrast, when a film is grown on a compliant substrate, the substrate also deforms as the system is being deformed. The stress in the film for a compliant substrate is

$$\sigma_f = \frac{\varepsilon_m E_F^*}{1 + \frac{E_F^* t_f}{E_S^* t_s}} \tag{4.5}$$

where ε_m is the misfit strain, E_F^* and E_S^* are the biaxial moduli of the film and substrate respectively and t_f and t_s are the film and substrate thicknesses respectively. For compliant substrates, the radius of curvature is given by [141]:

$$R = \frac{\left(\overline{E_s} t_s^2 - \overline{E_f} t_F^2\right)^2 + 4\overline{E_f E_S} t_f t_s \left(t_f + t_s\right)^2}{6\varepsilon_m (1+\upsilon)\overline{E_f} t_f t_s (t_F + t_s)} \tag{4.6}$$

4.2. *External Stresses*

This section is dedicated to discussing the stresses created in a bilayer structured caused by an eternally applied bending moment. When a simple bilayer structure is bent to a specific radius of curvature, with the film on the outside, the top surface of the structure is in tension while the bottom layer is in compression (as seen in Figure 4.1):

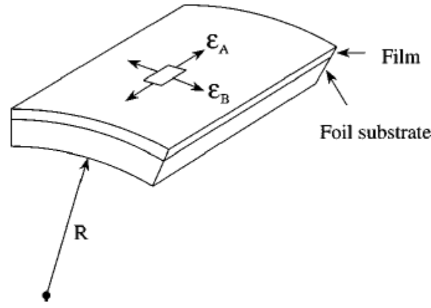

Figure 4.1: Bilayer structure bent to a specific radius of curvature using a cylinder [142]

Inside the structure, a surface exists that has no strain on it known as the neutral axis. When the films have comparable elastic moduli, the neutral axis is located at the midpoint of the structure so that the strain in the top surface of Figure 4.1 is equal to:

$$\varepsilon_{top} = \frac{t_f + t_s}{2R} \tag{4.7}$$

where ε_{top} is the strain in the top surface, R is the radius of curvature and t_f and t_s are the thickness of the film and substrate respectively.

When a more compliant substrate is used ($E_f > E_s$), the neutral axis shifts from the midpoint towards the film. The strain on the top surface of the film is [142]

$$\varepsilon_{top} = \frac{t_f + t_s}{2R} \frac{(\eta^2 + 2\eta + 1)}{(\eta + 1)(1 + \chi\eta)} \tag{4.8}$$

where

$$\chi = \frac{E_f}{E_s} \tag{4.9}$$

$$\eta = \frac{t_f}{t_s} \tag{4.10}$$

where E_f and E_s are the elastic moduli of the film and substrate respectively

4.3. *Mechanical test methods for Flexible Displays*

Mechanical test methods for flexible displays can be broken into 2 categories: the first involves determining the maximum strain a device can withstand until failure. The second type involves cyclic bending of a sample to a set radius of curvature (strain) from a relaxed state and recording the number of cycles to failure. In addition to the type of testing method, the type of test structure is also another important factor. The majority of published work on ITO has involved uniform forms with some work done on patterned samples. Traditionally, for strain to failure test methods, the critical strain value or crack onset strain (COS) is defined as the strain that results in a 10% change in resistance of the sample. Three main testing methods are utilized to determine strain to failure including the uniaxial testing method, the two point bending method and the biaxial method.

In the uniaxial fragmentation test, the sample is clamped at both ends and slowly pulled apart (seen below in Figures 4.2 and 4.3). While the sample is loaded in tension, an in-situ microscope is used to visually inspect for crack initiation and propagation while simultaneously monitoring changes in resistance. This method allows for precise monitoring but can be very tedious and time consuming.

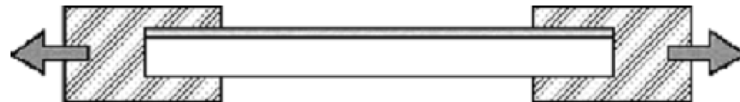

Figure 4.2: Schematic Representation of Uniaxial Test Method[9]

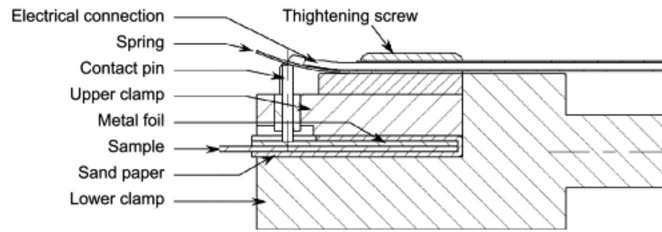

Figure 4.3: Detailed schematic of Uniaxial Testing Method [49]

In the two point bending method, the sample is placed between two parallel plates (as seen in Figure 4.4). Either one or both of plates is pushed inward, bending the sample to a finite radius of curvature with the maximum strain in the middle of the sample. Similar to the uniaxial test method, the two point bend method allows for the determination of the critical strain to failure, but does not allow for direct observation of the sample during testing. One of the additional benefits of the two point bend method is that is faster than the uniaxial testing method and it can be modified to perform fatigue testing. One of the drawbacks of this method is that the strain is not uniform across the sample. As the plates get closer together, the sample becomes more parallel to the plates causing a smaller portion of the sample to be bent. The second drawback is since the samples are mounted to the clamps, the sample is not allowed to achieve a fully relaxed state.

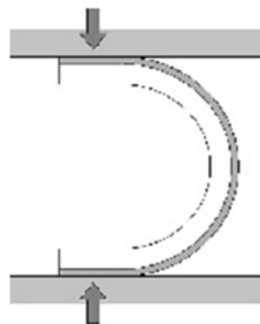

Figure 4.4: Schematic of Two Point Bending Method [143]

In the biaxial method [4], [144],the sample is clamped at the substrate edges and next a pressurized gas in injected. This causes the sample to bulge in the center and therefore the sample is bent to a set radius of curvature. A schematic of the test setup is shown below in Figure 4.5 and an example of a bulge in a film is shown in Figure 4.6:

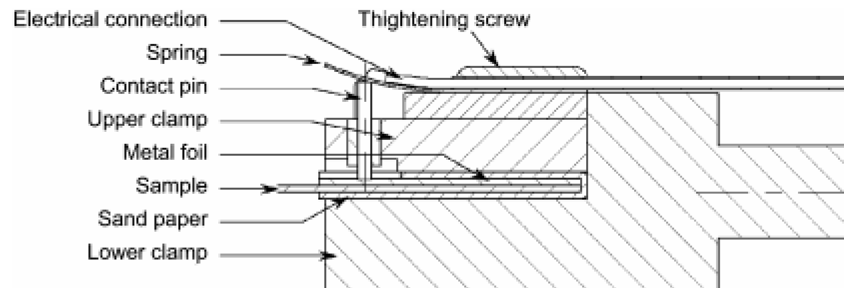

Figure 4.5: Schematic of Biaxial Test Method[144]

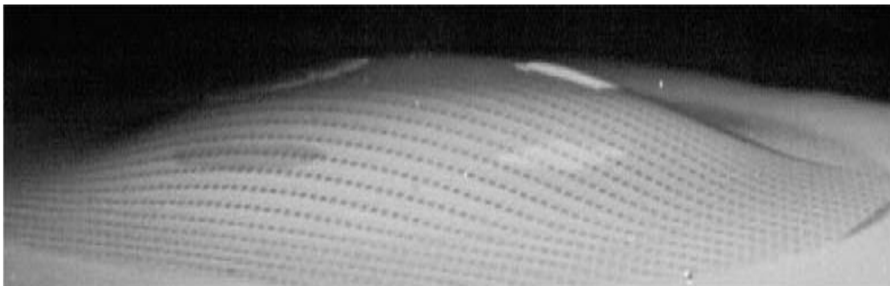

Figure 4.6: Polyimide foil with a-Si/SiN islands after deformation under the biaxial test method[145]

The final test setup that will be discussed is the cyclic mandrel test method developed by Gorkhali and Cairns in 2004 [52]. In this setup, a cyclic loading rig bends a sample around a mandrel to a set radius of curvature and then returns the sample to its original starting position. During the bending/unbending process, a multi-meter

measures changes in the resistance of the sample as a function of the number of cycles. A schematic illustration of this setup is shown below in Figure 4.7:

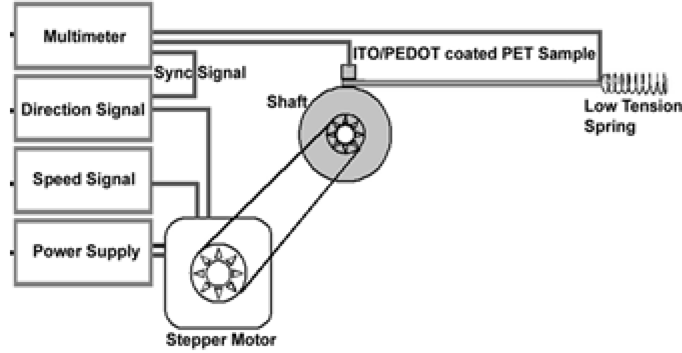

Figure 4.7: Schematic Illustration of Cyclic Mandrel Test Method [52]

4.4. Modeling of Bending Stresses in ITO and Graphene

In this next section, the bending stresses in patterned ITO, uniform ITO and uniform Graphene on Si_3N_4/PEN substrates will be simulated using 2 methods: first with solving Stoney's equation and the second is through the use of finite element analysis (FEA) via ANSYS.

4.4.1. Stoney's Equation

Stoney's formula allows one to determine the bending stress in the film given the radius of curvature the system is bent to as seen below:

$$\sigma_f = \left(\frac{E_s}{1-\upsilon_s}\right)\frac{t_s^2}{6t_f R} \tag{4.11}$$

where σ_f is the bending stress in the film, E_s is the elastic modulus of the substrate, ν_s is the Poisson's ratio of the substrate, t_s and t_f are the substrate and film thicknesses respectively and R is the radius of curvature.

As seen in Stoney's equation, the main factors affecting the bending stress observed are the respective film and substrate thicknesses, while the material properties of the film are not accounted for. The effect of varying the Graphene film thickness between 0.34 nm and 100 nm and varying the PEN thickness between 50 µm and 350 µm were studied. Similarly, the effect of varying the ITO film thickness between 50 nm and 500 nm and varying the PEN thickness between 50 µm and 350 µm were studied. The effect of varying the thicknesses of the Graphene, ITO thickness and PEN layer was determined using Stoney's equation for a bi-layer structure when bent to radii of curvature between 1.58 and 12.7 mm respectively. The elastic properties of PEN, ITO and Graphene used for this simulation are summarized in Table 4.1. The results are shown below in Figures 4.8 – 4.11[49], [130], [136], [137]

Table 4.1: Summary of elastic properties of PEN, ITO and Graphene used in Stoney's equation calculations for bending stresses in ITO/PEN and Graphene/PEN samples

	PEN	ITO	Graphene
Elastic Modulus	3.7 GPa	116 GPa	1 TPa
Poisson's Ratio	0.33	0.35	0.21

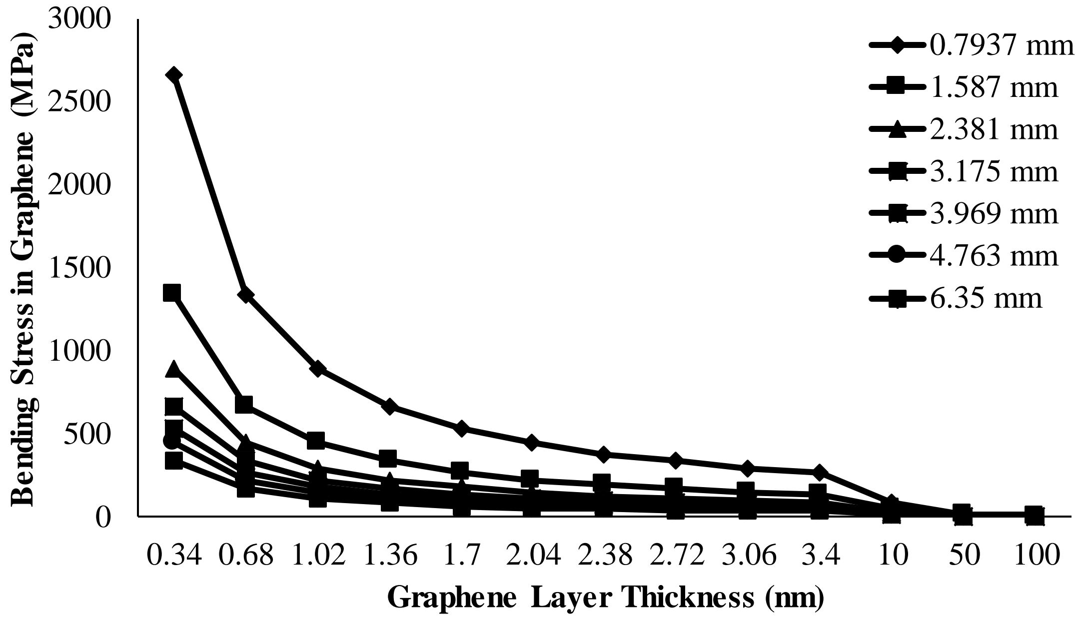

Figure 4.8: Effect of Graphene layer thickness on bending stress in Graphene layer using Stoney's Equation

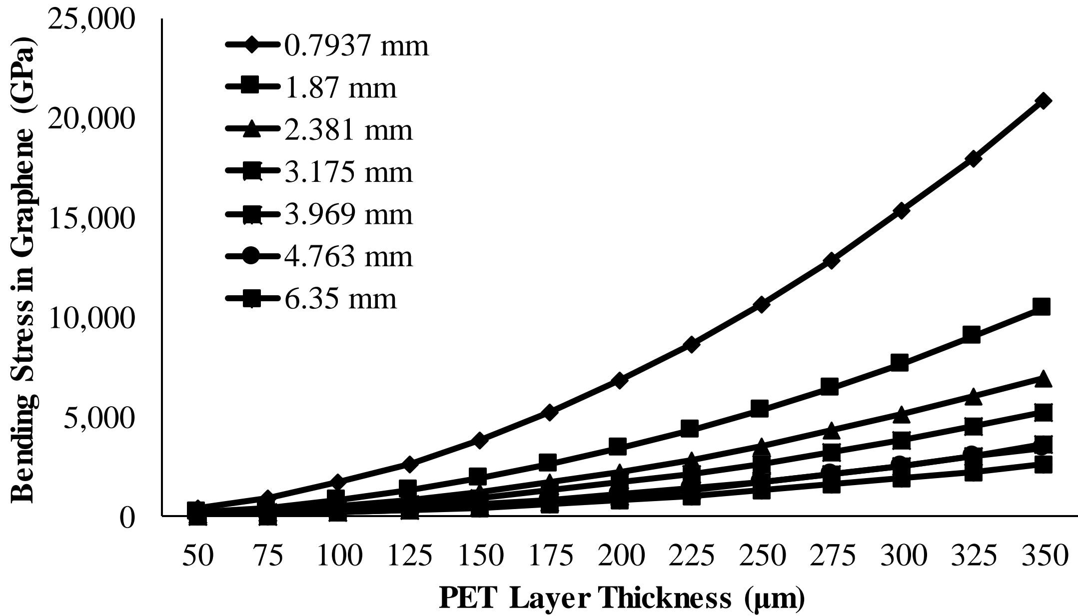

Figure 4.9: Effect of PET layer thickness on bending stress in Graphene layer using Stoney's Equation

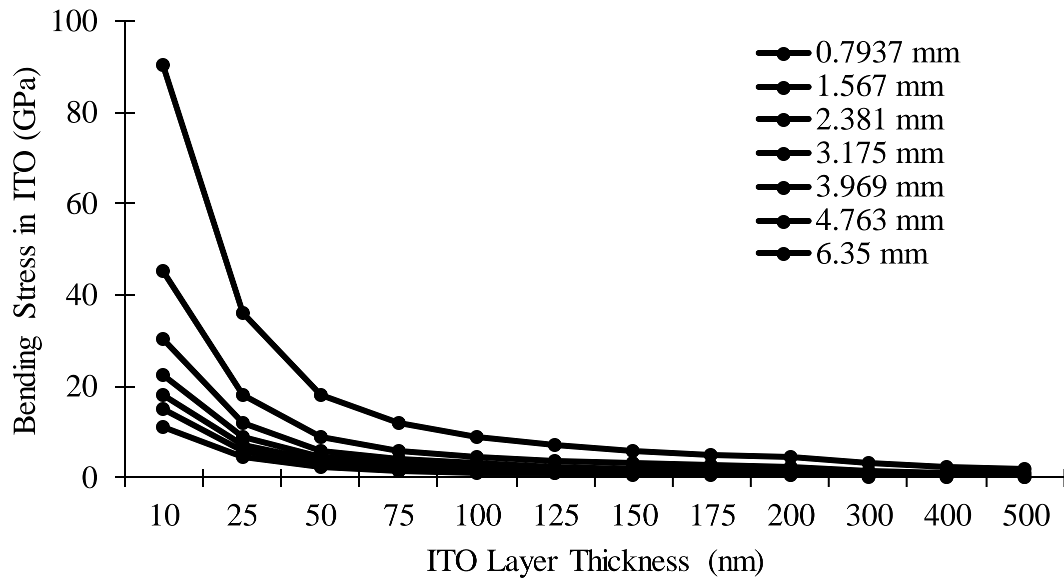

Figure 4.10: Effect of ITO layer thickness on bending stress in ITO layer using Stoney's Equation

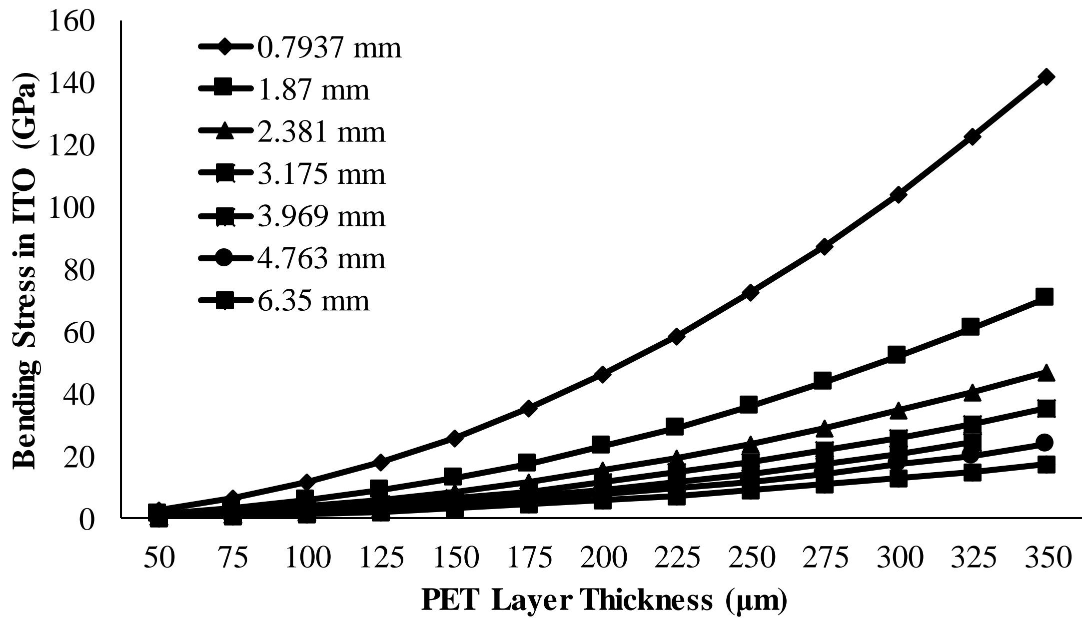

Figure 4.11: Effect of PET layer thickness on bending stress in ITO layer using Stoney's Equation

As expected, the results of the Stoney's equation calculations for both ITO and Graphene on PET show as the mandrel size decreases, a corresponding increase in the

bending stress was observed. This is due to the fact that smaller mandrel radii correspond to higher stress levels. As layer thicknesses were increased, the bending stress observed in both Graphene and ITO decreased. For the simulations for both Graphene and ITO, as the PET substrate thickness increased, a corresponding increase in the bending stress was observed.

4.4.2. Finite Element Analysis using ANSYS

Finite element analysis (FEA) using ANSYS was performed on multi-layered stacks of patterned ITO and uniform films of Graphene and ITO on Si_3N_4/PEN substrates. The purpose of the study was to look at the effect of various mandrel sizes on the bending stresses generated in patterned ITO, uniform films of Graphene and ITO on Si_3N_4/PEN substrates. The differences in bending stresses due to the change from ITO to Graphene was also be studied. A cross-section view of the layer stack structures that were analyzed using ANSYS and the mechanical properties used during this analysis are summarized in Figure 4.12a, 4.12b, 4.12c and Table 12:

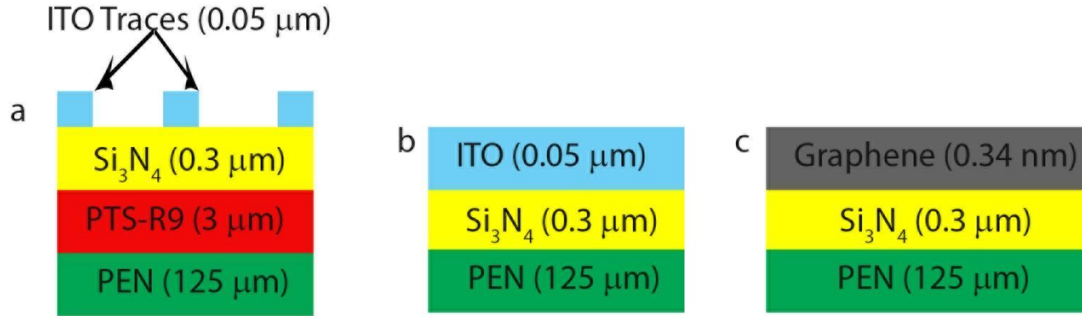

Figure 4.12: Cross section view of a) patterned ITO b) uniform ITO and c) uniform Graphene on Si_3N_4/PEN substrates.

Table 4.2: Summary of Mechanical Properties used for ANSYS Analysis [1], [49], [104], [130], [136], [137]

Layer	Layer Thickness	Elastic Modulus (GPa)	Poisson's Ratio
PEN	125 μm	3.7	0.33
Planarization Layer (PTS-R9)	2 μm	2.52	0.25
Si_3N_4	0.3 μm	122.5	0.23
ITO	0.05 μm	116	0.35
Graphene	0.34 nm	1000	0.21
Stainless Steel Mandrel		207	0.3

Using the cross-sections pictured above, two simple ANSYS models (as shown below in Figure 4.13) were created using shell elements in order to calculate the bending stresses for patterned ITO, uniform films of Graphene and ITO on Si_3N_4/PEN substrates. The ANYSYS model for the patterned ITO samples utilizes three individual traces to study the effect of the presence of multiple traces on the distribution of bending stresses. Shell elements 281 and 91 were used to model the multi-layer and the stainless steel mandrel respectively due to complexity of the samples as well as to reduce computation time. Both shell elements are 8 noded with 6 degrees of freedom. Each of the layers was assumed to be linear and isotropic for the simulations. Each of the layers was assumed to be perfectly adhered to each other

and no interfacial effects were studied however, this is a necessary area of research for future work.

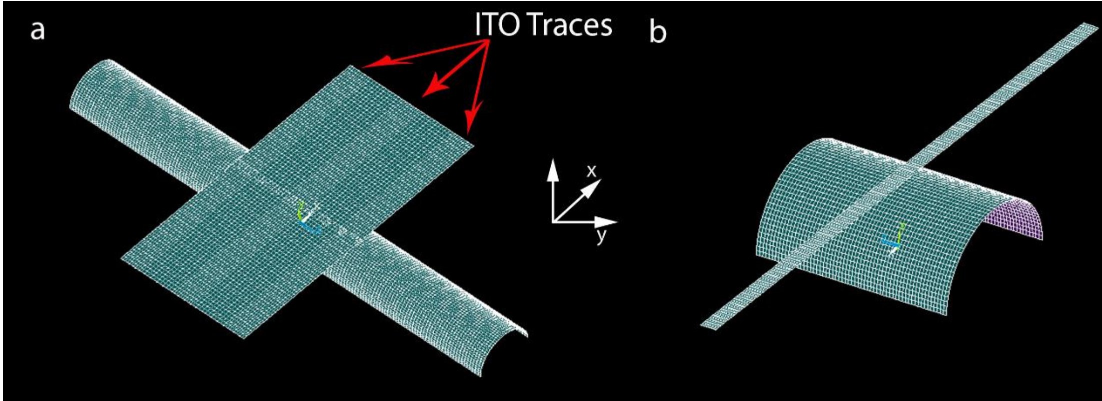

Figure 4.13: a) ANSYS Model used for modeling patterned ITO on Si_3N_4/PEN b) ANSYS Model used for modeling uniform ITO or Graphene on Si_3N_4/PEN

The models shown above had the following boundary conditions for the nodes on the center of the layer stack structure: The rotation was fixed in the y and z directions, displacement was fixed in the x direction and the first node was fixed in the z direction.

For each simulation, the sample was bent to a pre-determined radius of curvature and the stress distribution along the principal axis (x-direction) was calculated. First, the results of the patterned ITO on Si_3N_4/PEN simulations are presented. Figure 4.14 a-d shows the patterned ITO sample simulation (Figure 4.12a) bent using a 2 mm diameter mandrel with the stress distribution in the x-direction for each layer:

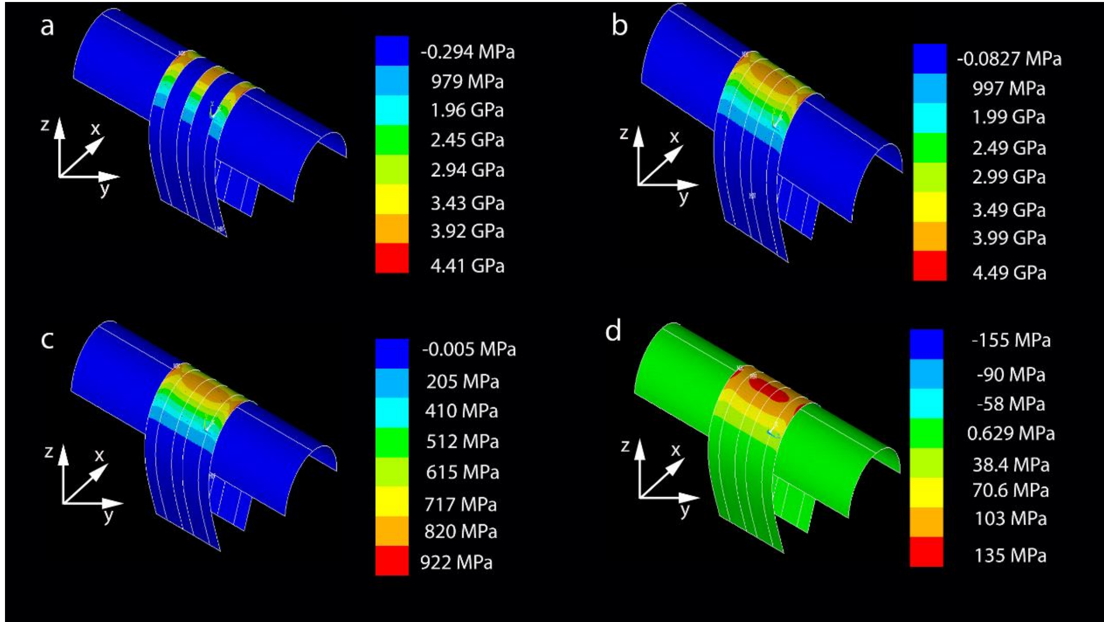

Figure 4.14: Stress distribution in the bending direction (x-direction) for a patterned ITO Sample bent to a radius of curvature of 2 mm for a) ITO layer b) Si_3N_4 layer c) PTS-R9 layer and d) PEN layer

As seen in Figure 4.14 a-d, the stress is concentrated at the center of each of the layers. This is expected behavior since this is where the sample is bent the most around the mandrel. When comparing the stresses between layers, the ITO and Si_3N_4 layers have higher bending stresses than the PTS-R9 and PEN layers due to the differences in layer thickness (0.05 and 0.3 µm vs. 3 µm and 125 µm respectively. The effect of mandrel size on the bending stress in each of the layers of Figure 4.12a was simulated for mandrel diameters ranging from 1.79 mm to 7.94 mm for 0.05 µm thick ITO traces as shown in Table 4.3 and Figure 4.15

Table 4.3: Effect of mandrel size on the bending stress in each of the layers of Figure 4.12a for mandrel diameters ranging from 1.79 mm to 7.94 mm for 0.05 µm thick ITO traces

Mandrel Diameter (mm)	Trace Length (mm)	Trace Length (mm)	Stress in ITO Layer (MPa)	Stress in Si_3N_4 Layer (MPa)	Stress in PTS-R9 Layer (MPa)	Stress in PEN Layer (MPa)
1.59	2.54	0.304	9449	9228	191	286
2.38	2.54	0.402	6705	6547	135	202
3.97	2.54	0.598	4063	3968	82	123
4.76	2.54	0.696	3371	3291	68	102
5.56	2.54	0.795	2795	2727	56	84
6.35	2.54	0.893	2517	2455	51	76
7.14	2.54	0.991	2240	2184	45	68
7.94	2.54	1.089	1999	1948	40	60

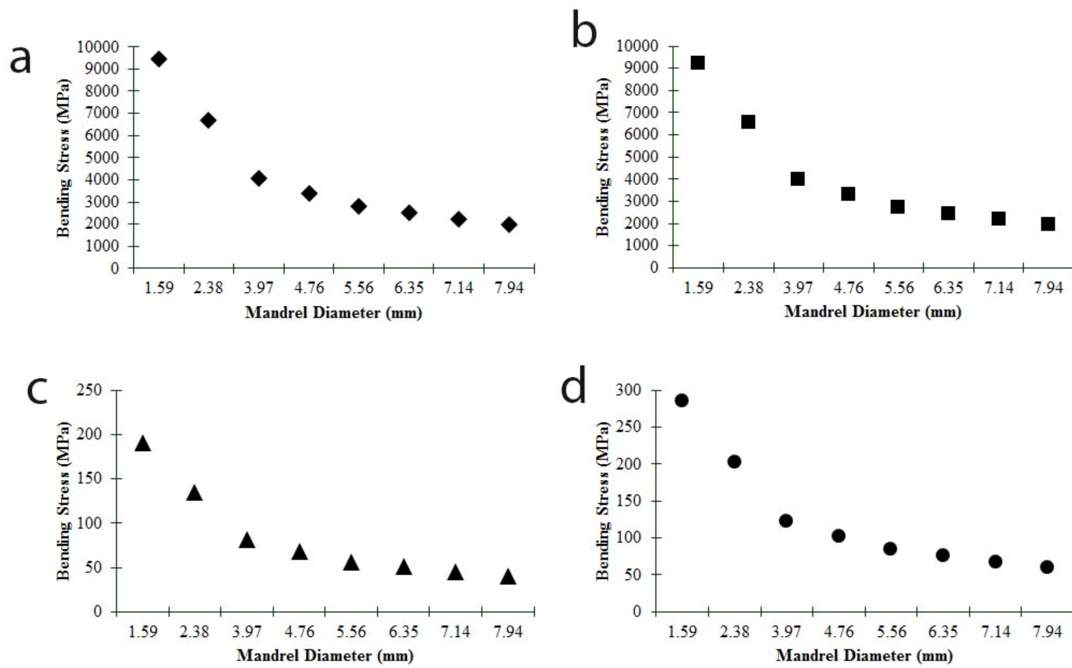

Figure 4.15: Effect of mandrel size on the bending stress in each of the layers a) ITO b) Si_3N_4 c) PTS-R9 and d) PEN of Figure 4.12a for mandrel diameters ranging from 1.79 mm to 7.94 mm for 0.05 µm thick ITO traces

In each of the layers, as the mandrel diameter increased, the bending stress decreased. A larger mandrel corresponding to smaller radii of curvature, leads to less stress being applied to the layer stack structure. The effect of trace thickness was simulated for

mandrel diameters ranging from 1.97 mm to 7.94 mm respectively. The results of this are shown below in Table 4.4 and Figure 4.16

Table 4.4: Effect of ITO trace thickness on the bending stress in each of the layers of Figure 4.12a for mandrel diameters ranging from 1.79 mm to 7.94 mm

Mandrel Diameter (mm)	ITO Bending Stress (MPa) for 0.05 µm thick trace	ITO Bending Stress (MPa) for 0.01 µm thick trace	ITO Bending Stress (MPa) for 0.1 µm thick trace
1.59	9449	9447	9104
2.38	6705	6779	6596
3.97	4063	4103	3872
4.76	3371	3399	3336
5.56	2795	2905	2763
6.35	2517	2538	2422
7.94	1999	2014	1981

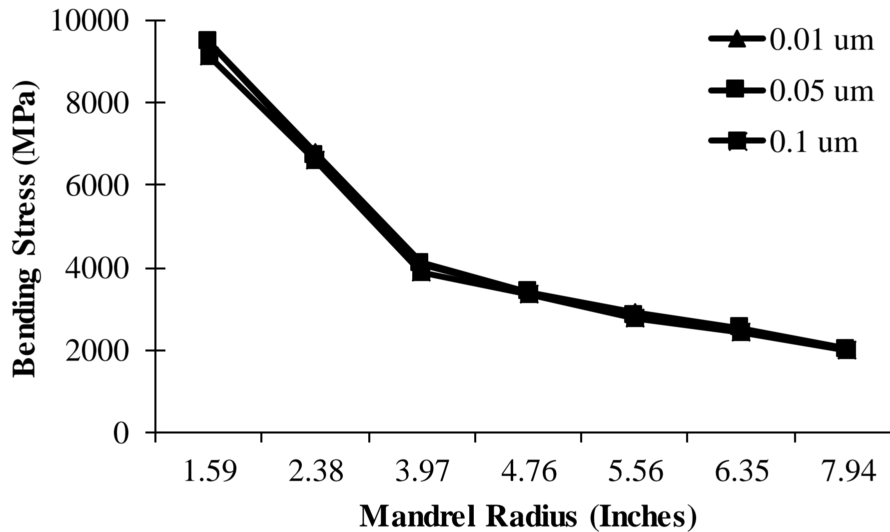

Figure 4.16: Effect of ITO trace thickness on the bending stress in each of the layers of Figure 4.12a for mandrel diameters ranging from 1.79 mm to 7.94 mm

Figure 4.16 shows that for each of the ITO trace widths (0.01, 0.05 and 0.1 µm), as the mandrel diameter increased, the bending stress decreased. From Figure 4.16, a

significant change in bending stress in the ITO layer was not observed when changing the ITO trace thickness.

The results of the uniform ITO on Si_3N_4/PEN and uniform Graphene on Si_3N_4/PEN simulations are presented next. The results of simulation of a uniform ITO sample (Figure 4.12a) and a uniform Graphene Sample (Figure 4.12b) bent using a 1.58 mm diameter mandrel are shown in Figure 4.18a-c with the stress distribution in the x-direction for each layer:

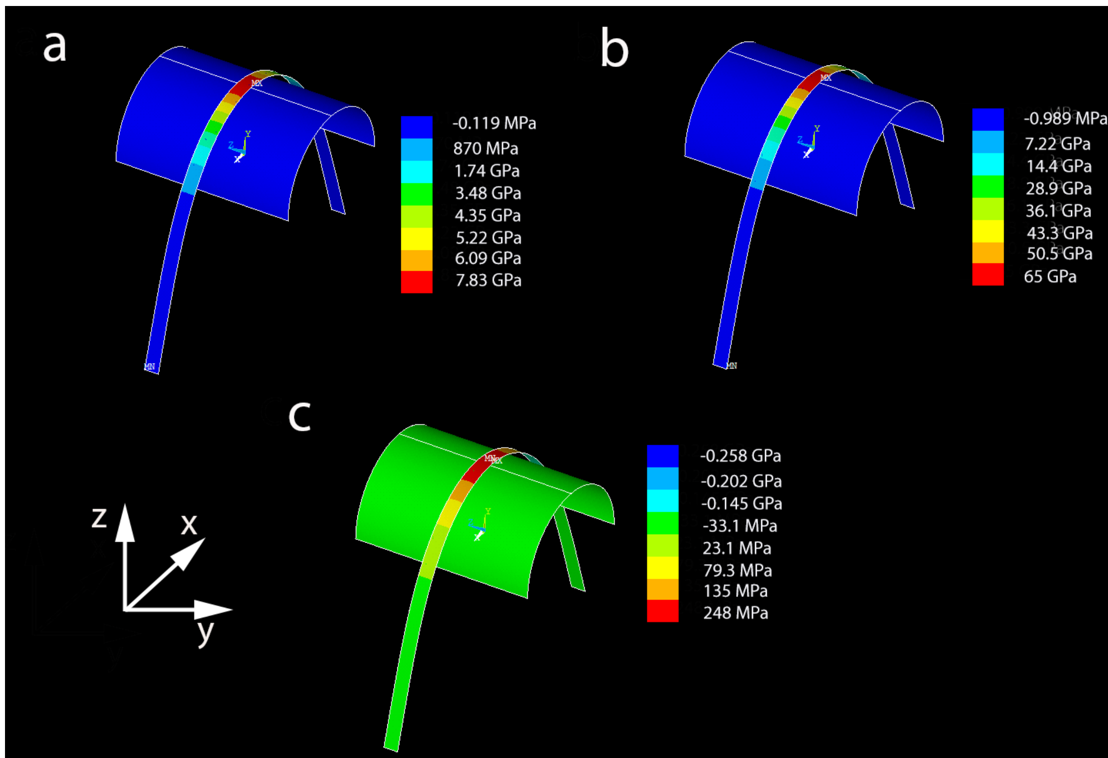

Figure 4.17: Stress distribution in the bending direction (x-direction) for a uniform ITO/PEN and uniform Graphene/PEN sample bent to a radius of curvature of 2 mm for a) ITO layer b) Graphene layer c)) PEN layer

As shown in Figure 4.18, the bending stress is concentrated at the center of the

respective layers for Graphene, ITO and PEN. The maximum bending stress in the Graphene, ITO and PEN layers is 65 GPa, 7.83 GPa and 248 MPa respectively. The thickness differences between the layers results in the PEN layer having an order of magnitude lower stress. When comparing the bending stress of ITO vs. Graphene, the Graphene layer has a 7x larger stress when compared to ITO. This is due to the elastic moduli difference between Graphene and ITO (116 GPa vs. 1 TPa). The effect of mandrel diameter on bending stress in ITO and Graphene layers was simulated for mandrel diameters ranging from 1 mm to 3 mm for a film thickness of 0.34 nm (monolayer of Graphene) and a substrate thickness of 125 µm. The results are summarized in Table 4.5 and Figure 4.18 below:

Table 4.5: Effect of Mandrel diameter on Bending Stress in ITO or Graphene layers for mandrel diameters ranging from 1-4 mm

Mandrel Diameter (mm)	Bending Stress (GPa) in ITO Layer	Bending Stress (GPa) in Graphene Layer	Difference between ITO and Graphene
0.79	7.83	65	730%
1.59	4.79	39.8	731%
2.38	3.33	27.7	732%
3.18	2.52	20.9	729%

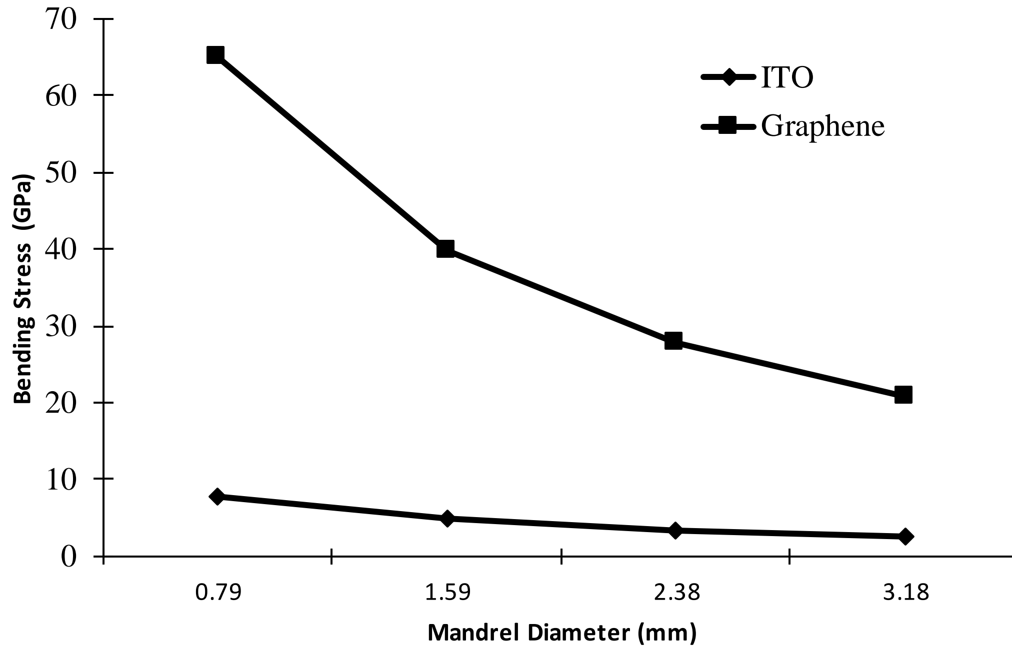

Figure 4.18: Effect of Mandrel diameter on Bending Stress in ITO or Graphene layers for mandrel diameters ranging from 1-4 mm

As seen in Table 4.5, changing from ITO to Graphene results in a large jump in the bending stress in the film, with an average increase of 731%. This is caused by Graphene's larger elastic modulus of 1 TPa compared to ITO's 116 GPa. The two curves in Figure 4.19 were both fitted with an inverse power law and the expressions for the Graphene and ITO are

ITO $$\sigma_f = 66.73d^{-0.813} \tag{4.12}$$

Graphene $$\sigma_f = 8.033d^{-0.813} \tag{4.13}$$

where σ_f is the bending stress in the layer and d is the mandrel diameter.

4.4.3. Determination of Mandrel Sizes for Fatigue Experiments

In the previous sections, the bending stresses in films was discussed including the results of FEA work to study the effect of various mandrel diameters on the bending stresses generated in the uniform ITO or Graphene layer on top of Si_3N_4/PEN. This section will present the results of the simulations used to determine the appropriate the mandrel diameters to be used in the present experimental work.

Using the stress-strain curves for ITO and Graphene respectively, the appropriate stresses for both Graphene and ITO were selected to stay within the low cycle fatigue regime during testing. The stresses selected for ITO were 600 MPa, 500 MPa, 450 MPa and 400 MPa while the stresses selected for Graphene were 80 GPa, 60 GPa, 50 GPa and 40 GPa respectively. Using FEA, the appropriate mandrel sizes (radii of curvatures) to achieve these stresses were determined and are summarized in Table 4.7

Table 4.6: Summary of FEA work to determine the mandrel diameters for experimental work

ITO		Graphene	
Desired Bending Stress Amplitude (GPa)	Required Mandrel Diameter (mm)	Desired Bending Stress Amplitude (GPa)	Required Mandrel Diameter (mm)
80	0.79	600	6
60	1.11	500	7
50	1.42	450	8
40	1.87	400	12

The next chapter will present the results of the materials characterization of Graphene and the bending fatigue studies of patterned ITO, uniform ITO and uniform Graphene on Si_3N_4/PEN substrates.

Chapter 5 : Results

5.1. Graphene Fabrication Vendor Selection

As, discussed in the previous chapter, three commercial vendors were selected as potential candidates to fabricate the Graphene samples used in this work. All three of the vendors used similar fabrication techniques to produce samples, so the quality of the received films was characterized using Raman Spectroscopy and Atomic Force Microscopy in order to select a final vendor for fabrication.

5.1.1. Raman Spectroscopy

Raman Spectroscopy has been used extensively as a means to characterize Graphene films [106], [146]–[151]. Raman spectroscopy involves inelastic scattering of monochromatic light (typically from a laser source). The sample is irradiated with a laser source; the photons interact with the sample and are ejected at either the same or a different frequency. These photons are then gathered by a system of lenses and sent through a spectrophotometer to obtain a Raman spectra. Raman spectroscopy can be used to both determine the presence of Graphene, quality of Graphene films and the number of layers present. A typical Raman spectra for Graphene is shown below in Figure 5.1a and 5.1b

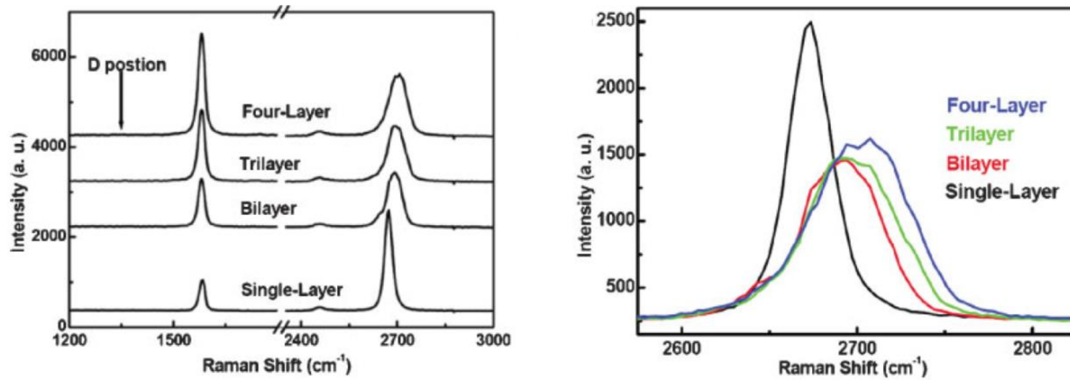

Figure 5.1: a) Raman Spectra of Graphene b) Effect of Number of Layers on 2D Peak [151]

When a 532 nm laser excites the surface of Graphene, Stokes phonon energy shift creates Graphene's three characteristic peaks in the Raman spectra:

D peak (1350 cm^{-1}), G peak (1580 cm^{-1}) & 2D peak (2700 cm^{-1}). The G peak is a primary in-plane vibration mode, while the 2D peak is a second order overtone of a different in-plane vibrational mode. The positions of the G and 2D peaks are dependent on the laser excitation energy [147], [148], [151]–[153]. The D peak is of significance because it is present when defects in the Graphene films are present. The D peak occurs when a charge carrier is excited and inelastically scattered by a phonon and then a second elastic scattering by a defect or zone boundary occurs resulting in recombination [152], [154]. As the number of layers is increased, the relative width of the 2D peak becomes broader and broader is due to increased phonon scattering modes as seen in Figure 5.1b. The ratio of the G/2D Peak intensities as well as the relative shapes of the 2D and G peaks allows one to determine the number of Graphene layers present.

Raman spectra of Bare PET, Graphene on SiO_2 and Graphene on PET for the three respective vendors was obtained using a Horiba Yvon LabRam ARAMIS system with a 532 nm laser. First, Raman spectra of a monolayer of Graphene on SiO_2 (Graphenesquare) at 3 different points along the sample surface was obtained as shown in Figure 5.2:

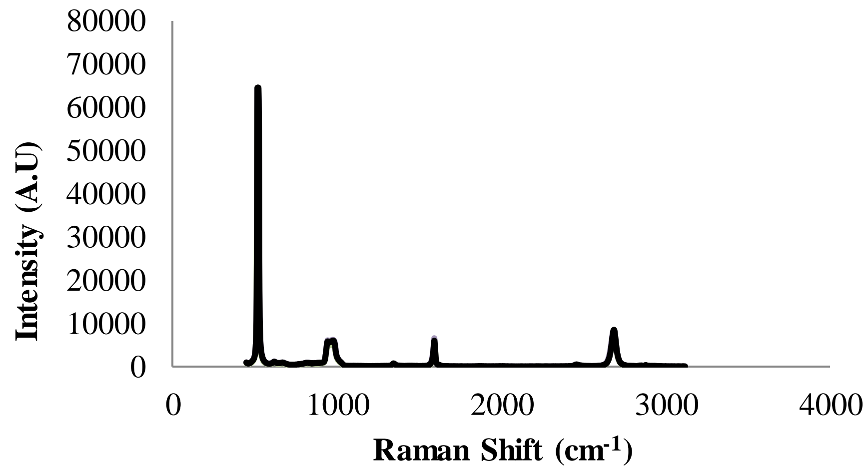

Figure 5.2: Raman spectra of a monolayer of Graphene on SiO_2 (Graphenesquare)

The Raman spectra of Graphene on SiO_2 shows Graphene's characteristic G and 2D while the D peak is not present. This spectra confirms a low defect Graphene film is present. Additionally Si's characteristic peaks were detected at 500 and 1000 cm^{-1} respectively. Raman spectra of a bare sheet of Polyethylene terephthalate (PET) is shown below in Figure 5.3.

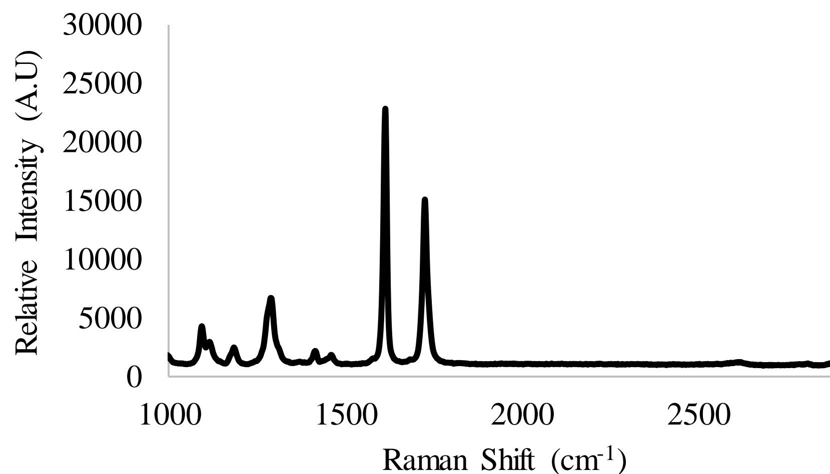

Figure 5.3: Raman spectra of a bare PET

Raman spectra for Graphene on PET for the three respective vendors is shown below in Figures 5.4 - 5.6:

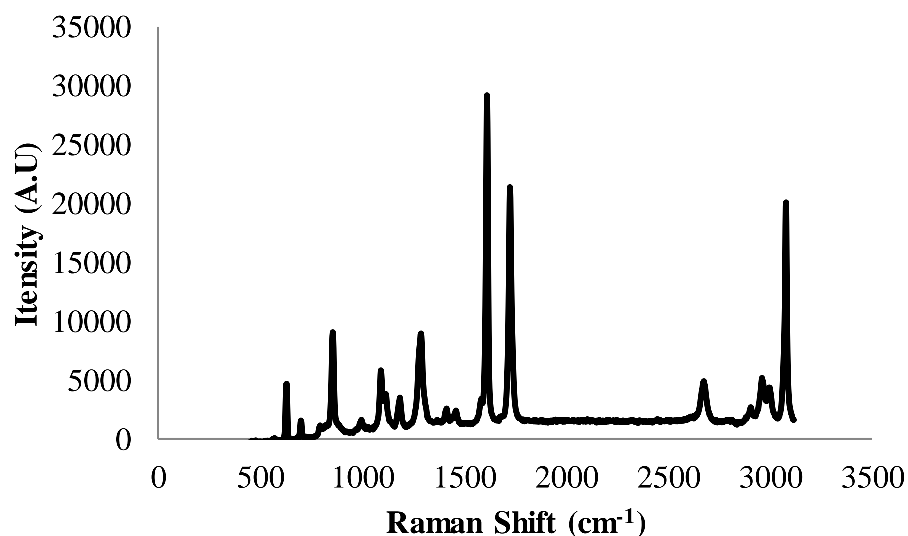

Figure 5.4: Raman spectra of a monolayer of Graphene on PET (ACS Materials)

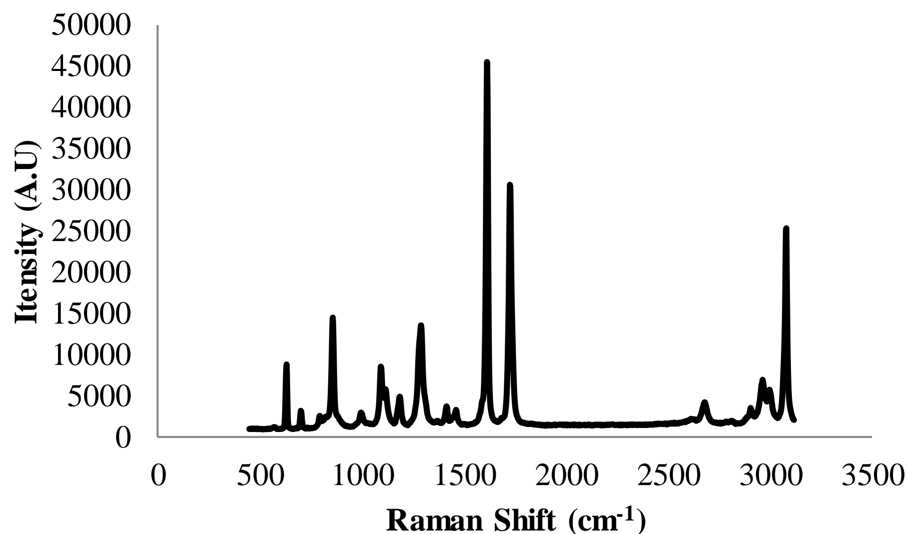

Figure 5.5: Raman spectra of monolayer of Graphene on PET (Graphene Square)

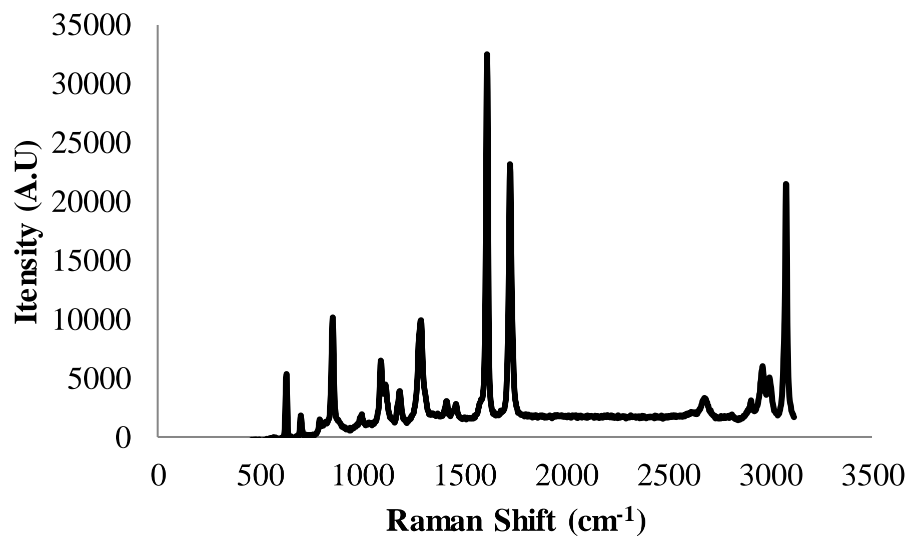

Figure 5.6: Raman spectra of monolayer of Graphene on PET (Graphene Supermarket)

The Raman spectra of Graphene on PET for the three vendors confirm the presence of Graphene with the presence of Graphene's characteristic G peak. It is also important to note from the Raman spectra for PET (Figure 5.3), PET has peaks located between 1500 – 1700 cm^2. This hinders the ability to determine the number of layers using the

ratio of 2D/G method because of PET's overlapping peaks at the location of the G peak (as seen in Figure 5.7).

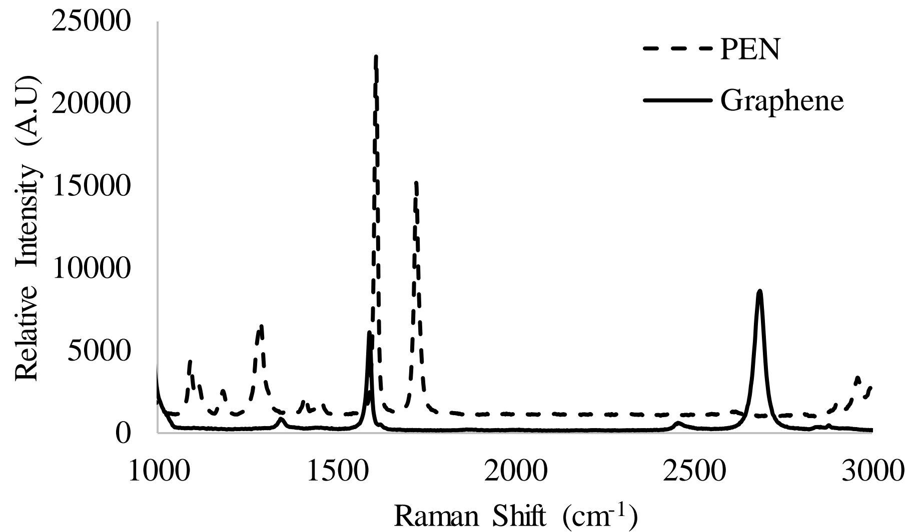

Figure 5.7: Raman spectra of monolayer of Graphene on SiO_2 and bare PET showing bare PET's overlapping peaks

5.1.2. Atomic Force Microscopy

Atomic Force Microscopy (AFM) was used to determine the quality of the samples in terms of surface uniformity, surface roughness and determination of the number of layers of Graphene using height measurements and the known height of a monolayer of Graphene to be 0.334 nm. AFM consists of a cantilever with a sharp tip that is rastered across the surface of a sample to determine the morphology of the samples surface. All microscopy work was done using a D3000 or Digital Instruments (Veeco) Multimode AFM in tapping mode. AFM images for each of the three vendors are shown below in Figures 5.8 – 5.10.

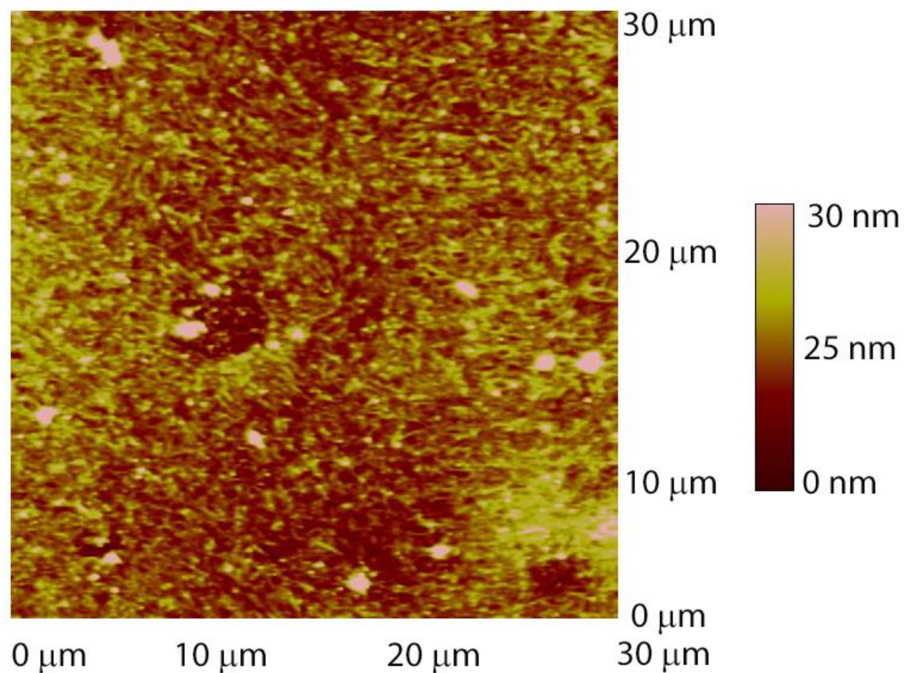

Figure 5.8: 10x10 um AFM (Tapping Mode) Image of ACS Material sample

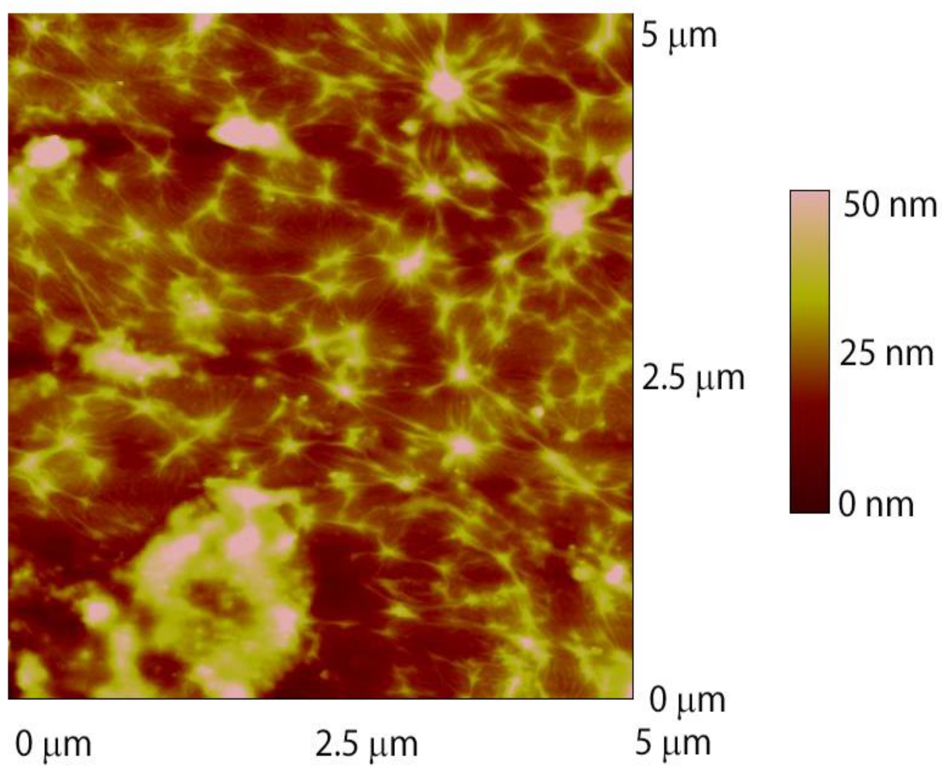

Figure 5.9: 5x5 um AFM (Tapping Mode) Image of Graphene Platform sample

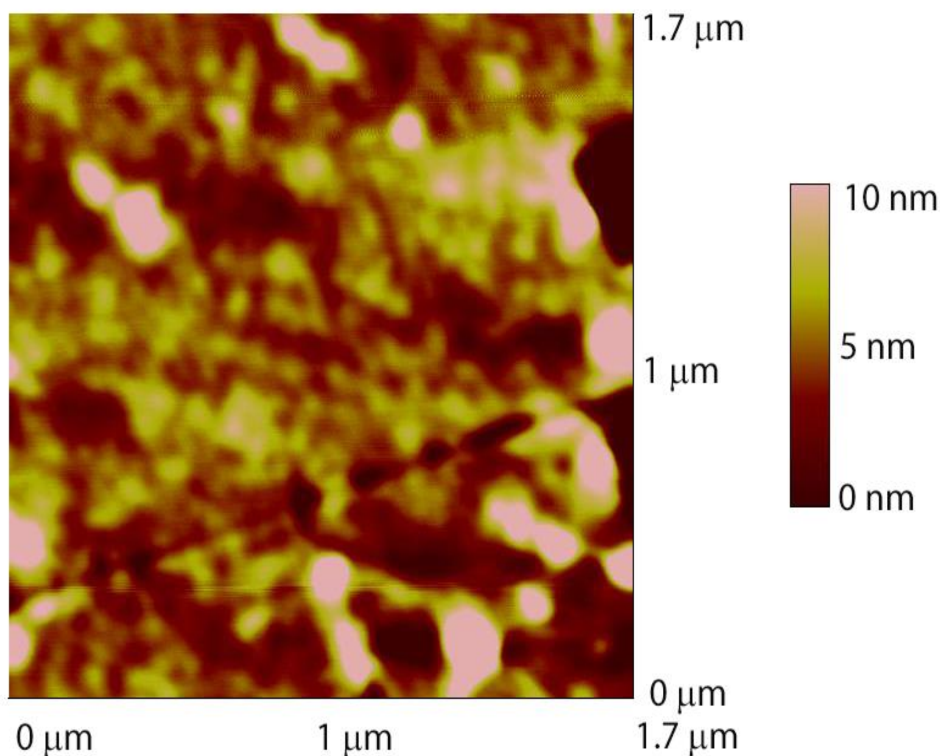

Figure 5.10: 1x1 um AFM (Tapping Mode) Image of Graphene Supermarket Sample

In Figures 5.8 – 5.10, hexagonal grains of Graphene confirm the presence of Graphene on the surface of the samples made by each individual vendor. Additionally, as shown in Figures 5.8 and 5.9, additional contaminants (white particles and wrinkles) which are a byproduct of the Graphene transfer process are present. This type of surface morphology has been observed by Fischella et al [155]. The contaminants are polymer residuals that are leftover from the transfer process. Small cracks may be present on the sample which are result are result of the mechanical handling during transfer. Wrinkles can by either formed during the cool down step of fabrication due to coefficient of thermal expansion (CTE) mismatch between Graphene and Cu or during the transfer process to the flexible substrate. In

all three of the vendor samples, the surface roughness of the underlying PET substrate contributes to the surface roughness of the Graphene layers as well. This made determining the number of layers via height measurements very difficult. Using the results of this analysis, ACS Materials was chosen due to it superior Graphene coverage, cost and ability to fabricate samples with the appropriate dimensions.

5.2. *Characterization of Graphene before testing*

Prior to fatigue testing, the initial quality of Graphene samples as received was characterized using AFM and Raman spectroscopy. Raman spectroscopy was used to confirm the presence of Graphene on the samples as well as to investigate the coverage of the Graphene on the samples.

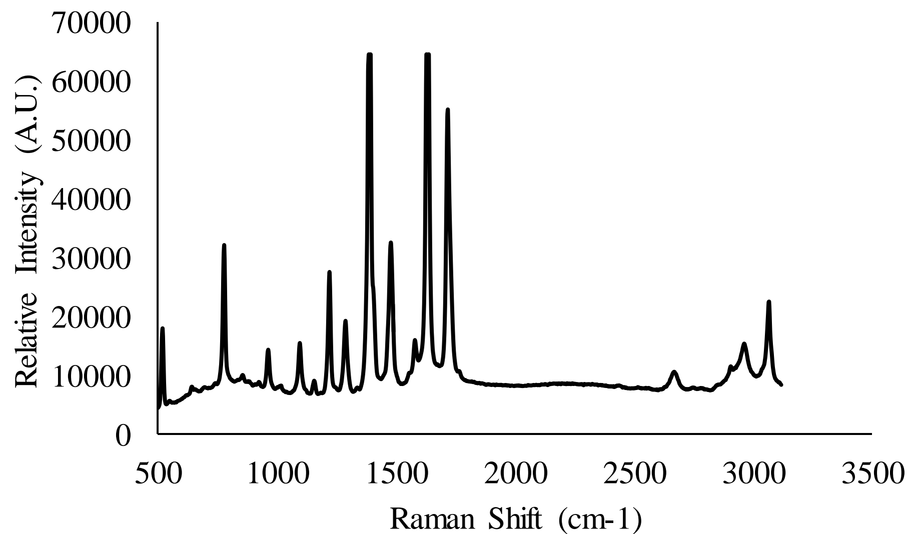

Figure 5.11: Raman Spectra of Graphene Samples for Initial Characterization

As shown in Figure 5.11, the presence of Graphene was confirmed with the presence of Graphene's characteristic G peak at 2680 cm^{-1}, but the number of layers of

Graphene present was not determined due to the overlapping signal of the Si_3N_4/PEN substrate. Using Graphene's characteristic Raman spectrum, Graphene coverage on the fabricated samples was investigated in a 20x20 um analytical grid located at the center of the samples. This grid was broken up into 2 µm intervals both horizontally and vertically. At each of these grid points, a Raman spectrum was obtained and the presence of Graphene's characteristic 2D peak was used as a measure of whether or not Graphene was present at that location. An illustration of this grid is shown below in Figure 5.12 followed by the resulting Graphene coverage maps for 12 different samples in Figure 5.13 a-l.

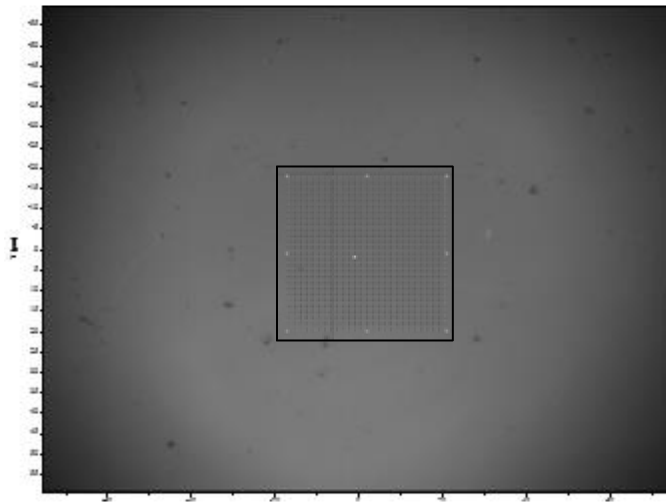

Figure 5.12: 20x20 µm grid used for Graphene coverage analysis using Raman spectroscopy

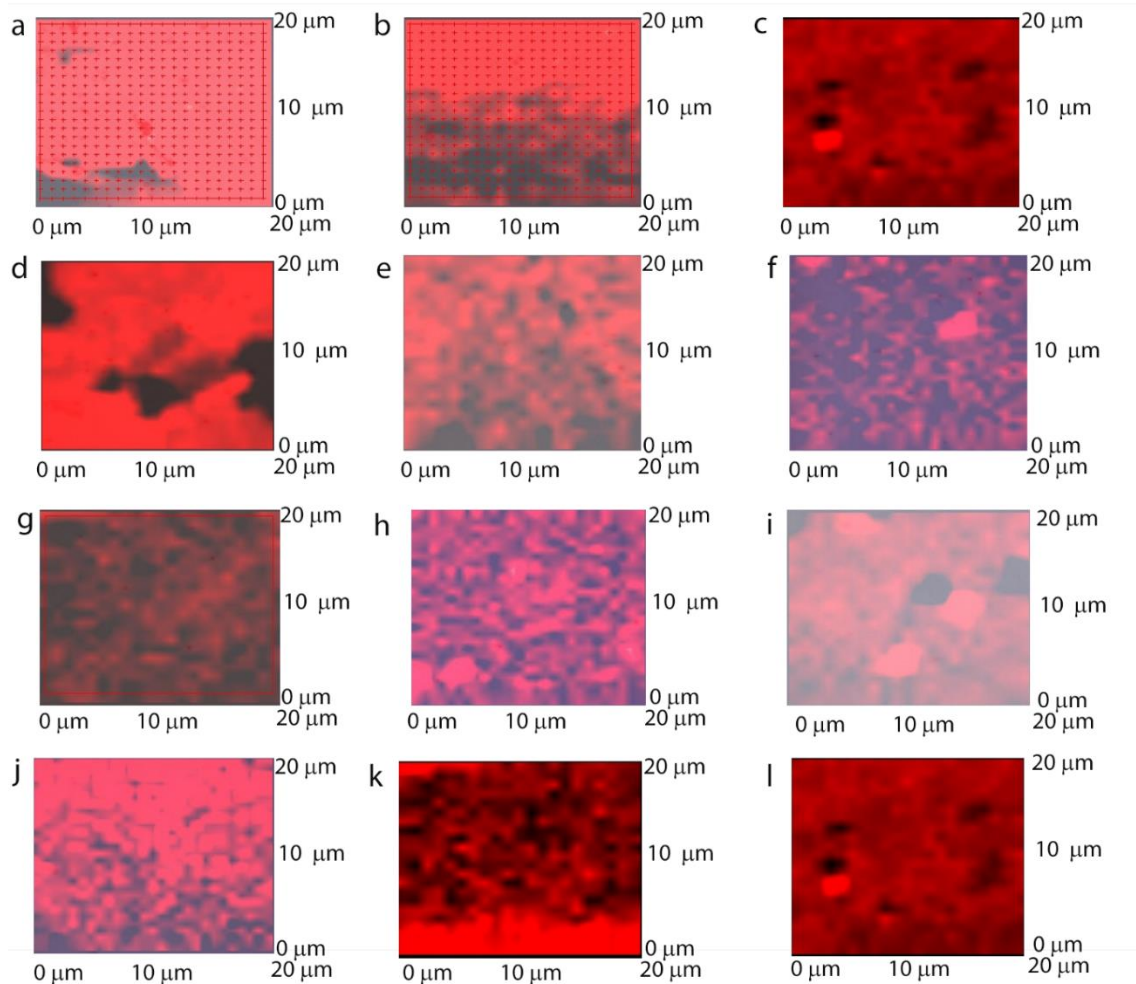

Figure 5.13a-l: 20x20 µm grids showing results Graphene coverage (red regions) analysis using Raman spectroscopy for 12 different samples

As shown in Figure 5.13, the coverage of Graphene on the Si_3N_4/PEN substrate is not uniform with patches of non-Graphene coverage. ImageJ software [156] was used to calculate the Graphene coverage in each of the grids in Figure 5.13 with the average Graphene coverage over the 12 samples being ≈ 68%.

Table 5.1: Summary of Graphene Coverage Analysis for 12 Different Samples

Sample #	% Graphene Coverage in 20x20 μm Grid
1	53
2	85
3	65
4	43
5	88
6	47
7	71
8	65
9	82
10	75
11	79
12	59

This lack of uniform coverage can be attributed to the transfer process from the CVD grown Graphene to the PEN substrate. A possible explanation for this type of coverage was explained by Bae et al. [79], where Graphene samples were fabricated using a roll to roll fabrication technique using thermal release tap on PET substrates. Bae et al. suggested that the adhesion force between the Graphene and PET competes with the force between the Graphene and thermal release tapes, leaving some residues and defects. As additional layers are added, the adhesive force between the thermal release tape and Graphene becomes smaller than Graphene-Graphene adhesion, therefore producing an almost complete transfer for subsequent layers Additionally, the Graphene coverage images shown in Figure 5.13 correlate well to the AFM images of the sample surfaces shown in Figure 5.8

Next, AFM was used to study the surface morphology and determine of layers present on the Graphene samples. AFM was used to investigate the effect of the various

stages of fabrication on the resulting surface roughness of the samples by determining the RMS roughness of Bare PEN, PEN with Si_3N_4, ITO on top of Si_3N_4/PEN and Graphene transferred to Si_3N_4/PEN. For the bare PEN, Si_3N_4/PEN and ITO/ Si_3N_4/PEN samples, four 20x20 um AFM tapping mode scans were obtained and then root-mean-square (RMS) roughness were taken for each sample. For the Graphene samples, two types of measurements were taken for 10 µm x 10 µm tapping mode AFM scans: one was the surface roughness of the entire image (area outlined by red box in Figure 5.14d) and the other was the surface roughness of the area outlined by the blue box in Figure 5.14d. AFM scans illustrating the morphology of each of the sample types are shown below Figure 5.14

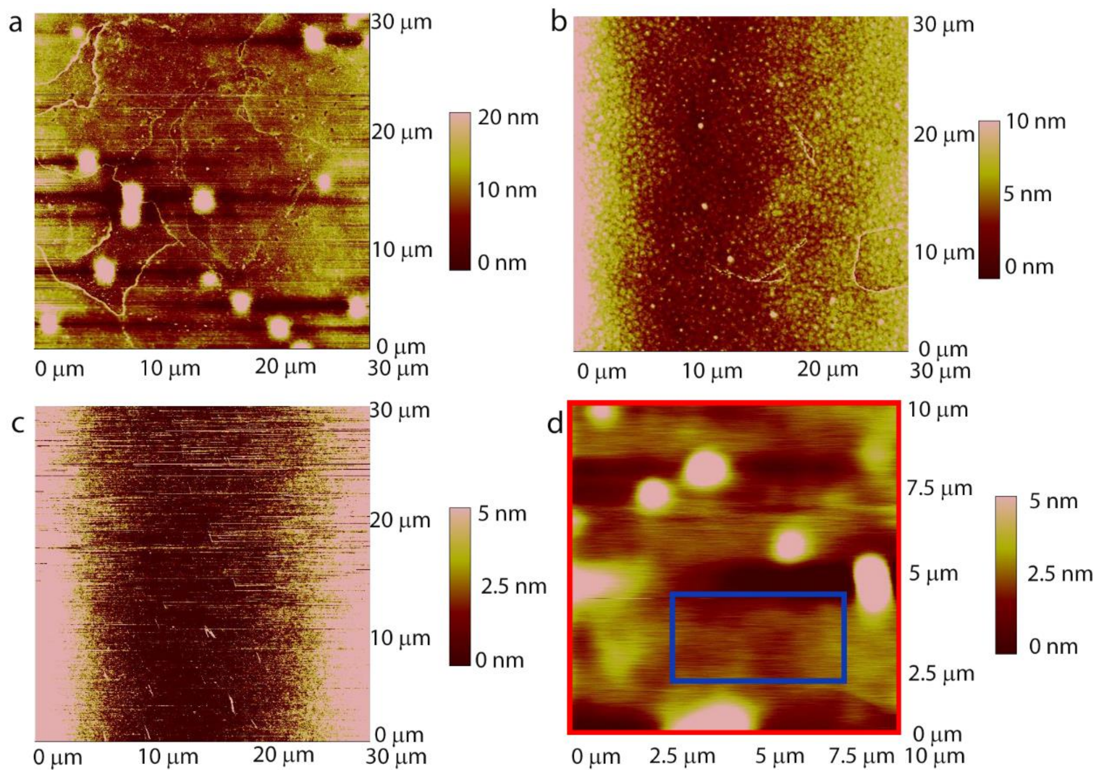

Figure 5.14: 20x20 µm Tapping mode AFM images of a) Bare PEN b) Si_3N_4/PEN c) ITO/Si_3N_4/PEN and d) Graphene/Si_3N_4/PEN used for the surface roughness analysis

The results of the RMS roughness analysis are shown below in Tables 5.2 and 5.3

Table 5.2: Summary of Average RMS Roughness Measurements for Bare PEN, Si_3N_4/PEN, ITO on Si_3N_4/PEN and Graphene on Si_3N_4/PEN

	RMS Roughness (nm)				
	Bare PEN	Si_3N_4 PEN	ITO Si_3N_4 PEN	Graphene Si_3N_4 PEN (Blue Box)	Graphene Si_3N_4 PEN (Red Box)
Average	3.99	2.00	1.01	0.50	2.32
STDEV	1.84	0.62	0.26	0.15	1.40

Table 5.3: Summary of Total Change in RMS Roughness for the various fabrication steps used to create the final samples of uniform ITO and Graphene samples

Fabrication Step	Total Change in RMS Roughness
Bare PEN → Si_3N_4/PEN	-50%
Si_3N_4/PEN → ITO/ Si_3N_4/PEN	-49%
Si_3N_4/PEN → Graphene (Red Box)/Si_3N_4/PEN	-75%
Si_3N_4/PEN → Graphene (Blue Box)/Si_3N_4/PEN	16%
Bare PEN → ITO/Si_3N_4/PEN	-88%
Bare PEN → Graphene (Red Box)/Si_3N_4/PEN	-42%
Bare PEN → Graphene (Blue Box)/Si_3N_4/PEN	-75%

As shown in Tables 5.2 and 5.3, the planarization of PEN with Si_3N_4 reduces the RMS roughness by 50% which is important because it is critical to have as smooth as a substrate as possible prior to ITO or Graphene growth. This is especially critical for monolayer Graphene samples because the layer is only 0.334 nm thick so it will conform to the roughness of the underlying substrate. When going from Bare PEN to PEN/Si_3N_4/ITO, there is an 88 % reduction in the RMS roughness of the final sample. The RMS roughness of the PEN/Si_3N_4/Graphene samples showed 2 distinct results:

the first is that the transfer process increases the roughness of the final films due to adhesion issues between Graphene and the Si_3N_4/PEN substrate as a result of the transfer process. The second result is that within localized regions, the surface roughness of Graphene is approximately 0.5 nm resulting in good Graphene coverage in localized regions.

Tapping mode AFM phase images of Si_3N_4/PEN and Graphene on Si_3N_4/PEN are shown in Figures 5.15a and 5.15b:

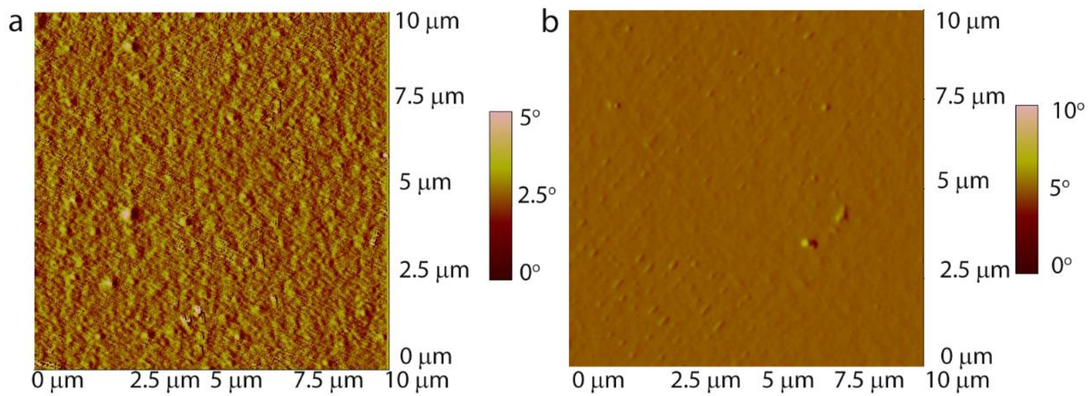

Figure 5.15: a) 10x10 um AFM (Tapping Mode) phase images of a) Si_3N_4/PEN and b) Graphene surface

As shown in Figures 5.15a and 5.15b, both Graphene and Si_3N_4/PEN have good phase homogeneity as well as very distinctive phases. Now, that the respective individual phases have been investigated, the interface between the two was next investigated.

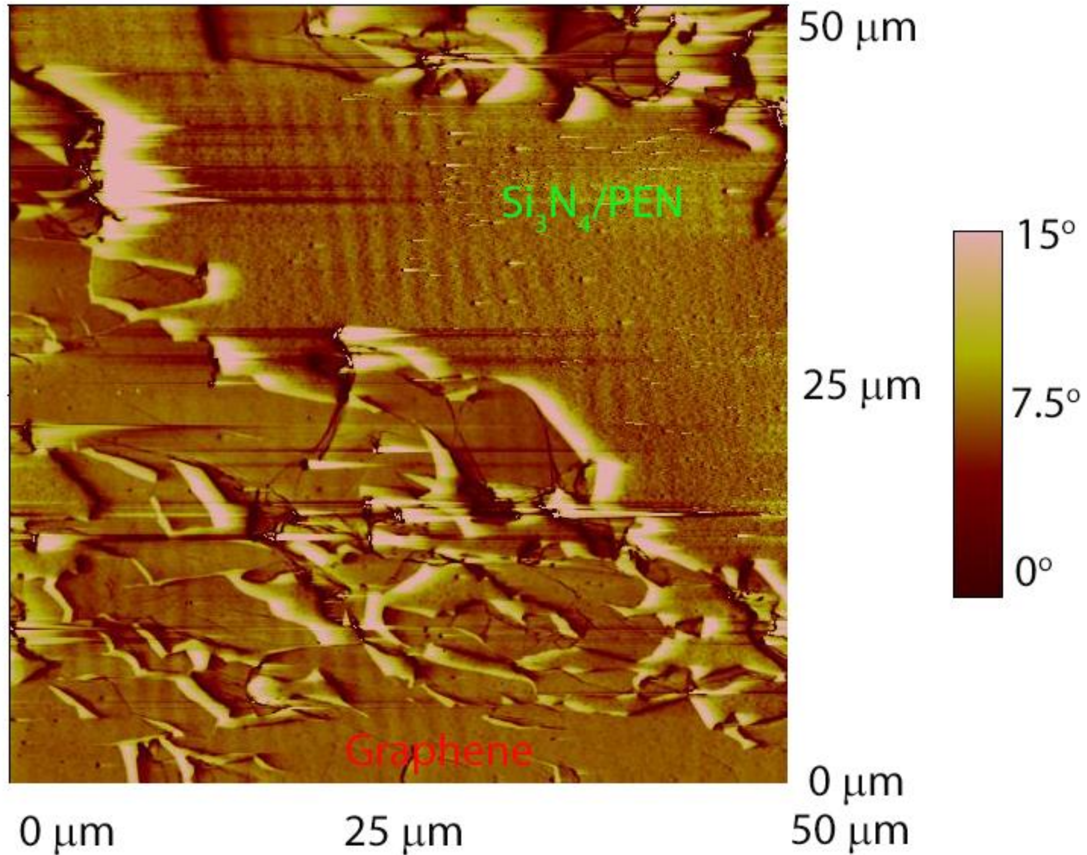

Figure 5.16: 10x10 um AFM (Tapping Mode) phase image of Graphene-Planarized PEN Interface

When looking at the interface between the Graphene and Si_3N_4/PEN (as shown in Figure 5.16), regions of Graphene are intermixed with regions of PEN in addition to the presence cracks and wrinkles as a result of the interfacial differences and the transfer process. This interface plays a critical role in fatigue behavior of the tested samples because it acts a stress concentrator and crack initation site.

Secondary Electron Scanning Electron Microscopy (SE-SEM) was used to investigate the interface between the Si_3N_4/PEN and Graphene. An SE-SEM image of the interface is shown in Figure 5.17 below, where at the interface, there are localized

regions of Si_3N_4/PEN located within the darker Graphene regions. This is a result of the transfer process which corresponds well with the previous AFM and Raman studies of Graphene coverage on Si_3N_4/PEN.

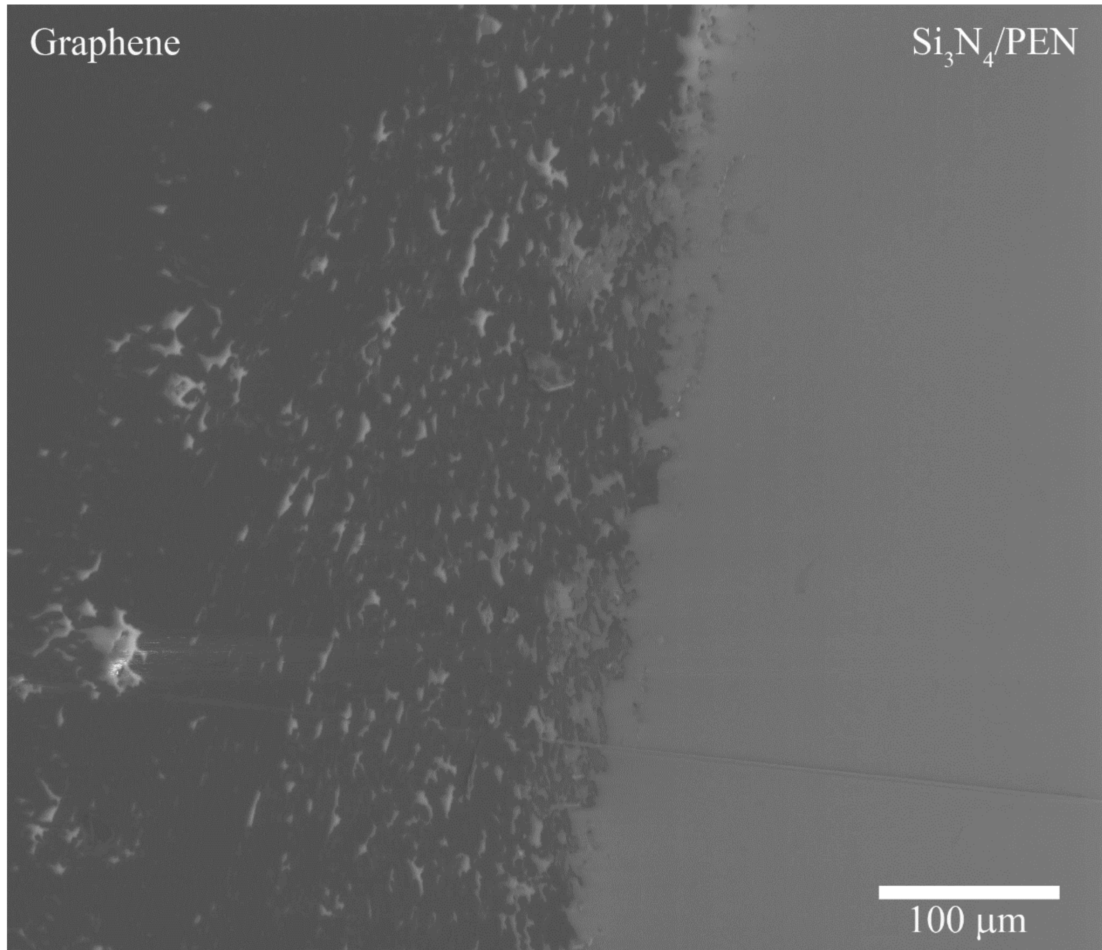

Figure 5.17: SE-SEM image of Graphene on Si_3N_4/PEN at the interface between the Graphene and Si_3N_4/PEN

The surface morphology of the Graphene samples was next looked at using the AFM. An AFM phase image of the Graphene-Si_3N_4/PEN interface is shown below in Figure 5.18, height measurements were taken at different points along the surface of the sample indicated by the various colored shapes.

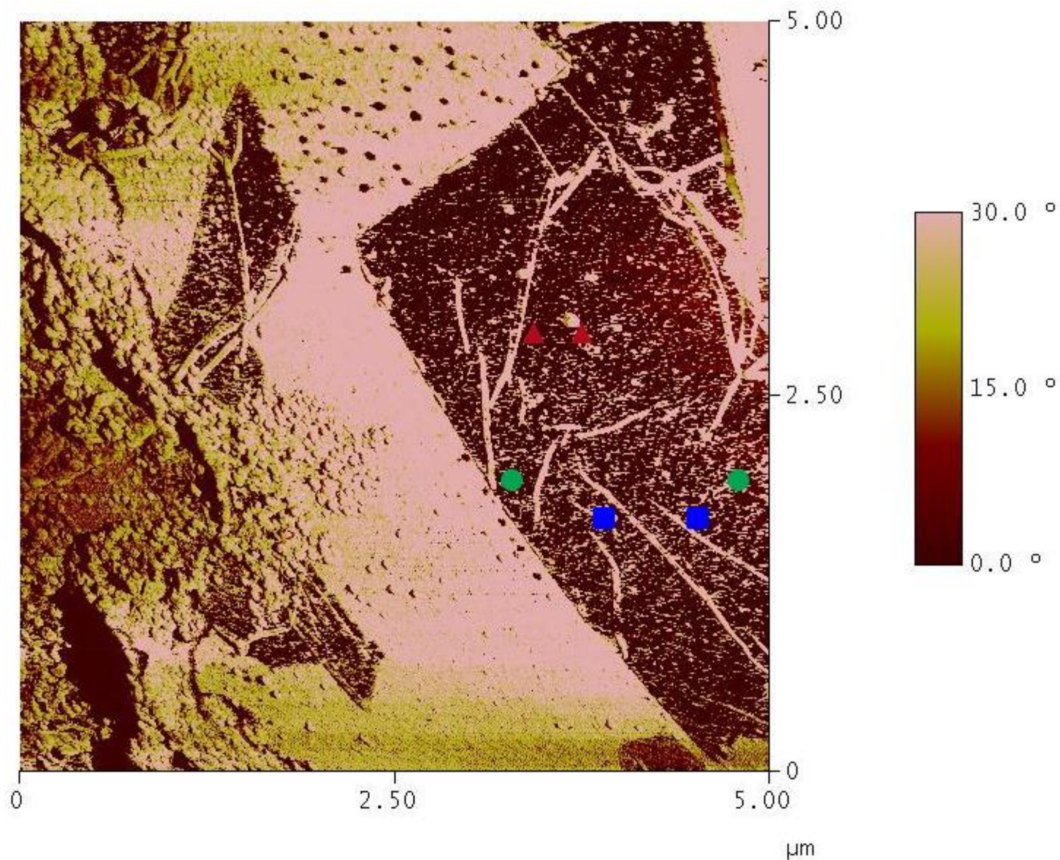

Figure 5.18: 10x10 um AFM (Tapping Mode) phase image of Graphene-Si_3N_4/PEN Interface

Figure 5.18 shows at the interface of Graphene and Si_3N_4/PEN, pockets of Graphene (dark regions), Si_3N_4/PEN (light colored regions) and wrinkles/cracks are present. In the large, dark region of Graphene in Figure 5.18, height measurements were taken at three separate locations: one between the two red triangles, the second between the green circles and finally between the two blue circles. In two of the locations (red triangles and blue circles), the height of the Graphene was found to be 0.334 and 0.342 nm respectively, confirming the presence of monolayer of Graphene. The surface roughness of the Graphene covered region between the two green circles in

Figure 5.18 was investigated through height measurements. The height profile of this region is shown below in Figure 5.19:

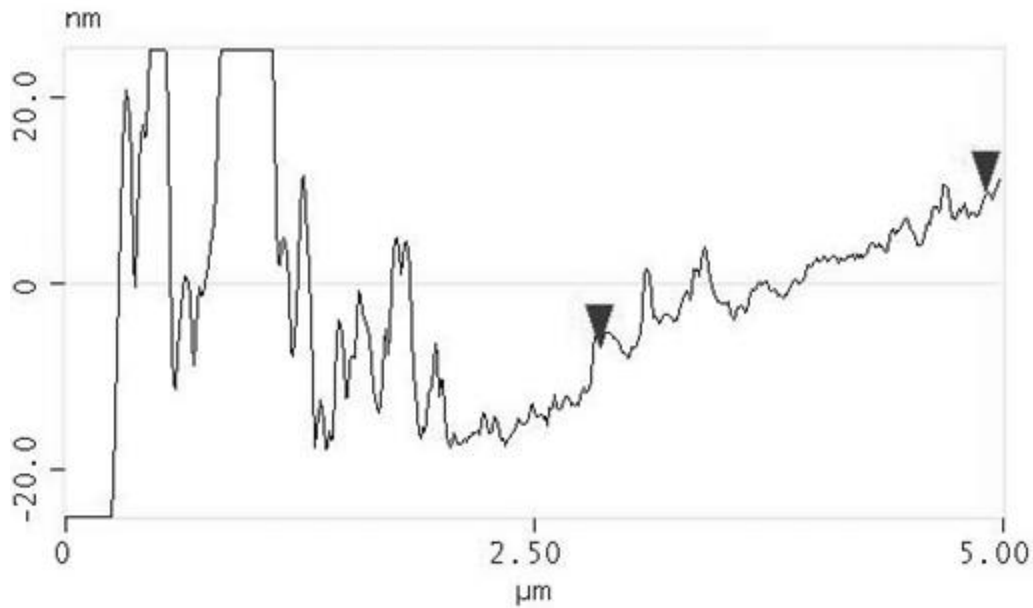

Figure 5.19: Height profile between the 2 green circles in Figure 5.18 showing surface roughness of Graphene on Si_3N_4/PEN

The surface roughness of the Graphene layer can be attributed to the surface roughness of the underlying substrate. Since Graphene is only a monolayer thick (0.34 nm), its surface morphology is strongly dependent on the substrate. The surface roughness of the substrate was investigated next using AFM height measurements.

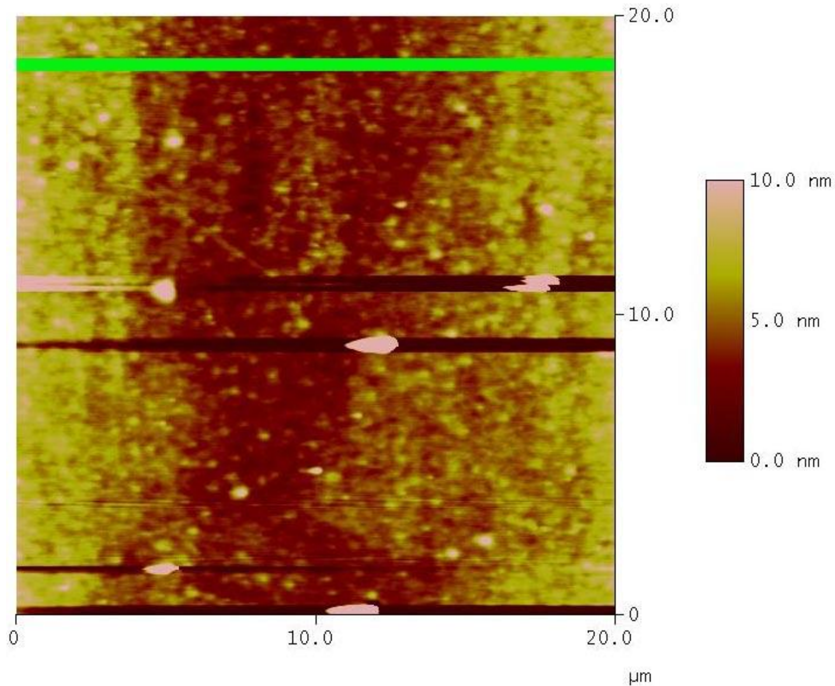

Figure 5.20: 10x10 um AFM (Tapping Mode) height image of Si_3N_4/PEN with green line denoting line across which height profile measurements were made

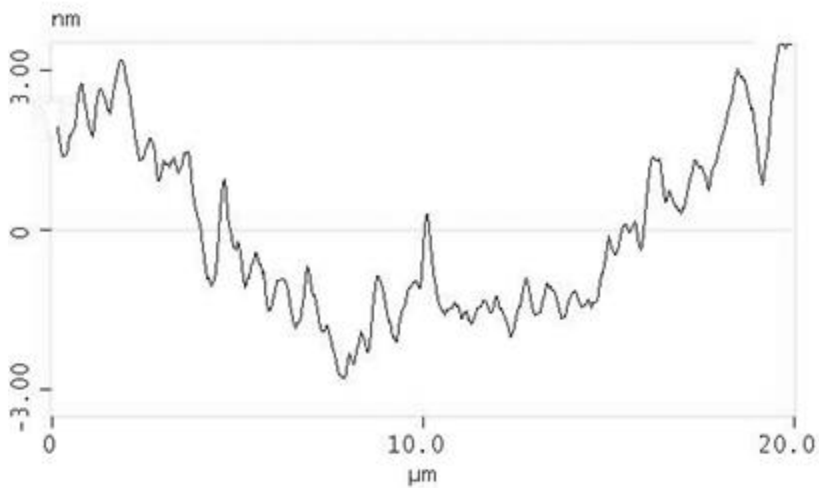

Figure 5.21: Height profile of green line shown in Figure 5.20

The Si_3N_4/PEN substrate roughness was found to be on average 2-3 nm. This surface roughness effects the surface roughness of the resulting Graphene layer, so it is very

important to control the underlying substrate roughness. In the present experimental work, it was not possible to fabricate an atomically smooth substrate layer, therefore the monolayer Graphene layer will not be perfectly smooth. In order to achieve better surface roughness, either the substrate roughness needs to be further planarized, additional Graphene layers could be grown reducing the overall surface roughness of the final Graphene layer or a transfer method for CVD grown Graphene to flexible substrates that's more efficient than current techniques needs to be developed.

5.3. *Fatigue testing*

After characterization of the Graphene samples prior to any fatigue testing, the next section will discuss the results of the bending fatigue studies of patterned ITO samples, uniform ITO samples and finally uniform Graphene samples on Si_3N_4/PEN substrates.

5.3.1. Patterned ITO Samples

This section will present data from the work done by Martin [1]. In the work done by Martin, three radii of curvature were selected based on FEA simulations and a summary of the test profiles used for the patterned ITO samples is shown below in Table 5.4 [1]:

Table 5.4: Profile of Life Tests performed on Patterned ITO Samples

Test Set #	Radius of Curvature (mm)	Film Strain (%)	Stress Amplitude (GPa)
1	6.35	1	1.22
2	4.76	1.4	1.66
3	3.18	2.2	2.54

The samples were continuously subjected to bending fatigue until a 10% change in normalized resistance was observed. An example of the electro-mechanical response for a patterned ITO sample is shown below in Figure 5.22

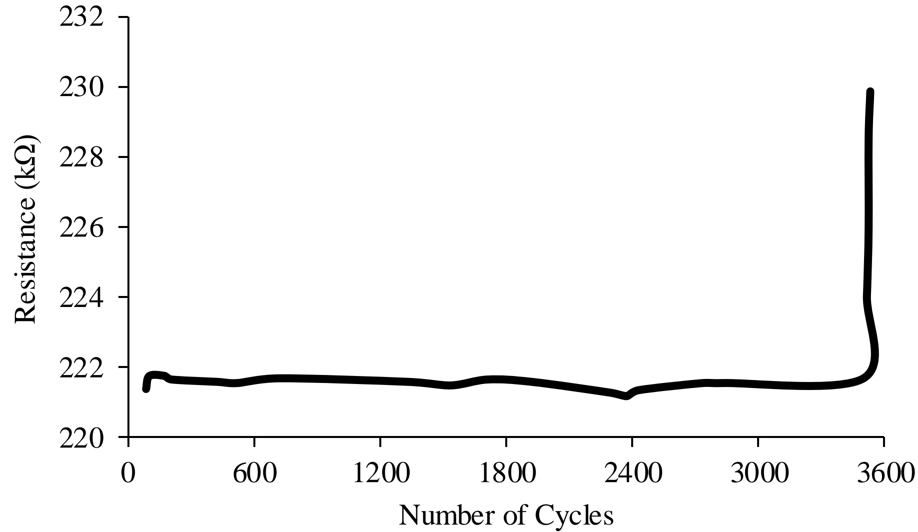

Figure 5.22: Resistance vs. Number of Cycles for a patterned ITO Sample

As shown in Figure 5.22, after 3500 cycles, a sharp change resistance was observed corresponding to crack initiation/propagation in the ITO layer. Simulations were performed in order to investigate the effect of radius of curvature and trace width on the change in resistance in the ITO films. The data generated from these simulations can be found in Appendix A and the results are shown graphically in Figures 5.23a and 5.23b. As shown in 5.23a and 5.23b, as both the radius of curvature and trace width decrease, a more pronounced change in the resistance was observed. This is expected because smaller mandrel radii correspond to larger applied bending stresses and narrow traces are subjected to larger stresses when compared to wider stresses given the same applied stress.

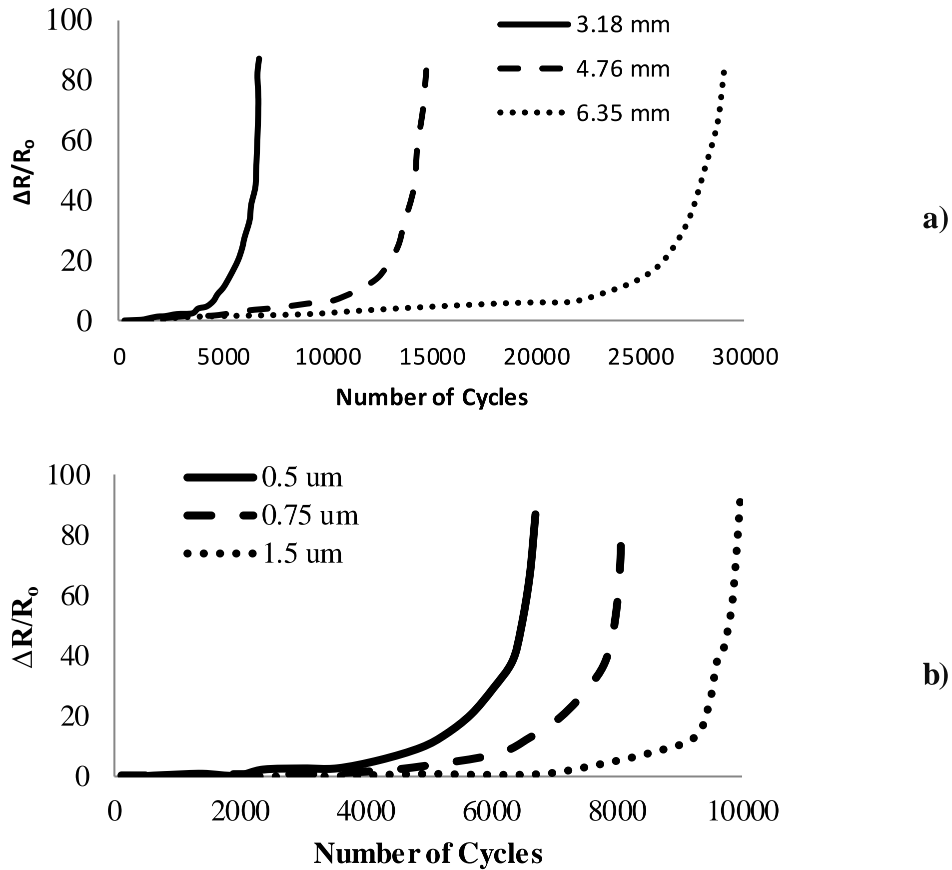

Figure 5.23: Effect of a) Radius of Curvature b) Trace Width on change in resistance in ITO Samples

Three patterned ITO samples were tested at three different stress amplitudes including 500, 100 and 2000 MPa respectively. The patterned ITO samples each have 6 sets of 10 traces with widths of 0.5 µm, 0.75 µm and 1.5 µm giving 60 samples tested at each stress level. The results of the fatigue testing of patterned ITO samples is shown below in Figure 5.24 and the data can be found in Appendix B.

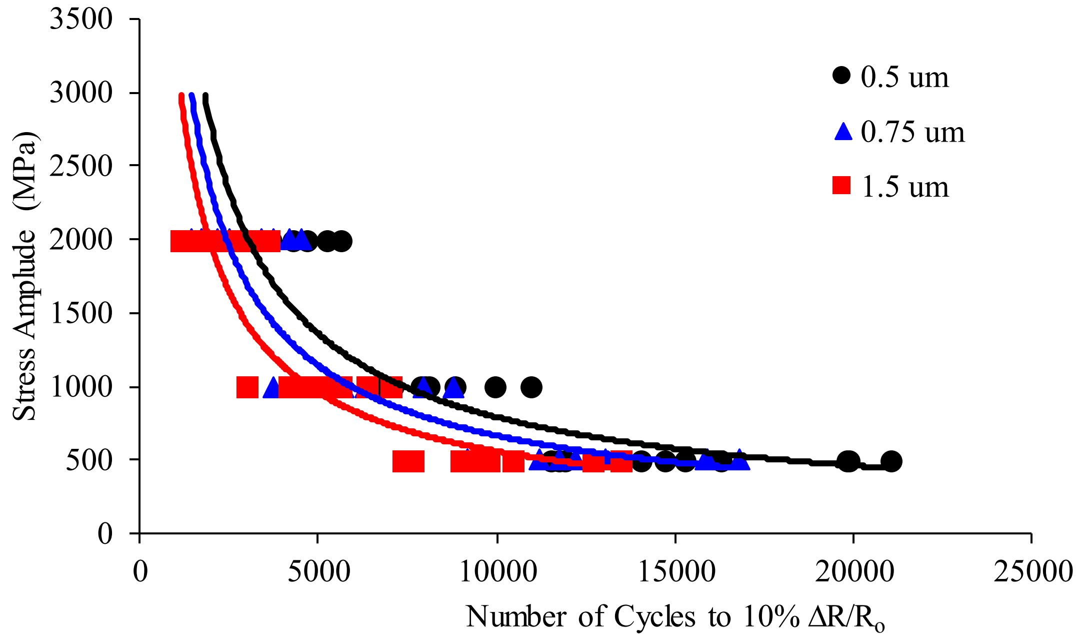

Figure 5.24: Stress vs. Number of Cylces for patterned ITO samples on Si_3N_4/PEN with trace widths of 0.5, 0.75 and 1.5 µm respectively under stress amplitudes of 500, 100 and 2000 MPa respectively

Figure 5.24 shows that higher applied stress amplitudes correspond to lower fatigue lives. As the trace width increased, the fatigue life also decreased. The S-N curve shown in Figure 5.24 for patterned ITO samples demonstrates a fatigue limit at 500 MPa. The fatigue limit is of importance because when the applied stress amplitudes are below the fatigue limit, failure due to fatigue will not occur. Each of the curves in Figure 5.24 was fitted to an inverse power law expression as shown below in Table 5.5.

Table 5.5: Effect of Trace width on C and m parameters of Power-Law model used to fit the patterned ITO data

Trace Width	C	m
0.5 μm	10,516	-0.778
0.75 μm	8,844	-0.778
1.5 μm	7,435	-0.778

The effect of trace width on the C and m parameters is that the m parameter is constant at -0.778 for all three trace widths, while the C parameter decreases linearly with trace width, x, according to the following expression. This linear dependence can be explained by increasing trace width corresponds to increased surface area so the bending stress generated in wider traces is larger than the bending stress generated in narrow traces when bent to the same radius of curvature.

$$C = -1540.6x + 12013 \tag{5.1}$$

Martin [1] compared three life distributions to fit the observed test data including the Exponential, the Weibull and the Lognormal distribution respectively. A brief explanation of each of these distributions will be briefly discussed next [26]–[28]. The exponential distribution describes the time between independent continuously occurring events at a constant average rate. The failure rate of the exponential distribution is:

$$f(t) = \lambda e^{-\lambda t} \tag{5.2}$$

where f(t) is the failure rate, t is the time and λ is a model parameter. The reliability of a component/system at a time, t_R, is evaluated as the probability of a given product failing during a mission time where $0 < t < t_R$

$$R(t_R) = e^{-\lambda t_R} \tag{5.3}$$

The Weibull distribution is a distribution that is used because of its ability to fit life data using a variety of shapes. The distribution can either be a two or three parameter model. The probability density function (PDF) for a two parameter Weibull model is given below:

$$f(T) = \frac{\beta}{\eta}\left(\frac{T}{\eta}\right)^{\beta-1} e^{-\left(\frac{T}{\eta}\right)^{\beta}} \tag{5.4}$$

where η is the time scale parameter and β is the shape or slope parameter. These parameters can be adjusted in order to better fit a given set of failure data. By adjusting either or both of these parameters one can fit an extensive variety of time to failure data to a Weibull distribution. The time scale parameter, η, effects the general shape of the resulting distribution where increasing η broadens the distribution while decreasing η makes the distribution narrower. The shape parameter, β, controls how the distribution will look as a function of time. When $\beta = 1$ the Weibull becomes an exponential distribution. When $\beta < 1$ the failure rate decreases over time and when $\beta > 1$ the failure rate increases with time (wear-out condition).

The Lognormal distribution is used to analyze cycles to failure of a particular structure or in fatigue testing. Since the logarithms of a lognormally distributed random variable are normally distributed, the PDF is:

$$f(t) = \frac{1}{\sigma t\sqrt{2\pi}} e^{\left(\frac{-[\ln(t)-\mu]^2}{2\sigma^2}\right)} \tag{5.5}$$

where σ is the standard deviation of the natural logarithms of the times to failure obtained during life testing and μ is the mean of the natural logarithms of the times to failure.

Typically in situations where mechanical stress dominated failure mechanism occur, an inverse power law mode is used where

$$N\ (\sigma) = \frac{1}{K\sigma^n} \tag{5.6}$$

where N is the Life, K and n are component/system dependent parameters, and σ is the mechanical stresses being applied to the component/system. The inverse power law model was considered by Martin because of the nature of the research is centered on the fatigue life of ITO interconnects subjected to varying stresses via different mandrel diameters.

When comparing the three distributions, Weibull distributions are a better fit for failures related to short failure times whereas the lognormal is better for predicting longer failure times. Both the Inverse Power Law (IPL) Weibull and IPL-Lognormal distributions were considered as potential candidates to fit the fatigue life data of ITO interconnects. The corresponding expressions for the respective IPL-Weibull and Lognormal distributions are given below where equation 5.6 was substituted into equations 5.4 and 5.5 for η and μ respectively:

$$f(t,V) = \beta K V^n (tKV^n)^{\beta-1} e^{-(tkV^n)^\beta} \tag{5.7}$$

$$f(T,V) = \frac{1}{T\sigma\sqrt{2\pi}} e^{-\frac{1}{2}\left(\frac{T' + \ln(K) + n\ln(V)}{\sigma}\right)^2} \tag{5.8}$$

where t = Cycles to Failure, V = Applied Bending stress, σ = Standard Deviation of the natural logarithms of the times to failure obtained during life testing, μ = mean of the natural logarithms of the times to failure, β = Shape/Slope Parameter and η = Time Scale Parameter .

Reliasoft's Weibull++ software [157] was used to determine the coefficients (β,η,μ σ) and the correlation value, p, for both the Weibull and Lognormal distributions using rank regression analysis for the data in Figure 5.24. Rank regression analysis is a mathematical approach to fit a line to a set of data points which allows one to determine the relationship between a dependent variable and one or more independent variables. The results are summarized in Table 5.6.

Table 5.6: Summary of Weibull and Lognormal goodness of fit for Patterned ITO Samples

Applied Bending Stress (MPa)	Weibull			Lognormal		
	β	η	p	μ	σ	P
500	4.336	38.515	0.966	3.523	0.295	0.992
1000	4.099	19.529	0.988	2.837	0.306	0.994
2000	2.821	8.613	0.967	1.959	0.452	0.995

For the three different stresses amplitudes, both distributions exhibit correlation high values (> 0.95), but the Weibull distribution has a slighter higher correlation value, so it was selected as the preferred life- stress model. Life vs. stress plots with mean life line and 95% confidence bounds of the mean life line for the three different stress levels (500, 1000 and 2000 MPa) are shown below for three different traces widths

(1.5, 0.75 and 0.5 μm) respectively in Figures 5.25 – 5.27 with 10 data points for each stress level:

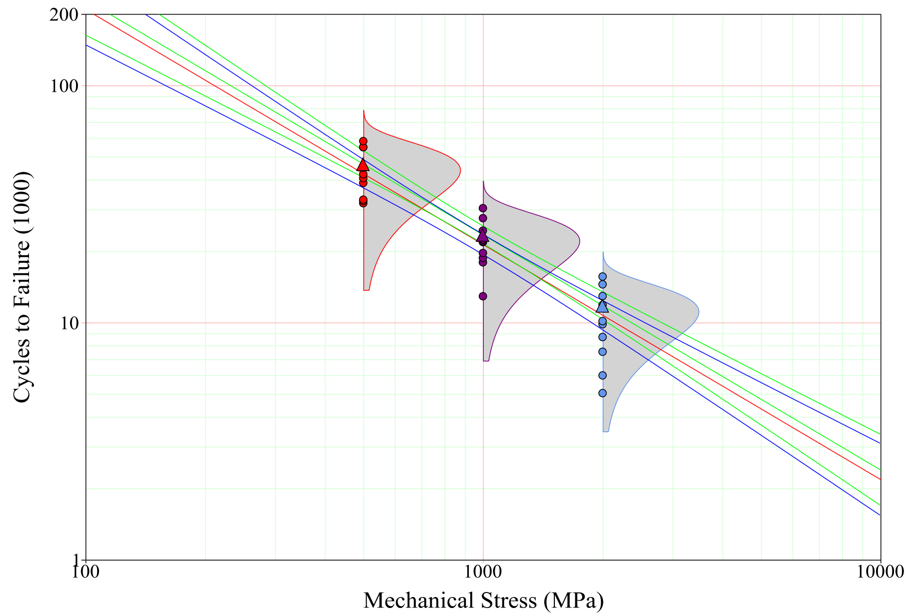

Figure 5.25: Life vs. Stress Curves for Fatigue Tests done at 3 Different Stress Levels (500, 1000 and 2000 MPa) for a 0.5 um wide ITO trace with 95% confidence bounds and the red line denoting the mean life

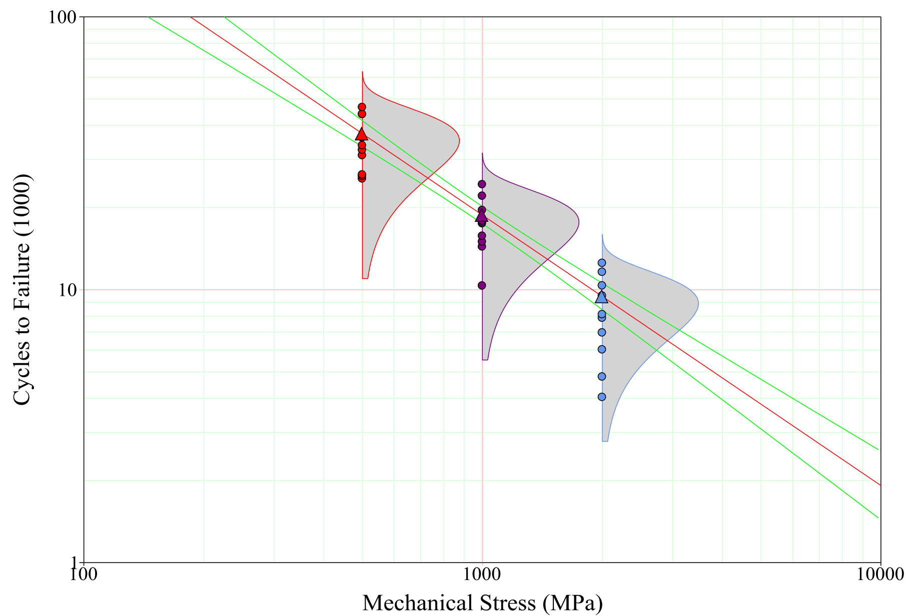

Figure 5.26: Life vs. Stress Curves for Fatigue Tests done at 3 Different Stress Levels (500, 1000 and 2000 MPa) for a 0.75 um wide ITO trace with 95% confidence bounds and the line denoting red the mean life

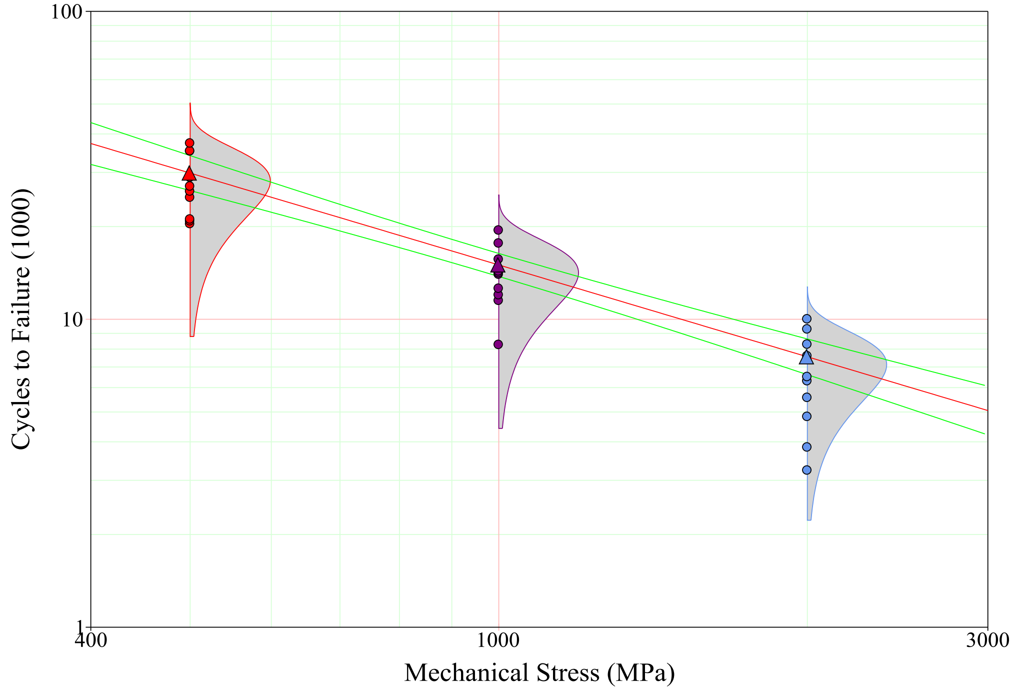

Figure 5.27: Life vs. Stress Curves for Fatigue Tests done at 3 Different Stress Levels (500, 1000 and 2000 MPa) for a 1.5 um wide ITO trace with 95% confidence bounds and the red line denoting the mean life

The mean with 95% confidence bounds of each of the distributions in Figures 5.25 – 5.27 is summarized in Table 5.7.

Table 5.7: Mean cycles to Failure for Patterned ITO samples tested at stress amplitudes of 500, 1000 and 2000 MPa respectively for trace widths of 0.5 μm, 0.75 μm and 1.5 μm respectively.

	Means Cycles to Failure for		
	Samples tested Stress Amplitude of 500 MPa	Samples tested Stress Amplitude of 1000 MPa	Samples tested Stress Amplitude of 2000 MPa
0.5 μm	47000	23000	12000
0.75 μm	37000	19000	9000
1.5 μm	30000	15000	8000

The analysis of the Life vs. Stress curves for Figures 5.25 – 5.27 show that increased stress amplitude and increased trace width both lead to decreased fatigue life due to

larger applied stress amplitudes and larger surface areas. Maximum Likelihood Estimation (MLE) was performed using Reliasoft's Weibull++ software to determine the parameters of K, n and β as well as the confidence limits for the results shown in Figures 5.25 - 5.27. MLE is a method of determining the parameters of a distribution by maximizing the value of the likelihood function. The likelihood function is a function of the parameters of a statistical model [26]–[28]. The results of this analysis are shown below in Table 5.8

Table 5.8: IPL-Weibull parameter estimation for 0.5, 0.75 and 1.5 um trace data

		Lower 90%	Lower 95%	Point Estimate	Upper 95%	Upper 90%
0.5 μm	β	1.38645	1.32551	1.75306	2.31851	2.21661
	K	8524	8234	10216	12676	12244

		Lower 90%	Lower 95%	Point Estimate	Upper 95%	Upper 90%
0.75 μm	β	1.38653	1.32559	1.75316	2.31864	2.21673
	K	6820	6587	8173	10141	9795

		Lower 90%	Lower 95%	Point Estimate	Upper 95%	Upper 90%
1.5 μm	β	1.38652	1.32558	1.75315	2.31864	2.21674
	K	5456	5270	6538	8113	7836

From the results of the parameter estimation using MLE, the effect of trace width on K and β was studied. All of the patterned ITO samples have β values greater than one corresponding to increasing failure rate with time (wear-out) condition. The K value (characteristic) life increases with decreasing applied stress amplitude. As the trace width, x, is increased, K increased slightly while β decreased exponentially according to:

$$K = 12770e^{-0.223x} \quad (5.9)$$

As expected, with increased trace width, the stress experienced by the trace increases because of the increased surface area, leading to a higher failure rate or higher β values.

5.3.2. Uniform ITO Samples

Uniform ITO samples were characterized using AFM and SEM prior to any fatigue testing. SEM and tapping mode height and phase profile AFM images of the untested ITO samples are shown below in Figures 5.28a, 5.28b and 5.29 below. From Figures 5.29a and 5.29b, the surface of the ITO samples are homogeneous and have a root mean squared (RMS) roughness of 1.648 nm.

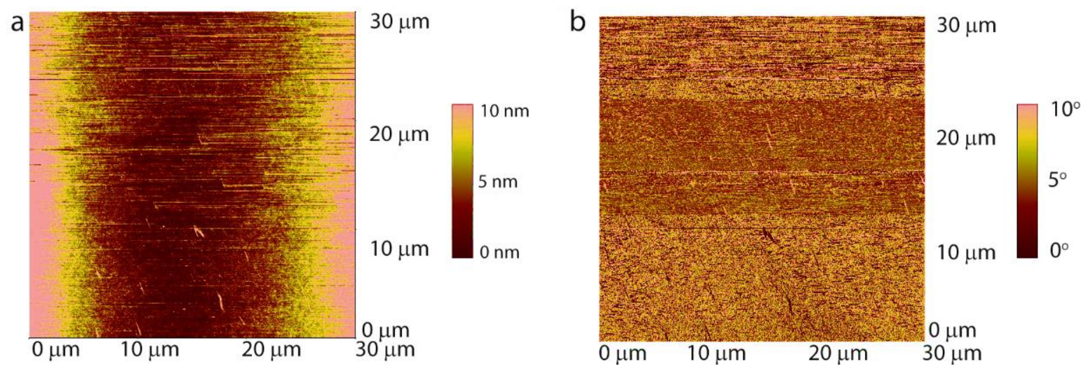

Figure 5.28: 30x30 um AFM (Tapping Mode) a) height image b) phase image of uniform untested uniform ITO on Si_3N_4/PEN substrate

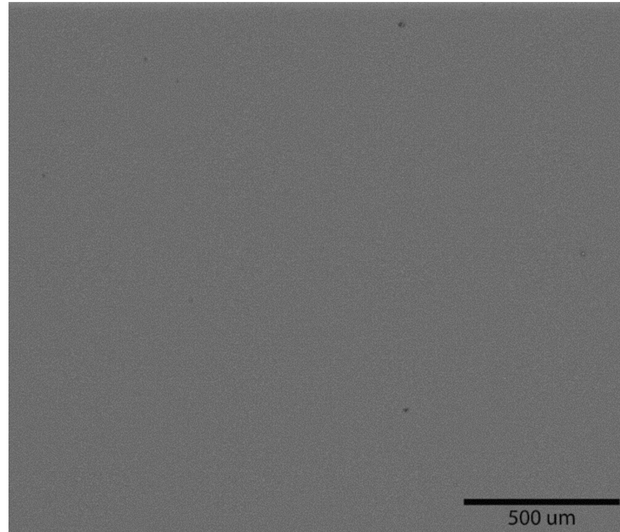

Figure 5.29: SE-SEM image of untested uniform ITO on Si_3N_4/PEN substrate

Uniform ITO samples were tested at 3 different applied bending stress amplitudes: 600, 500 and 400 MPa respectively. The samples were continuously subjected to bending fatigue until a 10% change in normalized resistance was observed. The typical electro-mechanical response of the ITO samples subjected to bending fatigue is shown below in Figure 5.30 for an ITO sample tested at 600 MPa where the normalized resistance increases as the number of cycles is increased as cracks initiate/propogate.

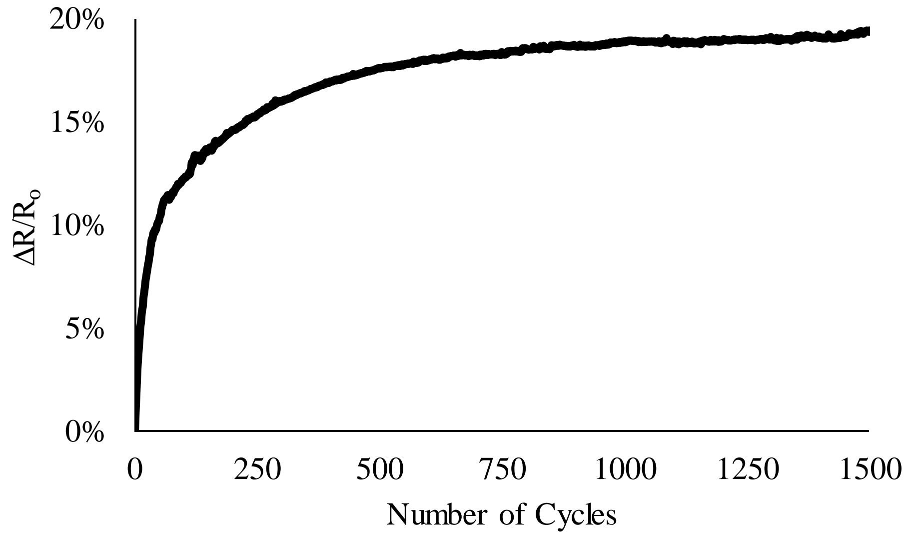

Figure 5.30: Change in Normalized Resistance ($\Delta R/R_o$) vs. Number of Cycles for an ITO on Si_3N_4/PEN tested at 600 MPa

The effect of applied bending stresses on the electro-mechanical response of the ITO samples was studied for ITO samples fatigued at stress amplitudes of 600, 500 and 400 MPa respectively. As the applied stress was increased, a sharper change in the normalized resistance of the samples was observed as seen in Figure 5.31. This is caused by higher stress amplitudes leading to more crack initiation/propagation resulting in more pronounced changes in resistance.

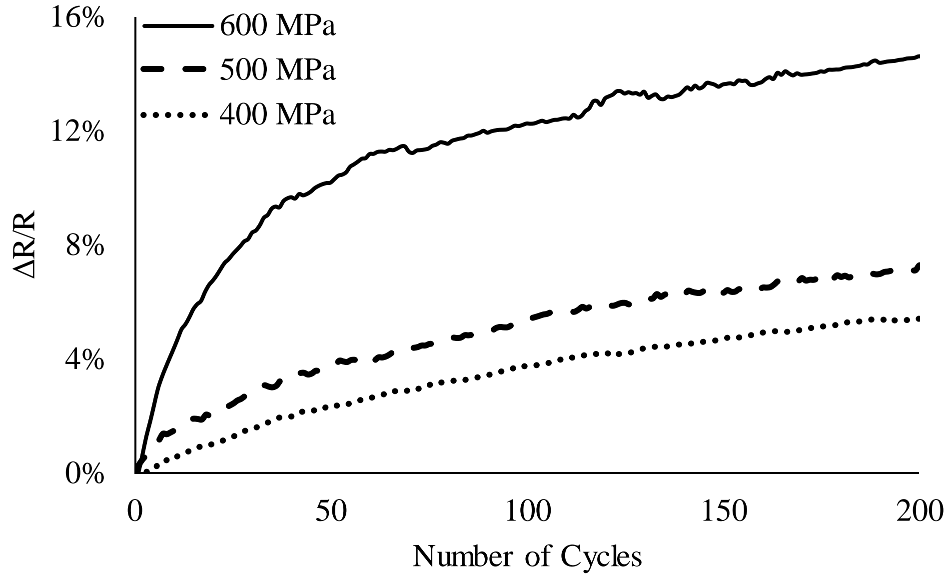

Figure 5.31: Change in Normalized Resistance ($\Delta R/R_o$) vs. Number of Cycles for ITO on Si_3N_4/PEN tested at 600, 500 and 400 MPa

The resistance values shown in Figures 5.30 and 5.31 were converted into strain values using the following procedure. First, resistance values for the sample both before and after bending can be expressed by:

$$R_o = \frac{\rho L_o}{w_o t_o} \tag{5.10}$$

$$R_d = \frac{\rho L_d}{w_d t_d} \tag{5.11}$$

where R_o and R_d are the resistances of the sample before and after bending, L_o and L_d are the lengths of the samples before and after bending, w_o and w_d are the widths of the samples before and after bending and t_o and t_d is the thickness before and after bending.

From elastic theory, it is known that

$$\varepsilon = \frac{\Delta L}{L_o} \tag{5.12}$$

$$\nu = -\frac{\varepsilon_x}{\varepsilon_z} \tag{5.13}$$

where ε is the strain, ΔL is the change in length of the sample, L_o is the original length of the sample, ν is the poison's ratio of the material, ε_x and ε_z are strain in the x and z directions respectively. Using those relations, the change in length and thickness of the samples can expressed in terms of strain as follows:

$$\Delta L = l\varepsilon_x \tag{5.14}$$

$$\Delta t = -\frac{h\varepsilon_x}{\nu} \tag{5.15}$$

Therefore the change in resistance in terms of strain can be expressed as

$$\Delta R = \frac{\rho}{w}\left[\frac{l_d}{t_d} - \frac{l_o}{t_o}\right] = \frac{\rho}{w}\left[\frac{l_o(1+\varepsilon_x)}{t_o\,(1+\varepsilon_z)} - \frac{l_o}{t_o}\right] = \frac{\rho l_o}{w t_o}\left[\frac{(1+\varepsilon_x)}{\left(1-\frac{\varepsilon_x}{\nu}\right)} - 1\right] \tag{5.16}$$

If a constant C is created and then defined as

$$C = \frac{\Delta R w t_o}{\rho l_o} \tag{5.17}$$

Then equation 5.17 can be expressed as

$$C = \left[\frac{(1+\varepsilon_x)}{\left(1-\frac{\varepsilon_x}{\nu}\right)} - 1\right] \tag{5.18}$$

Rearranging Equation 5.18 and substituting the definition of C back into it, gives the expression for strain

$$\varepsilon_x = \frac{\frac{\Delta R w t_o}{\rho l_o}}{\left(1 + \nu^{-1} + \frac{\frac{\Delta R w t_o}{\rho l_o}}{\nu}\right)} \tag{5.19}$$

Using Equation 5.19, resistance values were converted for all tested ITO samples and the resulting analogues strain version of Figure 5.31 is shown below in Figure 5.32

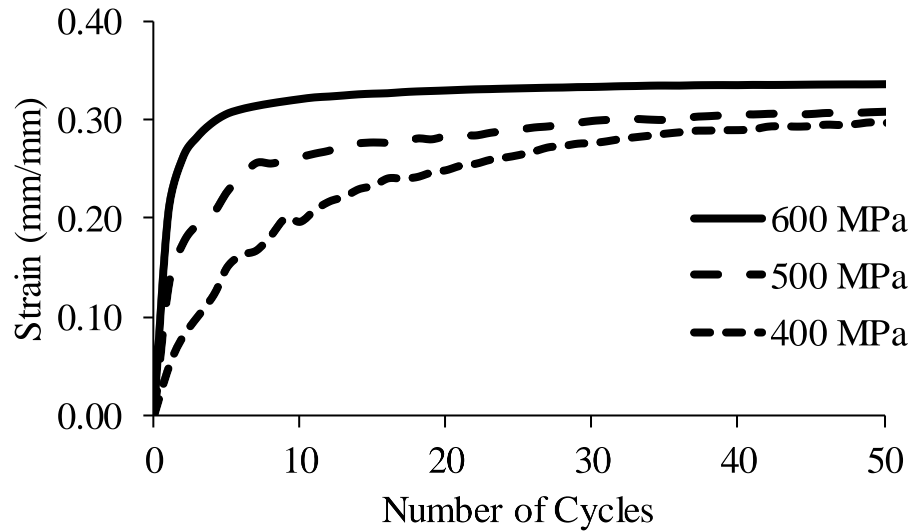

Figure 5.32: Change in Strain vs. Number of Cycles for ITO on Si_3N_4/PEN samples tested at 600, 500 and 400 MPa for the first 50 cycles

As seen in Figure 5.32, for all three applied stress levels there is an immediate response in the ITO films with higher applied stress amplitudes corresponding to sharper changes in the strain. Uniform ITO samples were continuously subjected to bending fatigue until a 10% change in normalized resistance was observed for 3 different applied bending stresses: 600, 500 and 400 MPa respectively. The results of this are shown below in the Stress-Life curve in Figure 5.33 and Table 5.9

Table 5.9: Summary of Stress-Life Data for bending fatigue studies for uniform ITO on Si_3N_4/PEN samples tested at 600, 500 and 400 MPa respectively

Sample #	Stress (MPa)	Number of Cycles to 10% ΔR/Ro
1	600	69
2	600	46
3	600	24
1	500	423
2	500	476
3	500	335
4	500	136
1	400	869
2	400	1715
3	400	1215

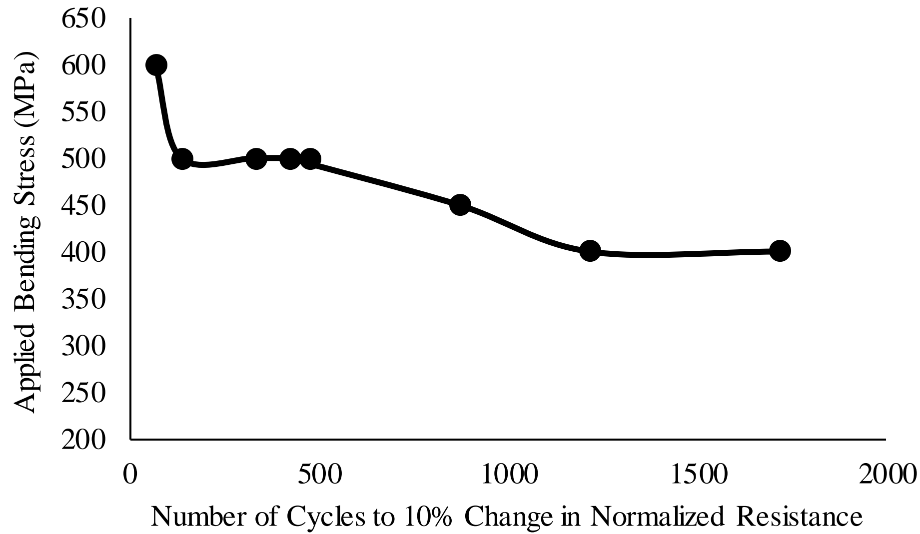

Figure 5.33: Stress vs. Number of Cycles for Uniform ITO Samples on Si_3N_4/PEN

The S-N curve in Figure 5.33 shows indication of a fatigue limit of 400 MPa for uniform ITO on Si_3N_4/PEN samples. The S-N curve in Figure 5.33 was fitted to an inverse power lay expression according to the following expression with an correlation factor of 0.8623:

$$\sigma = 960.22N^{-0.115} \tag{5.20}$$

where σ is the applied bending stress amplitude and N is the number of cycles to 10% change in normalized resistance. Similar to the analysis used in previous section on patterned ITO samples, Reliasoft's Weibull++ software was used to determine the coefficients (β,η,μ σ) and the correlation value, p, for both the Weibull and Lognormal distributions for the data shown in Table 5.9 is summarized in Table 5.10:

Table 5.10: Summary of Weibull and Lognormal goodness of fit for Uniform ITO Samples

Applied Bending Stress (MPa)	Weibull β	Weibull η	Weibull p	Lognormal μ	Lognormal σ	Lognormal P
600	1.812	54.594	0.999	3.747	0.644	0.991
500	1.869	399.641	0.951	5.735	0.610	0.913
400	2.848	1431.726	0.996	7.106	0.415	1.000

For the three different stresses amplitudes, both distributions exhibit correlation high values (> 0.95), but the Weibull distribution has a slighter higher correlation value, so it was selected as the preferred life- stress model. From the goodness of fit analysis shown in Table 5.10, the characteristic life of the uniform ITO samples decreases with increasing stress amplitude. Life vs. stress plots with mean life line and 95% confidence bounds of the mean life line for the four different stress levels (600, 500, 450 and 400 MPa) is shown below in Figure 5.34:

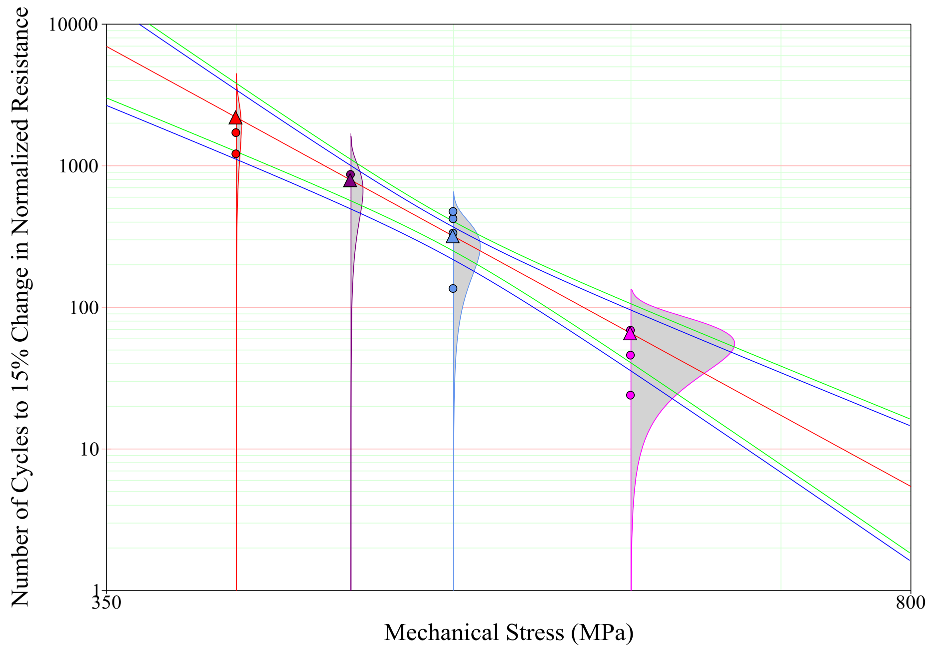

Figure 5.34: Life vs. Stress Curves for Fatigue Tests done at 4 Different Stress Levels (600, 500, 450 and 400 MPa) for Uniform ITO Samples on Si_3N_4/PEN with 95% confidence bounds and red line denoting mean life

As seen in Figure 5.34, a majority of the data points lie with the 95% confidence bounds of the mean life line suggesting that the data is well fitted by the IPL-Weibull distribution. The mean life with 95% confidence bounds of each of the distributions in Figure 5.35 is summarized in Table 5.11.

Table 5.11: Mean cycles to Failure for uniform ITO samples tested at stress amplitudes of 600, 500, 450 and 400 MPa respectively

Applied Bending Stress Amplitude (MPa)	Mean cycles to 10% change in normalized resistance
600	66
500	318
450	791
400	2194

The analysis of the Life vs. Stress curves in Figures 5.34 show that increased stress amplitude leads to decreased fatigue life due to larger applied stress amplitudes.

Maximum Likelihood Estimation (MLE) using Reliasoft's Weibull++ software was used to determine the parameters of K, n and β and the confidence limits for the results shown in Figures 5.34. The results of this analysis are shown below in Table 5.12

Table 5.12: IPL-Weibull parameter estimation for Uniform ITO on Si_3N_4/PEN Samples tested at 600, 500 and 400 MPa respectively

		Lower 90%	Lower 95%	Point Estimate	Upper 95%	Upper 90%
600 MPa	β	0.78	0.66	1.81	4.98	4.23
	K	29.42	26.14	54.59	114.03	101.30

		Lower 90%	Lower 95%	Point Estimate	Upper 95%	Upper 90%
500 MPa	β	0.87	0.75	1.87	4.63	4.00
	K	239.04	216.63	399.64	737.27	668.14

		Lower 90%	Lower 95%	Point Estimate	Upper 95%	Upper 90%
400 MPa	β	1.26	1.07	2.85	7.55	6.45
	K	983.43	915.15	1431.73	2239.88	2084.38

The results of this analysis (shown in Table 5.12) showed that all of the uniform ITO samples have β values greater than one corresponding to increasing failure rate with time (wear-out) condition. The K value (characteristic) life increases with decreasing applied stress amplitude.

5.3.3. Uniform Graphene Samples

Using the stress-strain of Graphene (Figure 5.34), four stresses (80 GPa, 60 GPa, 50 GPa and 40 GPa) were selected in order to stay well below the yield stress of Graphene but also within the low cycle fatigue regime. Using the results from the FEA work discussed earlier in Chapter 4, the appropriate mandrel sizes were determined.

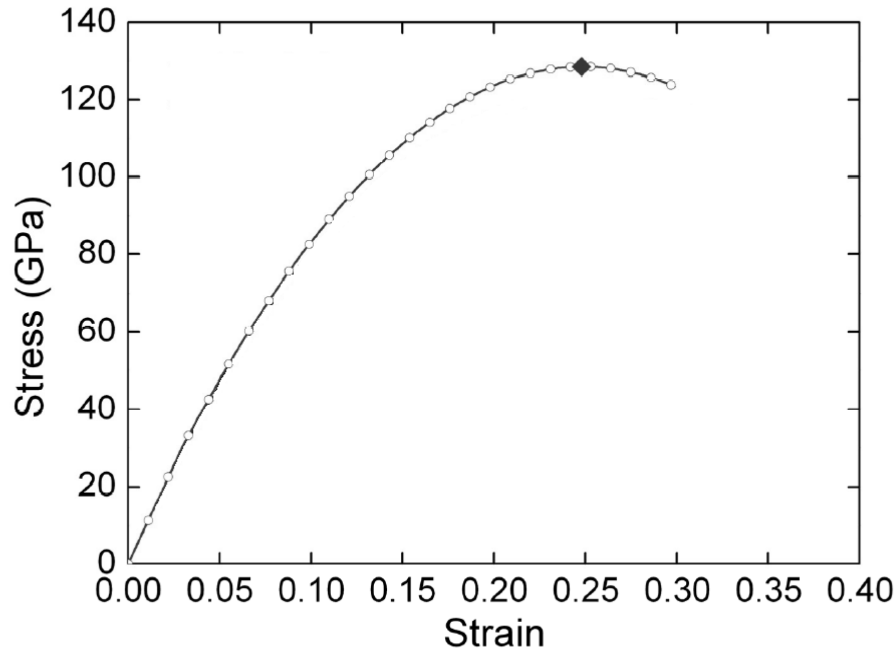

Figure 5.35: Stress-Strain Curve for Graphene as measured using nano-indentation AFM [130]

Uniform Graphene on Si_3N_4/PEN samples were continuously subjected to bending fatigue until a 15% change in normalized resistance was observed for 4 different applied bending stresses: 80, 60, 50 and 40 GPa respectively.

The typical electro-mechanical response of Graphene samples subjected to bending fatigue is shown below in Figure 5.36 for a Graphene sample tested at 80 MPa where the normalized resistance increases as the number of cycles is increased as cracks initiate/propagate.

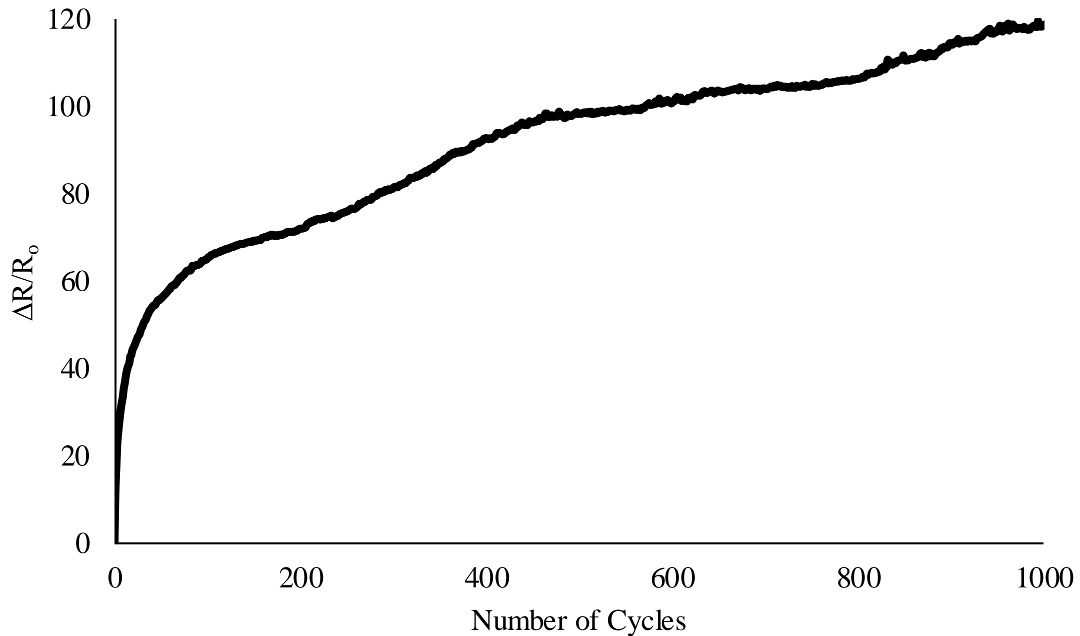

Figure 5.36: Change in Normalized Resistance ($\Delta R/R_0$) vs. Number of Cycles for a uniform Graphene on Si_3N_4/PEN sample tested at 80 GPa

The effect of applied bending stresses on the electro-mechanical response of the Graphene samples was studied for four stress amplitudes including 80, 60, 50 and 40 GPa. As the applied stress was increased, a sharper change in the normalized resistance of the samples was observed as seen in Figure 5.37 due to increased mechanical deformation at higher stress amplitudes. Additionally, as seen in Figure 5.37, samples tested at 80 and 60 GPa showed a significantly quicker change in resistance when compared to samples tested at 50 and 40 GPa.

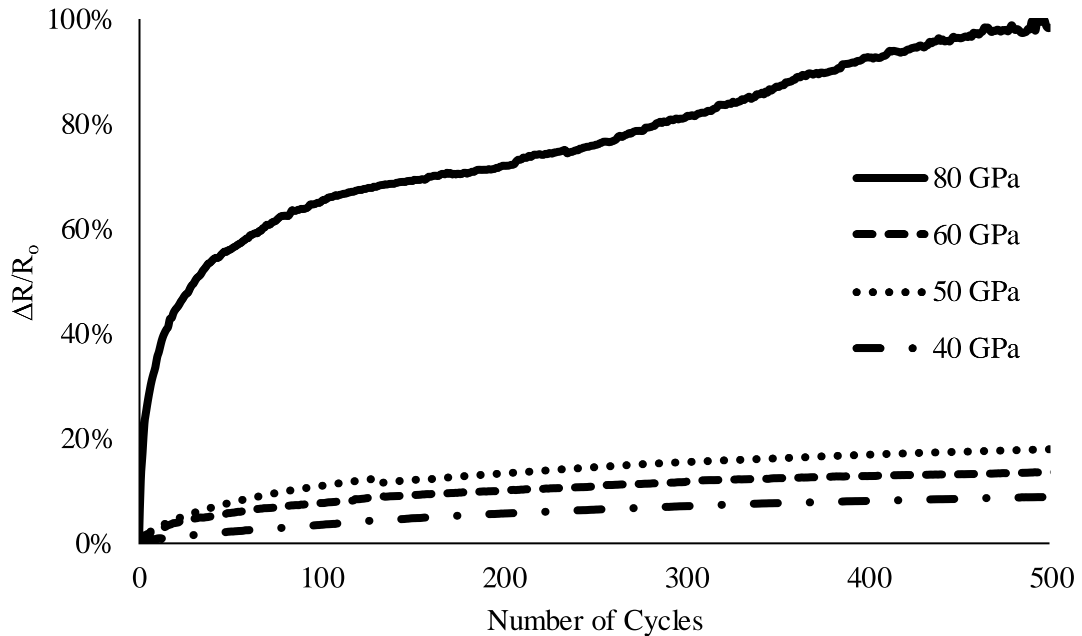

Figure 5.37: Change in Normalized Resistance ($\Delta R/R_0$) vs. Number of Cycles for uniform Graphene on Si_3N_4/PEN samples tested at 80, 60, 50 and 40 GPa

The resistance values shown in Figures 5.35 and 5.36 were converted into strain values using the same procedure described earlier. Using Equation 5.19, resistance values were converted for all tested Graphene samples and the analogous strain version of Figure 5.37 is shown below in Figure 5.38. As shown in Figure 5.38, strain increased with time and higher stress amplitudes lead to more pronounced changes in strain.

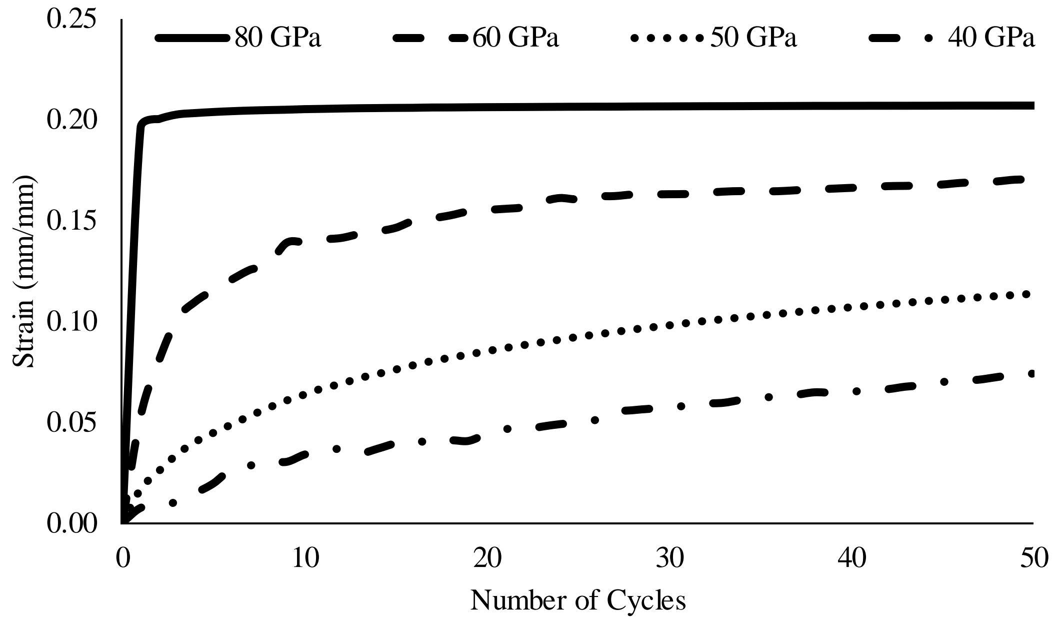

Figure 5.38: Change in Strain vs. Number of Cycles for uniform Graphene on Si_3N_4/PEN samples tested at 80, 60, 50 and 40 GPa for the first 50 cycles

Uniform Graphene samples were continuously subjected to bending fatigue until a 15% change in normalized resistance was observed for 4 different applied bending stresses: 80, 60, 50 and 40 GPa respectively. The results of this are shown below in the Stress-Life curve in Figure 5.39 and Table 5.13

Table 5.13: Summary of Stress-Life Data for bending fatigue studies uniform Graphene on Si_3N_4/PEN samples tested at 80, 60, 50 and 40 GPa respectively

Sample #	Stress (GPa)	Number of Cycles to 15% ΔR/Ro
1	80	3
2	80	2
3	80	15
4	80	31
1	60	82
2	60	158
3	60	77
4	60	276
5	60	57
6	60	185
1	50	567
2	50	775
1	40	2980
2	40	3230
3	40	2963

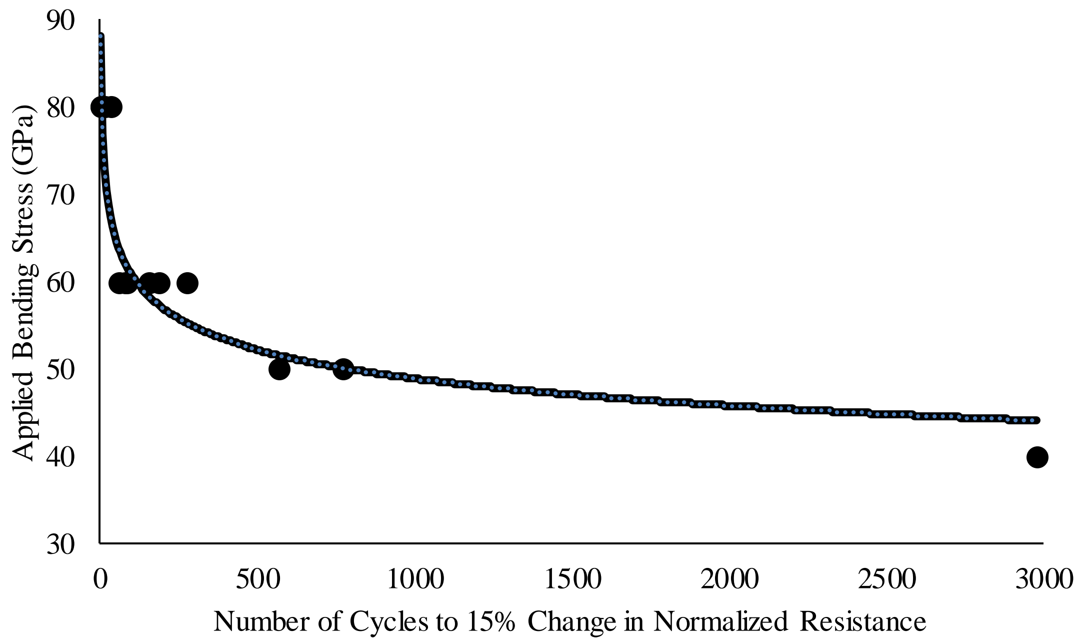

Figure 5.39: Stress vs. Number of Cycles for Uniform Graphene Samples on Si_3N_4/PEN

The S-N curve in Figure 5.39 shows indication of a fatigue limit at 40 GPa for the uniform Graphene on Si_3N_4/PEN samples. The S-N curve in Figure 5.40 was fitted to an inverse power lay expression according to the following expression with an correlation factor of 0.8631:

$$\sigma = 94.03N^{-0.095} \tag{5.22}$$

Similar to the analysis used in the previous section on uniform ITO on Si_3N_4/PEN samples, Reliasoft's Weibull++ software was used to determine the coefficients (β,η,μ σ) and the correlation value, p, for both the Weibull and Lognormal distributions for the data shown in Figure 5.39. The results as summarized in Table 5.14 below:

Table 5.14: Summary of Weibull and Lognormal goodness of fit for Uniform Graphene Samples

Applied Bending Stress (MPa)	Weibull			Lognormal		
	β	η	p	μ	σ	P
80 GPa	0.814	13.073	0.952	1.983	1.482	0.967
60 GPa	1.825	157.180	0.956	4.783	0.672	0.976
50 GPa	4.048	736.666	1.000	6.497	0.287	1.000
40 GPa	23.394	3115.731	0.854	8.025	0.053	0.894

In Table 5.14, for the four different stresses, both distributions exhibit correlation high values (> 0.95), but the Weibull distribution has a slighter higher correlation value, so it was selected as the preferred life- stress model. Similar to the results for patterned ITO and uniform ITO, Graphene on Si_3N_4/PEN's characteristic life increases with decreasing stress amplitude. Life vs. stress plots with mean life line and 95% confidence bounds of the mean life line for the four different stress levels (80, 60, 50 and 40 GPa) is shown below in Figures 5.40:

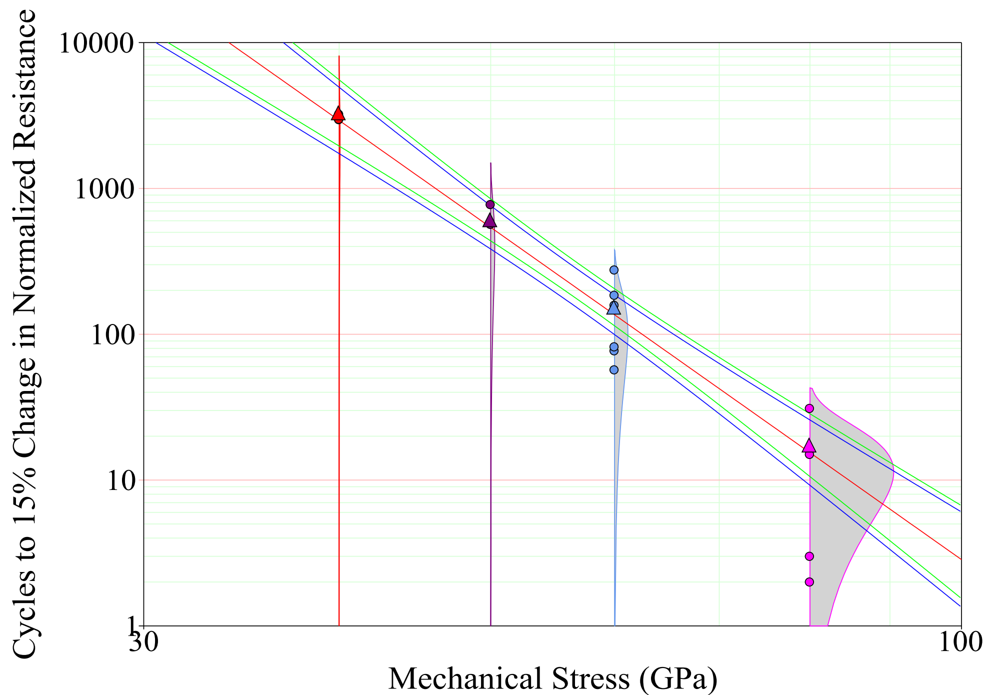

Figure 5.40: Life vs. Stress Curves for Fatigue Tests done at 4 Different Stress Levels (80, 60, 50, and 40 MPa) for uniform Graphene samples on Si_3N_4/PEN with 95% confidence bounds and red line denoting mean life

The mean with 95% confidence bounds of each of the distributions in Figures 5.40 is summarized in Table 5.15.

Table 5.15: Mean cycles to Failure for uniform Graphene samples tested at stress amplitudes of 80, 60, 50 and 40 GPa respectively

Applied Bending Stress Amplitude (GPa)	Mean cycles to 10% change in normalized resistance
80	17
60	153
50	609
40	3294

The analysis of the Life vs. Stress curves in Figures 5.41 show that increased stress amplitude leads to decreased fatigue life due to larger applied stress amplitudes. Maximum Likelihood Estimation (MLE) using Reliasoft's Weibull++ software was

used to determine the parameters of K, n and β as confidence limits for the results shown in Figures 5.41. The results of this analysis (shown in Table 5.16) showed that all of the uniform Graphene samples have β values greater than one corresponding to increasing failure rate with time (wear-out) condition. The K value (characteristic) life increases with decreasing applied stress amplitude.

Table 5.16: IPL-Weibull parameter estimation for Uniform Graphene on Si_3N_4/PEN Samples tested at 600, 500 and 400 MPa respectively

		Lower 90%	Lower 95%	Point Estimate	Upper 95%	Upper 90%
80 GPa	β	0.52	0.46	1.01	2.20	1.94
	K	5.37	4.55	12.78	35.86	30.38

		Lower 90%	Lower 95%	Point Estimate	Upper 95%	Upper 90%
60 GPa	β	1.08	0.97	1.83	3.42	3.10
	K	106.57	98.92	157.18	249.75	231.83

		Lower 90%	Lower 95%	Point Estimate	Upper 95%	Upper 90%
50 GPa	β	1.26	1.07	2.85	7.55	6.45
	K	983.43	915.15	1431.73	2239.88	2084.38

		Lower 90%	Lower 95%	Point Estimate	Upper 95%	Upper 90%
40 GPa	β	11.18	9.71	23.39	56.37	48.94
	K	2985.57	2961.26	3115.73	3278.26	3251.57

The IPL-Weibull distribution parameters for patterned ITO, uniform ITO and Graphene are summarized in Table 5.17:

Table 5.17: IPL-Weibull parameter estimation for patterned ITO, uniform ITO on Si_3N_4/PEN and uniform Graphene on Si_3N_4/PEN samples

Sample Type	β	η
0.5 μm ITO Trace	1.75306	10216
0.75 μm ITO Trace	1.75316	8173
1.5 μm ITO Trace	1.75315	6538
Uniform ITO (600 MPa)	1.8119	54.59
Uniform ITO (500 MPa)	1.869	399.6
Uniform ITO (400 MPa)	2.8478	1432
Uniform Graphene (80 GPa)	1.0051	12.78
Uniform Graphene (60 GPa)	1.8253	157.2
Uniform Graphene (50 GPa)	4.048	736.7
Uniform Graphene (40 GPa)	23.394	3116

From the IPL-Weibull parameter estimation, all of patterned ITO, uniform ITO and uniform Graphene samples have β values greater than 1, so the failure rates of these components will increase with time (wear-out condition). The β values for most of the samples was between 1 and 4 corresponding to low cycle fatigue behavior. The η parameter of patterned ITO, uniform ITO and uniform Graphene samples decreases with increasing applied stress amplitude. This is due to the fact that an inverse power law model was used where η was substituted with KV^n where K and n are material parameters and V is the applied stress.

The failure rates to 10,000 cycles of patterned ITO, uniform ITO and uniform Graphene samples were determined to be 6.7×10^{-5} Cycle^{-1}, 8.15×10^{-4} Cycle^{-1} and 2.6×10^{-4} Cycle^{-1} respectively. Mean time to Failure (MTTF) for a 10% change in normalized resistance for patterned ITO and uniform ITO was determined to be 6262 and 578 cycles respectively. The MTTF for a 15% change in normalized resistance for uniform Graphene samples were determined to be 771 cycles.

SEM was used to investigate any microstructural changes in the samples due to the fatigue process. SE-SEM images from samples tested at stress amplitudes of 80 GPa and 60 GPa are shown below in Figure 5.42

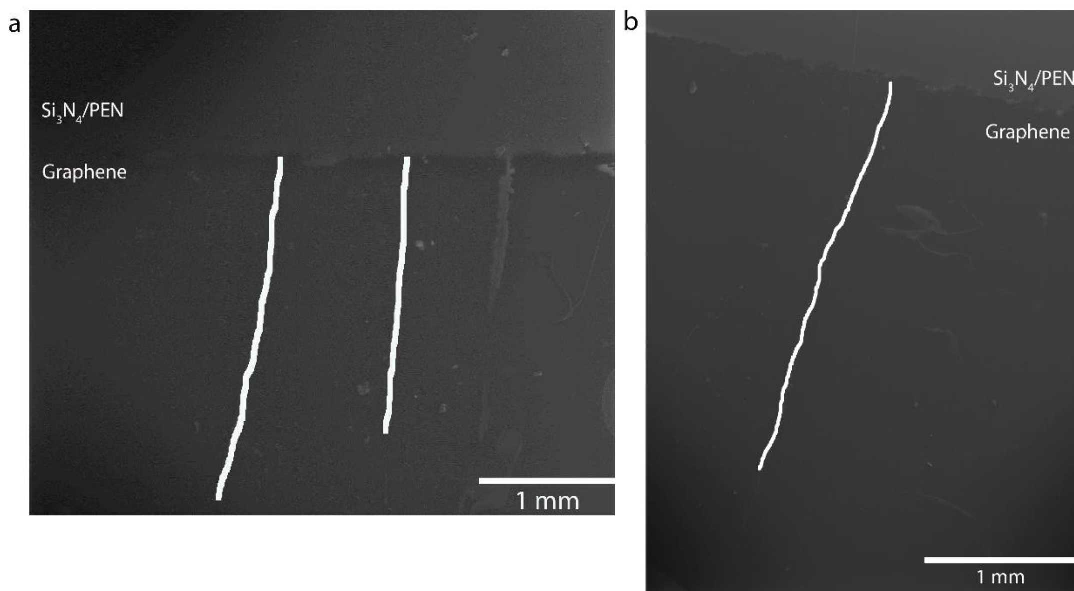

Figure 5.41: SE-SEM images of the Graphene-Si_3N_4/PEN interface illustrating crack formation/propagation (white lines) for samples tested at applied bending stress amplitudes of a) 80 GPa and b) 60 GPa

As seen in Figure 5.41, fatigue of the samples results in crack initiation/propagation as seen by the cracks present in Figures 5.41a and 5.41b. The lengths of the respective cracks shown above were determined using ImageJ software where the cracks in 5.42a were found to be 2.8 and 2.37 mm respectively, while the crack seen in Figure 5.42b was found to be 2.8 mm. The interface between Graphene and the Si_3N_4/PEN has lattice mismatch and adhesion issues to leading to a stress concentration being generated at the interface. This is in turn leads to crack initiation at this interface

which is undesirable. However with continued research into fabrication techniques, these adhesion and interfacial issues will be alleviated.

5.4. *Summary*

Materials characterization of Graphene prior to fatigue testing was performed using Raman spectroscopy, AFM and SEM. The results of the Raman and AFM show that the transfer process from CVD grown Graphene plays a critical role in the surface roughness and coverage of the Graphene on Si_3N_4/PEN substrates. Improved fabrication techniques should improve the mean Graphene coverage from 68% determined in this work and reduce interfacial issues will reduce stress concentrators at the in Graphene-Si_3N_4/PEN interface. The underlying flexible substrate needs to be as smooth as possible because the surface morphology of the Graphene layer is strongly dependent on the underlying substrate morphology.

The S-N fatigue behavior of Graphene on Si_3N_4/PEN and both patterned and uniform film ITO on Si_3N_4/PEN has been determined. The S-N behavior of patterned ITO and uniform ITO showed fatigue limits at 500 MPa and 400 MPa respectively. Graphene on a flexible substrates showed a well-defined fatigue limit of 40 GPa. The high magnitude of the fatigue limit indicates that it should resist fatigue failures as an interconnect for flexible electronics. Reliability analysis of the fatigue data for patterned ITO, uniform ITO and uniform Graphene samples were all fitted using an IPL-Weibull distribution. From the IPL-Weibull parameter estimation, all of the ITO samples have β values greater than 1, so the failure rates of these components will

increase with time (wear-out condition). The uniform Graphene on Si_3N_4/PEN samples exhibit a decreasing failure rate with time. The K parameter for the Graphene samples is higher than that of the ITO samples due to the limited number of test samples when compared to that of the ITO. The microstructural analysis by SEM and AFM did not reveal normal fatigue crack growth and propagation.

Chapter 6 : Conclusions and Future Work

6.1. Summary

This thesis presents the first determination of the fatigue properties of Graphene and Indium Tin Oxide (ITO), stressed in a configuration appropriate for flexible displays. This thesis also presents a materials based solution to the fatigue related reliability problem of flexible displays. The mechanical properties of ITO and Graphene have been presented as well as the first determination of the stress-amplitude relations for Graphene and ITO. The fatigue properties of Graphene and ITO were determined using the mandrel-fatigue experimental approach modified for the present experiments. The mandrel fatigue apparatus was designed to produce a stress amplitude necessary to determine S-N relationships of Graphene and ITO. The stress amplitudes achieved ranged from 2000 MPa to 400 MPa for both planar and patterned ITO samples and 80 GPa, 60 GPa, 50 GPa and 40 GPa for the Graphene samples. The higher stress amplitudes for Graphene were necessary due to the higher yield strength of Graphene.

In this work, planar Graphene and ITO samples were fabricated on Si_3N_4/ Polyethylene Naphthalate (PEN) substrates and in addition patterned ITO films on Si_3N_4/PEN were also fabricated. The preparation of the planar Si_3N_4/ PEN has been presented and consisted of a 0.3 μm layer of Si_3N_4 deposited on PEN using CVD techniques. The subsequent ITO layers were deposited using DC magnetron sputtering while the Graphene samples were deposited on Cu via CVD and transferred to the Si_3N_4/PEN substrate using the “Floating Graphene” technique. The

characterization of ITO and Graphene was carried out prior to testing. The Raman spectroscopy results confirmed the presence of Graphene and the mean Graphene coverage was determined to be 68%. The AFM results confirmed the presence of Graphene with height measurements of 0.334 and 0.342 nm respectively. AFM results showed an RMS surface roughness of 2.32 nm which is mainly due to the surface roughness of the Si_3N_4/PEN substrate (measured to be 2 nm).

The stresses generated in Graphene as well as in ITO were analytically calculated using a complaint substrate approach. Finite element analysis was carried out and these calculations showed a seven fold increase in the generated bending stress when replacing ITO with Graphene (65 GPa vs. 7.83 GPa) when bent to a radius of curvature of 1.58 mm, corresponding to a stress of 53.29 GPa for Graphene and 1.81 GPa for ITO.

The S-N fatigue behavior of Graphene on Si_3N_4/PEN and both patterned and uniform films of ITO on Si_3N_4/PEN has been determined. The S-N behavior of patterned ITO showed a fatigue limit at 500 MPa when subjected to stress amplitudes above 1000 MPa. The S-N behavior of uniform ITO showed a fatigue limit at 400 MPa when subjected to stress amplitudes between 400 – 600 MPa.. Graphene on a flexible substrate showed a well-defined fatigue limit of 40 GPa. The high magnitude of the fatigue limit indicates that it should resist fatigue failures when used as an interconnect for flexible electronics. Reliability analysis of the fatigue data for patterned ITO, uniform ITO and uniform Graphene samples were all fitted using an

IPL-Weibull distribution. From the IPL-Weibull parameter estimation, the β and K values of patterned ITO traces with varying widths (0.5 μm, 0.75 μm and 1.5 μm), uniform ITO and uniform Graphene on Si_3N_4/PEN substrates is summarized in Table 6.1:

Table 6.1: Summary of IPL-Weibull Parameter estimation for patterned ITO, Uniform ITO and Uniform Graphene Samples

Sample	β	K
0.5 μm ITO Trace	1.75306	10216
0.75 μm ITO Trace	1.75316	8173
1.5 μm ITO Trace	1.75315	6538
Uniform ITO tested at stress amplitude of 600 MPa	1.8119	54.59
Uniform ITO tested at stress amplitude of 500 MPa	1.869	399.6
Uniform ITO tested at stress amplitude of 400 MPa	2.8478	1432
Uniform Graphene tested at stress amplitude of 80 GPa	1.0051	12.78
Uniform Graphene tested at stress amplitude of 60 GPa	1.8253	157.2
Uniform Graphene tested at stress amplitude of 50 GPa	4.048	736.7
Uniform Graphene tested at stress amplitude of 40 GPa	23.394	3116

The β values for indicate that the failure rates of the ITO and Graphene samples will all decrease with time (wear-out condition). The differences in K values is due to the variability in sample size between ITO and Graphene. The microstructure analysis after fatigue tests showed crack initiation at the substrate-film interface. The failure rate to 10,000 cycles of uniform monolayer Graphene samples was determined to be 2.6×10^{-4} Cycle^{-1}. The MTTF for a 15% change in normalized resistance for uniform Graphene samples were determined to be 771 cycles. It is important to note that the failure rates and MTTF of monolayer Graphene was not compared to uniform ITO samples in this work. The low failure rate was achieved through the use of a single monolayer of Graphene and the failure rate could be further lowered with multiple layers of Graphene.

6.2. *Thesis Contributions*

- The contributions of the current research are as follows:
  - The determination of S-N behavior for Graphene and ITO.
  - The application of finite element models to predict the stresses generated in patterned or uniform film interconnect layers.
  - An approach to analyze ITO and Graphene properties via a combination of Raman spectroscopy, AFM and SEM.
  - The development of a probabilistic fatigue life model for ITO and Graphene interconnect traces, based on probability density functions to predict interconnect failure rate and mean time to failure.

- The major potential benefits of the research work include:
  - The qualification of Graphene as the interconnect capable of elimination or reducing line-out effects in flexible displays
  - The determination of S-N behavior for ITO and Graphene which may be useful for other flexible electronic products.

6.3. *Future Work*

In this section some topics for potential future work are presented.

- In the current experimental work, the transfer process from CVD grown Graphene to a polymer substrates leads to several interfacial issues. Further research into the development of a low cost and efficient alternative fabrication method for Graphene on compliant polymer based substrates should be investigated.

- In the current experimental work, the dedicated setup could be improved to address inconsistent resistance measurements and a more robust system to attach the contacts for the four probe measurement should be development to account for delamination of the contacts during fatigue testing.

- The focus of this work has been the fatigue studies of uniform Graphene samples but patterned Graphene interconnect samples are more applicable from a device standpoint, so a methodology needs to be development to fabricate and test these samples.

- The focus of this research has been the bending fatigue properties in tension, but a flexible display could be bent or rolled so that the system is in compression. Additional FEA simulations and fatigue testing should be conducted to understand this failure mechanism and to obtain a probabilistic life model for compression.

- Additional testing of patterned ITO, uniform ITO and uniform Graphene on Si_3N_4/PEN substrates should be conducted in order to update the parameters of the IPL-Weibull model developed in this work. This would improve the reliability predication capabilities for interconnects for flexible displays.

- The current research focused on one particular mode of the gate line interconnect, but there are numerous other associated failures modes including the source lines,

the thin film transistor, the electro-optical material and the encapsulation/barrier layer. These different failure modes need to be investigated in order to have a clear picture of the entire system reliability.

Appendix A: Raman Spectroscopy

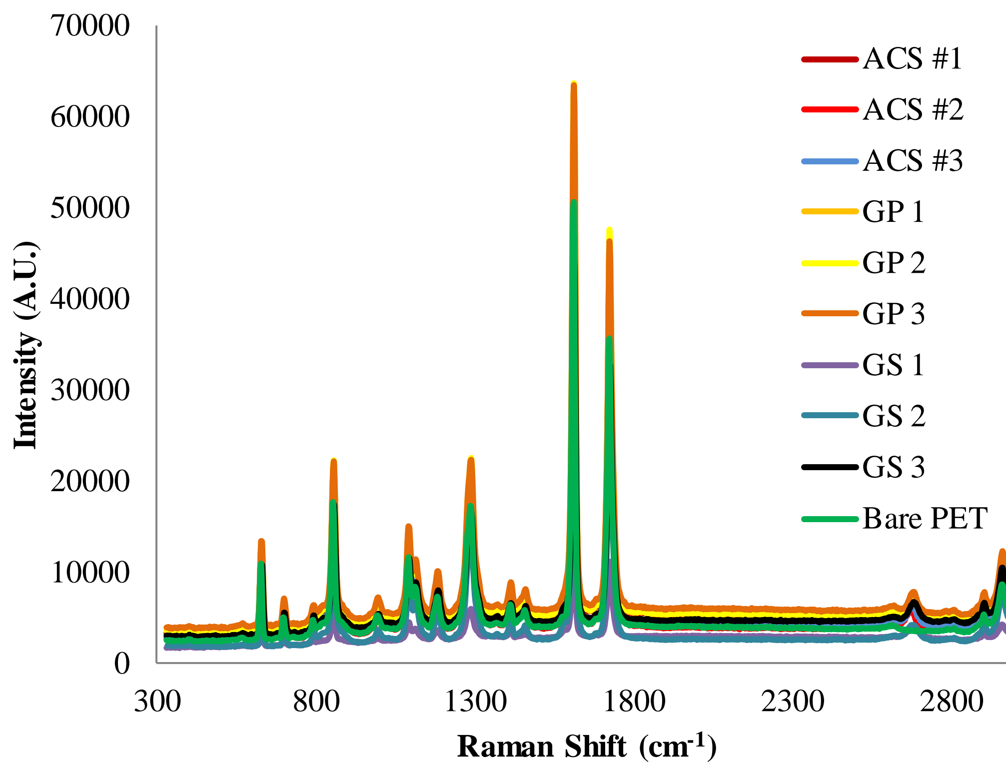

Figure A.1: Raman Spectrums for Graphene on PET for the three potential vendors (ACS Materials, Graphene Platform and Graphene Supermarket) and Bare PET

Appendix B: Atomic Force Microscopy Images

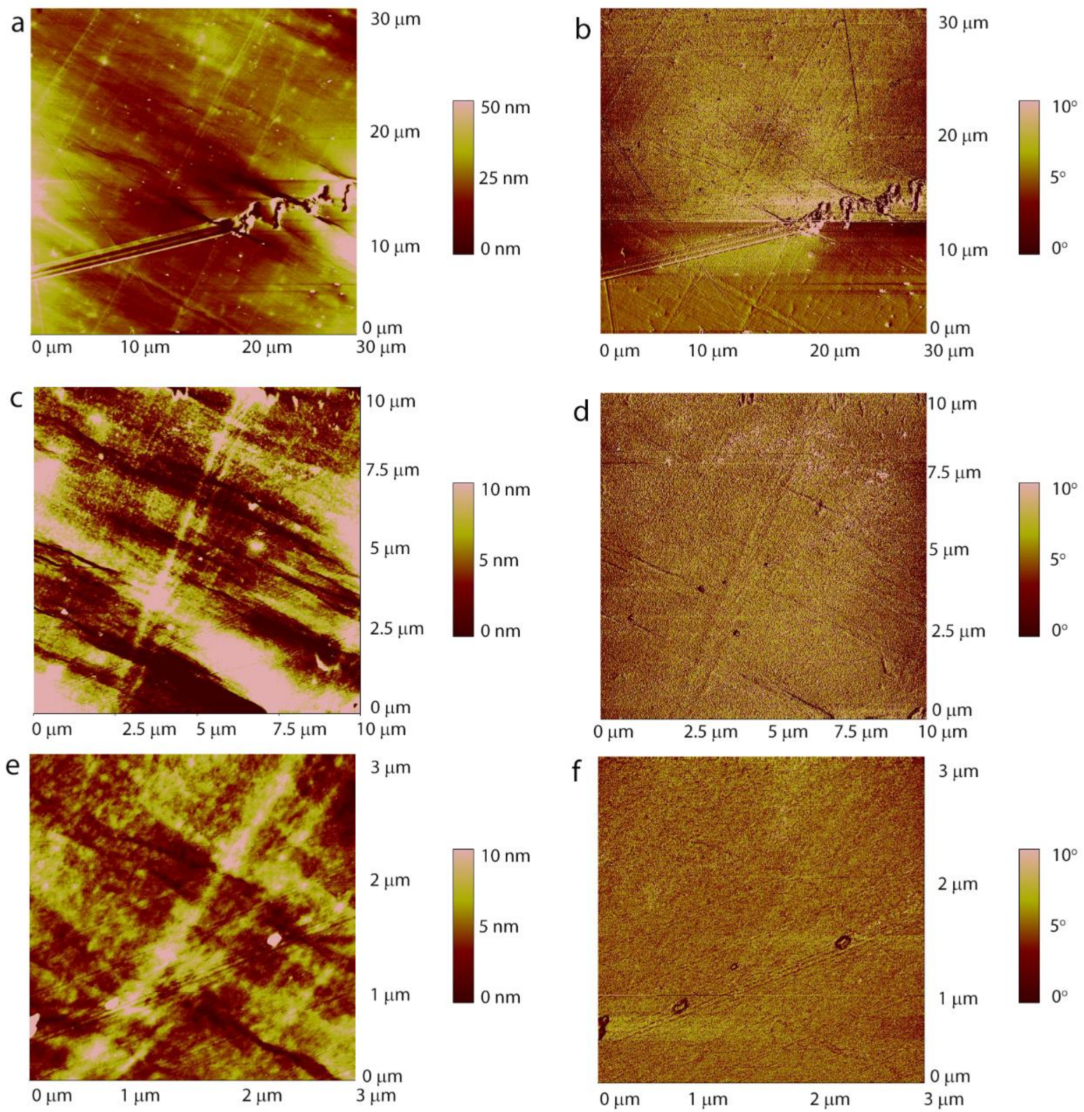

Figure B.1: Tapping mode AFM images of Bare PET a) 30 µm x 30 µm height image b) 30 µm x 30 µm phase image c) 10 µm x 10 µm height image d) 10 µm x 10 µm phase image e) 3 µm x 3 µm height image f) 3 µm x 3 µm phase image

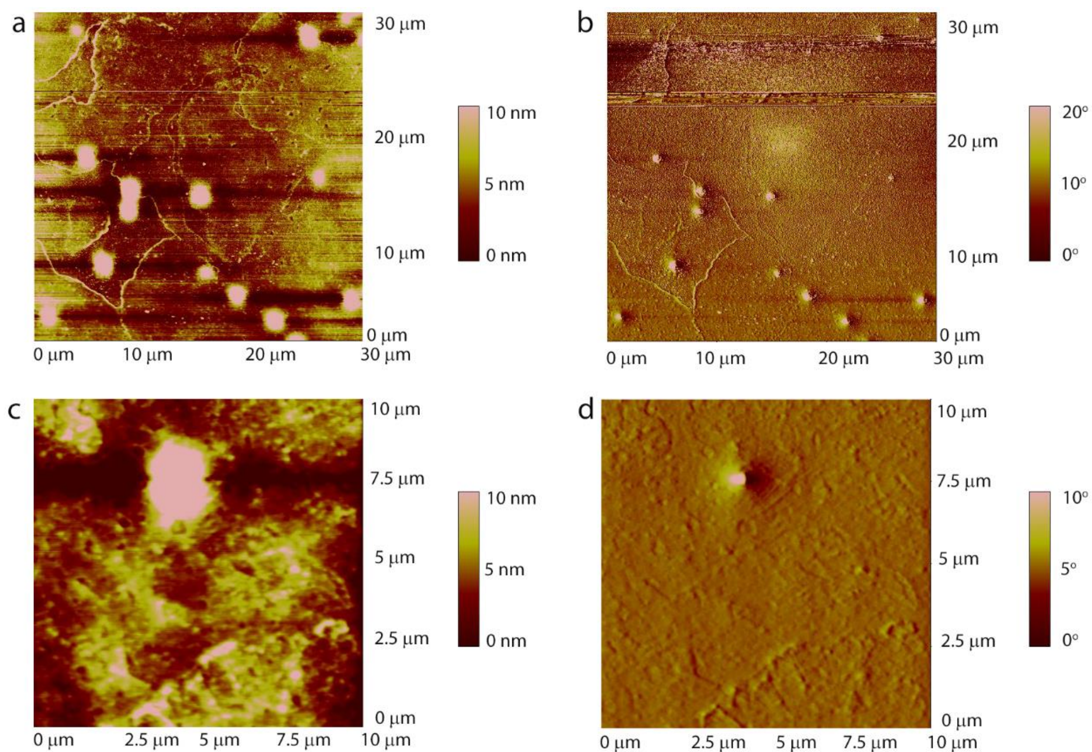

Figure B.2: Tapping mode AFM images of Bare PEN a) 30 µm x 30 µm height image b) 30 µm x 30 µm phase image c) 10 µm x 10 µm height image d) 10 µm x 10 µm phase image

c

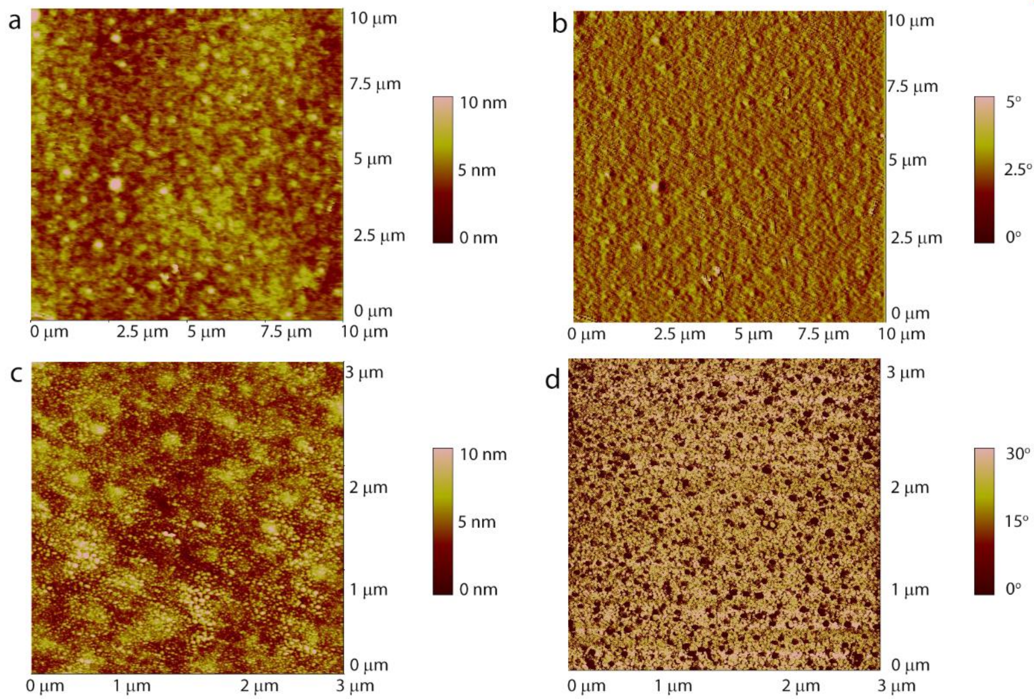

Figure B.2: Tapping mode AFM images of Si_3N_4/PEN a) 10 µm x 10 µm height image b) 10 µm x 10 µm phase image c) 3 µm x 3µm µm height image d) 3 µm x 3 µm µm phase image

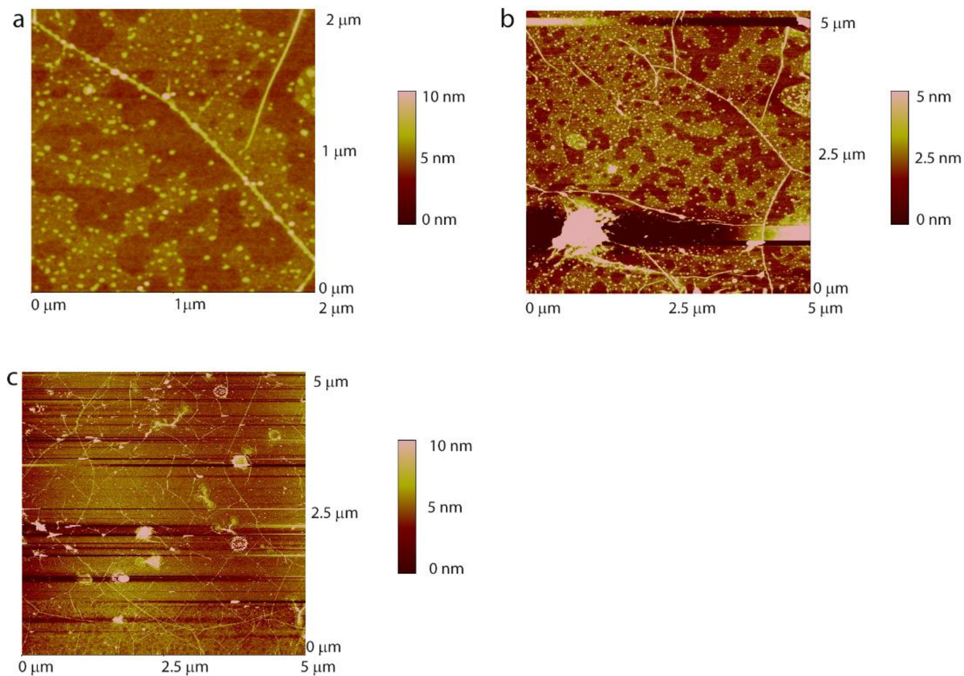

Figure B.4: Tapping mode AFM images of Graphene on SiO_2 (Graphene Square) a) 2 µm x 2 µm height image b) 5 µm x 5 µm phase image c) 5 µm x 5 µm height image

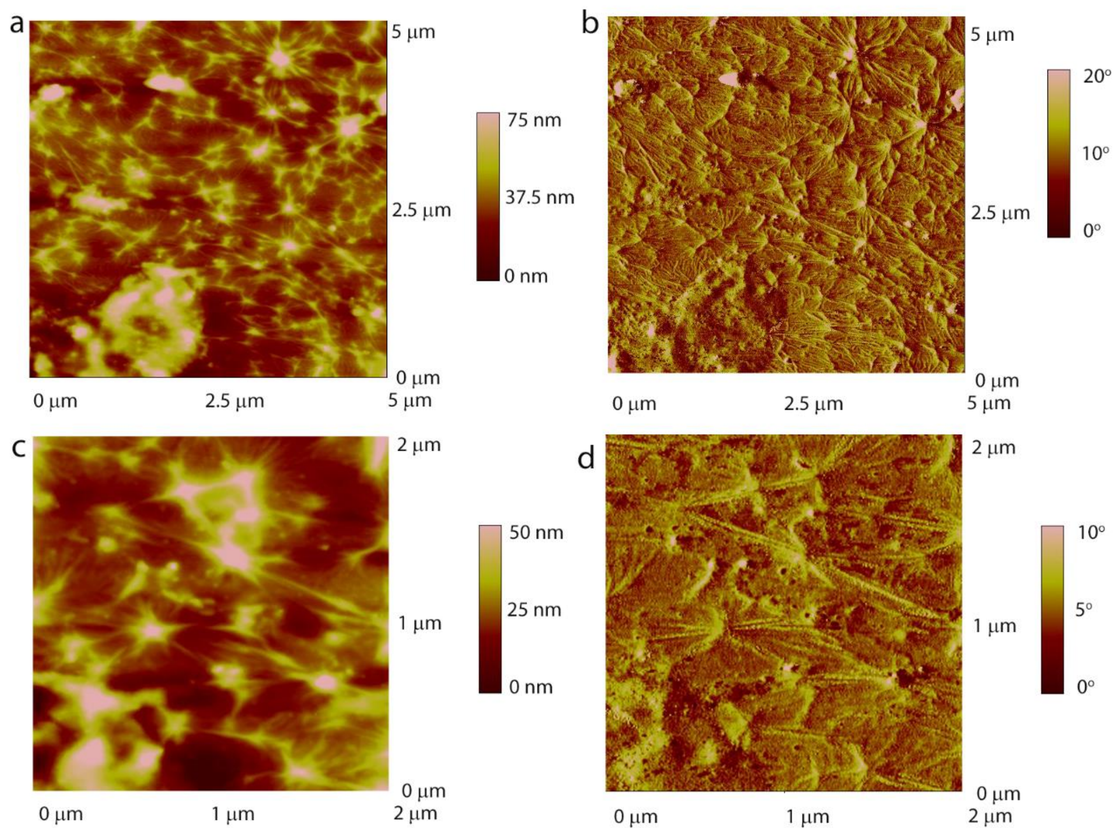

Figure B.5: Tapping mode AFM images of Graphene on PET (Graphene Platform) a) 5 µm x 5 µm height image b) 5 µm x 5 µm phase image c) 2 µm x 2 µm height image d) 2 µm x 2 µm phase image

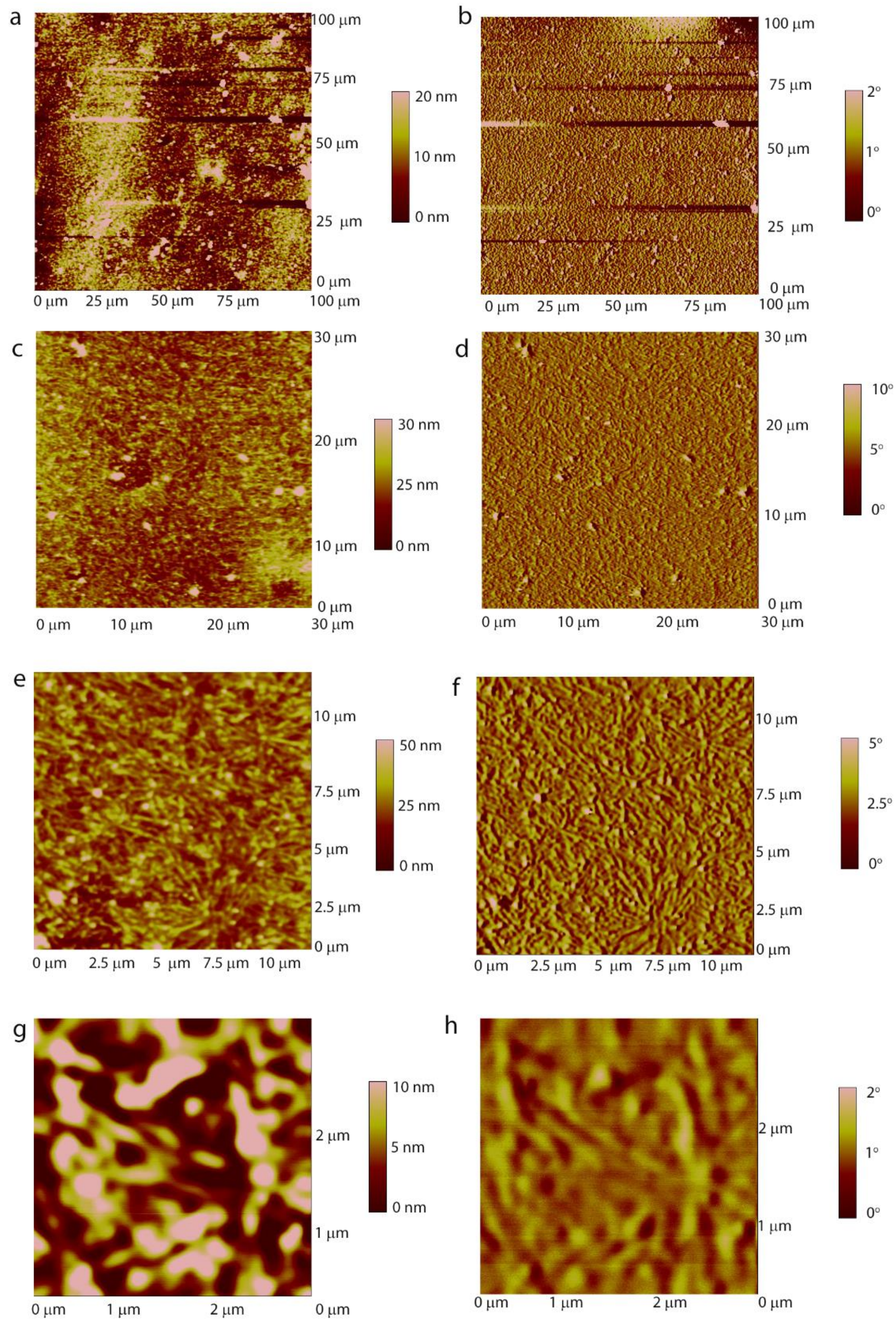

Figure B.6: Tapping mode AFM images of Graphene on PET (Graphene Platform) a) 100 µm x 100 µm height image b) 100 µm x 100 µm phase image c) 30 µm x 30 µm height image d) 30 µm x 30 µm phase image e) 11.7 µm x 11.7 µm height image f) 11.7 µm x 11.7 µm phase image g) 2.7 µm x 2.7 µm height image h) 2.7 µm x 2.7 µm phase image

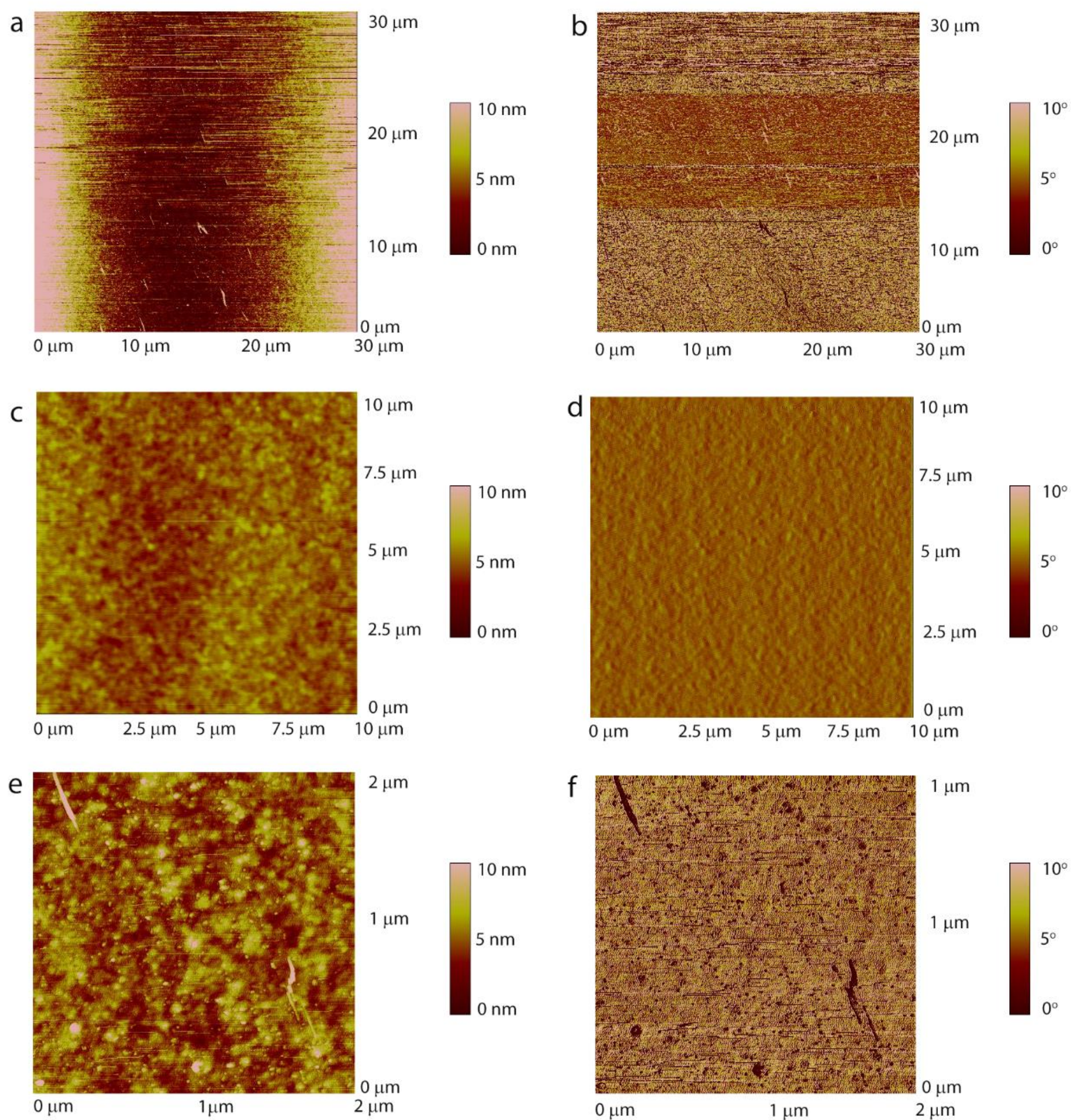

Figure B.7: Tapping mode AFM images of Graphene on PET (Graphene Platform) a) 30 µm x 30 µm height image b) 30 µm x 30 µm phase image c) 10 µm x 30 µm height image d) 10 µm x 10 µm phase image d) 2 µm x 2 µm height image 3) 2 µm x 2 µm phase image

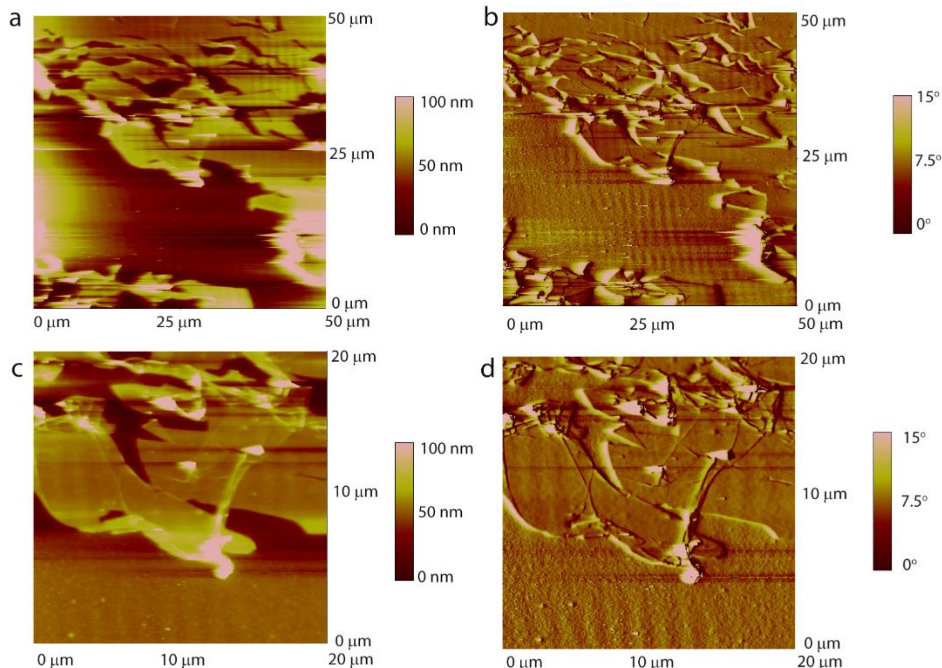

Figure B.8: Tapping mode AFM images of Graphene - Si_3N_4/PEN Interface (ACS Sample # 7) a) 50 µm x 50 µm height image b) 50 µm x 50 µm phase image c) 20 µm x 20 µm height image d) 20 µm x 20 µm phase image

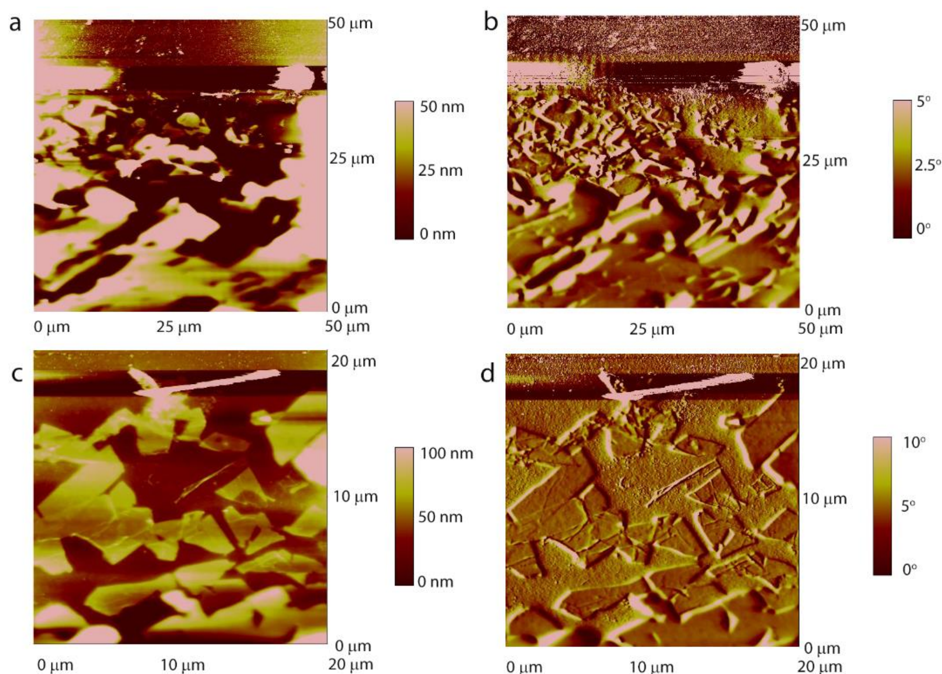

Figure B.9: Tapping mode AFM images of Graphene - Si_3N_4/PEN Interface (ACS Sample # 8) a) 50 µm x 50 µm height image b) 50 µm x 50 µm phase image c) 20 µm x 20 µm height image d) 20 µm x 20 µm phase image

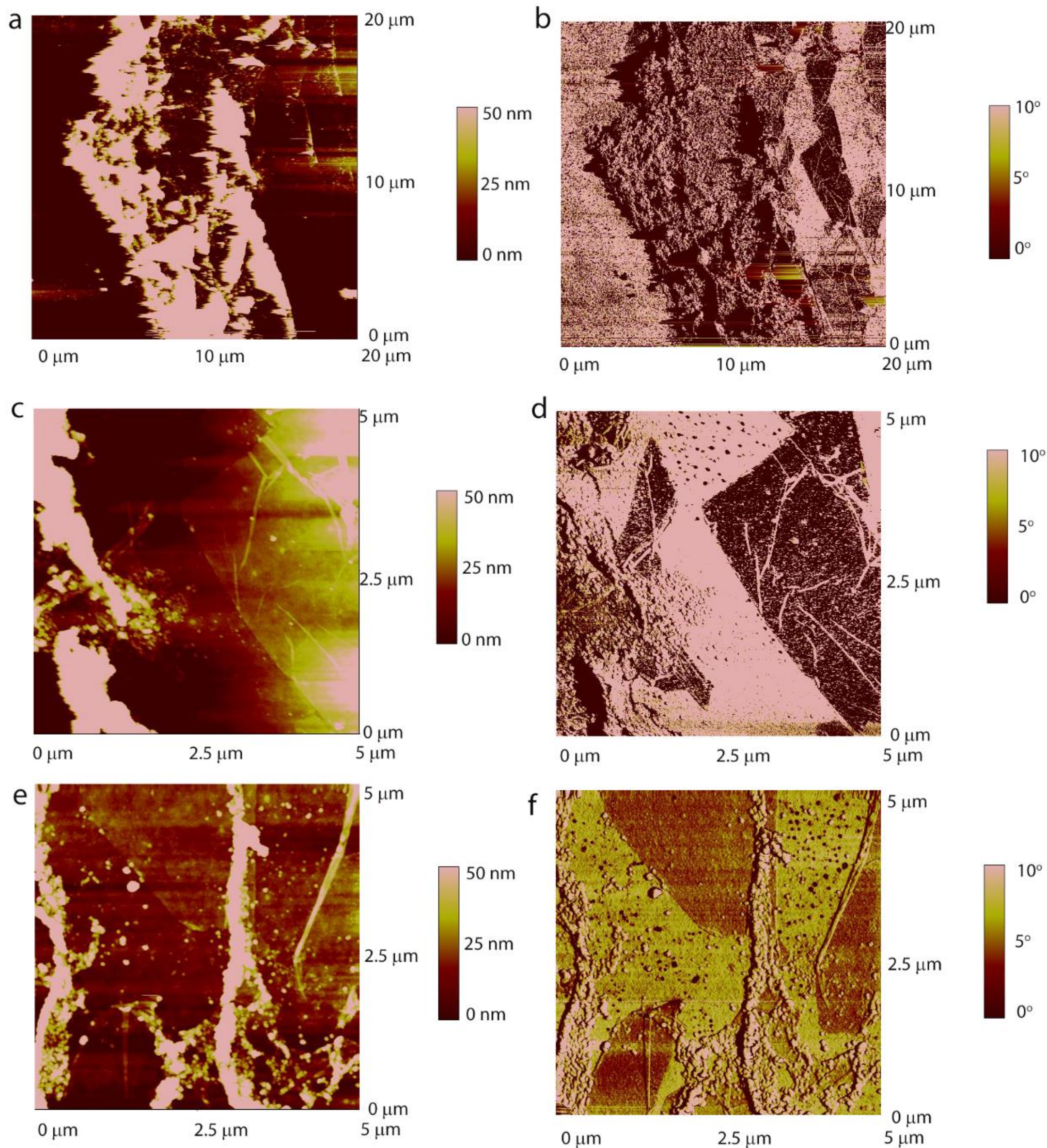

Figure B.9: Tapping mode AFM images of Graphene - Si_3N_4/PEN Interface (ACS Sample # 5) a) 20 µm x 20 µm height image b) 20 µm x 20 µm phase image c) 5 µm x 5 µm height image d) 5 µm x 5 µm phase image e) 5 µm x 5 µm height image f) 5 µm x 5 µm phase image

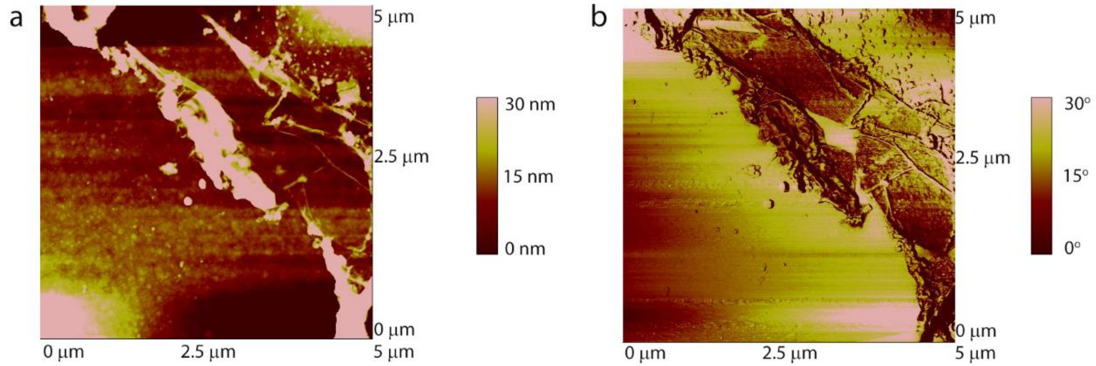

Figure B.10: Tapping mode AFM images of Graphene - Si_3N_4/PEN Interface (ACS Sample # 14) a) 5 μm x 5 μm height image b) 5 μm x 5 μm phase image

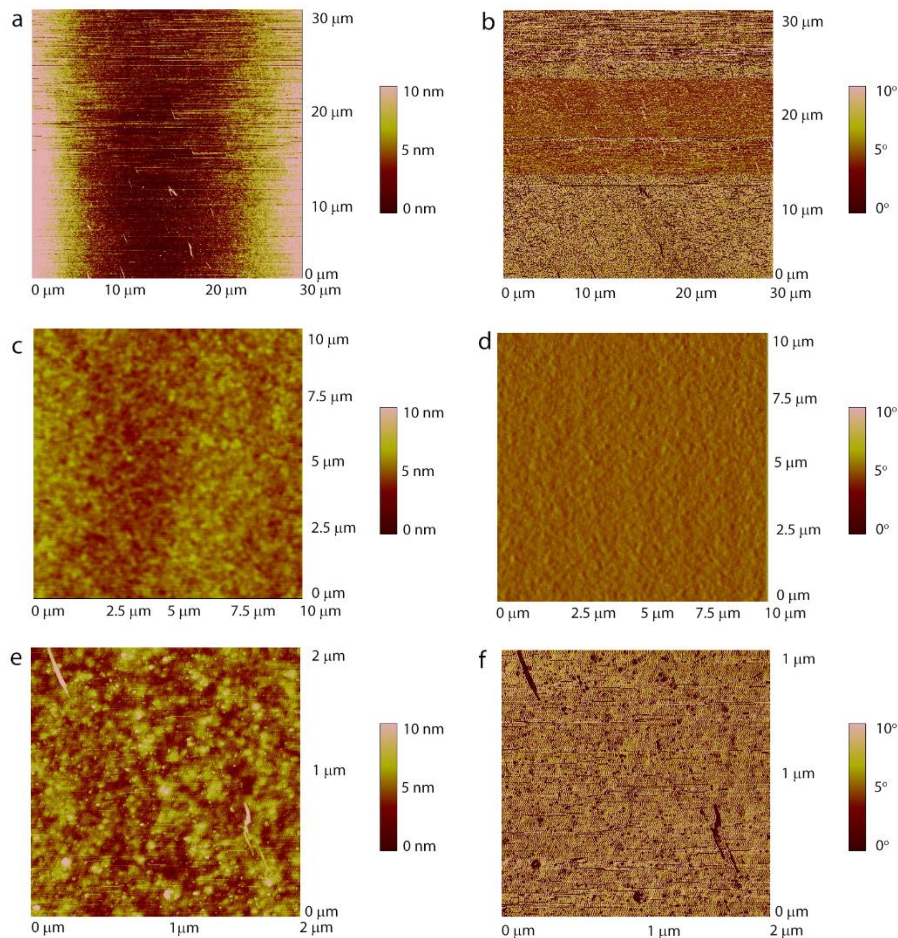

Figure B.11: Tapping mode AFM images of ITO on Si_3N_4/PEN a) 30 μm x 30 μm height image b) 30 μm x 30 μm phase image c) 10 μm x 10 μm height image d) 10 μm x 10 μm phase image e) 2 μm x 2 μm height image f) 2 μm x 2 μm phase image

Table B.1: RMS roughness measurements for surface roughness analysis of Bare PEN, Si_3N_4/PEN, ITO/Si_3N_4/PEN and Graphene/Si_3N_4/PEN

Point #	Bare PEN	Si_3N_4 PEN	ITO Si_3N_4 PEN	Graphene Si_3N_4 PEN (Blue Box)	Graphene Si_3N_4 PEN (Red Box)
1	3.064	2.518	1.14	0.375	2.51
2	5.604	1.132	1.28	0.418	0.721
3	5.438	1.953	0.95	0.703	1.947
4	1.858	2.381	0.688	0.484	4.089

Appendix C: Stoney's Equation and ANSYS

Table C.1: Effect of Graphene layer thickness on bending stress generated in Graphene layer using Stoney's equation for mandrel diameters ranging from 1.58 to 12.7 mm

Graphene Layer Thickness (nm)	Bending stress (GPa) generated in Graphene layer for mandrel diameter of (mm)						
	1.5874	3.174	4.762	6.35	7.938	9.526	12.7
0.34	2665	1333	888	666	533	444	333
0.68	1332	666	444	333	266	222	167
1.02	888	444	296	222	178	148	111
1.36	666	333	222	167	133	111	83
1.7	533	267	178	133	107	89	67
2.04	444	222	148	111	89	74	56
2.38	381	190	127	95	76	63	48
2.72	333	167	111	83	67	56	42
3.06	296	148	99	74	59	49	37
3.4	266	133	89	67	53	44	33
10	91	45	30	23	18	15	11
50	18	9	6	5	4	3	2
100	9	5	3	2	2	2	1

Table C.2: Effect of PET layer thickness on bending stress generated in Graphene layer using Stoney's equation for mandrel diameters ranging from 1.58 to 12.7 mm

PET Layer thickness (nm)	Bending stress (GPa) generated in Graphene layer for mandrel diameter of (mm)						
	1.5874	3.174	4.762	6.35	7.938	9.526	12.7
50	426	213	142	107	85	71	53
75	959	480	320	240	192	160	120
100	1705	853	568	426	341	284	213
125	2665	1333	888	666	533	444	333
150	3837	1919	1279	959	767	639	480
175	5223	2612	1741	1306	1044	870	653
200	6821	3412	2274	1705	1364	1137	853
225	8633	4318	2878	2158	1726	1439	1079
250	10658	5331	3553	2664	2131	1776	1332
275	12897	6450	4299	3224	2579	2149	1612
300	15348	7676	5116	3837	3069	2558	1918
325	18013	9009	6004	4503	3602	3002	2251
350	20890	10448	6964	5222	4178	3481	2611

Table C.3: Effect of ITO layer thickness on bending stress generated in ITO layer using Stoney's equation for mandrel diameters ranging from 1.58 to 12.7 mm

ITO Layer Thickness (nm)	Bending stress (GPa) generated in ITO layer for mandrel diameter of (mm)						
	1.5874	3.174	4.762	6.35	7.938	9.526	12.7
10	90.60	45.31	30.20	22.65	18.12	15.10	11.32
25	36.24	18.12	12.08	9.06	7.25	6.04	4.53
50	18.12	9.06	6.04	4.53	3.62	3.02	2.26
75	12.08	6.04	4.03	3.02	2.42	2.01	1.51
100	9.06	4.53	3.02	2.26	1.81	1.51	1.13
125	7.25	3.62	2.42	1.81	1.45	1.21	0.91
150	6.04	3.02	2.01	1.51	1.21	1.01	0.75
175	5.18	2.59	1.73	1.29	1.04	0.86	0.65
200	4.53	2.27	1.51	1.13	0.91	0.75	0.57
300	3.02	1.51	1.01	0.75	0.60	0.50	0.38
400	2.26	1.13	0.75	0.57	0.45	0.38	0.28
500	1.81	0.91	0.60	0.45	0.36	0.30	0.23

Table C.4: Effect of PET layer thickness on bending stress generated in ITO layer using Stoney's equation for mandrel diameters ranging from 1.58 to 12.7 mm

PET Layer thickness (nm)	Bending stress (GPa) generated in ITO layer for mandrel diameter of (mm)						
	1.5874	3.174	4.762	6.35	7.938	9.526	12.7
50	2.90	1.45	0.97	0.72	0.58	0.48	0.36
75	6.52	3.26	2.17	1.63	1.30	1.09	0.82
100	11.60	5.80	3.87	2.90	2.32	1.93	1.45
125	18.12	9.06	6.04	4.53	3.62	3.02	2.26
150	26.09	13.05	8.70	6.52	5.22	4.35	3.26
175	35.51	17.76	11.84	8.88	7.10	5.92	4.44
200	46.39	23.20	15.46	11.60	9.28	7.73	5.80
225	58.71	29.36	19.57	14.68	11.74	9.78	7.34
250	72.48	36.25	24.16	18.12	14.49	12.08	9.06
275	87.70	43.86	29.23	21.92	17.54	14.61	10.96
300	104.37	52.20	34.79	26.09	20.87	17.39	13.05
325	122.49	61.26	40.83	30.62	24.49	20.41	15.31
350	142.05	71.05	47.35	35.51	28.41	23.67	17.76

Table C.5: Effect of Graphene layer thickness on bending stress generated in Graphene layer using ANSYS for mandrel diameters ranging from 1.58 to 12.7 mm

Graphene Layer Thickness (nm)	Bending stress (GPa) generated in Graphene layer for shaft diameter of (mm)						
	1.5874	3.174	4.762	6.35	7.938	9.526	12.7
0.34	65	39.8	27.7	20.9	-	-	-
0.68	64.8	39.7	27.7	20.1	15.9	13.5	10.1
1.02	64.7	39.6	27.6	20	15.9	13.4	10
1.36	64.5	39.6	27.6	20	15.9	13.4	10
1.7	64.3	39.6	27.5	20	15.9	13.4	10
2.04	64.2	39.6	27.5	20	15.8	13.3	9.9
2.38	64	39.5	27.5	20	15.8	13.3	9.9
2.72	63.9	39.5	27.5	20	15.8	13.3	9.9
3.06	63.7	39.5	27.5	20	15.8	13.3	9.9
3.4	63.6	39.4	27.5	20	15.8	13.2	9.9
10	60.9	38.6	26.9	19.2	15.2	12.7	9.5
50	48.5	34.7	24	15.4	12.3	10.1	7.6
100	38.3	28.5	21	12.3	9.8	8.1	6

Table C.6: Effect of Graphene layer thickness on bending stress generated in PET layer using ANSYS for mandrel diameters ranging from 1.58 to 12.7 mm

Graphene Layer Thickness (nm)	Bending stress (GPa) generated in PEN layer for shaft diameter of (mm)						
	1.5874	3.174	4.762	6.35	7.938	9.526	12.7
0.34	247	151	108	79.6	-	-	-
0.68	246	151	105	76.2	60.4	51.2	38.3
1.02	246	151	108	76.2	60.3	51.1	38
1.36	245	151	105	76.1	60.3	51.1	38
1.7	245	150	105	76.1	60.3	50.8	37.9
2.04	244	150	105	76	60.2	50.7	37.8
2.38	243	150	105	76	60.2	50.6	37.7
2.72	243	150	104	75.9	60.1	50.5	37.6
3.06	242	150	104	75.9	60.1	50.4	37.5
3.4	242	150	104	75.8	60	50.3	37.5
10	232	147	102	73.2	57.9	48.3	36
50	186	132	91.6	58.8	46.8	38.7	28.9
100	147	109	80.1	46.9	37.3	30.8	23

Table C.7: Effect of ITO trace thickness on bending stress generated in ITO, Si_3N_4, PTS-R9 and PET layers using ANSYS for mandrel diameters ranging from 1.58 to 8 mm for ITO trace thicknesses of 0.05, 0.01 and 0.1 µm respectively

ITO Trace Thickness	Mandrel Diameter (mm)	Bending Stress (MPa) generated in			
		Middle ITO Strip	Si_3N_4	PTS-R9	PET
0.05 µm	1.59	9449	9228	190.88	285.51
	2.38	6705.2	6547.3	135.41	202.47
	3.97	4063.1	3968.4	82.073	122.66
	4.76	3371.1	3291.2	68.072	101.75
	5.56	2795.2	2727.3	56.409	84.336
	6.35	2517.3	2454.9	50.783	75.936
	7.14	2240.4	2183.8	45.177	67.566
	7.94	1999.3	1948	40.3	60.279

ITO Trace Thickness	Mandrel Diameter (mm)	Bending Stress (MPa) generated in			
		Middle ITO Strip	Si_3N_4	PTS-R9	PET
0.01 µm	1.5875	9446.9	9225.8	190.83	285.66
	2.38125	6778.6	6618.7	136.91	204.88
	3.96875	4103	4006.7	82.879	123.97
	4.7625	3399	3317.4	68.627	102.67
	5.55625	2904.5	2833.4	58.618	87.71
	6.35	2538.4	2474.8	51.203	76.634
	7.9375	2014.2	1961.8	40.594	60.772

ITO Trace Thickness	Mandrel Diameter (mm)	Bending Stress (MPa) generated in			
		Middle ITO Strip	Si_3N_4	PTS-R9	PET
0.1 µm	1.59	9103.7	8890.8	183.82	274.69
	2.38	6595.5	6440.1	1331.6	198.93
	3.97	3871.8	3781.9	78.188	116.74
	4.76	3335.6	3257.4	67.357	100.57
	5.56	2763.2	2696.3	55.756	83.285
	6.35	2422	2362.6	48.858	72.985
	7.14	2144.7	2091.2	43.248	64.613
	7.94	1980.5	1930.3	39.924	59.652

Appendix D: Fatigue Simulations and Results

Table D.1: Change in normalized resistance vs. Number of cycles for patterned ITO Samples on Si_3N_4/PEN

Number of Cycles	Resistance (kΩ)	Change in Normalized Resistance, $\Delta R/R_o$
89	221.38983	0.00%
105	221.76272	0.17%
177	221.76272	0.17%
209	221.66102	0.12%
427	221.59322	0.09%
523	221.55933	0.08%
724	221.69492	0.14%
1336	221.59322	0.09%
1537	221.49153	0.05%
1714	221.66102	0.12%
1924	221.59322	0.09%
3501	221.69492	0.14%
3517	224.03389	1.19%
3525	225.96611	2.07%
3525	228.50847	3.22%
3533	229.8644	3.83%

Table D.2: Simulations of effect of mandrel radius on the fatigue life of Patterned ITO Samples

Number of Cycles	R = 3.18 mm, 2.54 GPa	R = 4.76 mm, 1.66 GPa	R = 6.35 mm, 1.22 GPa
1	0.00	0.00	0.00
10	0.01	0.01	0.01
20	0.01	0.01	0.01
50	0.01	0.01	0.01
100	0.01	0.01	0.01
200	0.01	0.01	0.05
300	0.01	0.01	0.06
400	0.01	0.01	0.07
500	0.01	0.01	0.08
600	0.01	0.01	0.09
700	0.01	0.01	0.10
800	0.01	0.01	0.20
900	0.01	0.01	0.30
1000	0.01	0.01	0.40
1100	0.01	0.07	0.50
1200	0.01	0.14	0.60
1300	0.01	0.21	0.70
1400	0.01	0.28	0.80
1500	0.04	0.35	0.90
1600	0.07	0.42	1.00
1700	0.11	0.49	1.10
1800	0.14	0.56	1.20
1900	0.18	0.63	1.30
2000	0.21	0.70	1.40
2100	0.25	0.77	1.50
2200	0.28	0.84	1.60
2300	0.32	0.91	1.70
2400	0.35	0.98	1.80
2500	0.39	1.05	1.90
2600	0.42	1.12	2.00
2700	0.46	1.19	2.10
2800	0.49	1.26	2.20
2900	0.53	1.33	2.30
3000	0.56	1.40	2.40

Table D.2: (Cont) Simulations of effect of mandrel radius on the fatigue life of Patterned ITO Samples

Number of Cycles	R = 3.18 mm, 2.54 GPa	R = 4.76 mm, 1.66 GPa	R = 6.35 mm, 1.22 GPa
3100	0.60	1.47	2.50
3200	0.63	1.54	2.60
3300	0.67	1.61	2.70
3400	0.70	1.68	2.80
3500	0.74	1.75	2.90
3600	0.77	1.82	3.00
3700	0.81	1.89	3.30
3800	0.84	1.96	3.63
3900	0.88	2.03	3.99
4000	0.91	2.10	4.39
4100	0.95	2.17	4.83
4200	0.98	2.24	5.31
4300	1.02	2.31	5.85
4400	1.05	2.38	6.43
4500	1.09	2.45	7.07
4600	1.12	2.52	7.78
4700	1.16	2.59	8.56
4800	1.19	2.66	9.42
4900	1.23	2.73	10.36
5000	1.26	2.80	11.39
5100	1.30	2.87	12.53
5200	1.33	2.94	13.78
5300	1.37	3.01	15.16
5400	1.40	3.31	16.68
5500	1.44	3.15	18.35
5600	1.47	3.22	20.18
5700	1.51	3.29	22.20
5800	1.54	3.36	24.42
5900	1.58	3.43	26.86
6000	1.61	3.50	29.55
6100	1.65	3.57	32.50
6200	1.68	3.64	35.75
6300	1.72	3.71	39.33
6400	1.75	3.78	42.00

Table D.2: (Cont) Simulations of effect of mandrel radius on the fatigue life of Patterned ITO Samples

Number of Cycles	R = 3.18 mm, 2.54 GPa	R = 4.76 mm, 1.66 GPa	R = 6.35 mm, 1.22 GPa
6500	1.79	3.85	50.00
6600	1.82	3.92	65.00
6700	1.86	3.99	87.00
6800	1.89	4.06	
6900	1.93	4.13	
7000	1.96	4.20	
7100	2.00	4.27	
7200	2.03	4.34	
7300	2.07	4.41	
7400	2.10	4.48	
7500	2.14	4.55	
7600	2.17	4.62	
7700	2.21	4.69	
7800	2.24	4.76	
7900	2.28	4.83	
8000	2.31	4.90	
8100	2.35	4.97	
8200	2.38	5.04	
8300	2.42	5.11	
8400	2.45	5.18	
8500	2.49	5.25	
8600	2.52	5.32	
8700	2.56	5.39	
8800	2.59	5.46	
8900	2.63	5.53	
9000	2.66	5.60	
9100	2.70	5.67	
9200	2.73	5.74	
9300	2.77	5.81	
9400	2.80	5.88	
9500	2.84	5.95	
9600	2.87	6.02	
9700	2.91	6.09	
9800	2.94	6.16	
9900	2.98	6.23	
10000	3.01	6.42	
10100	3.05	6.61	

Table D.2: (Cont) Simulations of effect of mandrel radius on the fatigue life of Patterned ITO Samples

Number of Cycles	R = 3.18 mm, 2.54 GPa	R = 4.76 mm, 1.66 GPa	R = 6.35 mm, 1.22 GPa
10200	3.08	6.81	
10300	3.12	7.01	
10400	3.15	7.22	
10500	3.19	7.44	
10600	3.22	7.66	
10700	3.26	7.89	
10800	3.29	8.13	
10900	3.33	8.37	
11000	3.36	8.71	
11100	3.40	9.06	
11200	3.43	9.42	
11300	3.47	9.79	
11400	3.50	10.19	
11500	3.54	10.59	
11600	3.57	11.02	
11700	3.61	11.46	
11800	3.64	11.92	
11900	3.68	12.39	
12000	3.71	12.89	
12100	3.75	13.53	
12200	3.78	14.21	
12300	3.82	14.92	
12400	3.85	15.67	
12500	3.89	16.45	
12600	3.92	17.27	
12700	3.96	18.14	
12800	3.99	19.04	
12900	4.03	20.00	
13000	4.06	21.00	
13100	4.10	22.04	
13200	4.13	23.15	
13300	4.17	24.30	
13400	4.20	26.25	
13500	4.24	28.35	
13600	4.27	30.62	
13700	4.31	33.07	
13800	4.34	35.71	

Table D.2: (Cont) Simulations of effect of mandrel radius on the fatigue life of Patterned ITO Samples

Number of Cycles	R = 3.18 mm, 2.54 GPa	R = 4.76 mm, 1.66 GPa	R = 6.35 mm, 1.22 GPa
14000	4.41	41.65	
14100	4.45	46.24	
14200	4.48	51.32	
14300	4.52	55.43	
14400	4.55	61.52	
14500	4.59	68.29	
14600	4.62	75.80	
14700	4.66	83.38	
14800	4.69		
14900	4.73		
15000	4.76		
15100	4.80		
15200	4.83		
15300	4.87		
15400	4.90		
15500	4.94		
15600	4.97		
15700	5.01		
15800	5.04		
15900	5.08		
16000	5.11		
16100	5.15		
16200	5.18		
16300	5.22		
16400	5.25		
16500	5.29		
16600	5.32		
16700	5.36		
16800	5.39		
16900	5.43		
17000	5.46		
17100	5.50		
17200	5.53		
17300	5.57		
17400	5.60		
17500	5.64		
17600	5.67		

Table D.2: (Cont) Simulations of effect of mandrel radius on the fatigue life of Patterned ITO Samples

Number of Cycles	R = 3.18 mm, 2.54 GPa	R = 4.76 mm, 1.66 GPa	R = 6.35 mm, 1.22 GPa
17700	5.71		
17800	5.74		
17900	5.78		
18000	5.81		
18100	5.85		
18200	5.88		
18300	5.92		
18400	5.95		
18500	5.99		
18600	6.02		
18700	6.06		
18800	6.09		
18900	6.13		
19000	6.16		
19100	6.20		
19200	6.23		
19300	6.27		
19400	6.30		
19500	6.34		
19600	6.37		
19700	6.41		
19800	6.44		
19900	6.48		
20000	6.51		
20100	6.55		
20200	6.58		
20300	6.62		
20400	6.65		
20500	6.69		
20600	6.72		
20700	6.76		
20800	6.79		
20900	6.83		
21000	6.86		
21100	6.90		
21200	6.93		
21300	6.97		

Table D.2: (Cont) Simulations of effect of mandrel radius on the fatigue life of Patterned ITO Samples

Number of Cycles	R = 3.18 mm, 2.54 GPa	R = 4.76 mm, 1.66 GPa	R = 6.35 mm, 1.22 GPa
21400	7.00		
21500	7.04		
21600	7.07		
21700	7.11		
21800	7.14		
21900	7.18		
22000	7.32		
22100	7.46		
22200	7.61		
22300	7.77		
22400	7.92		
22500	8.08		
22600	8.24		
22700	8.41		
22800	8.57		
22900	8.75		
23000	8.92		
23100	9.10		
23200	9.28		
23300	9.47		
23400	9.66		
23500	9.85		
23500	9.85		
23600	10.05		
23700	10.25		
23800	10.45		
23900	10.77		
24000	11.09		
24100	11.42		
24200	11.76		
24300	12.12		
24400	12.48		
24500	12.86		
24600	13.24		
24700	13.64		
24800	14.05		
24900	14.47		

Table D.2: (Cont) Simulations of effect of mandrel radius on the fatigue life of Patterned ITO Samples

Number of Cycles	R = 3.18 mm, 2.54 GPa	R = 4.76 mm, 1.66 GPa	R = 6.35 mm, 1.22 GPa
25000	14.90		
25100	15.35		
25200	15.81		
25300	16.28		
25400	16.77		
25500	17.28		
25600	17.97		
25700	18.69		
25800	19.43		
25900	20.21		
26000	21.02		
26100	21.86		
26200	22.73		
26300	23.64		
26400	24.59		
26500	25.57		
26600	26.60		
26700	27.66		
26900	29.92		
27000	31.11		
27100	32.67		
27200	34.30		
27300	36.02		
27400	37.82		
27500	39.71		
27600	41.70		
27700	43.78		
27800	45.97		
27900	48.27		
28000	50.68		
28100	53.22		
28200	55.88		
28300	58.67		
28400	61.60		
28500	64.68		
28600	67.92		
28700	71.31		

Table D.2: (Cont) Simulations of effect of mandrel radius on the fatigue life of Patterned ITO Samples

Number of Cycles	R = 3.18 mm, 2.54 GPa	R = 4.76 mm, 1.66 GPa	R = 6.35 mm, 1.22 GPa
28800	74.88		
28900	78.62		
29000	82.56		
29100	86.68		

Table D.3: Simulations of effect of trace width on fatigue life of Patterned ITO Samples

Number of Cycles	0.5 μm	0.75 μm	1.5 μm
1	0.00	0.00	0.00
10	0.01	0.01	0.01
20	0.01	0.01	0.01
50	0.01	0.01	0.01
100	0.01	0.01	0.01
200	0.01	0.01	0.05
300	0.01	0.01	0.06
400	0.01	0.01	0.07
500	0.01	0.01	0.08
600	0.01	0.01	0.09
700	0.01	0.01	0.10
800	0.01	0.01	0.20
900	0.01	0.01	0.30
1000	0.01	0.01	0.40
1100	0.01	0.07	0.50
1200	0.01	0.14	0.60
1300	0.01	0.21	0.70
1400	0.01	0.28	0.80
1500	0.04	0.35	0.90
1600	0.07	0.42	1.00
1700	0.11	0.49	1.10
1800	0.14	0.56	1.20
1900	0.18	0.63	1.30
2000	0.21	0.70	1.40
2100	0.25	0.77	1.50
2200	0.28	0.84	1.60

Number of Cycles	0.5 μm	0.75 μm	1.5 μm
2300	0.32	0.91	1.70
2400	0.35	0.98	1.80
2500	0.39	1.05	1.90
2600	0.42	1.12	2.00
2700	0.46	1.19	2.10
2800	0.49	1.26	2.20
2900	0.53	1.33	2.30
3000	0.56	1.40	2.40
3100	0.60	1.47	2.50
3200	0.63	1.54	2.60
3300	0.67	1.61	2.70
3400	0.70	1.68	2.80
3500	0.74	1.76	2.90
3600	0.77	1.85	3.00
3700	0.81	1.94	3.30
3800	0.84	2.04	3.63
3900	0.88	2.14	3.99
4000	0.91	2.25	4.39
4100	0.95	2.36	4.83
4200	0.98	2.48	5.31
4300	1.02	2.61	5.85
4400	1.05	2.79	6.43
4500	1.09	2.98	7.07
4600	1.12	3.19	7.78
4700	1.16	3.42	8.56
4800	1.19	3.66	9.42

Table D.3: Simulations of effect of trace width on fatigue life of Patterned ITO Samples

Number of Cycles	0.5 µm	0.75 µm	1.5 µm
4900	1.23	3.91	10.36
5000	1.26	4.19	11.39
5100	1.30	4.48	12.53
5200	1.33	4.79	13.78
5300	1.37	5.13	15.16
5400	1.40	5.49	16.68
5500	1.44	5.87	18.35
5600	1.47	6.28	20.18
5700	1.51	6.72	22.20
5800	1.54	7.19	24.42
5900	1.58	7.69	26.86
6000	1.61	8.23	29.55
6100	1.65	8.81	32.50
6200	1.68	9.43	35.75
6300	1.72	10.09	39.33
6400	1.75	10.79	42.00
6500	1.79	11.76	50.00
6600	1.91	12.82	65.00
6700	2.04	13.97	87.00
6800	2.19	15.23	
6900	2.34	16.60	
7000	2.50	18.10	
7100	2.68	19.73	
7200	2.87	21.50	
7300	3.07	23.44	
7400	3.28	25.55	
7500	3.51	27.85	
7600	3.76	30.63	
7700	4.02	33.69	
7800	4.30	37.06	
7900	4.60	46.33	
8000	5.02	60.23	
8100	5.47	87.33	
8200	5.96		
8300	6.50		
8400	7.08		
8500	7.72		
8600	8.41		
8700	9.17		
8800	10.00		
8900	10.90		
9000	11.88		
9100	13.06		
9200	14.37		
9300	15.81		
9400	19.76		
9500	25.69		
9600	37.25		
9700	40.97		
9800	51.22		
9900	66.58		
10000	96.54		

Table D.4: Simulations of effect of mandrel radius and trace width on fatigue life of Patterned ITO Samples

Trace Number	Trace Width (μm)	Cycles to Failure for R = 3.18 mm	Cycles to Failure for R = 4.76 mm	Cycles to Failure for R = 6.35 mm
1	0.5	45,220	22,150	10,180
2	0.5	40,780	27,650	12,980
3	0.5	38,950	22,430	14,550
4	0.5	32,660	21,910	6,010
5	0.5	58,420	24,510	5,060
6	0.5	55,050	30,470	9,880
7	0.5	33,090	18,790	7,560
8	0.5	31,970	12,960	15,690
9	0.5	55,140	18,010	11,910
10	0.5	42,350	19,720	8,720
11	0.75	36,180	17,720	8,140
12	0.75	32,620	22,120	10,380
13	0.75	31,160	17,940	11,640
14	0.75	26,130	17,530	4,810
15	0.75	46,740	19,610	4,050
16	0.75	44,040	24,380	7,900
17	0.75	26,470	15,030	6,050
18	0.75	25,580	10,370	12,550
19	0.75	44,110	14,410	9,530
20	0.75	33,880	15,780	6,980
21	1.5	28,940	14,180	6,520
22	1.5	26,100	17,700	8,310
23	1.5	24,930	14,360	9,310
24	1.5	20,900	14,020	3,850
25	1.5	37,390	15,690	3,240
26	1.5	35,230	19,500	6,320
27	1.5	21,180	12,030	4,840
28	1.5	20,460	8,290	10,040
29	1.5	35,290	11,530	7,620
30	1.5	27,100	12,620	5,580

Table D.5: Fatigue data for patterned ITO Samples on Si_3N_4/PEN with trace widths of 0.5, 0.75 and 1.5 µm respectively under stress amplitudes of 500, 1000 and 2000 MPa respectively

0.5 µm		0.75 µm		1.5 µm	
State End Time (hr)	Stress (MPa)	State End Time (hr)	Stress (MPa)	State End Time (hr)	Stress (MPa)
31.97	500	25.58	500	20.46	500
32.66	500	26.13	500	20.9	500
33.09	500	26.47	500	21.18	500
38.95	500	31.16	500	24.93	500
40.78	500	32.62	500	26.1	500
42.35	500	33.88	500	27.1	500
45.22	500	36.18	500	28.94	500
55.05	500	44.04	500	35.23	500
55.14	500	44.11	500	35.29	500
58.42	500	46.74	500	37.39	500
12.96	1000	10.37	1000	8.29	1000
18.01	1000	14.41	1000	11.53	1000
18.79	1000	15.03	1000	12.03	1000
19.72	1000	15.78	1000	12.62	1000
21.91	1000	17.53	1000	14.02	1000
22.15	1000	17.72	1000	14.18	1000
22.43	1000	17.94	1000	14.36	1000
24.51	1000	19.61	1000	15.69	1000
27.65	1000	22.12	1000	17.7	1000
30.47	1000	24.38	1000	19.5	1000
5.06	2000	4.05	2000	3.24	2000
6.01	2000	4.81	2000	3.85	2000
7.56	2000	6.05	2000	4.84	2000
8.72	2000	6.98	2000	5.58	2000
9.88	2000	7.9	2000	6.32	2000
10.18	2000	8.14	2000	6.52	2000
11.91	2000	9.53	2000	7.62	2000
12.98	2000	10.38	2000	8.31	2000
14.55	2000	11.64	2000	9.31	2000
15.69	2000	12.55	2000	10.04	2000

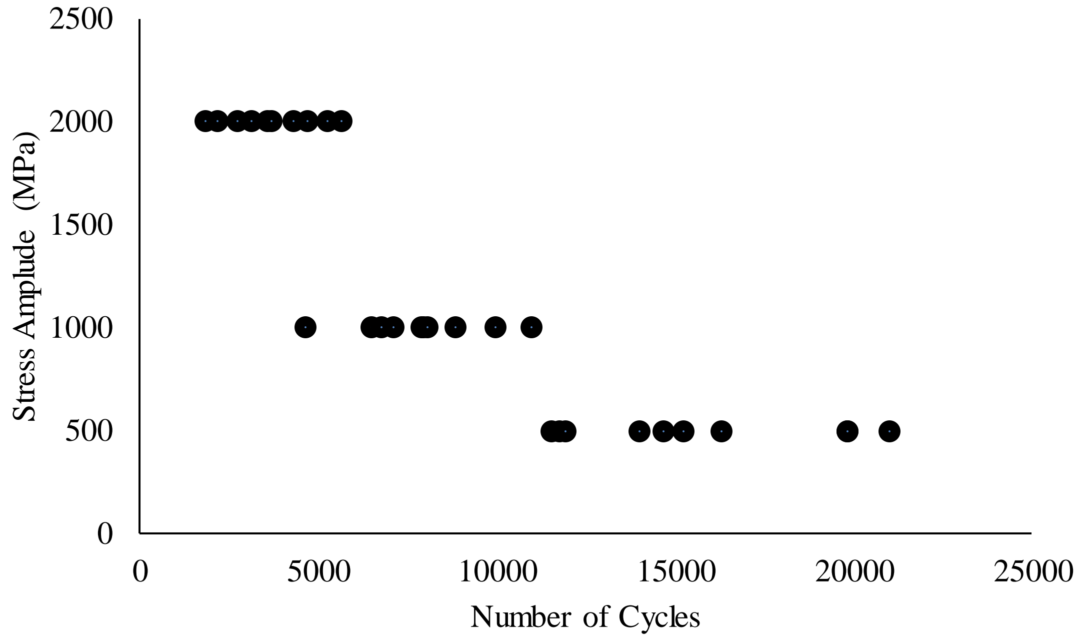

Figure D.1: S-N Curve for 0.5 µm patterned ITO traces tested at Stress amplitudes of 2000 MPa, 1000 MPa and 500 MPa tested until 10% change in normalized resistance was observed

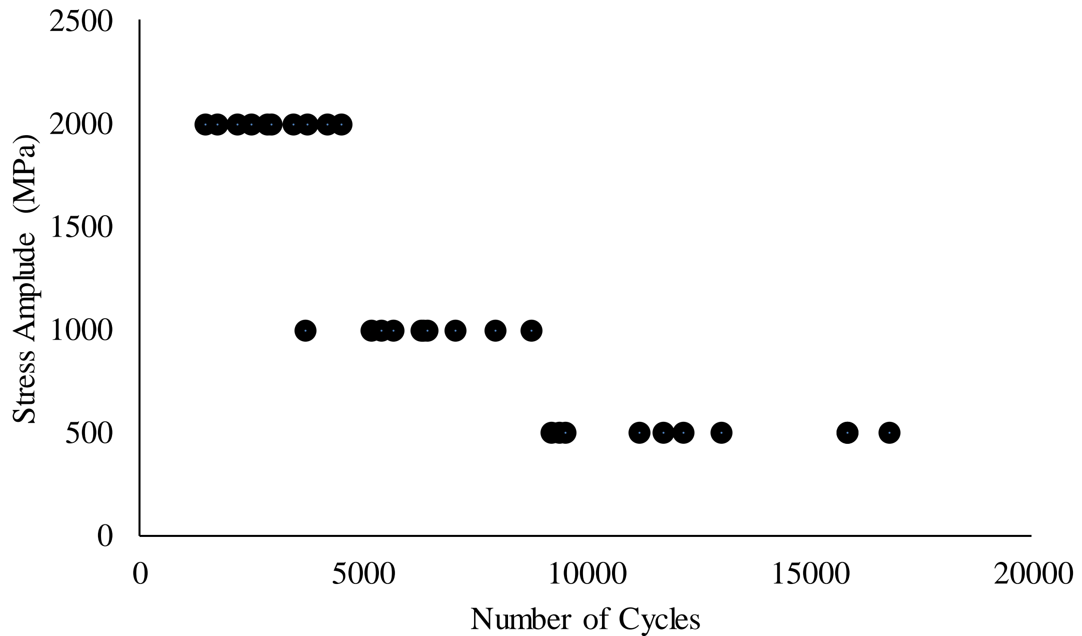

Figure D.2: S-N Curve for 0.75 µm patterned ITO traces tested at Stress amplitudes of 2000 MPa, 1000 MPa and 500 MPa tested until 10% change in normalized resistance was observed

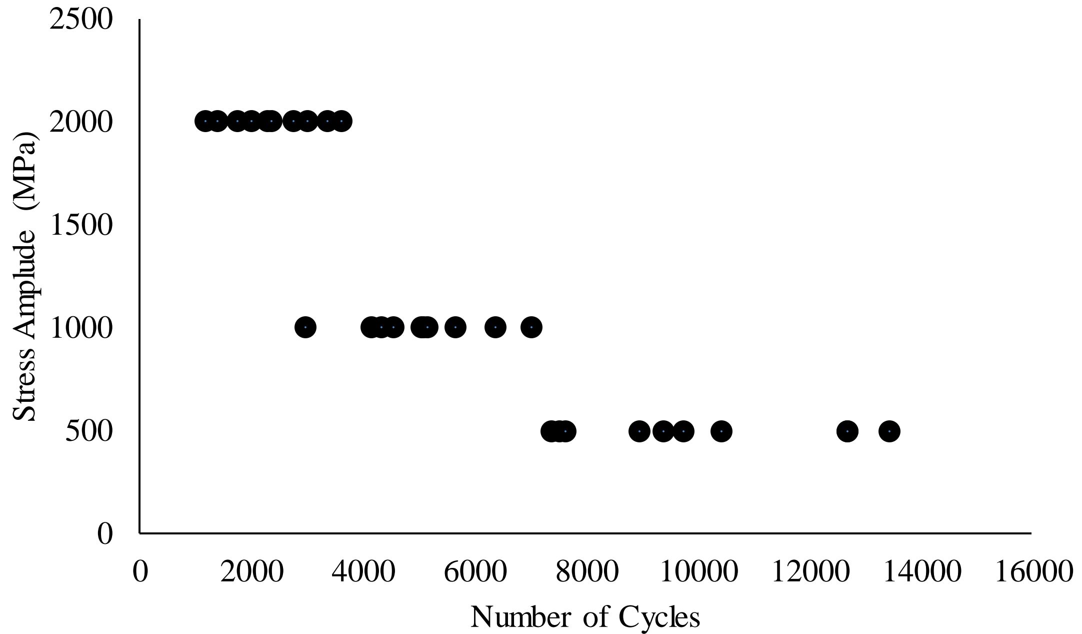

Figure D.3: S-N Curve for1.5 µm patterned ITO traces tested at Stress amplitudes of 2000 MPa, 1000 MPa and 500 MPa tested until 10% change in normalized resistance was observed

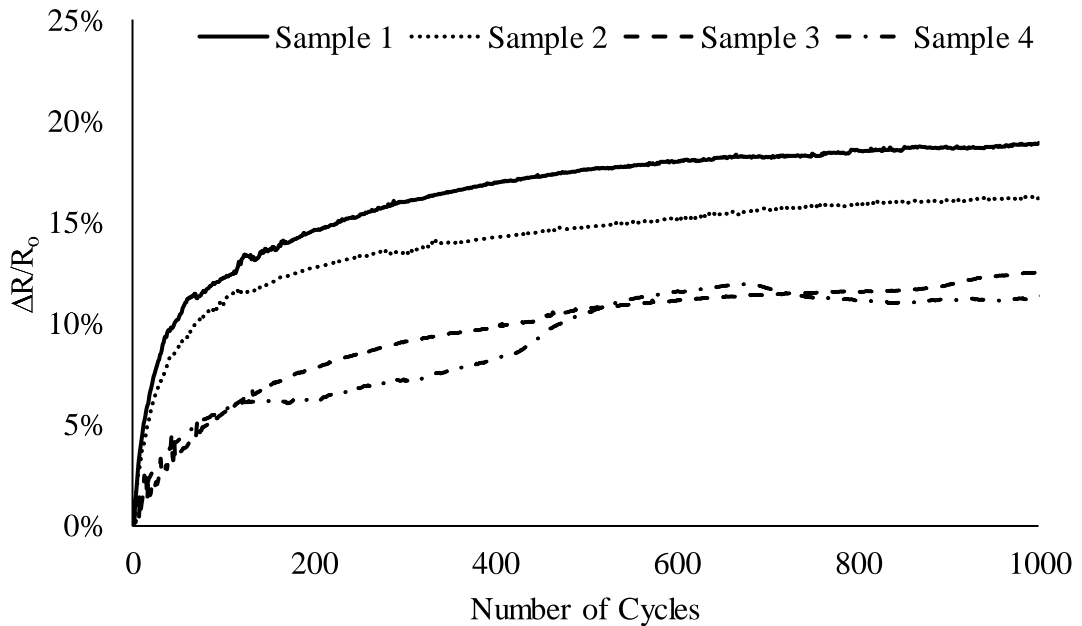

Figure D.4: Change in normalized resistance vs. Number of cycles for uniform ITO samples on Si_3N_4/PEN tested at 600 MPa

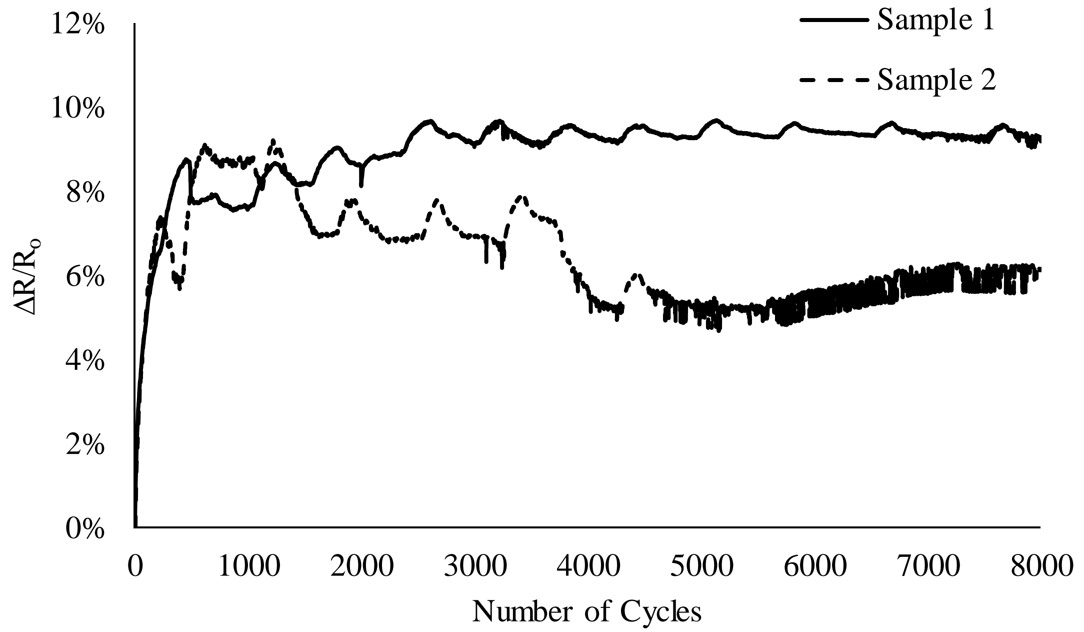

Figure D.5: Change in normalized resistance vs. Number of cycles for uniform ITO samples on Si_3N_4/PEN tested at 500 MPa

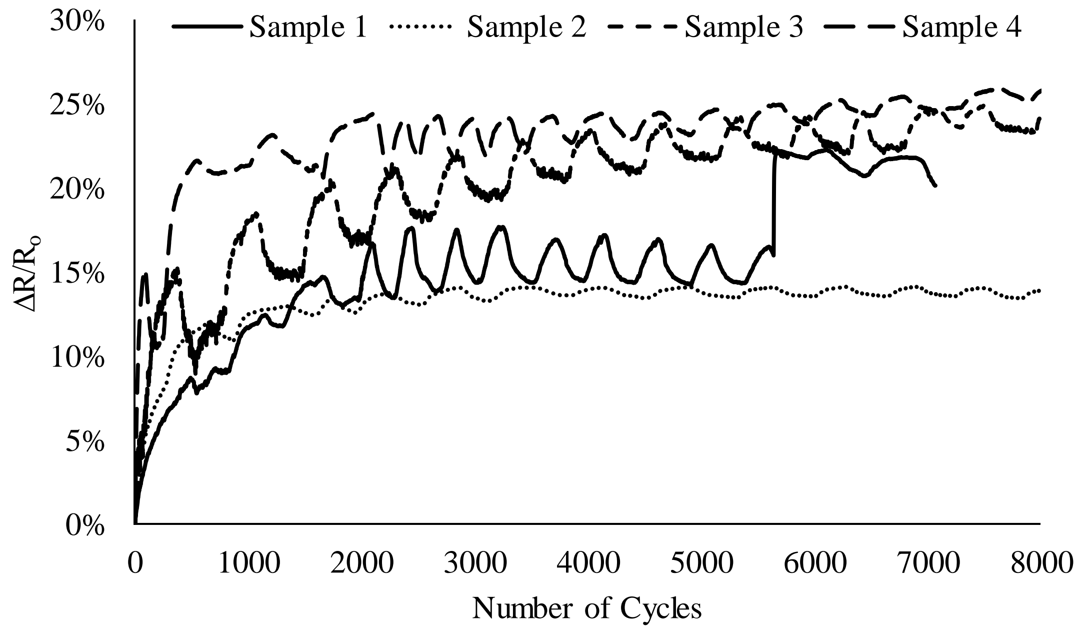

Figure D.6: Change in normalized resistance vs. Number of cycles for uniform ITO samples on Si_3N_4/PEN tested at 400 MPa

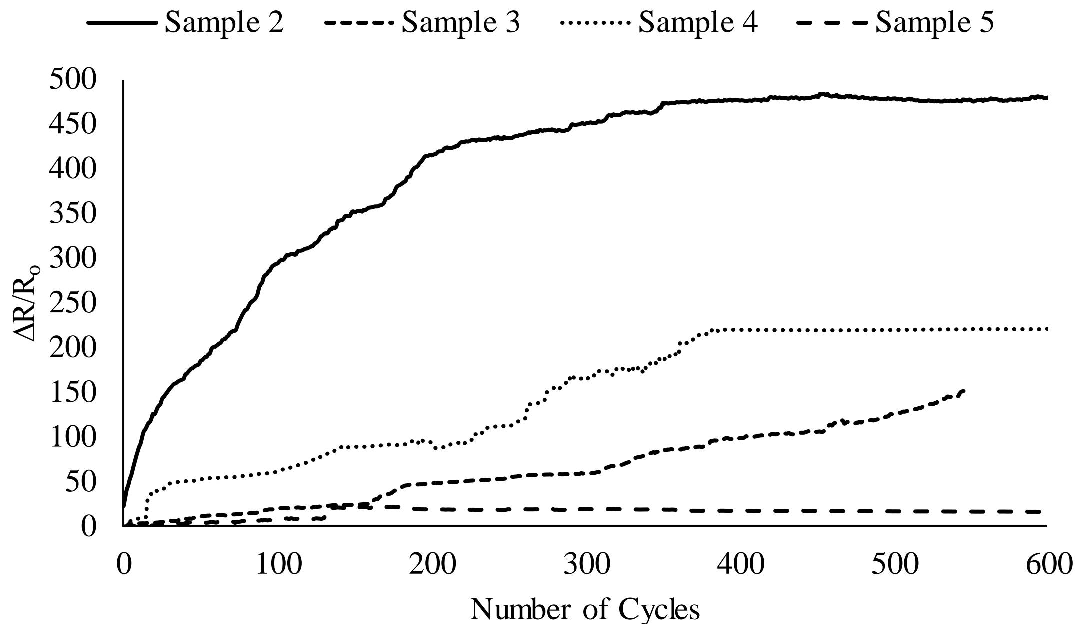

Figure D.7: Change in normalized resistance vs. Number of cycles for uniform Graphene samples on Si_3N_4/PEN tested at 80 GPa

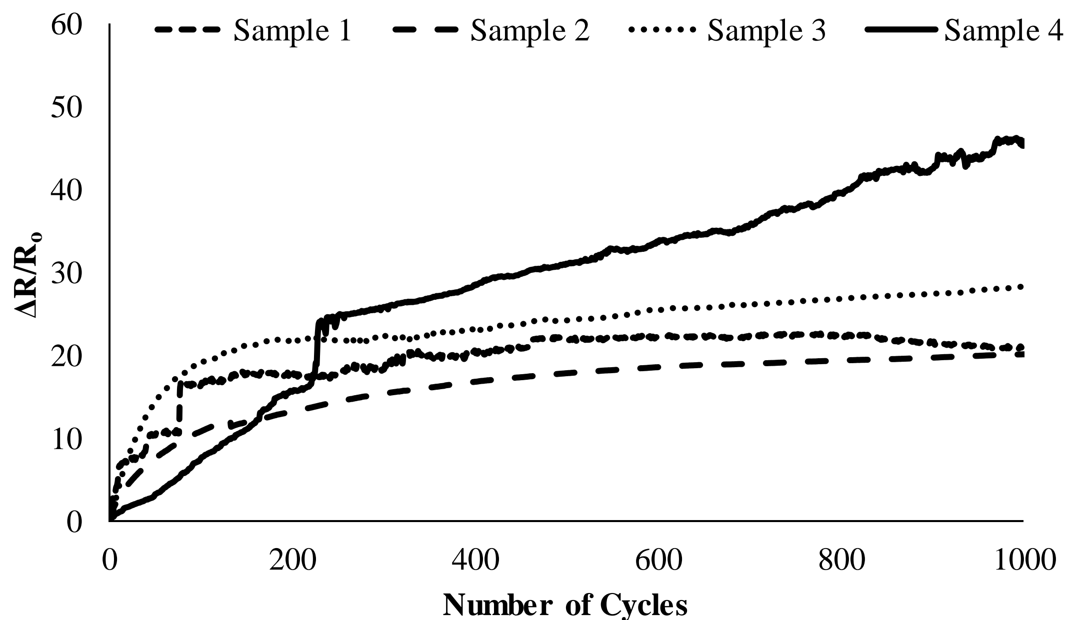

Figure D.8: Change in normalized resistance vs. Number of cycles for uniform Graphene samples on Si_3N_4/PEN tested at 60 GPa

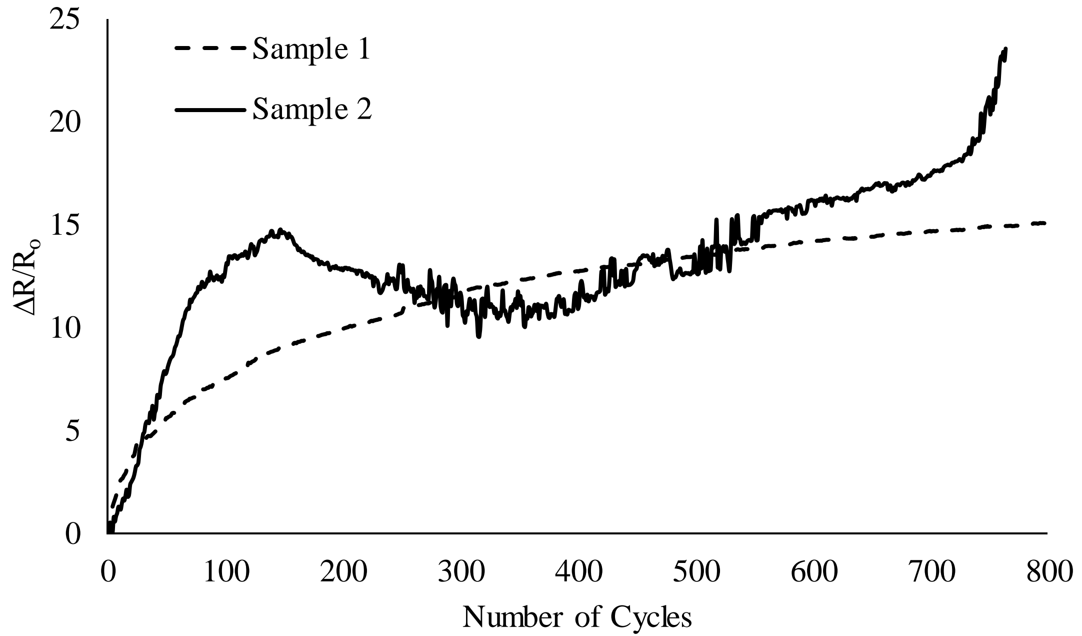

Figure D.9: Change in normalized resistance vs. Number of cycles for uniform Graphene samples on Si_3N_4/PEN tested at 50 GPa

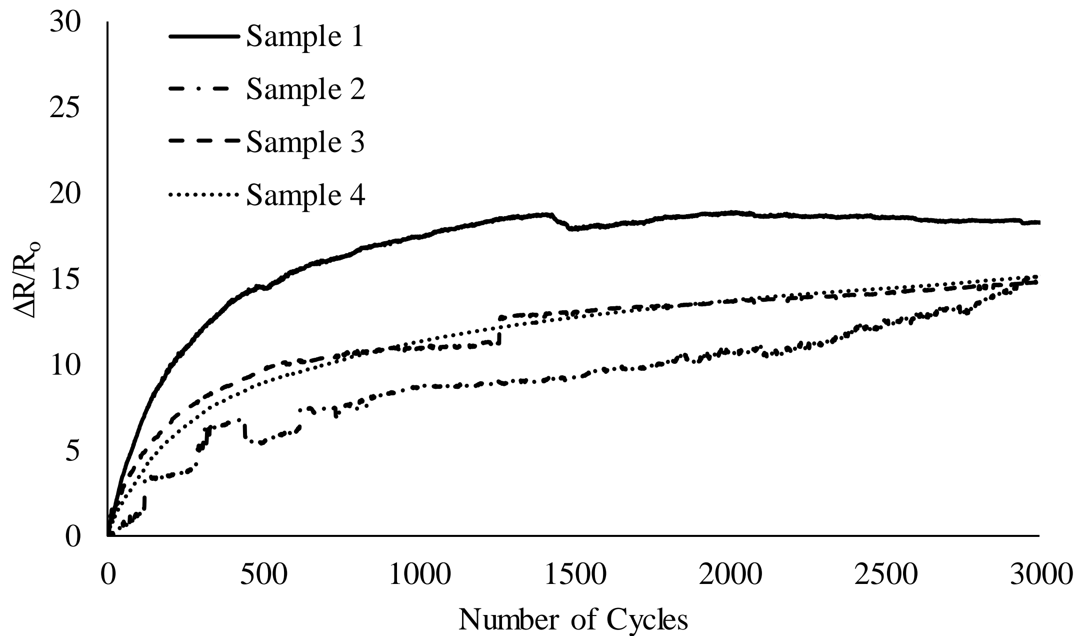

Figure D.10: Change in normalized resistance vs. Number of cycles for uniform Graphene samples on Si_3N_4/PEN tested at 40 GPa

Appendix E: Scanning Electron Microscopy Images

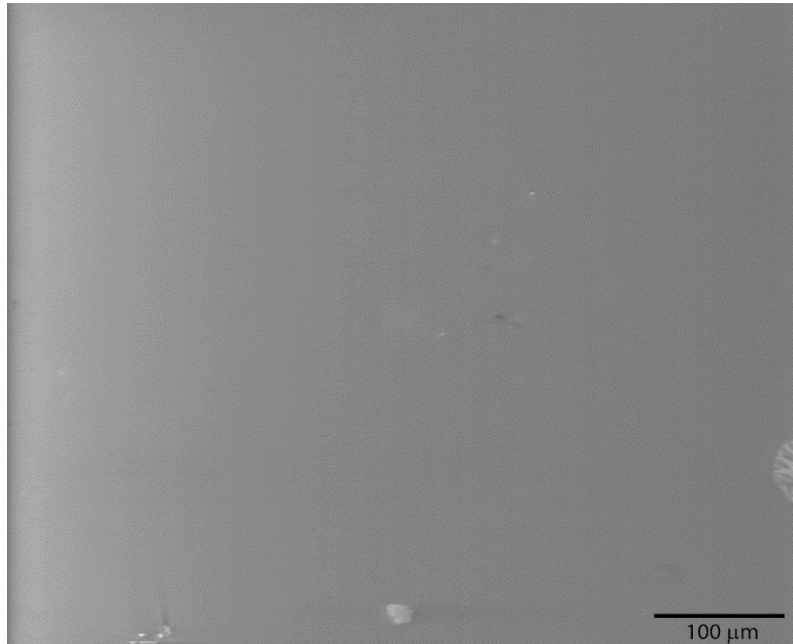

Figure E.1: SE-SEM image of Si_3N_4/PEN substrate taken at 500x

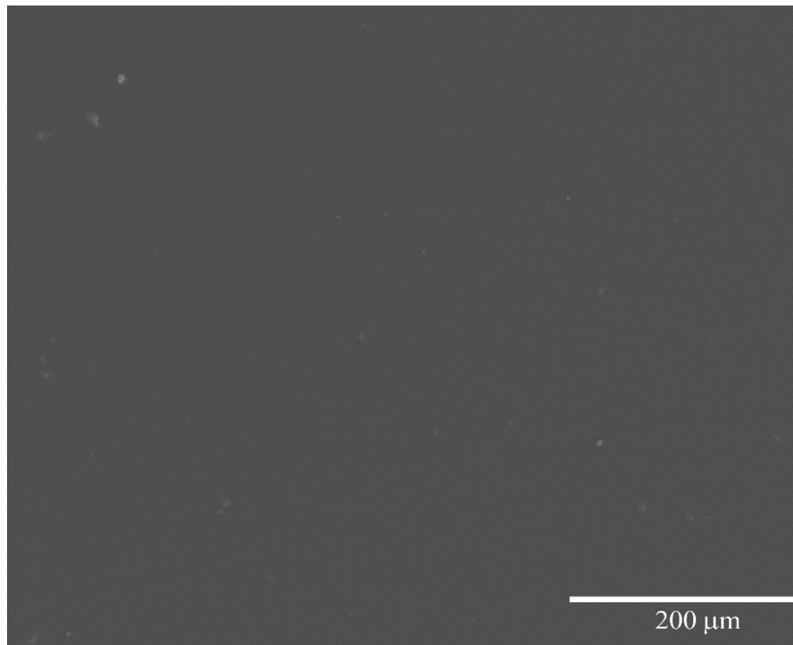

Figure E.2: SE-SEM image of Graphene taken at 424x

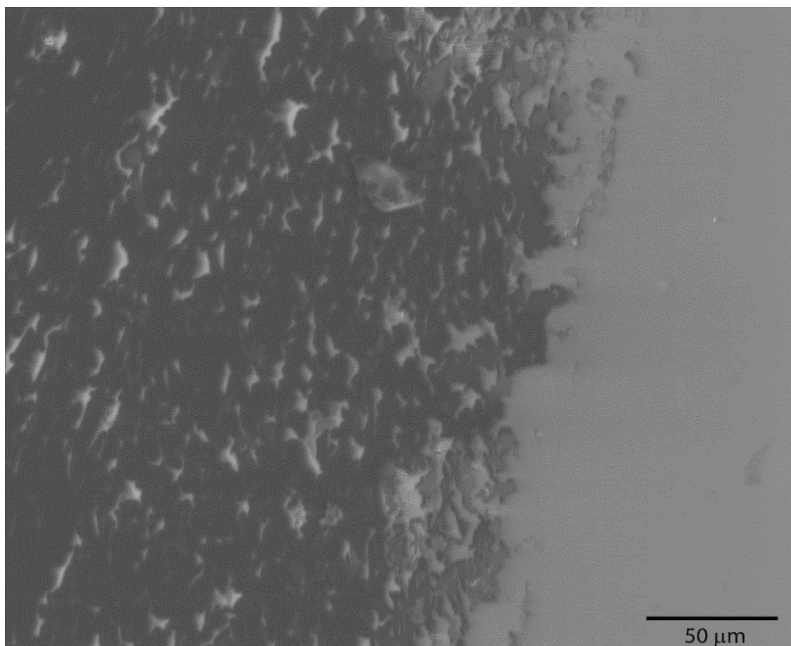

Figure E.3: SE-SEM image of Graphene-Si_3N_4/PEN interface taken at 500x

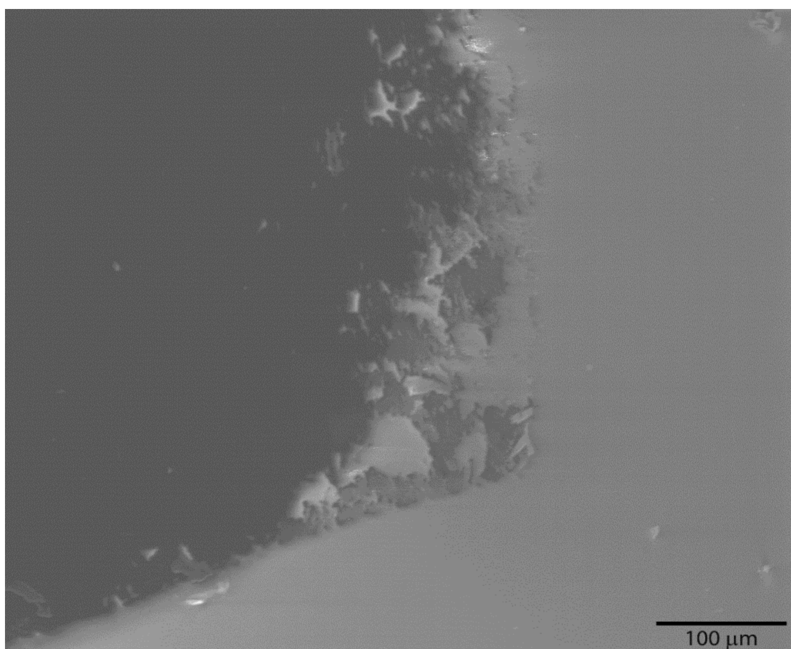

Figure E.4: SE-SEM image of Graphene-Si_3N_4/PEN interface taken at 1000x

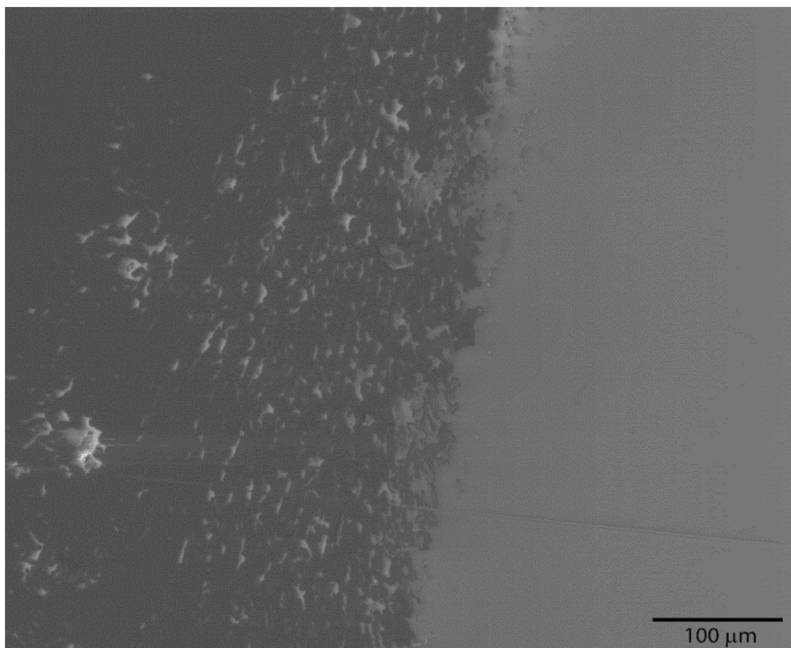

Figure E.5: SE-SEM image of Graphene-Si_3N_4/PEN interface taken at 1000x

References

[1] T. Martin, "A Physics of Failure Based Qualification Process for Flexible Display Interconnect Materials," University of Maryland, 2011.

[2] Z. Hutchinson, J.W, Suo, "Mixed Mode Cracking in Layered Devices," *Adv. Appl. Mechancis*, vol. 29, pp. 62–192, 1992.

[3] Z. Suo, "Fracture in thin films," *Encycl. Mater. Sci. Technol.*, pp. 1–17, 2001.

[4] J. Andersons, Y. Leterrier, and I. Fescenko, "Analysis of the initial fragmentation stage of oxide coatings on polymer substrates under biaxial tension," *Thin Solid Films*, vol. 434, no. 1–2, pp. 203–215, Jun. 2003.

[5] G. W. Tada H, Paris P C, Irwin, *The Stress Analysis of Cracks Handbook*. St. Louis, Missouri: Del Research,, 1985.

[6] D. Kolosov, D. S. English, V. Bulovic, P. F. Barbara, S. R. Forrest, and M. E. Thompson, "Direct observation of structural changes in organic light emitting devices during degradation," *J. Appl. Phys.*, vol. 90, no. 7, p. 3242, Oct. 2001.

[7] P. E. Burrows, V. Bulovic, S. R. Forrest, L. S. Sapochak, D. M. McCarty, and M. E. Thompson, "Reliability and degradation of organic light emitting devices," *Appl. Phys. Lett.*, vol. 65, no. 23, p. 2922, Dec. 1994.

[8] M. S. Weaver, L. A. Michalski, K. Rajan, M. A. Rothman, J. A. Silvernail, J. J. Brown, P. E. Burrows, G. L. Graff, M. E. Gross, P. M. Martin, M. Hall, E. Mast, C. Bonham, W. Bennett, and M. Zumhoff, "Organic light-emitting devices with extended operating lifetimes on plastic substrates," *Appl. Phys. Lett.*, vol. 81, no. 16, p. 2929, Oct. 2002.

[9] G. P. Crawford and B. Paine, D., Yeom, H., Yaglioglu, *Flexible Flat Panel Displays*. West Sussex, England: John Wiley & Sons, Ltd, 2005, pp. 79–98.

[10] A. S. da Silva Sobrinho, G. Czeremuszkin, M. Latrèche, and M. R. Wertheimer, "Defect-permeation correlation for ultrathin transparent barrier coatings on polymers," *J. Vac. Sci. Technol. A Vacuum, Surfaces, Film.*, vol. 18, no. 1, p. 149, Jan. 2000.

[11] G. Rossi and M. Nulman, "Effect of local flaws in polymeric permeation reducing barriers," *J. Appl. Phys.*, vol. 74, no. 9, p. 5471, Nov. 1993.

[12] E. H. H. Jamieson and A. H. Windle, "Structure and oxygen-barrier properties of metallized polymer film," *J. Mater. Sci.*, vol. 18, no. 1, pp. 64–80, Jan. 1983.

[13] W. Prins and J. J. Hermans, “Theory of Permeation through Metal Coated Polymer Films,” *J. Phys. Chem.*, vol. 63, no. 5, pp. 716–720, May 1959.

[14] Chatham H., “Oxygen diffusion barrier properties of transparent oxide coatings on polymeric substrates,” *Surf. Coatings Technol.*, vol. 78, no. 1, p. 9, 1996.

[15] W. Hanika, H., Langowski, H.-C., and Peukert, “Simulation and verification of defect-dominated permeation mechanisms in multiple structures of inorganic and polymeric barrier layers,” in *46th Annual Technical Conference Proceedings, Society of Vacuum Coaters*, 2003, pp. 592–599.

[16] B. . Henry, A. . Erlat, A. McGuigan, C. R. . Grovenor, G. A. . Briggs, Y. Tsukahara, T. Miyamoto, N. Noguchi, and T. Niijima, “Characterization of transparent aluminium oxide and indium tin oxide layers on polymer substrates,” *Thin Solid Films*, vol. 382, no. 1–2, pp. 194–201, Feb. 2001.

[17] Erlat A.G., Henry B.M., Ingram J.J., Mountain D.B., McGuigan A., Howson R.P., Grovenor C.R.M., Briggs G.A.D., and Tsukahara Y., “Characterisation of aluminium oxynitride gas barrier films,” *Thin Solid Films*, vol. 388, no. 1, p. 9.

[18] A. P. P. Roberts, B. M. M. Henry, A. P. P. Sutton, C. R. M. R. M. Grovenor, G. A. D. A. D. Briggs, T. Miyamoto, M. Kano, Y. Tsukahara, and M. Yanaka, “Gas permeation in silicon-oxide / polymer (SiOx/PET) barrier films : role of the oxide lattice, nano-defects and macro-defects,” *J. Memb. Sci.*, vol. 208, no. 1–2, pp. 75–88, Oct. 2002.

[19] B. Decker, W. Henry, “Basic Principles of thin film barrier coatings,” in *Soceity of Vacuum Coaters*, 2002, pp. 492–502.

[20] P. Schaepkens, M., Erlat, A. G., Kim, T.W., Jan, M., Heller, C. M. and McConnelee, “Ultra-high barrier coatings on polymer substrates for flexible optoelectronics: water vapor transport and measurement systems,” in *47th Annual Technical Conference Proceeding, Society of Vacuum Coaters*, 2004, p. 654.

[21] U. Hanika, H., Langowski, H.-C. and Moosheimer, “Layer defects and the synergetic effect between inorganic and organic barrier layers,” in *45th Annual Technical Conference Proceedings, Society of Vacuum Coaters*, 2002, pp. 519–524.

[22] L. . Coffin, “A study of the effects of cyclic thermal stresses on a ductile metal,” *ASME*, vol. 76, pp. 931–950, 1954.

[23] S. Manson, “Behavior of materials under conditions of thermal stress,” National Advisory Committee for Aeronautics, Cleveland OH, 1954.

[24] S. Manson, "Fatigue a Complex Subject - Some simple approximations," *Exp. Mech.*, vol. 5, no. 7, p. 193, 1965.

[25] J. Morrow, "Cyclic Plastic Strain Energy and Fatigue of Metals," *Am. Soc. Test. Mater.*, vol. 378, p. 45, 1964.

[26] D. of Defense, "Reliability Prediction of Electronic Equipmemnt - MIL-HDBK-217F," 1991.

[27] M. Modarres, M. Kaminskiy, and V. Krivtsov, *Realiability Engineering and Risk Analysis: A Practical Guide*, vol. 0. CRC Press, 1999, p. 542.

[28] P. O'Connor and A. Kleyner, *Practical reliability engineering*. 2011.

[29] W. Callister and D. Rethwisch, *Fundamentals of materials science and engineering: an integrated approach*. Wiley and Sons, 2012.

[30] J. . McPherson, *Reliability Physics and Engineering: Time To Failure Modeling*, 3rd ed. New York: Springer, 2010.

[31] G. Haacke, "New figure of merit for transparent conductors," *J. Appl. Phys.*, vol. 47, no. 9, p. 4086, 1976.

[32] I. Hamberg and C. G. Granqvist, "Evaporated Sn-doped In2O3 films: Basic optical properties and applications to energy-efficient windows," *J. Appl. Phys.*, vol. 60, no. 11, p. R123, 1986.

[33] A. Walsh and C. R. a. Catlow, "Structure, stability and work functions of the low index surfaces of pure indium oxide and Sn-doped indium oxide (ITO) from density functional theory," *J. Mater. Chem.*, vol. 20, no. 46, p. 10438, 2010.

[34] V. Korobov, M. Leibovitch, and Y. Shapira, "Structure and conductance evolution of very thin indium oxide films," *Appl. Phys. Lett.*, vol. 65, no. 18, p. 2290, 1994.

[35] X. W. Sun, H. C. Huang, and H. S. Kwok, "On the initial growth of indium tin oxide on glass," *Appl. Phys. Lett.*, vol. 68, no. 19, p. 2663, 1996.

[36] Y. Han, D. Kim, J.-S. Cho, Y.-W. Beag, S.-K. Koh, and V. S. Chernysh, "Effects of substrate treatment on the initial growth mode of indium-tin-oxide films," *J. Appl. Phys.*, vol. 97, no. 2, p. 024910, 2005.

[37] Y. Sato, M. Taketomo, N. Ito, A. Miyamura, and Y. Shigesato, "Comparative study on early stages of film growth for transparent conductive oxide films

deposited by dc magnetron sputtering," *Thin Solid Films*, vol. 516, no. 14, pp. 4598–4602, May 2008.

[38] C.-H. Liang, S.-C. Chen, X. Qi, C.-S. Chen, and C.-C. Yang, "Influence of film thickness on the texture, morphology and electro-optical properties of indium tin oxide films," *Thin Solid Films*, vol. 519, no. 1, pp. 345–350, Oct. 2010.

[39] Y. Shigesato, S. Takaki, and T. Haranou, "Crystallinity and electrical properties of tin-doped indium oxide films deposited by DC magnetron sputtering," *Appl. Surf. Sci.*, vol. 48–49, pp. 269–275, Jan. 1991.

[40] H. Kim, J. S. Horwitz, G. Kushto, a. Piqué, Z. H. Kafafi, C. M. Gilmore, and D. B. Chrisey, "Effect of film thickness on the properties of indium tin oxide thin films," *J. Appl. Phys.*, vol. 88, no. 10, p. 6021, 2000.

[41] W. Kostlin, H., Jost, R., Lems, "Optical and electrical properties of doped In2O3 Films," *Phys. Statis Solidi*, vol. 29, pp. 87–93, 1975.

[42] Y. Shigesato and D. C. Paine, "A microstructural study of low resistivity tin-doped indium oxide prepared by d.c. magnetron sputtering," *Thin Solid Films*, vol. 238, no. 1, pp. 44–50, Jan. 1994.

[43] W.-F. Wu, B.-S. Chiou, and S.-T. Hsieh, "Effect of sputtering power on the structural and optical properties of RF magnetron sputtered ITO films," *Semicond. Sci. Technol.*, vol. 9, no. 6, pp. 1242–1249, Jun. 1994.

[44] F. Kurdesau, G. Khripunov, a. F. da Cunha, M. Kaelin, and a. N. Tiwari, "Comparative study of ITO layers deposited by DC and RF magnetron sputtering at room temperature," *J. Non. Cryst. Solids*, vol. 352, no. 9–20, pp. 1466–1470, Jun. 2006.

[45] M. H. Eisa, M. G. Faraj, F. Azhari, M. Ali, K. Ibrahim, and O. Hamad, "Deposited indium tin oxide (ITO) thin films by dc-magnetron sputtering on polyethylene terephthalate substrate (PET)," *Rom J Phys*, vol. 56, no. 5–6, pp. 730–741, 2011.

[46] T. . Neerinck, D.G., Vink, "Depth profiling of thin ITO films by gazing incidence X-Ray diffraction," *Thin Film Solids*, vol. 278, pp. 12–17, 1996.

[47] J. Leterrier, Y, Medico, L, Bouton, PCP, De Geode, "Layer mechanics of optimized materials," 2003.

[48] D. R. Cairns, R. P. Witte, D. K. Sparacin, S. M. Sachsman, D. C. Paine, G. P. Crawford, R. R. Newton, and R. P. W. Ii, "Strain-dependent electrical

resistance of tin-doped indium oxide on polymer substrates," *Appl. Phys. Lett.*, vol. 76, no. 11, p. 1425, 2000.

[49] Y. Leterrier, L. Médico, F. Demarco, J. -a. E. Månson, U. Betz, M. F. Escolà, M. Kharrazi Olsson, and F. Atamny, "Mechanical integrity of transparent conductive oxide films for flexible polymer-based displays," *Thin Solid Films*, vol. 460, no. 1–2, pp. 156–166, Jul. 2004.

[50] D. R. Cairns and G. P. G. P. Crawford, "Electromechanical Properties of Transparent Conducting Substrates for Flexible Electronic Displays," *Proc. IEEE*, vol. 93, no. 8, pp. 1451–1458, Aug. 2005.

[51] P. Bouten, "On Integrity of flexible dispalys," in *Fracture Mechanics of Ceramics 8*, 2003, pp. 597–608.

[52] C. G. . Gorkhali, S.J, Cairns D.R and S. Gorkhali, "Reliability of transparent conducting substrates for rollable displays: A cyclic loading investigation," ... *Inf. Disp.*, vol. 12, pp. 45–49, 2004.

[53] K. Alzoubi, S. Lu, B. Sammakia, and M. Poliks, "Experimental and Analytical Studies on the High Cycle Fatigue of Thin Film Metal on PET Substrate for Flexible Electronics Applications," *IEEE Trans. Components, Packag. Manuf. Technol.*, vol. 1, no. 1, pp. 43–51, Jan. 2011.

[54] K. Alzoubi, M. M. Hamasha, S. Lu, and B. Sammakia, "Bending Fatigue Study of Sputtered ITO on Flexible Substrate," vol. 7, no. 11, pp. 593–600, 2011.

[55] R. Haering, "Band structure of rhombohedral graphite," *Can. J. Phys.*, vol. 36, no. 3, pp. 352 – 362, 1958.

[56] J. Warner, "Graphene fundamentals and emergent applications." Elsevier,, Amsterdam ;;New York :, 2013.

[57] A. Yacoby, "Graphene: Tri and tri again," *Nat. Phys.*, vol. 7, no. 12, pp. 925–926, Dec. 2011.

[58] J. S. Choi, J.-S. Kim, I.-S. Byun, D. H. Lee, M. J. Lee, B. H. Park, C. Lee, D. Yoon, H. Cheong, K. H. Lee, Y.-W. Son, J. Y. Park, and M. Salmeron, "Friction anisotropy-driven domain imaging on exfoliated monolayer graphene.," *Science*, vol. 333, no. 6042, pp. 607–10, Jul. 2011.

[59] Y. Hernandez, V. Nicolosi, M. Lotya, F. M. Blighe, Z. Sun, S. De, I. T. McGovern, B. Holland, M. Byrne, Y. K. Gun'Ko, J. J. Boland, P. Niraj, G. Duesberg, S. Krishnamurthy, R. Goodhue, J. Hutchison, V. Scardaci, A. C. Ferrari, and J. N. Coleman, "High-yield production of graphene by liquid-

phase exfoliation of graphite.," *Nat. Nanotechnol.*, vol. 3, no. 9, pp. 563–8, Sep. 2008.

[60] N. C. Johnson, S. Manchester, L. Sarin, Y. Gao, I. Kulaots, and R. H. Hurt, "Mercury Vapor Release from Broken Compact Fluorescent Lamps and In Situ Capture by New Nanomaterial Sorbents," *Environ. Sci. Technol.*, vol. 42, no. 15, pp. 5772–5778, Aug. 2008.

[61] K. Novoselov, A. Geim, and S. Morozov, "Electric field effect in atomically thin carbon films," *Science (80-.).*, vol. 306, no. 5696, pp. 666–669, 2004.

[62] W. Zhao, M. Fang, F. Wu, H. Wu, L. Wang, and G. Chen, "Preparation of graphene by exfoliation of graphite using wet ball milling," *J. Mater. Chem.*, vol. 20, no. 28, p. 5817, 2010.

[63] A. . Karu and M. J. Beer, "Pyrolytic formation of highly crystalline graphite films," *J. Appl. Phys.*, vol. 37, 1966.

[64] C. Mattevi, H. Kim, and M. Chhowalla, "A review of chemical vapour deposition of graphene on copper," *J. Mater. Chem.*, vol. 21, no. 10, p. 3324, 2011.

[65] A. Reina, X. Jia, J. Ho, D. Nezich, H. Son, V. Bulovic, M. S. Dresselhaus, and J. Kong, "Large area, few-layer graphene films on arbitrary substrates by chemical vapor deposition.," *Nano Lett.*, vol. 9, no. 1, pp. 30–5, Jan. 2009.

[66] M. Rümmeli and C. Rocha, "Graphene: Piecing it together," *Adv. ...*, 2011.

[67] Y. Zhang, L. Gomez, F. N. Ishikawa, A. Madaria, K. Ryu, C. Wang, A. Badmaev, and C. Zhou, "Comparison of Graphene Growth on Single-Crystalline and Polycrystalline Ni by Chemical Vapor Deposition," *J. Phys. Chem. Lett.*, vol. 1, no. 20, pp. 3101–3107, Oct. 2010.

[68] C. Oshima and A. Nagashima, "Ultra-thin epitaxial films of graphite and hexagonal boron nitride on solid surfaces," *J. Phys. Condens. Matter*, vol. 9, no. 1, pp. 1–20, Jan. 1997.

[69] M. H. Rümmeli, A. Bachmatiuk, F. Börrnert, F. Schäffel, I. Ibrahim, K. Cendrowski, G. Simha-Martynkova, D. Plachá, E. Borowiak-Palen, G. Cuniberti, and B. Büchner, "Synthesis of carbon nanotubes with and without catalyst particles.," *Nanoscale Res. Lett.*, vol. 6, no. 1, p. 303, Jan. 2011.

[70] T. Ong and F. Xiong, "Nucleation and growth of diamond on carbon-implanted single crystal copper surfaces," *J. Mater. ...*, vol. 7, no. 9, pp. 2429–2439, 1992.

[71] L. Constant, C. Speisser, and F. Le Normand, "HFCVD diamond growth on Cu(111). Evidence for carbon phase transformations by in situ AES and XPS," *Surf. Sci.*, vol. 387, no. 1–3, pp. 28–43, Oct. 1997.

[72] X. Li, W. Cai, J. An, S. Kim, J. Nah, D. Yang, R. Piner, A. Velamakanni, I. Jung, E. Tutuc, S. K. Banerjee, L. Colombo, and R. S. Ruoff, "Large-area synthesis of high-quality and uniform graphene films on copper foils.," *Science*, vol. 324, no. 5932, pp. 1312–4, Jun. 2009.

[73] M. P. Levendorf, C. S. Ruiz-Vargas, S. Garg, and J. Park, "Transfer-free batch fabrication of single layer graphene transistors.," *Nano Lett.*, vol. 9, no. 12, pp. 4479–83, Dec. 2009.

[74] W. Cai, Y. Zhu, X. Li, R. D. Piner, and R. S. Ruoff, "Large area few-layer graphene/graphite films as transparent thin conducting electrodes," *Appl. Phys. Lett.*, vol. 95, no. 12, p. 123115, 2009.

[75] Y. Lee, S. Bae, H. Jang, S. Jang, S.-E. Zhu, S. H. Sim, Y. Il Song, B. H. Hong, and J.-H. Ahn, "Wafer-scale synthesis and transfer of graphene films.," *Nano Lett.*, vol. 10, no. 2, pp. 490–3, Feb. 2010.

[76] Y.-H. Lee and J.-H. Lee, "Scalable growth of free-standing graphene wafers with copper(Cu) catalyst on SiO[sub 2]/Si substrate: Thermal conductivity of the wafers," *Appl. Phys. Lett.*, vol. 96, no. 8, p. 083101, 2010.

[77] A. Ismach, C. Druzgalski, S. Penwell, A. Schwartzberg, M. Zheng, A. Javey, J. Bokor, and Y. Zhang, "Direct chemical vapor deposition of graphene on dielectric surfaces.," *Nano Lett.*, vol. 10, no. 5, pp. 1542–8, May 2010.

[78] A. Srivastava, C. Galande, L. Ci, L. Song, C. Rai, D. Jariwala, K. F. Kelly, and P. M. Ajayan, "Novel Liquid Precursor-Based Facile Synthesis of Large-Area Continuous, Single, and Few-Layer Graphene Films," *Chem. Mater.*, vol. 22, no. 11, pp. 3457–3461, Jun. 2010.

[79] S. Bae, H. R. Kim, Y. Lee, X. Xu, J.-S. Park, Y. Zheng, J. Balakrishnan, T. Lei, Y. Il Song, Y.-J. Kim, K. S. Kim, B. Ozyilmaz, J.-H. Ahn, B. H. Hong, and S. Iijima, "Roll-to-roll production of 30-inch graphene films for transparent electrodes.," *Nat. Nanotechnol.*, vol. 5, no. 8, pp. 574–8, Aug. 2010.

[80] X. Li, C. W. Magnuson, A. Venugopal, J. An, J. W. Suk, B. Han, M. Borysiak, W. Cai, A. Velamakanni, Y. Zhu, L. Fu, E. M. Vogel, E. Voelkl, L. Colombo, and R. S. Ruoff, "Graphene films with large domain size by a two-step chemical vapor deposition process.," *Nano Lett.*, vol. 10, no. 11, pp. 4328–34, Nov. 2010.

[81] I. Vlassiouk, M. Regmi, P. Fulvio, S. Dai, P. Datskos, G. Eres, S. Smirnov, and C. Graphene, “Role of Hydrogen in Chemical Vapor Deposition Growth of Large Single-,” *ACS Nano*, vol. 5, no. 7, pp. 6069–6076, Jul. 2011.

[82] Y. A. Wu, A. W. Robertson, F. Schäffel, S. C. Speller, and J. H. Warner, “Aligned Rectangular Few-Layer Graphene Domains on Copper Surfaces,” *Chem. Mater.*, vol. 23, no. 20, pp. 4543–4547, Oct. 2011.

[83] F. Hao, D. Fang, and Z. Xu, “Mechanical and thermal transport properties of graphene with defects,” *Appl. Phys. Lett.*, vol. 99, no. 4, p. 041901, Jul. 2011.

[84] R. Ansari, B. Motevalli, A. Montazeri, and S. Ajori, “Fracture analysis of monolayer graphene sheets with double vacancy defects via MD simulation,” *Solid State Commun.*, vol. 151, no. 17, pp. 1141–1146, Sep. 2011.

[85] K. S. Kim, Y. Zhao, H. Jang, S. Y. Lee, J. M. Kim, K. S. Kim, J.-H. Ahn, P. Kim, J.-Y. Choi, and B. H. Hong, “Large-scale pattern growth of graphene films for stretchable transparent electrodes.,” *Nature*, vol. 457, no. 7230, pp. 706–10, Feb. 2009.

[86] Y.-C. Lin, C. Jin, J.-C. Lee, S.-F. Jen, K. Suenaga, and P.-W. Chiu, “Clean transfer of graphene for isolation and suspension.,” *ACS Nano*, vol. 5, no. 3, pp. 2362–8, Mar. 2011.

[87] A. Reina, H. Son, L. Jiao, B. Fan, M. S. Dresselhaus, Z. Liu, and J. Kong, “Transferring and Identification of Single- and Few-Layer Graphene on Arbitrary Substrates,” *J. Phys. Chem. C*, vol. 112, no. 46, pp. 17741–17744, Nov. 2008.

[88] W. Regan, N. Alem, B. Alemán, B. Geng, C. Girit, L. Maserati, F. Wang, M. Crommie, and a. Zettl, “A direct transfer of layer-area graphene,” *Appl. Phys. Lett.*, vol. 96, no. 11, p. 113102, 2010.

[89] V. P. Verma, S. Das, I. Lahiri, and W. Choi, “Large-area graphene on polymer film for flexible and transparent anode in field emission device,” *Appl. Phys. Lett.*, vol. 96, no. 20, p. 203108, May 2010.

[90] S. Dutta and S. K. Pati, “Novel properties of graphene nanoribbons: a review,” *J. Mater. Chem.*, vol. 20, no. 38, p. 8207, Sep. 2010.

[91] S. Reich, “Tight-binding description of graphene,” *Phys. Rev. B*, vol. 66, no. 3, 2002.

[92] P. R. Wallace, “The Band Theory of Graphite,” *Phys. Rev.*, vol. 71, no. 9, p. 622, 1947.

[93] J.-C. Charlier and S. Roche, "Electronic and transport properties of nanotubes," *Rev. Mod. Phys.*, vol. 79, no. 2, pp. 677–732, May 2007.

[94] a. H. Castro Neto, N. M. R. Peres, K. S. Novoselov, and a. K. Geim, "The electronic properties of graphene," *Rev. Mod. Phys.*, vol. 81, no. 1, pp. 109–162, Jan. 2009.

[95] a K. Geim and K. S. Novoselov, "The rise of graphene.," *Nat. Mater.*, vol. 6, no. 3, pp. 183–91, Mar. 2007.

[96] Y. Zhang, Y.-W. Tan, H. L. Stormer, and P. Kim, "Experimental observation of the quantum Hall effect and Berry's phase in graphene.," *Nature*, vol. 438, no. 7065, pp. 201–4, Nov. 2005.

[97] K. S. Novoselov, D. Jiang, F. Schedin, T. J. Booth, V. V Khotkevich, S. V Morozov, and a K. Geim, "Two-dimensional atomic crystals.," *Proc. Natl. Acad. Sci. U. S. A.*, vol. 102, no. 30, pp. 10451–3, Jul. 2005.

[98] K. S. Novoselov, a K. Geim, S. V Morozov, D. Jiang, M. I. Katsnelson, I. V Grigorieva, S. V Dubonos, and a a Firsov, "Two-dimensional gas of massless Dirac fermions in graphene.," *Nature*, vol. 438, no. 7065, pp. 197–200, Nov. 2005.

[99] M. Ishigami, J. H. Chen, W. G. Cullen, M. S. Fuhrer, and E. D. Williams, "Atomic structure of graphene on SiO2.," *Nano Lett.*, vol. 7, no. 6, pp. 1643–8, Jun. 2007.

[100] J. Moser, a. Barreiro, and a. Bachtold, "Current-induced cleaning of graphene," *Appl. Phys. Lett.*, vol. 91, no. 16, p. 163513, 2007.

[101] M. I. Katsnelson, K. S. Novoselov, and a. K. Geim, "Chiral tunnelling and the Klein paradox in graphene," *Nat. Phys.*, vol. 2, no. 9, pp. 620–625, Aug. 2006.

[102] J.-H. Chen, C. Jang, S. Adam, M. S. Fuhrer, E. D. Williams, and M. Ishigami, "Charged-impurity scattering in graphene," *Nat. Phys.*, vol. 4, no. 5, pp. 377–381, Apr. 2008.

[103] K. I. Bolotin, K. J. Sikes, Z. Jiang, M. Klima, G. Fudenberg, J. Hone, P. Kim, and H. L. Stormer, "Ultrahigh electron mobility in suspended graphene," *Solid State Commun.*, vol. 146, no. 9–10, pp. 351–355, Jun. 2008.

[104] C. R. Dean, a F. Young, I. Meric, C. Lee, L. Wang, S. Sorgenfrei, K. Watanabe, T. Taniguchi, P. Kim, K. L. Shepard, and J. Hone, "Boron nitride substrates for high-quality graphene electronics.," *Nat. Nanotechnol.*, vol. 5, no. 10, pp. 722–6, Oct. 2010.

[105] T. Ando, "Screening Effect and Impurity Scattering in Monolayer Graphene," *J. Phys. Soc. Japan*, vol. 75, no. 7, p. 074716, Jul. 2006.

[106] V. Cheianov and V. Fal'ko, "Friedel Oscillations, Impurity Scattering, and Temperature Dependence of Resistivity in Graphene," *Phys. Rev. Lett.*, vol. 97, no. 22, p. 226801, Nov. 2006.

[107] E. H. Hwang, S. Adam, and S. Das Sarma, "Carrier transport in 2D graphene layers," vol. 4111, 2006.

[108] E. Hwang, S. Adam, and S. Sarma, "Carrier Transport in Two-Dimensional Graphene Layers," *Phys. Rev. Lett.*, vol. 98, no. 18, p. 186806, May 2007.

[109] M. Katsnelson, F. Guinea, and a. Geim, "Scattering of electrons in graphene by clusters of impurities," *Phys. Rev. B*, vol. 79, no. 19, p. 195426, May 2009.

[110] K. Nomura and a. H. MacDonald, "Quantum Transport of Massless Dirac Fermions," *Phys. Rev. Lett.*, vol. 98, no. 7, p. 076602, Feb. 2007.

[111] K. Nomura and A. H. MacDonald, "Quantum Hall Ferromagnetism in Graphene," *Phys. Rev. Lett.*, vol. 96, no. 25, p. 256602, Jun. 2006.

[112] M. Trushin and J. Schliemann, "Conductivity of graphene: How to distinguish between samples with short- and long-range scatterers," *EPL (Europhysics Lett.*, vol. 83, no. 1, p. 17001, Jul. 2008.

[113] S. Adam, E. H. Hwang, V. M. Galitski, and S. Das Sarma, "A self-consistent theory for graphene transport.," *Proc. Natl. Acad. Sci. U. S. A.*, vol. 104, no. 47, pp. 18392–7, Nov. 2007.

[114] E. Hwang and S. Das Sarma, "Limit to two-dimensional mobility in modulation-doped GaAs quantum structures: How to achieve a mobility of 100 million," *Phys. Rev. B*, vol. 77, no. 23, p. 235437, Jun. 2008.

[115] Y.-W. Tan, Y. Zhang, K. Bolotin, Y. Zhao, S. Adam, E. H. Hwang, S. Das Sarma, H. L. Stormer, and P. Kim, "Measurement of Scattering Rate and Minimum Conductivity in Graphene," *Phys. Rev. Lett.*, vol. 99, no. 24, p. 246803, Dec. 2007.

[116] E. Hwang and S. Das Sarma, "Screening-induced temperature-dependent transport in two-dimensional graphene," *Phys. Rev. B*, vol. 79, no. 16, p. 165404, Apr. 2009.

[117] K. I. Bolotin, K. J. Sikes, J. Hone, H. L. Stormer, and P. Kim, "Temperature-Dependent Transport in Suspended Graphene," *Phys. Rev. Lett.*, vol. 101, no. 9, p. 096802, Aug. 2008.

[118] Y.-W. Tan, Y. Zhang, H. L. Stormer, and P. Kim, "Temperature dependent electron transport in graphene," *Eur. Phys. J. Spec. Top.*, vol. 148, no. 1, pp. 15–18, Sep. 2007.

[119] W. Zhu, V. Perebeinos, M. Freitag, and P. Avouris, "Carrier scattering, mobilities, and electrostatic potential in monolayer, bilayer, and trilayer graphene," *Phys. Rev. B*, vol. 80, no. 23, p. 235402, Dec. 2009.

[120] J.-H. Chen, C. Jang, S. Xiao, M. Ishigami, and M. S. Fuhrer, "Intrinsic and extrinsic performance limits of graphene devices on SiO2.," *Nat. Nanotechnol.*, vol. 3, no. 4, pp. 206–9, Apr. 2008.

[121] S. V Rotkin, V. Perebeinos, A. G. Petrov, and P. Avouris, "An essential mechanism of heat dissipation in carbon nanotube electronics.," *Nano Lett.*, vol. 9, no. 5, pp. 1850–5, May 2009.

[122] M. S. Fuhrer, "Textbook physics from a cutting-edge material," *Physics (College. Park. Md).*, vol. 3, p. 106, Dec. 2010.

[123] T. Stauber, N. Peres, and F. Guinea, "Electronic transport in graphene: A semiclassical approach including midgap states," *Phys. Rev. B*, vol. 76, no. 20, p. 205423, Nov. 2007.

[124] E. Hwang and S. Das Sarma, "Acoustic phonon scattering limited carrier mobility in two-dimensional extrinsic graphene," *Phys. Rev. B*, vol. 77, no. 11, p. 115449, Mar. 2008.

[125] T. Kawamura and S. Das Sarma, "Phonon-scattering-limited electron mobilities in Al_{x}Ga_{1-x}As/GaAs heterojunctions," *Phys. Rev. B*, vol. 45, no. 7, pp. 3612–3627, Feb. 1992.

[126] S. Das Sarma, S. Adam, E. H. Hwang, and E. Rossi, "Electronic transport in two-dimensional graphene," *Rev. Mod. Phys.*, vol. 83, no. 2, pp. 407–470, May 2011.

[127] S. V Morozov, K. S. Novoselov, M. I. Katsnelson, F. Schedin, D. C. Elias, J. A. Jaszczak, and A. K. Geim, "Giant Intrinsic Carrier Mobilities in Graphene and Its Bilayer," vol. 016602, no. January, pp. 11–14, 2008.

[128] X. Li, Y. Zhu, W. Cai, M. Borysiak, B. Han, D. Chen, R. D. Piner, L. Colombo, and R. S. Ruoff, "Transfer of large-area graphene films for high-performance transparent conductive electrodes.," *Nano Lett.*, vol. 9, no. 12, pp. 4359–63, Dec. 2009.

[129] R. Nair, P. Blake, and A. Grigorenko, "Fine structure constant defines visual transparency of graphene," *Science (80-.).*, vol. 320, no. June, p. 2008, 2008.

[130] C. Lee, X. Wei, J. W. Kysar, and J. Hone, “Measurement of the elastic properties and intrinsic strength of monolayer graphene.,” *Science*, vol. 321, no. July, pp. 385–8, Jul. 2008.

[131] H. Zhao, K. Min, and N. R. Aluru, “Size and chirality dependent elastic properties of graphene nanoribbons under uniaxial tension.,” *Nano Lett.*, vol. 9, no. 8, pp. 3012–5, Aug. 2009.

[132] X.-W. Fu, Z.-M. Liao, J.-X. Zhou, Y.-B. Zhou, H.-C. Wu, R. Zhang, G. Jing, J. Xu, X. Wu, W. Guo, and D. Yu, “Strain dependent resistance in chemical vapor deposition grown graphene,” *Appl. Phys. Lett.*, vol. 99, no. 21, p. 213107, 2011.

[133] M. Huang, T. a Pascal, H. Kim, W. a Goddard, and J. R. Greer, “Electronic--mechanical coupling in graphene from in situ nanoindentation experiments and multiscale atomistic simulations.,” *Nano Lett.*, vol. 11, no. 3, pp. 1241–6, Mar. 2011.

[134] V. Zardetto, T. M. Brown, A. Reale, and A. Di Carlo, “Substrates for flexible electronics: A practical investigation on the electrical, film flexibility, optical, temperature, and solvent resistance properties,” *J. Polym. Sci. Part B Polym. Phys.*, vol. 49, no. 9, pp. 638–648, May 2011.

[135] W. a. MacDonald, M. K. Looney, D. MacKerron, R. Eveson, R. Adam, K. Hashimoto, and K. Rakos, “Latest advances in substrates for flexible electronics,” *J. Soc. Inf. Disp.*, vol. 15, no. 12, p. 1075, 2007.

[136] P. C. P. Bouten, P. J. Slikkerveer, and Y. Leterrier, “Mechanics of ITO on Plastic Substrates for Flexible Displays,” in *Flexible Flat Panel Displays*, 2005.

[137] T. D. Films, “Properties of High Performance Films.” [Online]. Available: http://www.teijindupontfilms.jp/english/product/hi_film.html.

[138] Plasma.com, “Fabricating Color TFT LCD Displays,” *plasma.com*, 2010. [Online]. Available: http://www.plasma.com/classroom/fabricating_tft_lcd.htm. [Accessed: 07-Jun-2013].

[139] I. ANSYS, “ANSYS Academic Research.” Canonsburg, Pennsylvania, 2011.

[140] G. G. Stoney, “The Tension of Metallic Films Deposited by Electrolysis,” *Proc. R. Soc. A Math. Phys. Eng. Sci.*, vol. 82, no. 553, pp. 172–175, May 1909.

[141] Z. Gleskova, H., Wagner, S. and Suo, “a-Si:H TFTs made on polyimide foil by PECVD at 150C,” in *Materials Research Society Symposium Proceedings*, 1998, pp. 73–78.

[142] Z. Suo, E. Y. Ma, H. Gleskova, and S. Wagner, “Mechanics of rollable and foldable film-on-foil electronics,” *Appl. Phys. Lett.*, vol. 74, no. 8, p. 1177, 1999.

[143] P. C. . Bouton, “Failure Test for brittle conductive layers on flexible display strcutres,” in *Proceedings of Eurodisplay*, 2002, pp. 313–316.

[144] Y. Leterrier, D. Pellaton, and D. Mendels, “Biaxial fragmentation of thin silicon oxide coatings on poly (ethylene terephthalate),” *J. Mater. ...*, vol. 6, pp. 2213–2225, 2001.

[145] P. I. Hsu, R. Bhattacharya, H. Gleskova, M. Huang, Z. Xi, Z. Suo, S. Wagner, and J. C. Sturm, “Thin-film transistor circuits on large-area spherical surfaces,” *Appl. Phys. Lett.*, vol. 81, no. 9, p. 1723, 2002.

[146] F. Tuinstra, “Raman Spectrum of Graphite,” *J. Chem. Phys.*, vol. 53, no. 3, p. 1126, 1970.

[147] a. C. Ferrari, J. C. Meyer, V. Scardaci, C. Casiraghi, M. Lazzeri, F. Mauri, S. Piscanec, D. Jiang, K. S. Novoselov, S. Roth, and a. K. Geim, “Raman Spectrum of Graphene and Graphene Layers,” *Phys. Rev. Lett.*, vol. 97, no. 18, p. 187401, Oct. 2006.

[148] A. C. Ferrari, “Raman spectroscopy of graphene and graphite: Disorder, electron–phonon coupling, doping and nonadiabatic effects,” *Solid State Commun.*, vol. 143, no. 1–2, pp. 47–57, Jul. 2007.

[149] L. M. Malard, M. a. Pimenta, G. Dresselhaus, and M. S. Dresselhaus, “Raman spectroscopy in graphene,” *Phys. Rep.*, vol. 473, no. 5–6, pp. 51–87, Apr. 2009.

[150] P. W. Sutter, J.-I. Flege, and E. a Sutter, “Epitaxial graphene on ruthenium.,” *Nat. Mater.*, vol. 7, no. 5, pp. 406–11, May 2008.

[151] Y. Hao, Y. Wang, L. Wang, Z. Ni, Z. Wang, R. Wang, C. K. Koo, Z. Shen, and J. T. L. Thong, “Probing layer number and stacking order of few-layer graphene by Raman spectroscopy.,” *Small*, vol. 6, no. 2, pp. 195–200, Jan. 2010.

[152] I. Childres, L. Jauregui, W. Park, H. Cao, and Y. Chen, “RAMAN SPECTROSCOPY OF GRAPHENE AND RELATED MATERIALS,” *physics.purdue.edu*.

[153] A. C. Ferrari and D. M. Basko, "Raman spectroscopy as a versatile tool for studying the properties of graphene.," *Nat. Nanotechnol.*, vol. 8, no. 4, pp. 235–46, Apr. 2013.

[154] L. Cançado, A. Jorio, and E. Ferreira, "Quantifying defects in graphene via Raman spectroscopy at different excitation energies," *Nano ...*, pp. 1–7, 2011.

[155] G. Fisichella, S. Di Franco, P. Fiorenza, R. Lo Nigro, F. Roccaforte, C. Tudisco, G. G. Condorelli, N. Piluso, N. Spartà, S. Lo Verso, C. Accardi, C. Tringali, S. Ravesi, and F. Giannazzo, "Micro- and nanoscale electrical characterization of large-area graphene transferred to functional substrates.," *Beilstein J. Nanotechnol.*, vol. 4, no. 1, pp. 234–42, Jan. 2013.

[156] W. S. Rasband, "ImageJ," *U. S. National Institutes of Health*. [Online]. Available: http://imagej.nih.gov/ij/.

[157] R. Corporation, "Reliasoft Weibull++/ALTA Pro." Reliasoft Corporation, Tuscon, AZ.